Numerical Modelling of Breaking Waves under the Influence of Wind

Zhihua Xie

Submitted in accordance with the requirements for the degree of

Doctor of Philosophy

The University of Leeds

Centre for Computational Fluid Dynamics

March 2010

The candidate confirms that the work submitted is his own and that appropriate credit has been given where reference has been made to the work of others.

To My Parents

and

My Wife

Acknowledgements

I would like to express my sincere gratitude to my supervisors, Dr. Xianyun Wen and Dr. Andrew Ross, for their continuous support, guidance and encouragement. I am deeply indebted to my supervisor, Dr. Xianyun Wen, for his endless patience and constructive criticism, and for enlarging my knowledge of Computational Fluid Dynamics (CFD) and providing me academic freedom to pursue this research. I am greatly inspired by his attitude to novelty and high quality of the research. I would like to thank my supervisor, Dr. Andrew Ross, for his valuable suggestions. I am impressed by his broad knowledge of physics, and he always asked me to "dig deep" and "think more", which improved my understanding and interpretation of the results.

It is an honuor for me to have the opportunity to study at the Centre for CFD at the University of Leeds, where provided me the generous Marie Curie Fellowship for my Ph.D. study. I also would like to thank all the people there for their help and friendship. I own thanks to Dr. Alan Burns at Ansys Europe Ltd for his enthusiastic advice on multiphase flow and turbulence modelling, to Mr. James McKay for his administrative assistance along the way of my study, and to my former colleague, Dr. Ashish Raval, for his kind assistance at the beginning of my study and later discussion on water waves.

Many thanks are due to the people in the Scientific Computation Research Group in the School of Computing, especially to Professor Peter Jimack, Dr. Matthew Hubbard and Dr. Mark Walkley, for helping me gain insight into numerical methods and shallow water flow modelling. I really enjoyed the seminar series during last three years.

I would like to thank Dr. Andrew Sleigh in the School of Civil Engineering for fruitful discussions on free surface flows, and Dr. Jonathan Carrivick in the

School of Geography for providing me some experimental experiences for dam break flows.

I am grateful for my previous postgraduate supervisor, Professor Jianguo Lin at Dalian Maritime University, for leading me to the world of hydrodynamics and for his continuous encouragement.

I also would like to thank many researchers all over the world, who have patiently replied my questions regarding free surface flows through email, although we have never met before.

Finally, I would like to express my deepest appreciation to my family and friends. I cannot thank my parents enough for their support and attention throughout my whole life. My lovely wife, Yu Wang, deserves special thanks for her understanding and support during my study. I cannot accomplish this thesis without her smile and love every day.

Abstract

Wave breaking plays an important role in air-sea interaction, surf zone dynamics, nearshore sediment transport, marine hydrodynamics, and wave-structure interaction. When the wind is blowing over water waves, it not only enhances the exchanges of heat, mass and momentum on the air-water interface, but also affects the wave breaking process.

The objective of this thesis is to contribute to the understanding of breaking waves under the influence of wind. A two-phase flow model is presented to solve the flow in the air and water simultaneously. Two strategies for turbulence modelling, namely, the Reynolds-averaged Navier–Stokes (RANS) equations with the $k-\epsilon$ turbulence model and Large Eddy Simulation (LES) with the Smagorinsky subgrid-scale model, are employed to study two-dimensional (2D) and three-dimensional (3D) breaking waves, respectively. The governing equations are solved by the finite volume method in a Cartesian staggered grid and the partial cell treatment is implemented to deal with complex geometries. The SIMPLE or PISO algorithms are utilized for the pressure-velocity coupling and a backward finite difference discretization is used for the time derivative. The air-water interface is modelled by the interface capturing method via a high resolution VOF (Volume of Fluid) scheme. The numerical model is validated by simulating 2D overturning waves on a sloping beach and over a reef, and 3D solitary wave run-up on a conical island, in which good agreement between numerical results and experimental measurements is obtained. Moreover, the overturning jet and subsequent splash-up are captured in the computation.

The numerical model is further employed to investigate 2D breaking solitary waves on a sloping beach, 2D periodic breaking waves (both spilling and plunging breakers) in the surf zone, and 3D overturning waves over a submerged conical island. Numerical results in the absence of wind are presented and compared

with available experimental data, and then the effect of wind is included in the computation of breaking waves.

The key findings of this thesis are that the wind can influence the kinematics and dynamics of breaking waves, as onshore winds assist the development of water particle velocities towards the critical wave phase speed, cause the wave to break earlier in a deeper water further off shore. There is recirculation of air flow above the wave crest in the absence of wind whereas air flow separation is observed in the presence of a sufficiently strong wind. In addition, the wind affects the shape of the overturning jet, generation of vorticity, and energy transformation and dissipation during wave breaking.

This study has contributed to the characteristics of breaking waves, focusing on the period during wave overturning. The information gained in this study shed some light on wind effects on breaking waves, which have import implications for coastal engineering and air-sea interaction.

Contents

List of Figures

List of Tables

Nomenclature

Roman Symbols

A	the area of the face of a control volume	m^2	L^2	page 35
a	wave amplitude	m	L	page 2
a^ϕ	coefficients in algebraic equations			page 46
A^+	constant in the damping function			page 159
B	user specified boundary condition			page 30
b_{P}^ϕ	source term in algebraic equations			page 46
$\boldsymbol{g}$	gravitational acceleration vector	m/s^2	LT^{-2}	page 29
$\boldsymbol{i}$	unit vector in x direction			page 70
$\boldsymbol{j}$	unit vector in y direction			page 70
$\boldsymbol{k}$	unit vector in z direction			page 70
$\boldsymbol{n}$	unit outward normal vector to a surface			page 30
$\boldsymbol{t}$	unit tangential vector to a surface			page 30
$\boldsymbol{u}$	velocity vector $= (u, v, w)$	m/s	LT^{-1}	page 28
C	wave phase speed	m/s	LT^{-1}	page 2
$C_{1\epsilon}$	empirical coefficient in the $k-\epsilon$ model			page 67
$C_{2\epsilon}$	empirical coefficient in the $k-\epsilon$ model			page 67
C_μ	empirical coefficient in the $k-\epsilon$ model			page 67
C_S	Smagorinsky coefficient			page 158
D	water depth	m	L	page 2
d	local still water depth	m	L	page 124
$d_{\mathrm{w}}()$	damping function in the near-wall region			page 159
E^+	coefficient for a smooth wall			page 68
f	face of the control volume			page 33
F	volume fraction			page 29
f_w	wave frequency	Hz	T^{-1}	page 2
g	gravitational acceleration	m/s^2	LT^{-2}	page 2
$G(x, x')$	filter kernel in LES			page 156
H	wave height	m	L	page 2
h	local mean water depth $h = d + \overline{\zeta}$	m	L	page 124

H_0	deep water wave height	m	L	page 7
I	turbulent intensity			page 67
I_ϵ	the ratio between the μ_t and μ			page 67
k	turbulent kinetic energy	m^2/s^2	L^2T^{-2}	page 66
k_w	wavenumber	m^{-1}	L^{-1}	page 2
L	wave length	m	L	page 2
L_0	deep water wave length	m	L	page 7
L_S	Smagorinsky length scale	m	L	page 158
L_t	turbulent length scale	m	L	page 66
m	mass flux			page 39
m'	nonconservative form for the mass flux			page 41
N_ϕ	total number of the ensemble values			page 64
n^+	dimensionless distance from the wall			page 68
p	pressure	Pa	$ML^{-1}T^{-2}$	page 29
P_k	turbulent production term			page 67
Q_ϕ^{S0}	constant in the source term linearization			page 44
Q_ϕ^{S1}	constant in the source term linearization			page 44
Q_ϕ^{B}	body force term			page 45
Q_ϕ^{C}	convection term			page 38
Q_ϕ^{D}	diffusion term			page 43
Q_ϵ^{S}	source term discretization for ϵ			page 72
Q_k^{S}	source term discretization for k			page 72
Q_ϕ^{P}	pressure term			page 44
Q_ϕ^{S}	source term in the control volume			page 34
Q_ϕ^{T}	temporal discretization			page 45
Q_ϕ^{W}	the discretization of the diffusion flux on the solid boundary			page 44
R	run-up height or the height of the submerged body	m	L	page 92
r_{f}^m	the ratio of the mass flux between the conservative and nonconservative form			page 43
r_{f}^ϕ	the ratio of successive gradients of ϕ on the face of the control volume			page 40
S	the surface of the control volume	m^2	L^2	page 33
S_{ij}	strain rate	1/s	T^{-1}	page 158
T	wave period	s	T	page 2
t	time	s	T	page 28
U	wind speed	m/s	LT^{-1}	page 92
u	velocity in the x direction	m/s	LT^{-1}	page 28
u^+	shear velocity			page 68

u_τ	friction velocity			page 68
v	velocity in the y direction	m/s	LT^{-1}	page 28
V_t	turbulent velocity scale	m/s	LT^{-1}	page 66
w	velocity in the z direction	m/s	LT^{-1}	page 28
x	streamwise direction			page 2
y	spanwise direction			page 2
z	vertical direction			page 2

Greek Symbols

α_ϕ	under-relaxation factor			page 46
α	angle of the sloping wall or air-water interface			page 70
β	angle of the sloping beach			page 7
β_f	weight factor used in CICSAM scheme			page 58
δ_{ij}	Kronecker delta			page 66
Δx	grid length in the x direction	m	L	page 158
Δy	grid length in the y direction	m	L	page 158
Δz	grid length in the z direction	m	L	page 158
η	water surface elevation	m	L	page 2
Γ	viscosity			page 34
κ	von Kármán's constant			page 68
λ_f	the interpolation factor for face f=e, w, n, s, b, r			page 35
μ	dynamic viscosity of the fluid	Pa·s	$ML^{-1}T^{-1}$	page 29
μ^{SGS}	subgrid-scale eddy viscosity	Pa·s	$ML^{-1}T^{-1}$	page 158
μ_t	turbulent eddy viscosity	Pa·s	$ML^{-1}T^{-1}$	page 66
Ω	the volume of the control volume	m^3	L^3	page 33
ω	vorticity	1/s	T^{-1}	page 184
$\overline{\zeta}$	mean water surface elevation	m	L	page 124
ϕ	an arbitrary variable			page 64
$\Phi()$	step function			page 43
$\Psi()$	limiter function			page 40
$\partial\Omega$	boundary of the computational domain	m^2	L^2	page 30
ρ	the density of fluid	kg/m^3	ML^{-3}	page 28
σ	wave angular frequency	rad/s	T^{-1}	page 2
σ_ϵ	empirical coefficient in the $k-\epsilon$ model			page 67
σ_k	empirical coefficient in the $k-\epsilon$ model			page 67
Δt	time step	s	T	page 45
τ_{ij}^{SGS}	Subgrid-scale Reynolds stress in LES	Pa	$ML^{-1}T^{-2}$	page 157
τ_w	shear stress on the wall	Pa	$ML^{-1}T^{-2}$	page 69

θ	θ function for the control volume in FAVOR			page 37
Ω	a computational domain	m^3	L^3	page 30
ξ_0	surf similarity parameter, or Iribarren number			page 7
ζ	water surface elevation	m	L	page 124

Superscripts

*	Guessed value in pressure-velocity coupling	page 47
$'$	first corrected value in pressure-velocity coupling	page 47
$''$	second corrected value in pressure-velocity coupling	page 49
a	variable for the air	page 29
FOU	first order upwind scheme	page 39
HRS	high resolution scheme	page 40
n	value in previous time step	page 45
$n+1$	value in current time step	page 45
$\prime$	fluctuation of the variable in RANS and subgrid-scale property in LES	page 64
SOU	second order upwind scheme	page 40
w	variable for the water	page 29

Subscripts

A	value in the accepter cell	page 39
B	the value for back point of point P	page 37
b	the value for back face of the control volume P	page 37
c	the value for centre of the control volume P	page 37
D	value in the donor cell	page 39
E	the value for east point of point P	page 37
e	the value for east face of the control volume P	page 37
f	the value for the face of the control volume P	page 37
N	the value for north point of point P	page 37

n	the value for north face of the control volume P	page 37
P	the value for present point considered	page 37
R	the value for front point of point P	page 37
r	the value for front face of the control volume P	page 37
S	the value for south point of point P	page 37
s	the value for south face of the control volume P	page 37
U	value in the upwind cell	page 39
W	the value for west point of point P	page 37
w	the value for west face of the control volume P	page 37

Other Symbols

$\langle\underline{()}\rangle$	time averaging or ensemble averaging	page 64
$\overline{()}$	spatial filtering	page 156

Abbreviations

ADI	Alternating Direction Implicit
BEM	Boundary Element Method
BIEM	Boundary Integral Element Method
Bi-CGSTAB	Bi-Conjugate Gradients Stablized
CBC	Convection Boundedness Criteria
CFD	Computational Fluid Dynamics
CFL	Courant-Friedrichs-Lewy
CICSAM	Compressive Interface Capturing Scheme for Arbitrary Meshes
CIP	Constrained Interpolation Profile
CISPH	Correct Incompressible SPH
CLSVOF	Coupled Level Set and Volume Of Fluid
COBRAS	COrnell BReaking waves And Structures
DNS	Direct Numerical Simulation
DPIV	Digital Particle Image Velocimetry
FAVOR	Fractional-Area-Volume Obstacle Representation
FCT	Flux-Corrected Transport
FDM	Finite Difference Method
FEM	Finite Element Method
FVM	Finite Volume Method
GENSMAC	GENeralized Simplified Marker-And-Cell
KdV	Korteweg-de Vries
KP	Kadomtsev-Petviashvili
LANL	Los Alamos National Laboratory
LDV	Laser Doppler Velocimetry
LES	Large Eddy Simulation
MAC	Marker-And-Cell
MLPG_R	Meshless Local Petrov-Galerkin method based on Rankine source solution
MPS	Moving Particle Semi-implicit
NLS	NonLinear Schrödinger
NVD	Normalized Variable Diagram
NWT	Numerical Wave Tank
PDE	Partial Differential Equation
PFEM	Particle Finite Element Methods
PISO	Pressure-Implicit with Splitting of Operators

PIV	Particle Image Velocimetry
PLIC	Piecewise Linear Interface Calculation
RANS	Reynolds-Averaged Navier-Stokes
RIPPLE	A computer program for incompressible flows with free surfaces
RLW	Regularized Long Wave
RNG	Re-Normalized Group
SGS	Subgrid-Scale
SIMPLE	Semi-Implicit Method for Pressure-Linked Equations
SIMPLEC	SIMPLE-Consistent
SIMPLER	SIMPLE-Rivised
SIP	Strongly Implicit Procedure
SLIC	Simple Line Interface Calculation
SL-VOF	Segment Lagrangian - VOF
SMAC	Simplified Marker And Cell
SMMC	Surface Marker and Micro Cell
SOLA-VOF	A solution algorithm for transient fluid flow with multiple free boundaries
SPH	Smooth Particle Hydrodynamics
TDMA	Tridiagonal Matrix Algorithm
TVD	Total Variation Diminishing
VOF	Volume Of Fluid

Chapter 1

Introduction

The water wave problem has been one of the fascinating topics of fluid mechanics for many years. There have been no shortage of theoretical studies of water waves, motivated by mathematicians from the nineteenth century, and the problem has also attracted many researchers using experimental and numerical techniques to better understand the relevant processes associated with water waves. Water waves start to break when their amplitude reaches a critical level as widely seen in the ocean and nearshore region. Wave breaking plays an important role in air-sea interaction, surf zone dynamics, nearshore sediment transport, marine hydrodynamics, and wave-structure interaction.

Previous investigations of breaking waves have greatly improved our knowledge of the wave breaking process, but the present state-of-the-art is still far from satisfactory. This thesis deals with breaking waves under the influence of wind via numerical simulations. When the wind is blowing over water waves, it can not only enhance the exchanges of heat, mass and momentum on the air-water interface, but also affect the wave breaking process. This study tries to shed some light on this problem in order to better understand the kinematics and dynamics of breaking waves.

In this chapter, after introducing water wave mechanics, we review the background of breaking wave studies. Then the effects of wind on water waves are explored and some relevant investigations available in the literature are briefly discussed. After that, the scope of the thesis is described, and finally the outline of the thesis is presented.

1.1 Water Wave Mechanics

Unsteady free surface flows subjected to gravitational forces are called water waves (Mader, 2004). They are also called gravity waves. Gravity waves on an air-water interface are known as surface waves while internal gravity waves are named internal waves.

There are different water waves in nature (Mader, 2004), which include wind-generated waves in the open ocean, flood waves in rivers and lakes, seiche or long-period oscillations in harbour basins, wakes produced by moving ships, tidal bores or moving hydraulic jumps in estuaries, tsunami waves generated by underwater earthquakes or landslides, and waves generated by underwater explosions.

Figure 1.1 shows the characteristics of a water wave over a flat bottom, where L is the wave length, H is the wave height, D is the water depth, $a = H/2$ is the wave amplitude, η is the water surface elevation, and the coordinate axis that will be used in this study is located at the still water line. The angular wavenumber is defined as $k_w = 2\pi/L$, the angular frequency is $\sigma = 2\pi/T$, where T is the period of the wave, and the wave phase speed is $C = L/T$. Thus, three important parameters are:

- $\frac{D}{L}$: relative depth.
- $\frac{H}{D}$: relative height.
- $\frac{H}{L}$: wave steepness.

Water waves can be classified in a number of useful ways. One classification is by the frequency f_w, which is the reciprocal of the period T. Kinsman (1965) gave a schematic representation of surface water waves in the ocean by their categorized frequency, along with the primary disturbing and restoring forces, as shown in figure 1.2.

Another important wave classification is by the depth of water. They include shallow water waves ($D/L < 0.05$), intermediate water waves ($0.05 < D/L < 0.5$), and deep water waves ($D/L > 0.5$).

Water wave theories consist of linear wave and nonlinear wave theories. The development of water wave theory can be found in two review articles by Craik

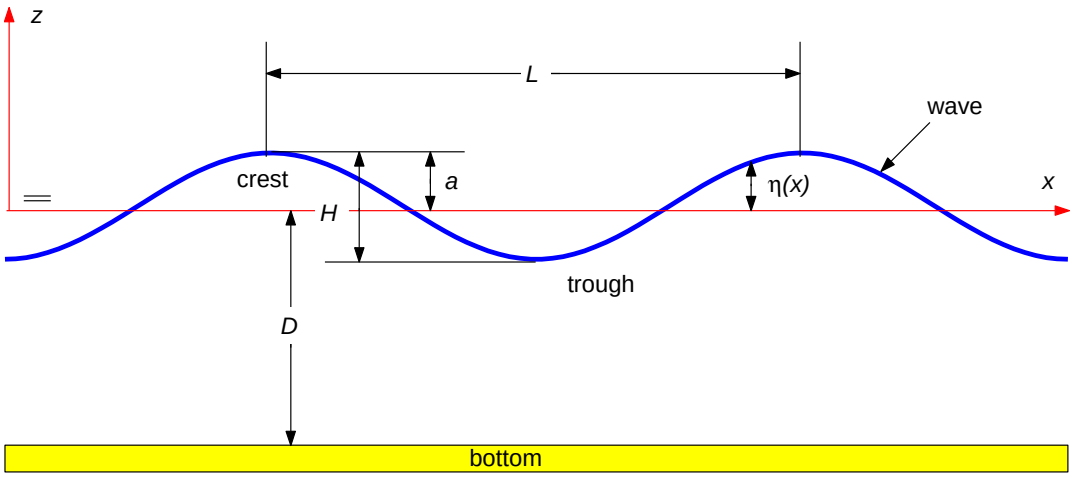

Figure 1.1: Characteristics of water waves.

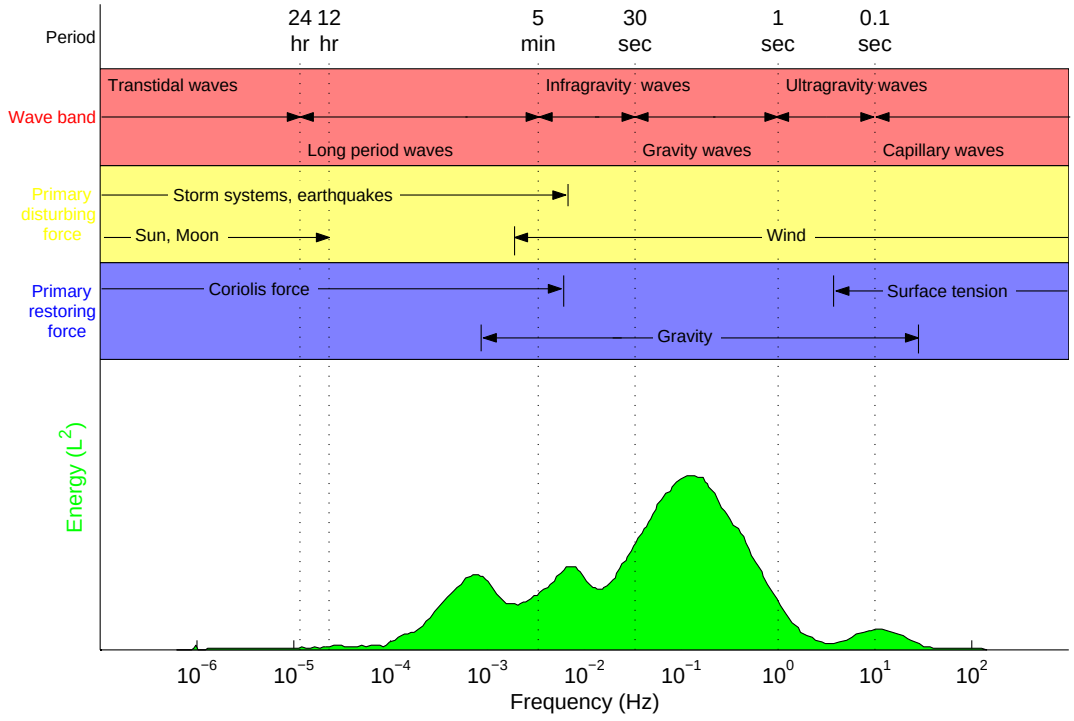

Figure 1.2: Schematic representation of the energy contained in the surface waves of the oceans. (After Kinsman, 1965)

Table 1.1: Water wave theories for irrotational flow on flat bottoms. (After Mader, 2004)

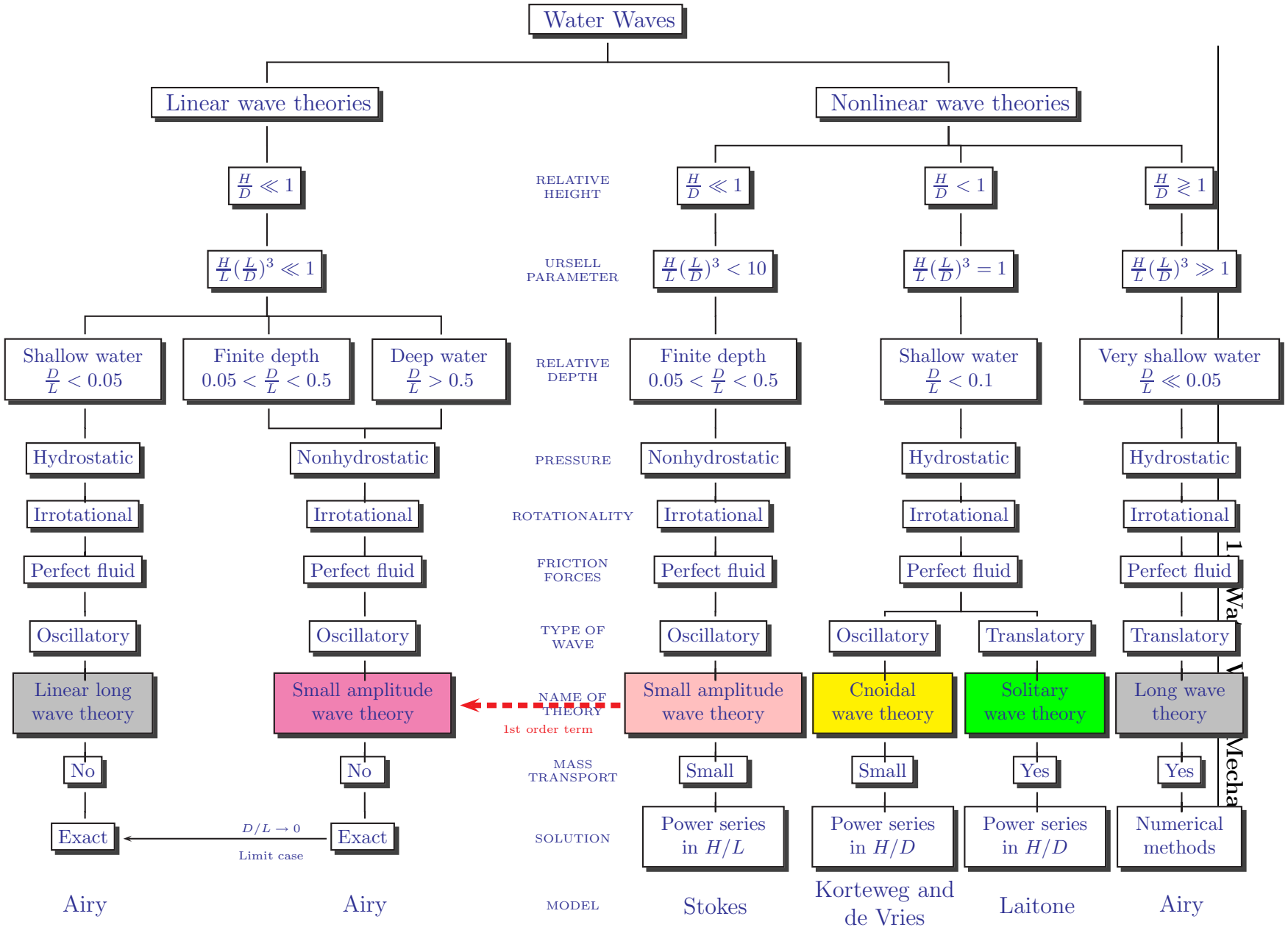

(2004, 2005). Mader (2004) presented a summary, shown in table 1.1, for the principles of different water wave theories. It is shown that all the water wave theories in table 1.1 are derived based on the assumptions of irrotational flows and flat bottoms. They are only valid in a specific region, when the characteristics of the wave and water depth are known. Further water wave theroy can be found in Mei (1989). Hence, the most suitable water wave theory must be chosen for the different problems we consider in later chapters.

1.2 Background of Breaking Wave Studies

1.2.1 Breaking Waves

In the open ocean, clearly visible 'whitecaps' are formed during wave breaking, enhancing the exchange of mass and momentum between the atmosphere and the ocean. The process of wave breaking on a beach is the most common wave breaking phenomenon seen in nature. Wave breaking is responsible for the dissipation of wave energy and the generation of turbulence, vorticity and nearshore currents in the surf zone. Over the last three decades, significant advances have been made in theoretical, experimental and numerical studies of the characteristics of breaking waves. There are some comprehensive reviews for water waves, such as breaking waves on beaches (Peregrine, 1983), wave breaking in deep water (Banner & Peregrine, 1993; Longuet-Higgins, 1987), surface waves in surf zone dynamics (Battjes, 1988), and coastal hydrodynamics (Mei & Liu, 1993).

Generally, breaking waves are classified into four basic types (Galvin, 1968), which are shown in figure 1.3:

- Spilling: Bubbles and turbulent water appear at the wave crest and spill down the front face of the wave.
- Plunging: A plunging jet is ejected from the wave crest as the wave overturns, curling over a large air pocket, impinging on the surface ahead and generating a subsequent splash-up.
- Collapsing: Lower half of the wave breaks without splash-up present.

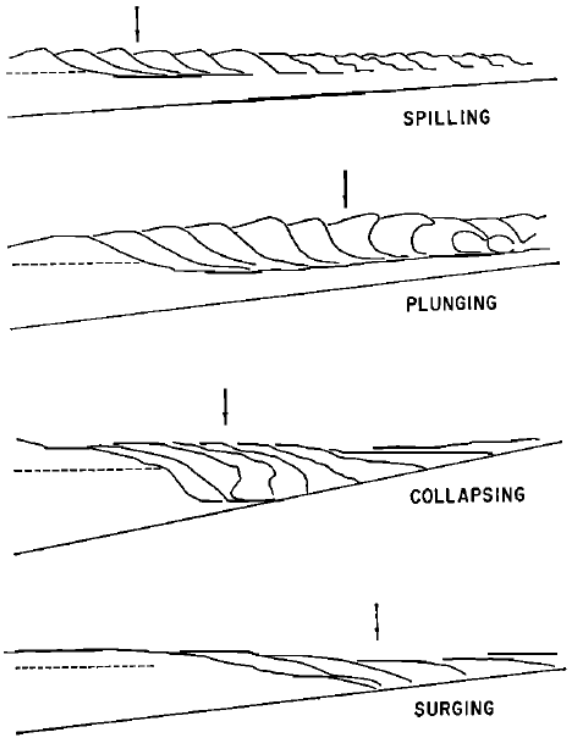

Figure 1.3: Breaking wave types (Galvin, 1968).

- Surging: Smooth wave profile is observed during wave run-up whereas ripples may be produced during wave run-down.

In deep water, most waves are observed as spilling or plunging breakers. In shallow water, the type of wave breaking depends on the characteristics of the wave and the slope of the beach. It is suggested that spilling breakers occur on mildly sloping beaches, whereas plunging breakers occur on steeper beaches, and collapsing and surging breakers occur on very steep beaches (Dean & Dalrymple, 1984; Svendsen, 2005). A prediction of the breaker type can be made with the surf similarity parameter, or Iribarren number, as (Battjes, 1974):

$$\xi_0 = \frac{\tan(\beta)}{\sqrt{\frac{H_0}{L_0}}}, \tag{1.1}$$

where β is the angle of the sloping beach with respect to the flat bottom, H_0 and

Table 1.2: The surf similarity parameter corresponding to different breaker types (Battjes, 1974).

Breaker type	surf similarity parameter ξ_0
Spilling	$\xi_0 < 0.5$
Plunging	$0.5 < \xi_0 < 3.3$
Surging/collapsing	$\xi_0 > 3.3$

L_0 represent the deep water wave height and length, respectively. The values of the surf similarity parameter corresponding to different breaker types are given in table 1.2.

For further details of the mechanisms of how waves break, refer to Longuet-Higgins (1996) for deep water breaking waves and Svendsen (2005) for shallow water breaking waves, respectively.

1.2.2 Experimental Studies

Much of our knowledge of breaking waves comes from laboratory measurements as the characteristics of breaking waves are much more difficult to capture in field measurements. Several systematic studies have been done in the past for steady (or quasi-steady) breaking waves, unsteady deep-water breaking waves, and unsteady breaking waves in the surf zone.

Steady breaking waves

The steady breaking waves are usually caused by moving submerged objects in the water (view from the frame of the objects) or a steady current over fixed objects. They are always classified as spilling breakers with small free surface distortions. In this case, small-amplitude waves are generated above the submerged objects and start to break when the depth of submergence is small enough (Duncan, 1983). The turbulent flow field, generated downstream of breaking waves, resembles that in a self-similar turbulent wake (Battjes & Sakai, 1981). The evolution of a quasi-steady breaker from the onset of a capillary pattern to a fully evolved breaking wave was investigated by Lin & Rockwell (1995). Based on different Froude numbers, they presented the distortion of the water surface, near-surface

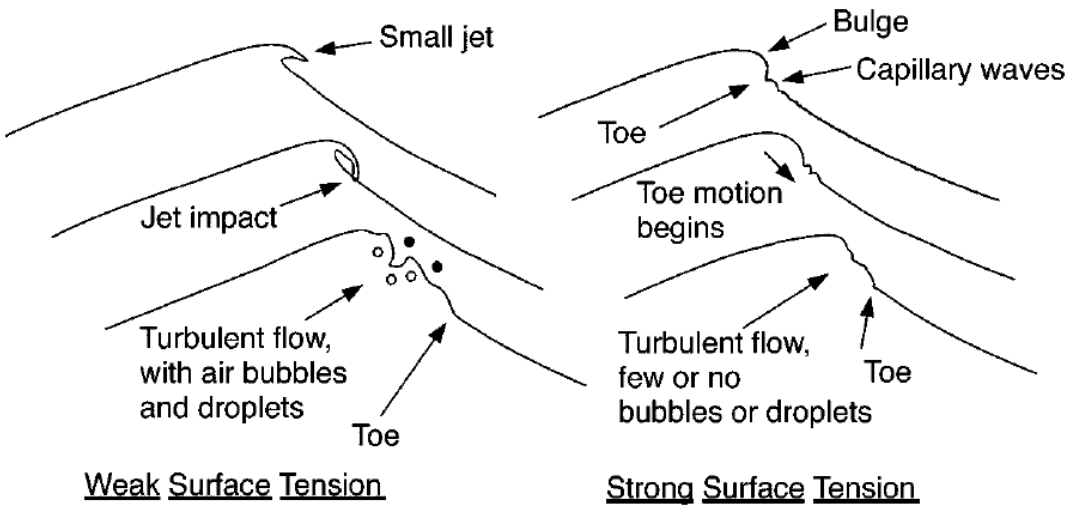

Figure 1.4: The effect of surface tension on spilling breakers (Duncan, 2001).

velocity field and the vorticity in the mixing layer, and found that flow separation occurs at higher Froude number. Duncan (2001) gave a review of this kind of spilling breakers and discussed the effect of surface tension on spilling breakers (see figure 1.4). It was indicated that the surface tension effects, which can alter the shape of breaking waves, become increasing important for short waves.

Unsteady deep-water breaking waves

In contrast to steady breaking waves, unsteady breaking waves often occur in the ocean and nearshore region, break at a special circumstance and last for a short period of time.

There are a variety of experimental investigations of unsteady deep-water breaking waves. Earlier research is based on photographic techniques for wave instability (Melville, 1982) and details of flow visulization in the breaking region (Bonmarin, 1989; Rapp & Melville, 1990). Waves become more and more asymmetric during wave pre-breaking and the asymmetry is more apparent for plunging breakers than spilling breakers. After the impingement, the splash-up can rise as high as the original overturning jet and the potential energy decreases gradually during the jet-splash cycles (Bonmarin, 1989).

To measure the internal kinematics of deep-water breaking waves, laser doppler velocimetry (LDV) and particle image velocimetry (PIV) are usually employed in experiments (Grue & Jensen, 2006; Perlin *et al.*, 1996; Skyner, 1996). Skyner (1996) obtained a good agreement between experiment and potential flow model for the velocity field in the plunging jet. Perlin *et al.* (1996) found that parasitic capillary waves form on the forward face of the wave and the maximum velocity is located in the overturning jet with a magnitude of $1.3C$. In contrast to the findings of Skyner that particle velocities are nearly horizontal in the rear side of the wave, they found that velocities in the plunging breaker are in a circular-like motion. During wave overturning, the horizontal and vertical accelerations were found up to $1.1g$ and $1.5g$ on the front face of the wave (Grue & Jensen, 2006), respectively, where g is the acceleration of gravity.

Much research has focused on the wave dissipation and energy loss of breaking waves. During wave breaking in deep water, the energy loss was found to range from 10% for spilling breakers to as much as 25% for plunging breakers. In addition, it was indicated that about 90% of the energy is dissipated within four wave periods (Rapp & Melville, 1990). With the developing digital particle image velocimetry (DPIV) technique, Melville *et al.* (2002) measured the velocity field under breaking waves and found that the kinetic energy, vorticity and Reynolds stress decay approximately as t^{-1}. Banner & Peirson (2007) carried out a laboratory investigation of the breaking initiation and subsequent energy loss for two-dimensional deep-water wave groups. Recently, Drazen *et al.* (2008) and Drazen & Melville (2009) using DPIV investigated the turbulence and mixing in unsteady deep-water breaking waves. Energy dissipation during wave breaking plays an important role in better understanding the coupling between the wave field and the dynamics of the upper ocean, therefore the study of the scaling of energy dissipation will lead the improvement in modelling air-sea interaction. The measured turbulent structure of breaking waves provides insight into the post-breaking wave field and will guide numerical studies of breaking waves.

Unsteady breaking waves in the surf zone

When water waves approach the beach, due to the shoaling effect, the wave height increases while the water depth decreases. Eventually, the wave will break

on the beach. To better understand this process and get insight into the velocity, vorticity, and turbulence fields, several laboratory studies have been carried out for unsteady breaking wave in the surf zone. Most experiments are based on LDV measuremnts (Nadaoka *et al.*, 1989; Stansby & Feng, 2005; Stive & Wind, 1982; Ting & Kirby, 1994, 1995, 1996), where the mean velocity is obtained by time-averaging or phase-averaging procedure while turbulent fluctuations are obtained from the instantaneous velocity. Large-scale eddies, referred to as 'horizontal eddies' and 'obliquely descending eddies', were observed by Nadaoka *et al.* (1989) under breaking waves in the surf zone. A systematic study of the structure of the undertow and turbulence in the laboratory surf zone was carried out by Ting & Kirby (1994, 1995, 1996). It is indicated that there are fundamental differences in the dynamics of turbulence between spilling and plunging breakers. Compared to spilling breakers, plunging breakers have much higher turbulence levels and much smaller vertical variations of undertow and turbulence intensity. It was also found that turbulence is transported seaward by spilling breakers and shoreward by plunging breakers.

With the development of measurement techniques, it is capable of using PIV to capture the detailed kinematics during wave breaking. Chang & Liu (1998) carried out PIV measurements of the fluid particle velocity, acceleration and vorticity in the overturning jet of a breaking wave and their further study of turbulence under breaking waves was reported later in Chang & Liu (1999). It was found that the maximum velocity in the water is about $0.86C$ when the wave is close to the breaking point, $1.07C$ when the wave starts to overturn, $1.47C$ when the overturning jet curls down, and $1.68C$ when the overturning jet strikes the water surface with an acceleration of $1.1g$ at an angle of 88^o downward, respectively. Recently, detailed PIV measurements of surf zone breaking waves were performed by Kimmoun & Branger (2007) and they presented a complete space-time evolution of the velocity field in the laboratory surf zone. It was found that the maximum shoreward transport is in the splash-up locations whereas the maximum seaward transport is near the bottom after the first splashing region. Several vortices were generated during wave breaking and the front of the breaking crest was found to be the initiation point for kinetic energy production.

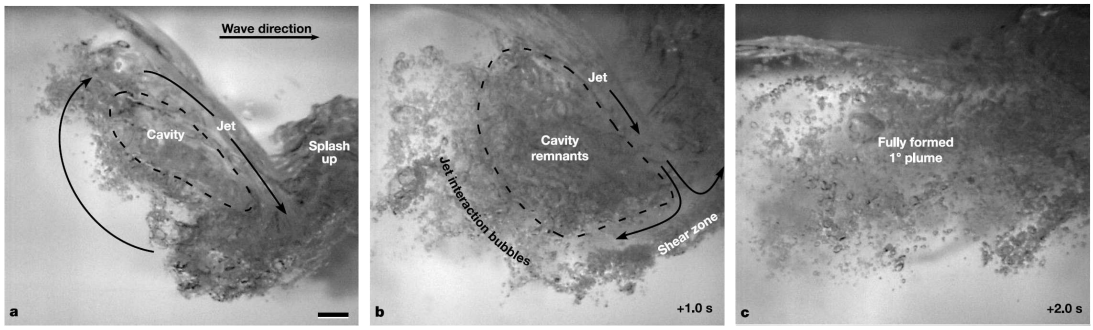

Figure 1.5: Bubble creation mechanisms in breaking waves (Deane & Stokes, 2002).

Air entrainment

Air entrainment during wave breaking plays an important role in heat and mass transfer across the air-sea interface. Several attempts have been made to measure void fraction and energy dissipation for deep-water breaking waves (Deane & Stokes, 2002; Lamarre & Melville, 1991) and breaking waves in the surf zone (Chanson & Lee, 1997; Cox & Shin, 2003; Hoque & Aoki, 2005; Jansen, 1986; Lin & Hwung, 1992). Deane & Stokes (2002), using a high-speed video camera, presented a detailed view of wave-generated bubbles when the plunging jet strikes the water surface ahead (see figure 1.5). It is suggested that the jet/wave-face interaction and the collapsing cavity are the two distinct flow features driving bubble creation, and distinct vortices can be observed during the splash-up. For breaking waves in the surf zone, it was found that the void fraction decays exponentially with the depth (Hoque & Aoki, 2005; Kimmoun & Branger, 2007), and air entrainment and splash-up account for $4-9\%$ and $2.5-5\%$ of the total energy dissipation during wave breaking, respectively (Blenkinsopp & Chaplin, 2007).

Three-dimensional breaking waves

It is worth remarking that most laboratory investigations of breaking waves are two-dimensional or through incident two-dimensional waves leading to break due to three-dimensional instability (Melville, 1982; Su *et al.*, 1982). Only a few

experiments have been carried out for fully three-dimensional breaking waves generated by spatially focusing or diffracting waves (Nepf *et al.*, 1998; She *et al.*, 1997; Wu & Nepf, 2002). As wave directionality varies from diffraction to positive focusing, both the steepness and severity of breaking waves increase monotonically (Nepf *et al.*, 1998). The energy loss for focusing waves is higher than that for diffracting waves, and both are comparable to the energy loss of two-dimensional breaking waves with the same spectral shape (Wu & Nepf, 2002). For the internal kinematics during wave breaking, She *et al.* (1997) found the ratio of the crest velocity to the wave speed is approximately unity while Wu & Nepf (2002) found the ratio of local particle velocity to the wave speed is larger than unity. This discrepancy may be caused by different laboratory setups.

For water waves propagating over irregular bathymetry, several laboratory investigations have been performed for non-breaking waves over a semi-circular shoal (Whalin, 1971) and a sloping elliptic shoal (Berkhoff *et al.*, 1982), and breaking waves over a submerged elliptic shoal (Vincent & Briggs, 1989) and a circular shoal (Chawla *et al.*, 1998). The refraction and diffraction of waves passing over a varying bathymetry provide more information to the coastal engineering community.

Summary of experimental studies

Overall, with the development of measurement techniques, physical experiments have provided much insight into the kinematics and dynamics of breaking waves. However, the process of wave breaking has not yet been fully understood due to its complexity and experimental investigations still struggle to provide the detailed flow field, especially during wave overturning in three dimensions. Moreover, conducting physical experiments cost a lot of money and are also very time-consuming. Thus, a variety of numerical studies, which are cost-effective and can provide the detailed flow field, act as a complementary approach to study breaking waves.

1.2.3 Numerical Studies

Considering the scope of the present study, only the numerical studies dealing with breaking waves will be discussed here. There are a variety of mathematical models for water waves, of varying degrees of complexity, which are shown in table 1.3.

Depth-integrated models

To simplify the problem into horizontal 1D or 2D, the depth-integrated models are usually utilized for the water wave propagation. The radiative transfer equation is often used to describe the large scale waves in a complex sea state in terms of the spectral energy in directional wave-number space. This equation is the foundational model for wind-wave prediction (Sobey, 1986).

For unidirectional wave propagation in 1D, the evolution of long waves is based on the Korteweg-de Vries (KdV) equation (Korteweg & de Vries, 1895) and the regularized long wave (RLW) equation (Benjamin *et al.*, 1972) which is similar to the KdV equation but with a different dispersive term. These equations are widely used for solitary wave interactions and some other physical problems. For 2D, the Kadomtsev-Petviashvili (KP) equation (Kadomtsev & Petviashvili, 1970), which is the extension of the KdV equation in 2D, is used to model the long wave propagation, while the nonlinear Schrödinger (NLS) equation is used for the evolution of the envelope of wave groups (Dingemans & Otta, 2001).

Under the assumption of slowly varying bathymetry, the mild slope equation is used to model the wave refraction and diffraction in horizontal 2D (Berkhoff *et al.*, 1982; Kirby & Dalrymple, 1983; Liu & Tsay, 1984), and also for breaking waves over irregular bathymetry (Chawla *et al.*, 1998).

When the horizontal length scale is much greater than the vertical length scale, the shallow water equations are used to model 1D long wave propagation including wave breaking (Li & Raichlen, 2002; Titov & Synolakis, 1995), 2D long wave run-up (Hubbard & Dodd, 2002; Liu *et al.*, 1995; Titov & Synolakis, 1998) and some dam-break flows. The shallow water equations are widely used in free surface flows as they can provide satisfactory results with low computational cost.

Table 1.3: Water wave models

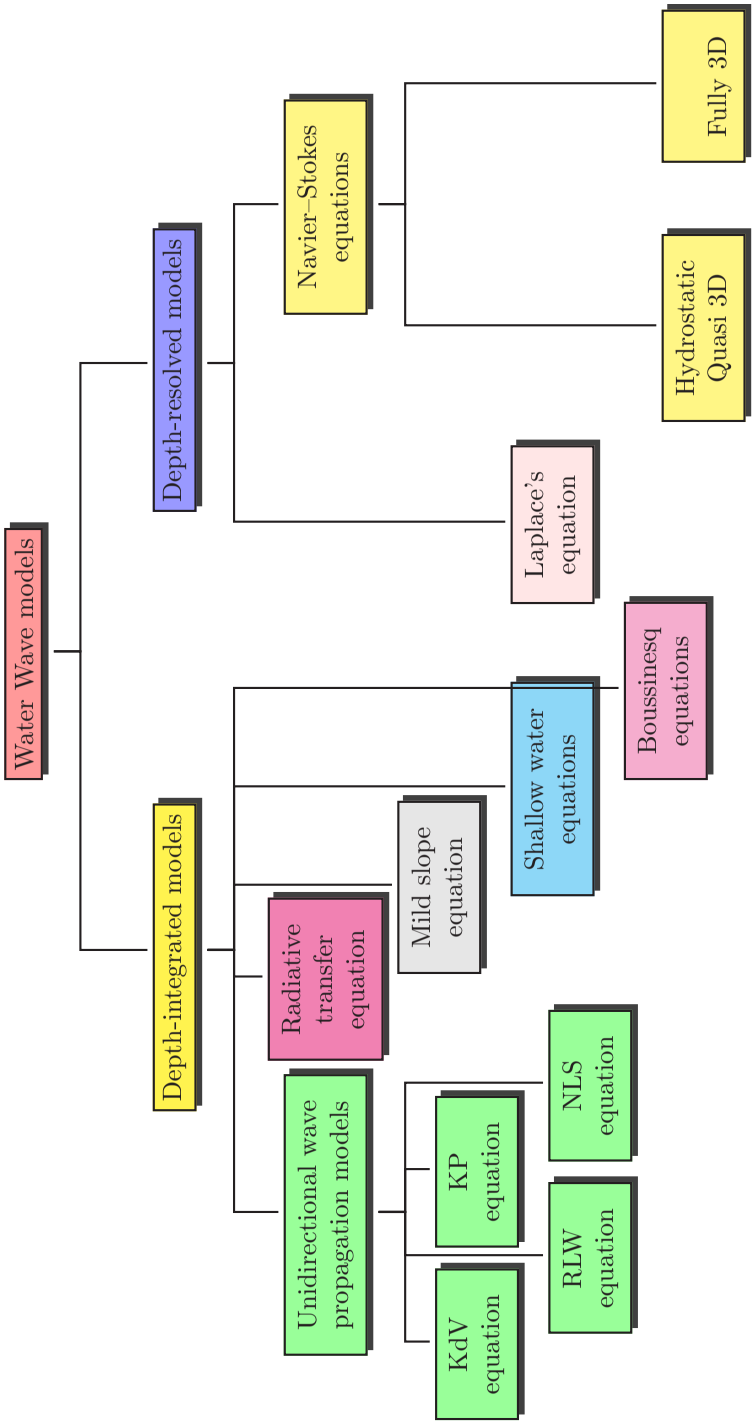

Using the approximation for weakly nonlinear and dispersive water waves, Boussinesq (1872) derived the equation for wave propagation over a flat bottom which was called the original Boussinesq equations. Peregrine (1967) proposed the standard Boussinesq equations for variable depth. After that, many Boussinesq-type equations were introduced by researchers in order to improve the nonlinearity and dispersion of the model. The Boussinesq-type models have wide applications in surf zone dynamics including wave breaking, wave run-up and wave-current interaction. The wave breaking process can be modelled in the Boussinesq-type equations by the eddy viscosity concept (Chen *et al.*, 2000; Karambas & Koutitas, 1992; Zelt, 1991), surface roller model (Madsen *et al.*, 1997; Schaffer *et al.*, 1993; Sorensen *et al.*, 2004), and vorticity transport model (Svendsen *et al.*, 1996; Veeramony & Svendsen, 2000). Comprehensive reviews of the Boussinesq-type equations can be found in Madsen & Schaffer (1999) and Kirby (2003), and will not be discussed here.

Actually, it is worth remarking that although the depth-integrated models are widely used in modelling surface wave propagation, they cannot capture the realistic wave breaking and overturning processes.

Potential flow models

In order the obtain the kinematics and dynamics of breaking waves, depth-resolved models must be used. One of these is the fully nonlinear potential flow model based on Laplace's equation with inviscid and irrotational assumptions, which can simulate the deep-water breaking wave in a periodic space domain and the physics of wave shoaling on the beach up to the early stage of wave breaking.

Longuet-Higgins & Cokelet (1976), using the theory of potential flow and conformal mapping, studied periodic two-dimensional deep water overturning waves by specifying an artificial pressure force on the free surface. The detailed process before, during and after wave breaking was described by Cokelet (1977). Since then, several numerical methods are developed to extend the application of the potential flow model (Baker *et al.*, 1982; Dold & Peregrine, 1986; Dommermuth *et al.*, 1988; New *et al.*, 1985; Roberts, 1983; Vinje & Brevig, 1981), and the comparison between potental flow model and experimental results confirmed the

validity of potential-theory calculations for such breaking waves and indicated that other physical mechanisms have little effect up to the wave re-entry (Dommermuth *et al.*, 1988). Compared to deep-water breaking waves, shallow water breaking waves develop faster and have a larger overturning jet (Vinje & Brevig, 1981). For the internal kinematics, it was found that the horizontal velocities and acceleration during wave overturning are in the range of $1.5-2C$ and $5-6g$, respectively. In addition, a remarkable similarity of wave profiles was found in the overturning regions of many breaking waves (New *et al.*, 1985).

Combining the high order time stepping method of Dold & Peregrine (1986) and a high order boundary element method (BEM), Grilli *et al.* (1989) developed a two-dimensional fully nonlinear potential flow model for nonlinear water waves. This model was subsequently applied to study breaking solitary waves over breakwaters (Grilli *et al.*, 1994*a*), shoaling of a solitary wave on a sloping beach (Grilli *et al.*, 1994*b*), wave breaking induced by moving boundaries (Grilli & Subramanya, 1996), and periodic waves in a numerical wave tank (NWT) (Grilli & Horrillo, 1997). Grilli *et al.* (1997) investigated the breaking criterion and characteristics for solitary waves on slopes. Several cases for different slopes and wave steepnesses were studied and detailed information for breaking waves was presented up to the point at which the plunging jet of breaking waves impinged on the free surface. It was found that the slope is more important than the incident wave height to determine the shape of breaking waves.

It is worth noticing that all the computations described above terminate before the plunging jet impinges on the water surface, however, Wang *et al.* (1995) developed a 2D potential flow model based on a multi-subdomain approach and the BEM, which was able to simulate the initial stage of jet closure and splash of overturning waves.

Few attempts have been made with potential flow models to simulate three-dimensional breaking waves. Motivated by Longuet-Higgins & Cokelet (1976), Xü (1992) and Xü & Yue (1992) simulated three-dimensional overturning waves, which were generated by applying an artificial three-dimensional pressure force on a progressive two-dimensional Stokes wave in a periodic domain. An interesting phenomenon was found that although the maximum forcing pressure is along the central line, the overturning waves develop either at the centre or at the

edges depending on the ratio of the width of the tank to the wave length. Since then, the method of Xü (1992) was advanced by Xue *et al.* (2001) and Liu *et al.* (2001) to study the kinematics and dynamics of three-dimensional overturning waves, steep crescent waves and wave-body interactions. For applications in non-periodic domains, there are other research for overturning solitary waves over a sand bank (Broeze *et al.*, 1993), three-dimensional shoaling and overturning of solitary waves over a sloping ridge (Grilli *et al.*, 2001; Guyenne & Grilli, 2006), and three-dimensional overturning waves over a non-symmetrical seabed or multiple reefs (Yan & Ma, 2010).

The potential flow models, which are very efficient and only need one or two hours on a normal PC for 3D computation (Yan & Ma, 2010), are capable of simulating breaking waves and can provide insight into the kinematics and dynamics of water waves during wave overturning. However, these models usually terminate before the plunging jet touches down and cannot provide any information after wave breaking. In addition, the potential flow models are limited in the application when the generation of vorticity and turbulence is important, such as breaking waves in the surf zone.

Navier–Stokes models

Another depth-resolved model to study breaking waves is based on the Navier–Stokes equations. One of this kind is the quasi-3D model (Casulli & Cheng, 1992), which is based on the hydrostatic pressure assumption. Under this assumption, the pressure is replaced by the water surface elevation, which is governed by the kinematic free surface boundary condition, thus the coupling between the velocity and pressure is avoided. Though the quasi-3D model is not able to capture the interface during wave breaking, the computation is more efficient and this model is always used to simulate large-scale water waves like tides and ocean currents. The full Navier–Stokes equations can also be solved with an interface tracking or capturing, as in the following discussion.

For quasi-steady breaking waves, spilling breaking waves generated by two-dimensional submerged hydrofoils (Duncan, 1983) were simulated by RANS models (Muscari & Di Mascio, 2003; Rhee & Stern, 2002) and a domain decomposition

approach (Iafrati & Campana, 2005), where the Navier–Stokes model is used near the interface while the potential flow model is employed far from the interface. Good agreement between these numerical results and experimental data was obtained and turbulent flows generated downstream were discussed.

Several numerical studies of deep-water breaking waves have been done in the past (Chen *et al.*, 1999; Hendrickson, 2005; Iafrati, 2009; Song & Sirviente, 2004). In these studies, a steep Stokes wave, which leads to a plunging breaker, was simulated in a periodic space domain. The vorticity generation, energy dissipation and detailed kinematics during wave overturning, including the splash-up, were shown and discussed in Chen *et al.* (1999). It was found that the maximum horizontal velocity is about $1.76C$ and the maximum acceleration is $3.62g$ just before the plunging jet touches the surface. In addition, strong vortices were generated during the wave breaking process, and t^{-1} dependence was found for the energy dissipation after two wave periods, which has also been observed in laboratory experiments (Melville *et al.*, 2002; Rapp & Melville, 1990). A further study was conducted by Song & Sirviente (2004), but attention was paid to surface tension, density ratio and viscosity effects. Hendrickson (2005) presented a comprehensive analysis of the energy dissipation and the transfer of energy at the air-water interface during wave breaking and found that there is no flow separation in the water while air flow separation is observed on the front face of the wave and over the crest. More recently, the effects of the breaking intensity on deep-water breaking waves were investigated by Iafrati (2009). It can be seen from above that deep-water breaking waves are computed in a periodic space domain in most numerical studies, however, Zwart (1999), using a integrated space-time finite volume method under the inviscid assumption, studied an overturning wave generated in a water channel by a piston wavemaker, which was previously investigated by Dommermuth *et al.* (1988). The numerical results for the water surface elevations at various locations were compared with experimental data and good agreement was obtained. The profiles and detailed moving meshes of the plunging jet were presented just before the impingement and it was indicated that the shape of the plunging jet differs somewhat from the more vertical plunge predicted by the potential flow model (Dommermuth *et al.*, 1988). This descrepancy between the potential flow model and Navier–Stokes model was

also observed in Chen *et al.* (1999) and it was shown that more rounded plunging jet is predicted in Navier–Stokes simulations.

To better understand breaking waves in shallow water of varying depth, several numerical investigations of two-dimensional breaking waves on a sloping beach have been performed for breaking solitary waves (Chan & Street, 1970; Guignard *et al.*, 1999, 2001; Helluy *et al.*, 2005; Khayyer *et al.*, 2008; Lachaume *et al.*, 2003; Lin, 2007; Lin *et al.*, 1999; Lo & Shao, 2002; Ma & Zhou, 2009; Xie *et al.*, 2009) and periodic breaking waves (Bakhtyar *et al.*, 2009; Bradford, 2000; Hieu *et al.*, 2004; Lee & Heo, 2005; Lemos, 1992; Lin & Liu, 1998*a*,*b*; Mayer & Madsen, 2000; Shao, 2006; Shao & Ji, 2006; Takikawa *et al.*, 1997; Wang *et al.*, 2009*b*; Watanabe & Saeki, 2002; Zhao *et al.*, 2004). A more detailed discussion will be given in Chapter 4 and Chapter 5 respectively.

For breaking waves in ship hydrodynamics, an early attempt at studying breaking waves was presented by Miyata (1986). Various techniques that are suitable for ship hydrodynamics were implemented in the code including irregular boundary treatment. There are also some applications for water impact on a two-dimensional flat-bottomed body (Ng & Kot, 1992) and plunging breaking waves over a submerged bump (Wang *et al.*, 2009*a*). Andrillon & Alessandrini (2004) developed a fully coupled method to solve the Navier–Stokes equations, which does not require a correction step. Several cases for sloshing and dam break problems were shown and this model was employed to simulate the bow wave around the Wigley hull.

With increases in computational power and developments in numerical methods, some attempts have been made to investigate three-dimensional breaking waves. Applications include finite-amplitude waves in turbulent channel flow (Hodges & Street, 1999), deep-water breaking waves in a periodic domain (Lubin *et al.*, 2006), periodic breaking waves in the surf zone (Christensen, 2006; Christensen & Deigaard, 2001; Liovic & Lakehal, 2007; Watanabe & Saeki, 1999; Watanabe *et al.*, 2005), breaking solitary waves (Biausser *et al.*, 2004; Mutsuda & Yasuda, 2000), landslide-generated waves (Liu *et al.*, 2005; Wu, 2004), ship hydrodynamics (Miyata *et al.*, 1996; Yang & Stern, 2009), and a viscous numerical wave tank (Park *et al.*, 1999; Wang, 2007). More details will be discussed in Chapter 6.

Recently, the coupling of different wave models to investigate breaking waves has been developed, such as the coupling between potential flow model and the Navier–Stokes equations with the VOF (Biausser *et al.*, 2004) or level set (Iafrati & Campana, 2005) methods. More recently, Sitanggang & Lynett (2010) developed a hybrid wave model for simulating water wave propagation from deep water to shoreline, in which the horizontal 1D Boussinesq and 2D RANS equations were employed in pre-breaking zone and nearshore region, respectively. It was suggested that the hybrid model is able to perform large-scale tsunami simulations with good accuracy and efficient computational time.

Commerical codes

Nowadays, there are a number of commerical codes (CFX, FLUENT, STAR-CD, FLOW3D, to name a few) available as a computational fluid dynamics (CFD) tool for general fluid flow problems. Most of these CFD software are based on the finite volume method (FVM) and they are all capable of simulating turbulent free surface flows, including breaking waves. However, as they are designed for general-purpose engineering simulation, additional effort is required for water wave modelling such as wave generation at the inlet or wave damping at the outlet.

1.3 Wind Effects on Water Waves

When the wind is blowing over water waves, it will enhance the exchanges of heat, mass and momentum on the air-water interface (see figure 1.6 for example). Some important effects of wind on water waves have been discussed by Sobey (1986), Melville (1996) and Jahne & Haussecker (1998). One of the most important effect of wind on water waves is the generation of surface waves. In the comprehensive review of the knowledge more than five decades ago, Ursell (1956) opened in the statement that "wind blowing over a water surface generated waves in the water by physical processes which cannot be regarded as known" and concluded that "the present state of our knowledge is profoundly unsatisfactory". Since

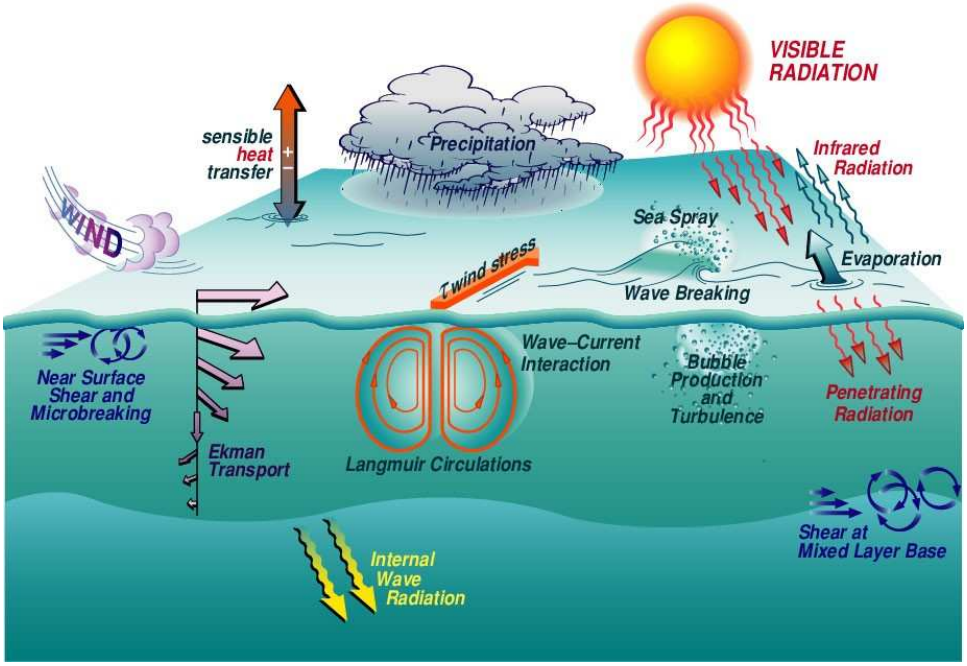

Figure 1.6: Wind wave interaction. Picture from the Coupled Boundary Layers Air-Sea Transfer Defense Research Initiative (`http://www.whoi.edu/science/AOPE/dept/CBLASTmain.html`).

then, numerous theoretical, experimental and numerical investigations have been carried out to advance our understanding of wind-wave interactions.

Theoretical studies

An early calculation for wave generation is the Jeffreys' sheltering theory. Jeffreys (1925) supposed that the air flow over waves may be unable to follow the deformed surface but separated at the leeward region of the wave crest, which was known as the sheltering effect. Thus, the pressure difference across the moving wave could result in energy transfer from the air to the water if the wind is moving faster than the wave. Jeffreys found that the skin friction is negligible and a sheltering coefficient was obtained through the energy balance of the wave motion. However, the pressure differences, found in several laboratory experiments on wavy walls, were much smaller than the value proposed by Jeffreys (Phillips, 1977).

Phillips (1957) presented the resonance mechanism for wave generation by wind. The correlations between air and water motions are neglected, and the turbulent pressure fluctuation on the water surface is responsible for wave generation. The resonance model predicts that most of the growth of waves occurs in the principal stage of development and follows a linear growth rate.

Nearly at the same time, Miles (1957) proposed the shear-flow model for wave generation. Miles neglected the turbulent fluctuations and made the interaction between mean air flow and waves as the essential mechanism. Under some assumptions, the problem is governed by an inviscid Orr–Sommerfeld equation, which is often called the Rayleigh equation. Benjamin (1959) studied the same problem in terms of local orthogonal coordinates. Later, Lighthill (1962) presented physical interpretation of the shear-flow theory, and Kawai (1979) carried out a laboratory investigation of the generation of initial wavelets.

Experimental studies

Many laboratory studies have been carried out to investigate wind-wave interactions. Most works were mainly focused on wind profiles, wave surface elevation, wind-induced drift currents and wave growth rate. In experiments, the logarithmic wind profile was observed near the air-water interface (Bole & Hsu, 1969; Wu, 1968). Under the influence of wind, the wave grows with the fetch and the wave growth rate is reduced in water containing surfactants (Mitsuyasu & Honda, 1982). When the wind is blowing in the opposite direction to the wave propagation. It was shown that the wave attenuation rate is approximately 2.5 times greater than the wave growth rate for comparable wind forcing (Peirson *et al.*, 2003). With wave breaking in the presence of wind drift and swell, the surface drift was found to be of the order of 3% of the wind speed (Phillips & Banner, 1974) and Banner & Phillips (1974) found the 'micro-breaking' for deep-water breaking waves, which is important in the energy and momentum transfer from the wave to near surface turbulence and currents.

Some experimental investigations have also been carried out for the surface pressure, shear stress and turbulence field. Banner (1990) investigated the influence of wave breaking on the surface pressure distribution in wind-wave interaction and found that the form drag and wind stress increase during wave breaking.

Thais & Magnaudet (1996) used LDV to investigate the turbulent structure beneath water waves sheared by the wind. With the development of visualization and PIV techniques, the aqueous surface sublayer flows beneath the wind-driven air-water interface and microscale breaking wind waves have been investigated by Banner & Peirson (1998) and Peirson & Banner (2003), respectively. Banner & Peirson found that the tangential stress contributes to the entire wind stress before the formation of wind waves while the wave form drag provides the major portion of the wind stress beyond the early growth stage. Peirson & Banner indicated that microscale breaking plays an important role in the direct transport of fluid from the surface to the highly turbulent region below, enhancing the air-sea exchange under moderate winds. Recently, Kharif *et al.* (2008) investigated the influence of wind on extreme wave events, and found that the focusing point is shifted downstream, and the height and duration of the extreme waves increase in the presence of wind.

When the wind is blowing over water waves, air flow separation occurs ahead of the wave crest at the onset of wave breaking (Banner & Melville, 1976). Air flow separation was also observed in short wind waves (Kawai, 1982) and steep wave events (Kharif *et al.*, 2008). Recently, Reul *et al.* (2008) used DPIV to investigate the air flow velocity, vorticity and streamline patterns over breaking waves propagating in groups. The air flow structure was captured at different stages of wave breaking, various wind speeds and breaking intensities. It was found that air flow separation which occurs near the crest is very similar to the flow separation over a backward step. Furthermore, a steeper wave crest leads to an increase in the height of the separated layer and the downstream reattachment length.

In contrast to the experimental studies of wind effects on deep-water waves, the influence of wind on nearshore breaking waves was investigated by Galloway *et al.* (1989) using an empirical approach based on in-situ measurements, and by Douglass (1990) and King & Baker (1996) in a laboratory wind-wave flume. The wind has significant effects on the breaker location, geometry and type. Onshore winds enhance the development of spilling breakers whereas offshore winds assist the formation of plunging breakers (Galloway *et al.*, 1989). In addition, Douglass found that onshore winds cause waves to break earlier and in deeper water further

from shore; offshore winds cause waves to break later and in shallower water closer to shore. He found that the effect of wind on breaker depth is significant while the effect on breaker height is slight. Douglass indicated that the primary mechanism for wind affecting breaking waves appears to be shear, not normal stress and concluded that "Surf zone dynamics models that ignore wind or include wind only as a surface shear may be missing a very important effect of the wind—its effect on the initiation and mechanics of wave breaking." Similar results were also observed by King & Baker (1996) and they further studied the motion of suspended particles and found that the generation of a wind drift layer can affect particle drift velocities. During wave shoaling, it was suggested that low wind speeds have little effect on run-up heights, but high wind speeds significantly increase run-up heights (Ward *et al.*, 1998). Moreover, wind increases the shoaling wave energy and has a significant effect on the wave shape (e.g. changes wave skewness and asymmetry) (Feddersen & Veron, 2005).

Numerical studies

A few numerical studies have been done for the air flow over waves. Early works are based on numerical models with turbulence closure schemes (Al-Zanaidi & Hui, 1984; Chalikov, 1978; Davis, 1970; Gent & Taylor, 1976; Harris *et al.*, 1996; Townsend, 1972), and with more detail in two PhD theses (Li, 1995; Mastenbroek, 1996). Belcher & Hunt (1998) presented a review on the turbulent flow over hills and waves up to 1998.

With increases in computer power and developments in CFD, there are some numerical studies employing direct numerical simulation (DNS) or large eddy simulation (LES) to investigate turbulent air flow over stationary wavy surfaces (Cherukat *et al.*, 1998; De Angelis *et al.*, 1997; Henn & Sykes, 1999) or moving wavy surfaces (Shen *et al.*, 2003; Sullivan *et al.*, 2000). The turbulent flow beneath a sheared interface has been investigated with a specified shear stress at the surface using DNS (Tsai *et al.*, 2005) and LES (Kawamura, 2000). In contrast to the decoupled models discussed above, in which only the flows in the air or in the water are solved (one-phase flow), there are some numerical studies for the coupled air-water interface (two-phase flow), in which the two phases are coupled

at the interface by the continuity of the velocities and shear stresses. Lombardi *et al.* (1996) employed DNS to study near-interface turbulence and the detail of the interfacial sublayer was further explored by Fulgosi *et al.* (2003). Recently, Lin *et al.* (2008) utilized DNS to investigate wind-wave generation processes.

It is worth remarking that all the numerical studies discussed above are performed in a periodic space domain and have not considered wind effects on breaking waves. For air flow over wavy surfaces (either stationary or moving), the wavy interface is not deformable. For turbulent flow beneath a sheared interface, the effect of the air flow is only modelled by a specified shear stress. For the coupled air-water interfacial flow, although the interaction between the air and water is taken into account, the strong topological changes of the interface, such as wave breaking, have not been considered yet.

Recently, a few numerical studies have began to investigate the influence of wind on water waves. Chen *et al.* (2004) implemented a parameterized wind stress into Boussinesq wave models to investigate the nearshore wave propagation and horizontal circulation. Kharif *et al.* (2008) applied an empirical wind pressure distribution on the free surface using Jeffreys' sheltering theory (Jeffreys, 1925) in their potential flow model, to calculate the influence of wind on extreme wave events. However, wave breaking is neglected and the effect of wind on the onset of wave breaking has not been investigated in these studies.

1.4 Scope of the Present Study

From the above discussion, it is apparent that little attention has been paid to investigate breaking waves under the influence of wind, either by experimental measurements or numerical simulations. Thus, this study tries to shed some light on this problem in order to better understand the wave breaking process.

The aim of the present study is to investigate breaking water waves under the influence of wind. A two-phase flow model, which solves the flow in the air and water simultaneously, is developed here and solved by the widely used finite volume method. The model is based on the RANS (Reynolds Averaged Navier-Stokes) equations with the $k - \epsilon$ turbulence model in 2D and LES in 3D. The pressure correction method, either the SIMPLE (Semi-Implicit Method

for Pressure-Linked Equations) (Patankar, 1980) or the PISO (Pressure-Implicit with Splitting of Operators) (Issa, 1986) methods, are employed to solve the governing equations, and the air-water interface is captured by a high resolution VOF scheme CICSAM (Compressive Interface Capturing Scheme for Arbitrary Meshes) developed by Ubbink (1997). The model is validated in the absence of wind using a variety of benchmark problems from the literature, including breaking solitary waves, breaking periodic waves in the surf zone and solitary wave run-up on a conical island. The effect of wind is included to investigate the kinematics and dynamics of breaking waves in both 2D and 3D.

1.5 Outline of Thesis

This thesis consists of seven chapters, one of which is the introduction chapter. The reminder of the thesis is organized as follows:

In Chapter 2, the mathematical model and numerical implementation are presented. The Navier–Stokes equations and the VOF equation for capturing the air-water interface are described along with corresponding initial and boundary conditions. The finite volume discretization for the governing equations and pressure-velocity coupling are described in detail. After briefly reviewing the techniques for interface calculations, the description of the CICSAM scheme used for the VOF equation is included.

In Chapter 3, the RANS modelling of two-dimensional breaking waves is introduced. The RANS equations and the $k - \epsilon$ turbulence model are presented in detail. Two experiments for overturning waves, which include the free surface profiles during wave overturning, are employed to validate the model. Good agreement between numerical results and experimental data shows the capability of the present model in simulating breaking waves, including the overturning jet.

In Chapter 4, the RANS model is utilized to study two-dimensional breaking solitary waves. First, the run-up of breaking solitary waves on a 1:19.85 slope in the absence of wind is computed and compared with experimental measurements. Then, detailed results of winds effects on breaking solitary waves are presented.

In Chapter 5, the RANS model is further used to study two-dimensional periodic breaking waves in the surf zone. Both the spilling and plunging breakers on a

1:35 slope in the absence of wind are simulated and compared with experimental measurements as well as other previous numerical results in the literature. After that, periodic breaking waves under the influence of wind are investigated and the effects of wind on the breaking characteristics are discussed.

In Chapter 6, the large eddy simulation of three-dimensional breaking waves is introduced. The filtered Navier–Stokes equations for LES are described and the conventional Smagorinsky model is adopted as the subgrid-scale model. First, the solitary wave run-up on a conical island is simulated to validate the 3D code and numerical results are compared with experimental measurements in terms of free surface elevations and maximum run-up heights. Then, the overturning of a solitary wave over a submerged conical island is investigated and the detailed kinematics and dynamics of overturning waves are presented. Finally, the overturning wave under the influence of wind is studied.

In Chapter 7, the main findings and conclusions are summarized and the future work is discussed.

Chapter 2

Mathematical Model and Numerical Implementation

In this chapter, the mathematical model and numerical implementation are presented. It is noted that only the Navier-Stokes equations are described here and different turbulence models will be discussed in later chapters. Then the finite volume discretization for the governing equations and pressure-velocity coupling are described in detail. After briefly reviewing the techniques for interface calculations, the volume of fluid (VOF) method used in this study to capture the air-water interface is presented.

2.1 Navier–Stokes Equations

The governing equations for incompressible Newtonian fluid flow are the Navier–Stokes equations. Mass conservation is described by the continuity equation

$$\frac{\partial \rho}{\partial t} + \boldsymbol{\nabla} \cdot (\rho \boldsymbol{u}) = 0, \tag{2.1}$$

where ρ is the density, t is the time and $\boldsymbol{u} = (u, v, w)$ is the velocity vector.

If we assume that the fluid is incompressible ($\frac{\mathrm{d}\rho}{\mathrm{d}t} = 0$), then the continuity equation can be simplified to

$$\boldsymbol{\nabla} \cdot \boldsymbol{u} = 0. \tag{2.2}$$

The momentum conservation is expressed as

$$\frac{\partial(\rho \boldsymbol{u})}{\partial t} + \boldsymbol{\nabla} \cdot (\rho \boldsymbol{u} \otimes \boldsymbol{u}) = -\boldsymbol{\nabla} p + \boldsymbol{\nabla} \cdot [\mu(\boldsymbol{\nabla} \boldsymbol{u} + \boldsymbol{\nabla}^{\mathrm{T}} \boldsymbol{u})] + \rho \boldsymbol{g}, \tag{2.3}$$

where p represents pressure, $\boldsymbol{g}$ the gravitational acceleration vector, μ the dynamic viscosity of the fluid and the superscript T denotes the transpose.

The momentum equation is closed with the constitutive relations for the density and dynamic viscosity of the fluid

$$\rho = F\rho^{\mathrm{w}} + (1 - F)\rho^{\mathrm{a}}, \tag{2.4}$$

$$\mu = F\mu^{\mathrm{w}} + (1 - F)\mu^{\mathrm{a}}, \tag{2.5}$$

where the superscript w and a denotes fluid water and air, respectively. F is the volume fraction defined as

$$F = \begin{cases} 1, & \text{if only water is present;} \\ 0, & \text{if only air is present.} \end{cases} \tag{2.6}$$

The air-water interface is then within the cells where $0 < F < 1$. A particle on surface stays on surface and the volume fraction F has a zero material derivative

$$\frac{\mathrm{d}F}{\mathrm{d}t} = \frac{\partial F}{\partial t} + \boldsymbol{u} \cdot \boldsymbol{\nabla} F = 0. \tag{2.7}$$

The equations (2.2, 2.3, 2.7) complete the mathematical description of the two-phase flow model.

The above governing equations can also be rewritten in tensor forms as

$$\frac{\partial u_i}{\partial x_i} = 0, \tag{2.8}$$

$$\frac{\partial(\rho u_i)}{\partial t} + \frac{\partial(\rho u_j u_i)}{\partial x_j} = -\frac{\partial p}{\partial x_i} + \frac{\partial}{\partial x_j}\left[\mu\left(\frac{\partial u_i}{\partial x_j} + \frac{\partial u_j}{\partial x_i}\right)\right] + \rho g_i, \tag{2.9}$$

$$\frac{\partial F}{\partial t} + u_i \frac{\partial F}{\partial x_i} = 0. \tag{2.10}$$

where x_i, x_j $(i, j = 1, 2, 3)$ or (x, y, z) are the streamwise, spanwise and vertical coordinates, and u_i, u_j or (u, v, w) are the components of the velocity vector $\boldsymbol{u}$.

2.2 Initial and Boundary Conditions

2.2.1 Boundary Conditions

In order to completely describe the mathematical model it is necessary to define the boundary conditions in a computational domain. Consider a computational domain Ω which has the boundary $\partial\Omega$, the unit outward normal vector to the boundary is $\boldsymbol{n}$ and the unit tangential vector to the boundary is $\boldsymbol{t}$. Mathematically, there are three main types of boundary conditions:

- Dirichlet boundary condition: where the value is specified on the boundary for the arbitrary variable ϕ

$$[\phi]_{\partial\Omega} = B, \tag{2.11}$$

  where B is a user specified function.

- Neumann boundary condition: where the gradient of the value is specified on the boundary

$$\left[\frac{\partial\phi}{\partial n}\right]_{\partial\Omega} = B. \tag{2.12}$$

- Robin boundary condition (Eriksson *et al.*, 1996): where the following equation is applied on the boundary

$$\left[a\phi + b\frac{\partial\phi}{\partial n}\right]_{\partial\Omega} = B, \tag{2.13}$$

  where the constants a and b are nonzero.

However, in studying water wave problems, it is more appropriate to specify boundary conditions based on the feature of the considered water wave problems, which will be discussed as follows.

Inlet boundary condition

During the calculation, water waves are generated at the inlet of the computational domain. The time history of the velocity field and the volume fraction at the inlet are obtained from an analytical solution of water waves, namely,

$$[\boldsymbol{u}]_{\text{inlet}} = B_1(\boldsymbol{u}_{\text{wave}}), \tag{2.14}$$

$$[F]_{\text{inlet}} = B_2(\eta_{\text{wave}}), \tag{2.15}$$

where B_1 and B_2 are user specified functions.

Open or radiative boundary condition

When there is a sloping beach at the outlet, the wave will eventually break on the beach and there is no need to define the outlet boundary for water waves. However, when reducing the computational domain where the sloping beach is absent, in order to let the water wave propagating out without reflection, the Sommerfeld radiation condition is used at the outlet of the computational domain (Lin *et al.*, 2008)

$$\frac{\partial \phi}{\partial t} + C_0 \frac{\partial \phi}{\partial n} = 0, \tag{2.16}$$

where C_0 is the characteristic velocity of water waves. For long waves, $C_0 = \sqrt{g(D+H)}$, and for regular short waves, $C_0 = \sqrt{\frac{g}{k_w}\tanh(k_w D)}$ (Lin *et al.*, 2008).

The implementation of the radiative boundary condition has been demonstrated in regular wave tests during code development. It should be noted that the Sommerfeld radiation condition is very effective for long waves, but for short waves, the combination of the Sommerfeld radiation condition and a damping zone will help to reduce the reflection from the outlet.

Free surface boundary condition

As both fluids in the air and water are solved simultaneously in the present two-phase flow model, the kinematic free surface boundary condition and the dynamic

free surface boundary condition are already implemented and they do not need to be specified explicitly at the air-water interface.

Wall boundary condition

At a wall, there are two main types of boundary conditions: no-slip and free-slip conditions. The no-slip condition is used in this study and it ensures that the fluid at the boundary will have zero velocity relative to the wall, e.g. if the wall is stationary

$$[u_n]_{\text{wall}} = 0, \quad [u_t]_{\text{wall}} = 0, \tag{2.17}$$

where u_n and u_t are the velocity components normal and tangential to the wall, respectively. The shear stress on the wall is obtained as

$$\tau_{\text{w}} = \mu \frac{\partial u_t}{\partial n}. \tag{2.18}$$

2.2.2 Initial Conditions

In the computation, the initial flow field at $t = 0$ has to be prescribed. This can be obtained from laboratory data or user-specified values. For calculations with the fluids initially at rest, the flow field is initialized with zero velocity and hydrostatic pressure, and the volume fraction is computed from the initial water depth. When the wave is initialized in the computational domain, the water velocities and water surface are specified using the corresponding analytical solution for water waves. The velocity in the air is initialized as zero in this case as little is known about the flow in the air and the pressure distribution in the whole domain is hydrostatic.

2.3 Finite Volume Discretization

2.3.1 Introduction

In order to solve the mathematical model proposed in the previous sections, a numerical discretization method is needed. There are several discretization approaches for numerical solution of partial differential equations (PDEs), such

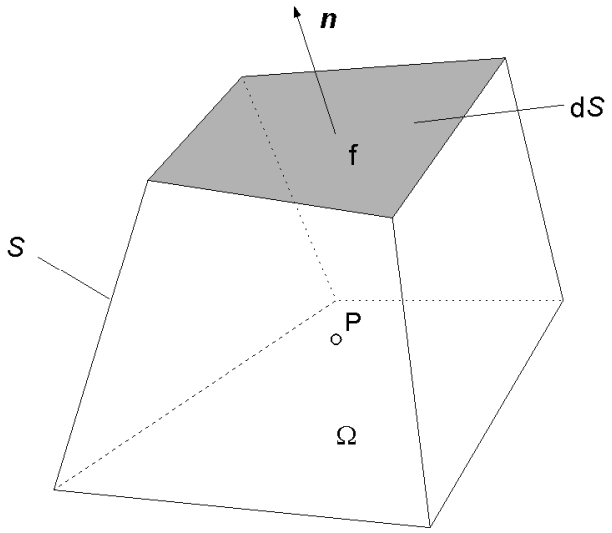

Figure 2.1: A control volume.

as the finite difference method (FDM), finite element method (FEM), meshless methods, and the finite volume method (FVM).

In the FVM, also known as the control volume method, the whole domain is divided into a number of control volumes, such that there is a control volume surrounding each grid point. The differential equation is integrated over each control volume in order to derive the algebraic equation containing the grid-point values of ϕ, where ϕ is the considered variable. The discretized equation expresses the conservation principle for a finite control volume, just as the differential equation expresses it for an infinitesimal control volume. The FVM is conservative and can deal with complex geometries (Ferziger & Peric, 2002; Hirsch, 2007), thus it is especially suitable for modelling free surface flows due to the requirement of mass conservation and the deformed interface, therefore it is adopted in the present study.

2.3.2 Discretization of the Governing Equations

Consider a volume of fluid Ω which has an arbitrary domain shown in figure 2.1, the surface of the control volume is S and the unit outward normal vector to the face f is $\boldsymbol{n}$. All the governing equations can be recast into a general integral formulation as below

$$\iiint_{\Omega} \frac{\partial}{\partial t}(\rho\phi)\mathrm{d}\Omega + \iint_{S} (\rho \boldsymbol{u} \cdot \boldsymbol{n})\phi \mathrm{d}S = \iint_{S} \Gamma \frac{\partial \phi}{\partial n}\mathrm{d}S + \iiint_{\Omega} Q_{\phi}^{\mathrm{S}}\mathrm{d}\Omega, \qquad (2.19)$$

where ϕ denotes the dependent variable, Γ is the viscosity and Q_{ϕ}^{S} is the source term in the control volume.

Table 2.1 shows the various values of ϕ, Γ and Q_{ϕ}^{S} in the general integral formulation to represent the Navier–Stokes equations. It is noted that the final form of the continuity equation (2.2) used here is obtained under the assumption that the fluid is incompressible.

Table 2.1: Values of ϕ, Γ and Q_{ϕ}^{S} in the general integral formulation to represent the Navier–Stokes equations.

Equation	ϕ	Γ	Q_{ϕ}^{S}
Continuity	1	0	0
Momentum	$\boldsymbol{u}$	μ	$-\boldsymbol{\nabla} p + \rho \boldsymbol{g}$

2.3.3 Variable Arrangement on the Staggered Grid

The staggered grid (Arakawa-C grid), which has the advantage of strong coupling between the velocity and the pressure, is used in this study. Figure 2.2 shows a typical variable arrangement in a 3D Cartesian grid, in which the velocities are located on the face centre of the control volume, and the pressure, all other scalar variables and the volume fraction F are stored at the cell centre.

2.3.4 Notation Used in a Control Volume

Figure 2.3 shows a typical control volume used in the present study, in which P is the present node, the upper-case letter E, W, N, S, B, and R denote neighbouring nodes on the east, west, north, south, back, and front with respect to the central node P. The lower-case e, w, n, s, b, and r denote the corresponding face of the control volume whereas c denotes the centre of the control volume. Δx, Δy and

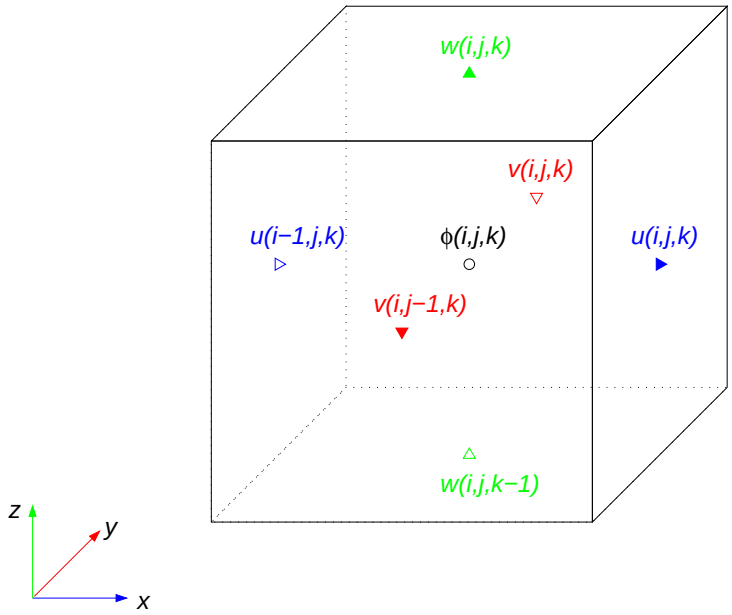

Figure 2.2: Variables used for the control volume (i, j, k) in a 3D staggered grid. Velocities $u(i, j, k)$, $v(i, j, k)$ and $w(i, j, k)$ are stored at the centre of the east, back and north face of the control volume. Pressure and other variables $\phi(i, j, k)$ are stored at the centre of the control volume.

Δz are the cell length in the x, y and z directions, respectively. Thus, the cell volume is obtained as

$$\iiint_{\Omega} \mathrm{d}\Omega = \Delta x \Delta y \Delta z. \tag{2.20}$$

The area of the face A is similarly calculated, e.g. the one of the east face A_e is

$$A_\mathrm{e} = \iint_{\mathrm{e}} \mathrm{d}S = \Delta y \Delta z. \tag{2.21}$$

Unless stated otherwise the variable on the face is predicted with linear interpolation

$$\phi_\mathrm{e} = \lambda_\mathrm{e}\phi_\mathrm{P} + (1 - \lambda_\mathrm{e})\phi_\mathrm{E}, \tag{2.22}$$

where λ_e is the interpolation factor defined as

$$\lambda_\mathrm{e} = \frac{|\mathrm{eE}|}{|\mathrm{PE}|}. \tag{2.23}$$

Analogous expressions can be derived for all other faces (f=w, n, s, b, r) by

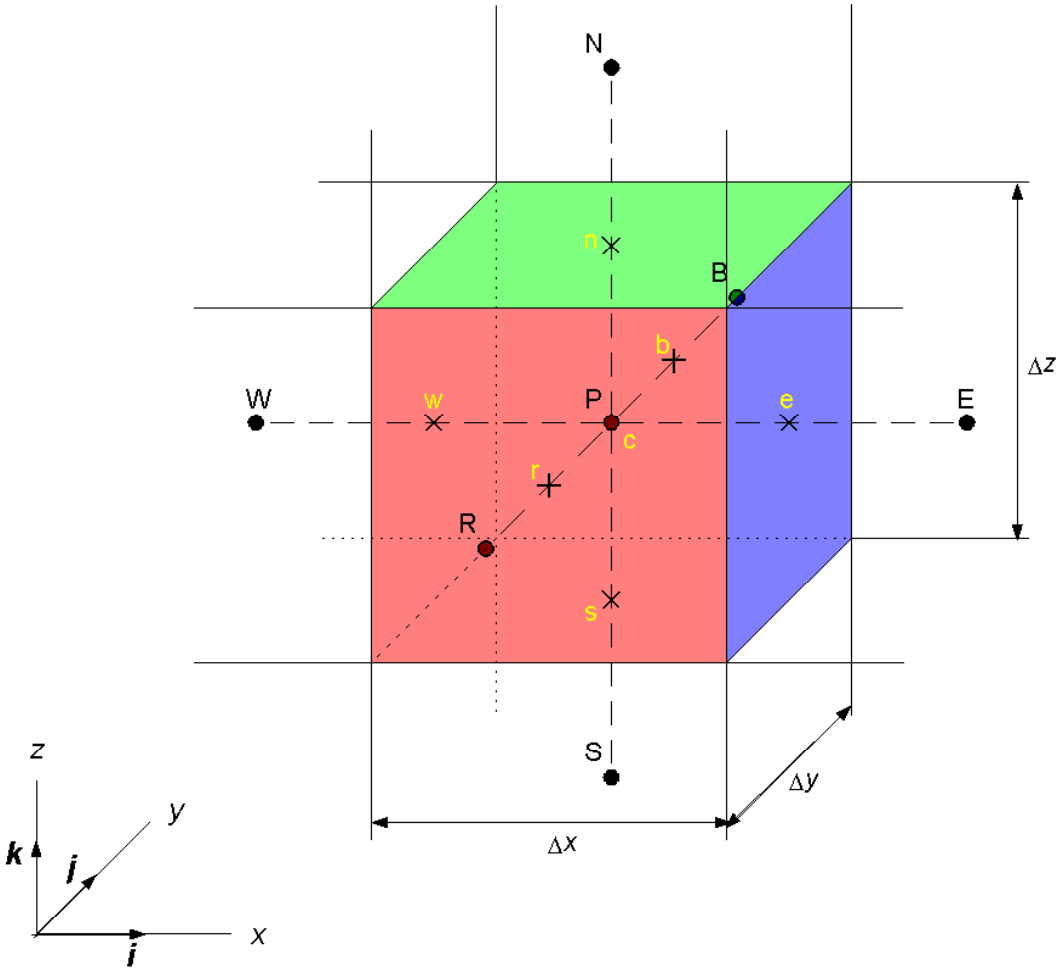

Figure 2.3: A control volume and the notation used for a 3D Cartesian grid. The upper-case letter E, W, N, S, B, and R denote neighbouring nodes on the east, west, north, south, back, and front with respect to the central node P. The lower-case e, w, n, s, b, and r denote the corresponding face of the control volume whereas c denotes the centre of the control volume. Δx, Δy and Δz are the cell length, and $\boldsymbol{i}$, $\boldsymbol{j}$ and $\boldsymbol{k}$ are unit vectors in the x, y and z directions, respectively.

making appropriate index substitutions and will not be shown here.

2.4 The Complex Geometry Treatment in Cartesian Grid

To deal with complex geometries in engineering applications, overlapping grids, boundary-fitted grids and unstructured grids can be used. However, the programming of these methods can be complicated and generating such a grid is usually very cumbersome. Cartesian grid methods which can simulate flow with complex geometries on Cartesian grids, avoid these problems. The most popular methods are the immersed boundary method (Mittal & Iaccarino, 2005) and Cartesian cut cell method (Ingram *et al.*, 2003). The primary advantage of the Cartesian grid method is that only little modification of the program on Cartesian grids is needed to account for the complex geometries. It also has the advantage of simplified grid generation and simulating flow with moving boundaries due to the use of stationary, nondeforming grids. The drawback of these methods is that implementing boundary conditions is not straightforward and instability problems may occur in small cells when explicit schemes are used. Thus, the cell-merging technique (Causon *et al.*, 2000) and using slightly different control volumes (Kleefsman *et al.*, 2005) are developed to avoid this instability, both of which effectively increase the size of the cut cell.

In this study, the partial cell treatment is used and a typical θ function in a control volume, arises from FAVOR (Fractional-Area-Volume Obstacle Representation) method (see for example Torrey *et al.*, 1985), is introduced in the finite volume discretization. The θ function is defined whose value is 1 for a point accessible to fluid and 0 for a point inside an obstacle. The average of this function over a control volume or cell face is the fraction of the volume or area available to the flow. Figure 2.4 shows a typical cut cell in a 2D Cartesian grid and analogous expressions can be obtained in 3D. To prevent the instability in small cells, an implicit scheme is employed for the governing equations.

In contrast to a full cell, the convective and diffusive fluxes at cell faces are modified in a cut cell, which will be presented in the following discretization.

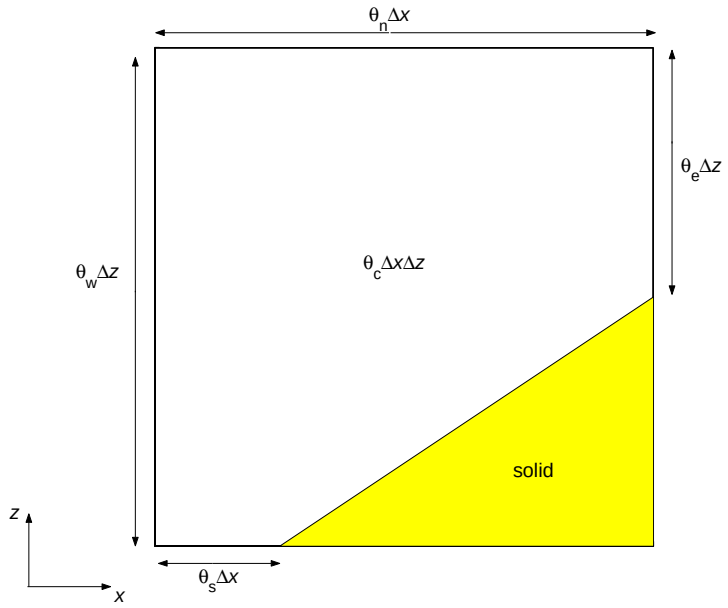

Figure 2.4: θ function for a typical cut cell in a 2D Cartesian grid, in which the length of the face is represented as $\theta \cdot \Delta x$ or $\theta \cdot \Delta z$, and the volume of the cell is represented by $\theta_{\mathrm{c}} \cdot \Delta x \Delta z$.

2.5 Discretization of Spatial Terms

2.5.1 Convection Term

The finite volume discretization of the convection term is obtained as

$$\begin{aligned} Q_{\phi}^{\mathrm{C}} = \iint_{S} (\rho \boldsymbol{u} \cdot \boldsymbol{n}) \phi \mathrm{d}S &= \sum_{\mathrm{f}} (\theta A)_{\mathrm{f}} \left[(\rho \boldsymbol{u} \cdot \boldsymbol{n}) \phi \right]_{\mathrm{f}} \\ &= \sum_{\mathrm{f}} (\rho \boldsymbol{u} \cdot \boldsymbol{n} \theta A)_{\mathrm{f}} \phi_{\mathrm{f}} \\ &= \sum_{\mathrm{f}} m_{\mathrm{f}} \phi_{\mathrm{f}}, \end{aligned} \tag{2.24}$$

where the subscript f denotes the corresponding face of the control volume, A is the area of the face and m is the mass flux through the face

$$m = \rho \boldsymbol{u} \cdot \boldsymbol{n} \theta A. \tag{2.25}$$

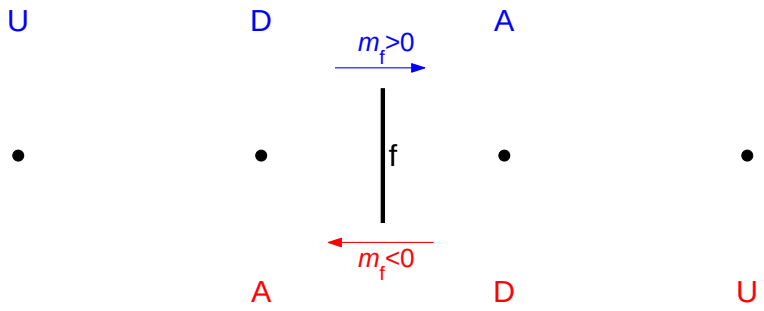

Figure 2.5: Notation of the cells for the interpolation at the face f: D, A, and U denote donor cell, acceptor cell and upwind cell, respectively.

The mass flux at the faces of the momentum control volume can be obtained by the interpolation of values of ρ and $\boldsymbol{u}$, such as $m_\mathrm{f} = \rho_\mathrm{f}\boldsymbol{u}_\mathrm{f} \cdot \boldsymbol{n}\theta_\mathrm{f}A_\mathrm{f}$, however, the mass conservation in the momentum control volume can be only guaranteed to the accuracy of the interpolation procedure (Ferziger & Peric, 2002). Thus, in this study, the m_f is obtained from the interpolation of the mass fluxes, which is already available at the faces of the continuity control volumes. The face value ϕ_f can be obtained from different schemes and will be described in detail as follows.

First order upwind scheme

The upwind scheme implies that the convection is received from upstream and transmitted to the next control volume downstream. In the first order upwind (FOU) scheme, the value of ϕ on the face of the control volume is taken by the constant extrapolation of the value of ϕ at the grid point of the donor cell, e.g.

$$\phi_\mathrm{f}^\mathrm{FOU} = \phi_\mathrm{D}, \tag{2.26}$$

where subscripts D, A, and U denote donor cell, acceptor cell and upwind cell, which is shown in figure 2.5.

If the first order upwind scheme is used, the convection term in the east face of the control volume can be expressed as

$$m_\mathrm{e}\phi_\mathrm{e} = \max(m_\mathrm{e}, 0)\phi_\mathrm{P} - \max(-m_\mathrm{e}, 0)\phi_\mathrm{E}. \tag{2.27}$$

High order schemes

Among all the possible schemes, the first order upwind scheme has the best convergence property but the aim of other schemes is to improve the accuracy. Thus when a high order scheme is used, it is advantageous to also use the first order formulation and the difference between the first order upwind and the other scheme gives rise to an additional source term Q_ϕ^{H}, used in the deferred correction approach (Ferziger & Peric, 2002).

Second order upwind scheme In the second order upwind (SOU) scheme, the value at the face of the control volume is obtained by the linear extrapolation of the value of ϕ at two upstream cells as

$$\begin{aligned}\phi_{\mathrm{f}}^{\mathrm{SOU}} &= \frac{3}{2}\phi_{\mathrm{D}} - \frac{1}{2}\phi_{\mathrm{U}} \\ &= \phi_{\mathrm{D}} + \frac{1}{2}(\phi_{\mathrm{D}} - \phi_{\mathrm{U}}) \\ &= \phi_{\mathrm{f}}^{\mathrm{FOU}} + \frac{1}{2}(\phi_{\mathrm{D}} - \phi_{\mathrm{U}}).\end{aligned} \tag{2.28}$$

The QUICK scheme can also be implemented in a similar way, however it was found that it led to some convergence problems in the simulation due to the implicit scheme used for the momentum equation.

High resolution scheme

It is well known that unphysical wiggles (numerical oscillations) will appear in numerical simulations with high order schemes under some circumstances. Thus, a high resolution scheme (Hirsch, 2007), which combines the high order accuracy with monotonicity, is used in this study to discretize the value at the face as

$$\phi_{\mathrm{f}}{}^{\mathrm{HRS}} = \phi_{\mathrm{f}}^{\mathrm{FOU}} + \Psi(r_{\mathrm{f}}^{\phi})(\phi_{\mathrm{f}}^{\mathrm{SOU}} - \phi_{\mathrm{f}}^{\mathrm{FOU}}), \tag{2.29}$$

in which $\Psi()$ is the limiter function where the minmod limiter (Roe, 1986), which is one of the simplest second-order TVD (Total Variation Diminishing) schemes,

is used here

$$\Psi(r) = \max[0, \min(r, 1)]. \tag{2.30}$$

Similar results were obtained by using other limiter functions and a general review of various limiter functions can be found in Waterson & Deconinck (2007) and will not be presented here. r_{f}^{ϕ} represents the ratio of successive gradients of ϕ on the solution mesh and obtained as

$$r_{\mathrm{f}}^{\phi} = \frac{\phi_{\mathrm{A}} - \phi_{\mathrm{D}}}{\phi_{\mathrm{D}} - \phi_{\mathrm{U}}}. \tag{2.31}$$

Discussion

The convection term plays an important role in numerical solution of the Navier–Stokes equations. For a two-phase flow model, the convection term can be discretized in two different ways: conservative form and nonconservative form.

When nonconservative form is employed, the density in the centre of the control volume is used and the mass flux on the face m'_{f} can be obtained as

$$m'_{\mathrm{f}} = \rho_{\mathrm{c}}(\boldsymbol{u} \cdot \boldsymbol{n}\theta A)_{\mathrm{f}}. \tag{2.32}$$

As we assume that the velocity does not vary discontinuously near an interface, the resulting mass flux is continuous in a control volume but discontinuous between the control volumes. Many people used the nonconservative form as it is simple for numerical implementation. However, the nonconservative form will violate the rule for consistency at control volume faces proposed by Patankar (1980):

> **Consistency at control volume faces** When a face is common to two adjacent control volumes, the flux across it must be represented by the *same* expression in the discretization equations for the two control volumes.

For example on the east face of the control volume P, the mass flux is expressed as $\rho_{\mathrm{P}}(\boldsymbol{u} \cdot \boldsymbol{n}\theta A)_{\mathrm{e}}$ when the control volume surrounding P is considered, and as $\rho_{\mathrm{E}}(\boldsymbol{u} \cdot \boldsymbol{n}\theta A)_{\mathrm{e}}$ when the control volume surrounding E is considered. In the vicinity of the

interface, the mass flux across the face between the control volumes surrounding P and E will be inconsistent when $\rho_{\mathrm{P}} \neq \rho_{\mathrm{E}}$.

Therefore, the conservative form for the mass flux

$$m_{\mathrm{f}} = (\rho \boldsymbol{u} \cdot \boldsymbol{n} \theta A)_{\mathrm{f}}, \tag{2.33}$$

is employed in this study.

In the available literature, the conservative form is only used in a few two-phase flow models (Bussmann *et al.*, 2002; Rudman, 1998; Ubbink, 1997; Udaykumar *et al.*, 1997; Unverdi & Tryggvason, 1992). It is mentioned that special attention has to be paid in the discretization of the conservative form of the convection term, otherwise, high and irregular velocities near the interface can sometimes destroy the solution (Prosperetti & Tryggvason, 2007), and one way to overcome this is to use the nonconservative form of the convection term (Esmaeeli & Tryggvason, 2005). In addition, special attention should be paid to the discretization of the body force, otherwise non-physical velocities will be generated for the quiescent fluid (Mencinger & Zun, 2007; Wemmenhove, 2008).

The idea of consistency between mass and momentum conservation has been proposed in the conservative form (Bussmann *et al.*, 2002; Rudman, 1998; Ubbink, 1997). For collocated grids, Ubbink (1997) used the face value for F_{f} calculated from the VOF equation to obtain the mass flux for the momentum equation while Bussmann *et al.* (2002) explicitly calculated the exact mass flux based on the volume tracking method. It is not easy to calculate consistent mass fluxes across cell faces for a staggered grid, Rudman (1998) introduced a twice-as-fine sub-mesh nested within the underlying solver mesh for mass convection, in order to overlap the control volumes for the mass and momentum to get the consistency. Rudman used the explicit scheme for the momentum equation, and calculated the mass fluxes based on the volume fraction which was obtained from the Youngs' VOF method. However, it is not clear yet how to deal with this consistency in a single staggered grid if the mass flux is not calculated based on the explicit interface advection (such as surface capturing methods), and especially when the implicit scheme is employed for the momentum equation.

It is worth remarking that the mass flux is discontinuous in a control volume in the conservative form due to the density variation between the cell face and cell centre. Sometimes, the combination of the conservative form and the high resolution scheme may lead to some convergence problems in the simulation. Thus, a step function for the mass flux is introduced to the high resolution scheme to get more robust and accurate solution as

$$\phi_{\mathrm{f}}^{\mathrm{HRS}} = \phi_{\mathrm{f}}^{\mathrm{FOU}} + \Phi(r_{\mathrm{f}}^{m})\Psi(r_{\mathrm{f}}^{\phi})(\phi_{\mathrm{f}}^{\mathrm{SOU}} - \phi_{\mathrm{f}}^{\mathrm{FOU}}), \tag{2.34}$$

where $\Phi()$ is the step function and r_{f}^{m} is the variation for the mass which is defined as the ratio of the mass flux between the conservative and nonconservative form

$$r_{\mathrm{f}}^{m} = \frac{m_{\mathrm{f}}}{m_{\mathrm{f}}'}. \tag{2.35}$$

The step function $\Phi()$ takes the form

$$\Phi(r) = \begin{cases} 1, & \text{if } |r| \leq 1; \\ 0, & \text{otherwise,} \end{cases} \tag{2.36}$$

which means that the present high resolution scheme switches to the first order upwind scheme when the density on the cell face is larger than the density in the cell centre.

2.5.2 Diffusion Term

The finite volume discretization of the diffusion term is obtained as

$$Q_{\phi}^{\mathrm{D}} = \iint_{S} \Gamma \frac{\partial \phi}{\partial n} \mathrm{d}S = \sum_{\mathrm{f}} \Gamma_{\mathrm{f}} \frac{\partial \phi}{\partial n} (\theta A)_{\mathrm{f}} + Q_{\phi}^{\mathrm{W}}, \tag{2.37}$$

where the viscosity on the face is obtained by the harmonic mean (Patankar, 1980), for example, on the east face

$$\Gamma_{\mathrm{e}} = \frac{\Gamma_{\mathrm{P}}\Gamma_{\mathrm{E}}}{\lambda_{\mathrm{e}}\Gamma_{\mathrm{P}} + (1 - \lambda_{\mathrm{e}})\Gamma_{\mathrm{E}}}. \tag{2.38}$$

Analogous expressions can be derived for all other faces (f=w, n, s, b, r) by making appropriate index substitutions and will not be shown here.

The gradient at the face is calculated by the finite difference approach as

$$\frac{\partial \phi}{\partial n} = \frac{\phi_{\mathrm{nb}} - \phi_{\mathrm{P}}}{\Delta_{\mathrm{Pnb}}}, \tag{2.39}$$

where Δ_{Pnb} is the distance from the present point P to the neighbouring point nb.

Q_ϕ^{W}, which is zero in full cells, is the discretization of the diffusion flux on the solid boundary in cut cells, which will be discussed later in the implementation of boundary conditions.

2.5.3 Source Term

Source term linearization

When the source term Q_ϕ^{S} is a function of ϕ then there are many ways in which the Q_ϕ^{S0} and Q_ϕ^{S1} can be chosen to satisfy (Patankar, 1980)

$$Q_\phi^{\mathrm{S}} = Q_\phi^{\mathrm{S0}} + Q_\phi^{\mathrm{S1}}\phi, \quad Q_\phi^{\mathrm{S1}} < 0. \tag{2.40}$$

The term in Q_ϕ^{S} without ϕ goes into the term Q_ϕ^{S0}. The term which includes ϕ is modified as $Q_\phi^{\mathrm{S1}}\phi$ provided $Q_\phi^{\mathrm{S1}} < 0$ is satisfied, otherwise, it goes into the term Q_ϕ^{S0}. The advantage of this way is that once substituting the discretized source term into the governing equation, the term $Q_\phi^{\mathrm{S1}}\phi$ may be moved to left-hand side of the equation, yields an equation which has a stronger diagonal dominance and therefore a better and faster rate of convergence will be achieved.

Pressure term

The finite volume discretization of the pressure term is obtained as

$$Q_\phi^{\mathrm{p}} = \iiint_\Omega -\boldsymbol{\nabla} p \mathrm{d}\Omega = -\boldsymbol{\nabla} p \theta_{\mathrm{c}} \Omega, \tag{2.41}$$

and the pressure gradient is calculated as

$$\begin{aligned}\boldsymbol{\nabla} p &= (\frac{\partial p}{\partial x}, \frac{\partial p}{\partial y}, \frac{\partial p}{\partial z}) \\ &= (\frac{p_{\mathrm{e}} - p_{\mathrm{w}}}{\Delta x}, \frac{p_{\mathrm{b}} - p_{\mathrm{r}}}{\Delta y}, \frac{p_{\mathrm{n}} - p_{\mathrm{s}}}{\Delta z}).\end{aligned} \tag{2.42}$$

Body force term

The finite volume discretization of the body force term is obtained as

$$Q_{\phi}^{\mathrm{B}} = \iiint_{\Omega} \rho \boldsymbol{g} \mathrm{d}\Omega = \rho_{\mathrm{c}} \boldsymbol{g} \theta_{\mathrm{c}} \Omega, \tag{2.43}$$

where the value in the centre of the control volume is obtained by the volume averaging of two values on the face of the control volume.

2.6 Temporal Discretization

A backward finite difference is used for the time derivative, which leads to an implicit scheme for the governing equations

$$Q_{\phi}^{\mathrm{T}} = \iiint_{\Omega} \frac{\partial}{\partial t}(\rho\phi)\mathrm{d}\Omega = \frac{\rho_{\mathrm{c}}^{n+1}\phi^{n+1} - \rho_{\mathrm{c}}^{n}\phi^{n}}{\Delta t}\theta_{\mathrm{c}}\Omega, \tag{2.44}$$

where Δt is the time step and the superscripts $n+1$ and n mean the value in current and previous time step, respectively. The implicit scheme has the advantage of unconditional stability and thus can prevent the instability problem in small cut cells. Higher order schemes such as Gear's method can also be used, which can reduce the amplitude decay for the regular or solitary wave propagation when a large time step is used in the simulation.

2.7 General Form of the Discretization

Substituting all the above discretized terms into (2.19) and subtracting the continuity equation multiplied by ϕ_{P}^{n+1}, leads to

$$a_{\mathrm{P}}^{\phi}\phi_{\mathrm{P}}^{n+1} = \sum a_{\mathrm{nb}}^{\phi}\phi_{\mathrm{nb}}^{n+1} + b_{\mathrm{P}}^{\phi}, \tag{2.45}$$

where a^{ϕ} is the coefficient, the subscripts P and nb $= \mathrm{E}, \mathrm{W}, \mathrm{N}, \mathrm{S}, \mathrm{B}, \mathrm{R}$ denote the variables in the present and neighbouring cells respectively and b_{P}^{ϕ} is the source term.

In nonlinear problems it is often desirable to slow down the change in the predicted change of the dependent variable and in such circumstances under-relaxation (Patankar, 1980) is used, thus the equation (2.45) may be written as

$$\phi_{\mathrm{P}}^{n+1} = \phi_{\mathrm{P}}^{0} + \alpha_{\phi}\left(\frac{\sum a_{\mathrm{nb}}^{\phi}\phi_{\mathrm{nb}}^{n+1} + b_{\mathrm{P}}^{\phi}}{a_{\mathrm{P}}^{\phi}} - \phi_{\mathrm{P}}^{0}\right), \tag{2.46}$$

or

$$\frac{a_{\mathrm{P}}^{\phi}}{\alpha_{\phi}}\phi_{\mathrm{P}}^{n+1} = \sum a_{\mathrm{nb}}^{\phi}\phi_{\mathrm{nb}}^{n+1} + b_{\mathrm{P}}^{\phi} + \frac{1-\alpha_{\phi}}{\alpha_{\phi}}\phi_{\mathrm{P}}^{0}, \tag{2.47}$$

where ϕ_{P}^{0} is the value from the previous iteration and $0 < \alpha_{\phi} < 1$ is the under-relaxation factor. There are no general rules for choosing the best value for the under-relaxation factor (Patankar, 1980), thus from our experience $\alpha_{\phi=u,v,w} = 0.7$ is used for the momentum equations in this study.

The coefficients depend on the approximations used and the first order upwind scheme is used in this study as the basis of the formulation, high resolution scheme is implemented using the deferred correction method via source term Q_{ϕ}^{H} (Ferziger & Peric, 2002).

For example, the coefficients for momentum equation $\phi = u, v, w$ are

$$\begin{aligned} a_{\mathrm{nb}}^{\phi} &= \max(-m_{\mathrm{f}}^{\phi}, 0) + \frac{\Gamma_{\mathrm{f}}(\theta A)_{\mathrm{f}}}{\Delta_{\mathrm{Pnb}}}, \\ a_{\mathrm{P}}^{\phi} &= \frac{\rho_{\mathrm{c}}\theta_{\mathrm{c}}\Omega}{\Delta t} + \sum_{\mathrm{nb}} a_{\mathrm{nb}}^{\phi}, \\ b_{\mathrm{P}}^{\phi} &= Q_{\phi}^{\mathrm{p}} + Q_{\phi}^{\mathrm{B}} + \frac{\rho_{\mathrm{c}}\theta_{\mathrm{c}}\Omega}{\Delta t}\phi_{\mathrm{P}}^{n} + Q_{\phi}^{\mathrm{H}}. \end{aligned} \tag{2.48}$$

2.8 Pressure-Velocity Coupling

In the incompressible Navier–Stokes equations pressure and velocity are decoupled as the pressure term does not appear in the continuity equation. For some numerical discretizations this may cause convergence problems. However, when a staggered mesh is used, as in this work, coupling occurs as a result of the discretization, as velocity updates on cell faces contain pressure terms. In the control volume for the pressure, shown in figure 2.3, the discretization equations for momentum $\boldsymbol{u}$ on the face f can also be expressed by moving the pressure term out from the source term in equation (2.47) as

$$\frac{a_{\mathrm{P}}^{\boldsymbol{u}}}{\alpha_{\boldsymbol{u}}}\boldsymbol{u}_{\mathrm{f}} = \sum a_{\mathrm{nb}}^{\boldsymbol{u}}\boldsymbol{u}_{\mathrm{nb}} + b_{\mathrm{P}}^{\boldsymbol{u}} + \frac{1-\alpha_{\boldsymbol{u}}}{\alpha_{\boldsymbol{u}}}\boldsymbol{u}_{\mathrm{f}}^{0} + A_{\mathrm{f}}(p_{\mathrm{P}} - p_{\mathrm{nb}}). \tag{2.49}$$

For a guessed pressure distribution p^*, the above momentum equations can be solved to produce the fluid velocities $\boldsymbol{u}^*$, which satisfy

$$\frac{a_{\mathrm{P}}^{\boldsymbol{u}}}{\alpha_{\boldsymbol{u}}}\boldsymbol{u}_{\mathrm{f}}^{*} = \sum a_{\mathrm{nb}}^{\boldsymbol{u}}\boldsymbol{u}_{\mathrm{nb}}^{*} + b_{\mathrm{P}}^{\boldsymbol{u}} + \frac{1-\alpha_{\boldsymbol{u}}}{\alpha_{\boldsymbol{u}}}\boldsymbol{u}_{\mathrm{f}}^{0} + A_{\mathrm{f}}(p_{\mathrm{P}}^{*} - p_{\mathrm{nb}}^{*}). \tag{2.50}$$

Suppose the correct pressure is obtained by a pressure correction p', e.g.

$$p = p^* + p', \tag{2.51}$$

similarly the correct fluid velocities are obtained by the velocity correction $\boldsymbol{u}'$

$$\boldsymbol{u} = \boldsymbol{u}^* + \boldsymbol{u}'. \tag{2.52}$$

If the equations (2.49) are subtracted from equations (2.50), then the fully implicit velocity correction equations are obtained as

$$\frac{a_{\mathrm{P}}^{\boldsymbol{u}}}{\alpha_{\boldsymbol{u}}}\boldsymbol{u}_{\mathrm{f}}' = \sum a_{\mathrm{nb}}^{\boldsymbol{u}}\boldsymbol{u}_{\mathrm{nb}}' + A_{\mathrm{f}}(p_{\mathrm{P}}' - p_{\mathrm{nb}}'), \tag{2.53}$$

where the velocity correction at any point is connected to all of the velocity correction in the computational domain.

In the SIMPLE algorithm (Patankar, 1980), the velocity correction equations are approximated by dropping the $\sum a_{\mathrm{nb}}^{\boldsymbol{u}}\boldsymbol{u}_{\mathrm{nb}}'$ terms on the right-hand side of the

equations (2.53) and we obtain

$$\boldsymbol{u}'_{\mathrm{f}} = \frac{\alpha_{\boldsymbol{u}} A_{\mathrm{f}}}{a_{\mathrm{P}}^{\boldsymbol{u}}}(p'_{\mathrm{P}} - p'_{\mathrm{nb}}). \tag{2.54}$$

Thus far we have only considered the momentum equations, nevertheless, the velocity field is also subject to the constraint that it should satisfy the continuity equation (2.2). The discretized form for the continuity equation in the continuity control volume (see figure 2.3) is

$$u_{\mathrm{e}}\theta_{\mathrm{e}}A_{\mathrm{e}} - u_{\mathrm{w}}\theta_{\mathrm{w}}A_{\mathrm{w}} + v_{\mathrm{b}}\theta_{\mathrm{b}}A_{\mathrm{b}} - v_{\mathrm{r}}\theta_{\mathrm{r}}A_{\mathrm{r}} + w_{\mathrm{n}}\theta_{\mathrm{n}}A_{\mathrm{n}} - w_{\mathrm{s}}\theta_{\mathrm{s}}A_{\mathrm{s}} = 0. \tag{2.55}$$

To obtain the pressure correction, equations (2.52) and (2.54) are substituted into the discretized continuity equation (2.55) and the resulting pressure correction equation has the following form

$$a_{\mathrm{P}}^{p} p'_{\mathrm{P}} = \sum a_{\mathrm{nb}}^{p} p'_{\mathrm{nb}} + b'_{\mathrm{P}}, \tag{2.56}$$

where the coefficients are

$$\begin{aligned}
a_{\mathrm{E}}^{p} &= \left(\frac{\alpha_u \theta A^2}{a_{\mathrm{P}}^{u}}\right)_{\mathrm{e}}, a_{\mathrm{W}}^{p} = \left(\frac{\alpha_u \theta A^2}{a_{\mathrm{P}}^{u}}\right)_{\mathrm{w}}, \\
a_{\mathrm{B}}^{p} &= \left(\frac{\alpha_v \theta A^2}{a_{\mathrm{P}}^{v}}\right)_{\mathrm{b}}, a_{\mathrm{R}}^{p} = \left(\frac{\alpha_v \theta A^2}{a_{\mathrm{P}}^{v}}\right)_{\mathrm{r}}, \\
a_{\mathrm{N}}^{p} &= \left(\frac{\alpha_w \theta A^2}{a_{\mathrm{P}}^{w}}\right)_{\mathrm{n}}, a_{\mathrm{S}}^{p} = \left(\frac{\alpha_w \theta A^2}{a_{\mathrm{P}}^{w}}\right)_{\mathrm{s}}, \\
a_{\mathrm{P}}^{p} &= \sum_{\mathrm{nb}} a_{\mathrm{nb}}^{p}, \\
b'_{\mathrm{P}} &= -\Big(u^*_{\mathrm{e}}\theta_{\mathrm{e}}A_{\mathrm{e}} - u^*_{\mathrm{w}}\theta_{\mathrm{w}}A_{\mathrm{w}} \\
&\qquad + v^*_{\mathrm{b}}\theta_{\mathrm{b}}A_{\mathrm{b}} - v^*_{\mathrm{r}}\theta_{\mathrm{r}}A_{\mathrm{r}} \\
&\qquad + w^*_{\mathrm{n}}\theta_{\mathrm{n}}A_{\mathrm{n}} - w^*_{\mathrm{s}}\theta_{\mathrm{s}}A_{\mathrm{s}}\Big).
\end{aligned} \tag{2.57}$$

The term b'_{P}, called the mass residual, in the pressure correction equation is the left-hand side of the discretized continuity equation (2.55) evaluated in terms of the fluid velocity components u^*, v^* and w^*. If b'_{P} is zero then the fluid velocity satisfies the continuity equation and the solution to the problem has

been obtained.

After the pressure correction equation (2.56) is solved, the pressure is updated by

$$p = p^* + \alpha_p p', \tag{2.58}$$

where the under-relaxation factor for the pressure $\alpha_p = 0.3$ is used in this study following the expression proposed by Ferziger & Peric (2002), stated that from their experience the optimum value of α_p is given by $\alpha_p = 1 - \alpha_{\boldsymbol{u}}$. Velocities are updated by equations (2.52) and (2.54).

In the PISO algorithm (Issa, 1986), a second correction step is introduced as

$$\frac{a_{\mathrm{P}}^{\boldsymbol{u}}}{\alpha_{\boldsymbol{u}}} \boldsymbol{u}_{\mathrm{f}}'' = \sum a_{\mathrm{nb}}^{\boldsymbol{u}} \boldsymbol{u}_{\mathrm{nb}}' + A_{\mathrm{f}}(p_{\mathrm{P}}'' - p_{\mathrm{nb}}''), \tag{2.59}$$

where

$$\begin{aligned} \boldsymbol{u} &= \boldsymbol{u}^* + \boldsymbol{u}' + \boldsymbol{u}'', \\ p &= p^* + p' + p''. \end{aligned} \tag{2.60}$$

The $\sum a_{\mathrm{nb}}^{\boldsymbol{u}} \boldsymbol{u}_{\mathrm{nb}}'$ terms, which has been neglected in the first correction step, are now included in the second correction step as we have already obtained the value of $\boldsymbol{u}_{\mathrm{nb}}'$ from the first correction step. Then, substitution of the above expression (2.60) and (2.59) into the continuity equation (2.55) leads to the second pressure-correction equation as

$$a_{\mathrm{P}}^p p_{\mathrm{P}}'' = \sum a_{\mathrm{nb}}^p p_{\mathrm{nb}}'' + b_{\mathrm{P}}'', \tag{2.61}$$

where the coefficients have the same value in the first pressure correction equation shown in (2.57) and the source term has been changed to

$$\begin{aligned} b_{\mathrm{P}}'' = -\Bigg[& \left(\frac{\alpha_u}{a_{\mathrm{P}}^u} \sum a_{\mathrm{nb}}^u u_{\mathrm{nb}}' \right)_{\mathrm{e}} \theta_{\mathrm{e}} A_{\mathrm{e}} - \left(\frac{\alpha_u}{a_{\mathrm{P}}^u} \sum a_{\mathrm{nb}}^u u_{\mathrm{nb}}' \right)_{\mathrm{w}} \theta_{\mathrm{w}} A_{\mathrm{w}} \\ & + \left(\frac{\alpha_v}{a_{\mathrm{P}}^v} \sum a_{\mathrm{nb}}^v v_{\mathrm{nb}}' \right)_{\mathrm{b}} \theta_{\mathrm{b}} A_{\mathrm{b}} - \left(\frac{\alpha_v}{a_{\mathrm{P}}^v} \sum a_{\mathrm{nb}}^v v_{\mathrm{nb}}' \right)_{\mathrm{r}} \theta_{\mathrm{r}} A_{\mathrm{r}} \\ & + \left(\frac{\alpha_w}{a_{\mathrm{P}}^w} \sum a_{\mathrm{nb}}^w w_{\mathrm{nb}}' \right)_{\mathrm{n}} \theta_{\mathrm{n}} A_{\mathrm{n}} - \left(\frac{\alpha_w}{a_{\mathrm{P}}^w} \sum a_{\mathrm{nb}}^w w_{\mathrm{nb}}' \right)_{\mathrm{s}} \theta_{\mathrm{s}} A_{\mathrm{s}} \Bigg]. \end{aligned} \tag{2.62}$$

After the second pressure correction equation (2.61) is solved, all solutions are updated by equation (2.60).

It is worth remarking that under-relaxation is not needed in the PISO algorithm and all under-relaxation factors are $\alpha_\phi = 1$.

Both SIMPLE and PISO algorithms are the pressure-correction method and they are widely used in CFD as well as in some commercial software. The SIMPLE method is very robust to deal with steady problems while the PISO method is more efficient in solving transient problems. At the beginning of the development of the code, the SIMPLE algorithm is used to simulate 2D breaking solitary waves, whereas the PISO algorithm, which can reduce the computational effort and CPU time, is further implemented for 2D periodic breaking waves and 3D breaking waves.

2.9 Interface Calculations

A key requirement for modelling two-phase flow is a method of calculating the shape of the interface. There are essentially two types of method (Ferziger & Peric, 2002):

- interface tracking,
- interface capturing.

Table 2.2 gives a brief overview of the numerical methods for interfacial flows. In this section, we review different methods for interface calculations first and then we present the method used in this study.

2.9.1 Interface Tracking

In interface tracking methods, the exact position of the interface is known during the computation, and boundary conditions can be applied at the interface. During each time step, the location of the interface has to be advanced with the solution in the background mesh (fixed or moving) or meshless domain.

Table 2.2: Interface calculation methods

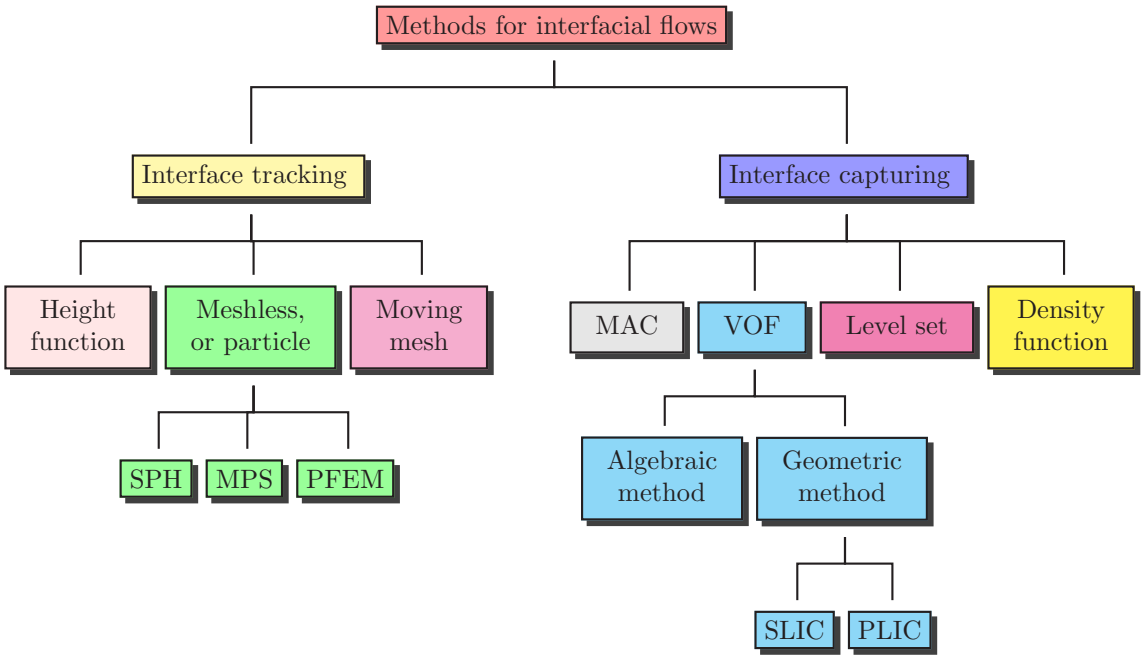

Height function method

In the height function method (Nichols & Hirt, 1973), the location of the free surface is represented by a height relative to the reference elevation. The evolution of the height function is governed by the kinematic free surface boundary condition and solved with the fluid velocities to track the interface. This method is very efficient in 2D or 3D free surface flows as the problem can be transformed to horizontal 1D or 2D. The major limitation of this method is that breaking and overturning waves cannot be simulated because the height function remain single-valued at horizontal locations.

Moving mesh or boundary fitted method

Moving mesh methods, utilize boundary fitted grids that follow an interface as it moves, so that boundary conditions can be applied at cell faces. The grid adapts to the position of the surface at each time step. Many finite-element

or unstructured finite-volume (Zwart, 1999) methods use this approach. The advantage of this method is that we can get the sharp interface and the exact position is known throughout the computation. The limitation of the methods is that it is difficult to track surfaces that interact or break up, such as wave post-breaking and the splash-up.

Particle and meshless method

Apart from the Eulerian method mentioned above, in which the results are based on a fixed or moving grid, there are also some meshless Lagrangian or particle methods, such as the smooth particle hydrodynamics (SPH) (Monaghan, 1994), moving particle semi-implicit (MPS) (Koshizuka *et al.*, 1995) and particle finite element methods (PFEM) (Idelsohn *et al.*, 2004). In these methods, particles are calculated in Lagrangian approach and advection is computed directly through particle motion without numerical diffusion. Particles are advanced at each time step, and thus the interface can be determined. These methods have advantages to deal with moving bodies, large deformation such as wave post-breaking but the difficulty and limitation is that it involves heavy computational demands especially in 3D applications and the treatment of boundary conditions is not as straightforward as in mesh-based methods (Nguyen *et al.*, 2008).

The particle method has been increased rapidly recently including some applications for breaking waves (Dalrymple & Rogers, 2006; Gotoh & Sakai, 1999, 2006; Khayyer *et al.*, 2008; Landrini *et al.*, 2007; Lo & Shao, 2002; Ma & Zhou, 2009; Shao, 2006; Shao & Ji, 2006).

2.9.2 Interface Capturing

In contrast to interface tracking methods, interface capturing methods are implemented on a fixed grid, which often extends beyond the free surface and includes the whole computational domain. The methods are relatively simple to implement and require less computational effort compared to interface tracking methods, as the grid remains fixed.

Marker methods

The Marker-and-Cell (MAC) method (Harlow & Welch, 1965) was the earliest numerical method, which is based on a fixed, Eulerian grid of control volumes, for solving the unsteady free surface flow problems. Massless marker particles are introduced in the calculation and advanced in each time step. The fluid is determined by the cells, which contain markers. After that, later improvement includes the SMAC (Simplified Marker-And-Cell) (Amsden & Harlow, 1970) and GENSMAC (GENeralized Simplified Marker-And-Cell) (Tome & Mckee, 1994) methods. The advantage of the MAC method is that it can deal with a wide range of free surface flows including wave breaking, and the limitation is that considerable computational effort is needed to advance the markers especially in 3D.

In contrast to the MAC method, the SMMC (Surface Marker and Micro Cell) method (Chen *et al.*, 1997), which only introduces markers on the interface rather than in the interior fluid, is more efficient in the computational effort and it is also more straightforward to apply free surface boundary conditions on the markers.

Density function method

The density function method, is a front-capturing method used to resolve complex free surface profiles. The density function usually has different values in each phase and the interface between phases is represented by the contour of the average value of the density function. In order to obtain a sharp interface, high order difference schemes, such as the CIP (Constrained Interpolation Profile) method (Yabe *et al.*, 2001), are often employed to avoid numerical diffusion in the advection equation. The density function method is efficient to deal with multiphase flows, but its drawback is that the interface may be smeared when using low order schemes.

Level set method

The level set method was derived by Osher & Sethian (1988). A continuous scalar function, which is a distance function from the interface, is introduced over the whole computational domain. The level set function is propagated with time by

solving a scalar convection equation. Thus, the interface is defined to be where the function has a value of zero. The advantage of this approach is that the level set function varies smoothly across the interface, nevertheless, special attention has to be given to ensure mass conservation. Sussman *et al.* (1994) presented a level set approach for simulating two-phase flows and later improvements include the coupled level set and volume of fluid (CLSVOF) method (Sussman & Puckett, 2000) and the hybrid particle level set method (Enright *et al.*, 2002). Reviews of the level set method can be found in Osher & Fedkiw (2001) and Sethian & Smereka (2003).

The level set method has been employed to investigate steady breakers generated by the flow over a submerged hydrofoil (Iafrati & Campana, 2005), deep-water breaking waves (Hendrickson, 2005; Iafrati, 2009), breaking solitary waves (Lin, 2007), breaking waves in the surf zone (Wang *et al.*, 2009*b*), plunging breaking waves over a submerged bump (Wang *et al.*, 2009*a*) and ship hydrodynamics (Yang & Stern, 2009).

Volume of Fluid (VOF) method

Numerous methods have been proposed and used for the simulation of interfacial flows. However, the Volume of Fluid (VOF) method for tracking the interface is the most popular one due to its advantages: mass conservation, computational efficiency and easy implementation. Rider & Kothe (1998) and Scardovelli & Zaleski (1999) have given an excellent review on the VOF methods. At the beginning of VOF methods, fluid volumes are initialized for the computational domain from a specified initial interface geometry. The volume for each cell is expressed by the volume fraction F, where cells across the interface will have a volume fraction F between zero and one, and cells without interfaces will have a value equal to zero or unity. During the computation, interfaces are tracked in VOF methods through the evolution of the volume fraction F. From a general point of view, there are two classes of algorithms to solve the F transport equation: algebraic and geometric computation (Rider & Kothe, 1998).

Geometric computation Most geometric VOF methods are based on a two-stage process. Firstly, interfaces are reconstructed from the volume fraction data

so that a geometric profile is found which approximates the actual interface location. Changes in volume fraction values are then calculated by integrating volume fluxes across cell boundaries, using the geometric profile of the reconstructed interface. Typical implementation of these algorithms are one-dimensional, with multidimensionality obtained via operator splitting (Rider & Kothe, 1998).

With respect to the interface reconstruction, the various VOF methods can be classified into two categories which are described below:

i. Simple Line (Piecewise Constant) Interface Calculation (SLIC)
In piecewise constant methods, the interface within each cell is assumed to be a line (in 2D) or plane (in 3D) that is aligned parallel with one of the grid axes. It is very easy and straightforward to implement, but has low accuracy. Implementations of this method include the SLIC method of Noh & Woodward (1996) and the VOF method of Hirt & Nichols (1981).

ii. Piecewise Linear Interface Calculation (PLIC)
In PLIC method, the interface within a cell, which represented as a slope line in 2D (a plane in 3D), can be presented at any angle with respect to the mesh axes. The slope of the line is given by an interface normal (the gradient of the volume fraction), and the intercept by conservation of volume within a cell (Rider & Kothe, 1998). PLIC methods are more accurate than piecewise constant methods because they represent a more realistic topology of the interface. Most PLIC methods reconstructed the interface within each cell whereas Ashgriz & Poo (1991) reconstructed it across cell faces. Implementations of this method include Youngs (1982), Rider & Kothe (1998) , Gueyffier *et al.* (1999) and Pilliod & Puckett (2004).

Algebraic computation In the algebraic computation, the interface is captured by solving the F transport equation using a high-order difference scheme without interface reconstruction. If the numerical scheme is too diffusive, the value of F between 0 and 1 will spread over several cells and thus a sharp interface cannot be captured. Moreover, mass conservation cannot be guaranteed in the computation.

Rudman (1997) proposed a FCT-VOF algorithm based on the concept of flux-corrected transport (FCT). Firstly, the intermediate value of F is calculated based on a low-order flux on cell boundaries, and then an anti-diffusive flux is given by the difference between the high and low order flux approximation, finally, the intermediate value and the correct anti-diffusive flux are used to advance the F value at the new time. The comparison with other geometric VOF methods for various test problems is shown in that paper. In order to avoid oscillations for high-order schemes, Vincent & Caltagirone (1999) employed the TVD SUPERBEE scheme for the volume fraction equation. Ubbink (1997) developed a compressive difference scheme, named CICSAM (Compressive Interface Capturing Scheme for Arbitrary Meshes), for the volume fraction equation to capture sharp fluid interface, which is available in the commercial codes STAR-CD and FLUENT.

Overall, both geometric and algebraic VOF methods have been used in a wide range of studies for breaking waves, such as the deep-water breaking waves (Chen *et al.*, 1999; Lubin *et al.*, 2006; Song & Sirviente, 2004), periodic breaking waves in the surf zone (Bradford, 2000; Christensen, 2006; Hieu *et al.*, 2004; Lemos, 1992; Lin & Liu, 1998*a*,*b*; Liovic & Lakehal, 2007; Mayer & Madsen, 2000; Zhao *et al.*, 2004), breaking solitary waves (Biausser *et al.*, 2004; Guignard *et al.*, 2001; Lin *et al.*, 1999; Xie *et al.*, 2009), wave overtopping (Stansby *et al.*, 2007), wave run-up from three-dimensional sliding masses (Liu *et al.*, 2005), wave-structure interactions (Chang *et al.*, 2001, 2005; Hsu *et al.*, 2002; Wu, 2004) and ship hydrodynamics (Andrillon & Alessandrini, 2004).

2.9.3 VOF Scheme for Interface Capturing

Algebraic computation has a great advantage over geometric computation since the interface is not required to be reconstructed during the calculation. Some successful implementations have been done for two-dimensional interface reconstruction, however, it is not so easy to reconstruct the interface in three dimensions (Gueyffier *et al.*, 1999). In addition, the programming is much simpler in algebraic computation. Thus, considering the advantages of the VOF method and efficiency in algebraic computation, the high resolution VOF scheme CICSAM

is employed in this study to capture the air-water interface for breaking waves. CICSAM is a high resolution scheme based on the Normalized Variable Diagram (NVD) used by Leonard (1991). It contains two high resolution schemes and the weighting factor is based on the angle between the interface and the direction of motion. An outline of CICSAM is given below. Refer to Ubbink (1997) for the details.

The normalized variable $\tilde{F}$ is defined as

$$\tilde{F} = \frac{F - F_{\mathrm{U}}}{F_{\mathrm{A}} - F_{\mathrm{U}}}, \tag{2.63}$$

where the subscript A indicates the acceptor and U the upwind cell. The Hyper-C scheme (Leonard, 1991) (see figure 2.6(a)), which follows the upper bound of the Convection Boundedness Criteria (CBC) is used as it is highly compressive and can convert a smooth gradient into a sharp step.

$$\tilde{F}_{\mathrm{f_{CBC}}} = \begin{cases} \min\left\{1, \dfrac{\tilde{F}_{\mathrm{D}}}{c_{\mathrm{D}}}\right\}, & \text{when } 0 \leq \tilde{F}_{\mathrm{D}} \leq 1 \\ \tilde{F}_{\mathrm{D}}, & \text{when } \tilde{F}_{\mathrm{D}} < 0, \tilde{F}_{\mathrm{D}} > 1 \end{cases} \tag{2.64}$$

where subscript D indicates donor cell, $c_{\mathrm{D}} = \sum_{\mathrm{f}} \max\left\{\frac{-V_{\mathrm{f}}\Delta t}{\Omega_{\mathrm{D}}}, 0\right\}$ is the Courant number of the donor cell and V_{f} is the volumetric flux. However, the Hyper-C scheme is inadequate to preserve the shape of an interface which lies tangentially to the flow direction. Thus CICSAM switches to the ULTIMATE-QUICKEST (UQ) scheme (Leonard, 1991) (see figure 2.6(b))

$$\tilde{F}_{\mathrm{f_{UQ}}} = \begin{cases} \min\left\{\dfrac{8c_{\mathrm{D}}\tilde{F}_{\mathrm{D}} + (1 - c_{\mathrm{D}})(6\tilde{F}_{\mathrm{D}} + 3)}{8}, \tilde{F}_{\mathrm{f_{CBC}}}\right\}, & \text{when } 0 \leq \tilde{F}_{\mathrm{D}} \leq 1 \\ \tilde{F}_{\mathrm{D}}, & \text{when } \tilde{F}_{\mathrm{D}} < 0, \tilde{F}_{\mathrm{D}} > 1 \end{cases} \tag{2.65}$$

in this case.

Thus, depending on the angle between the interface and the flow, CICSAM combines these two schemes, then

$$\tilde{F}_{\mathrm{f}} = \gamma_{\mathrm{f}}\tilde{F}_{\mathrm{f_{CBC}}} + (1 - \gamma_{\mathrm{f}})\tilde{F}_{\mathrm{f_{UQ}}}, \tag{2.66}$$

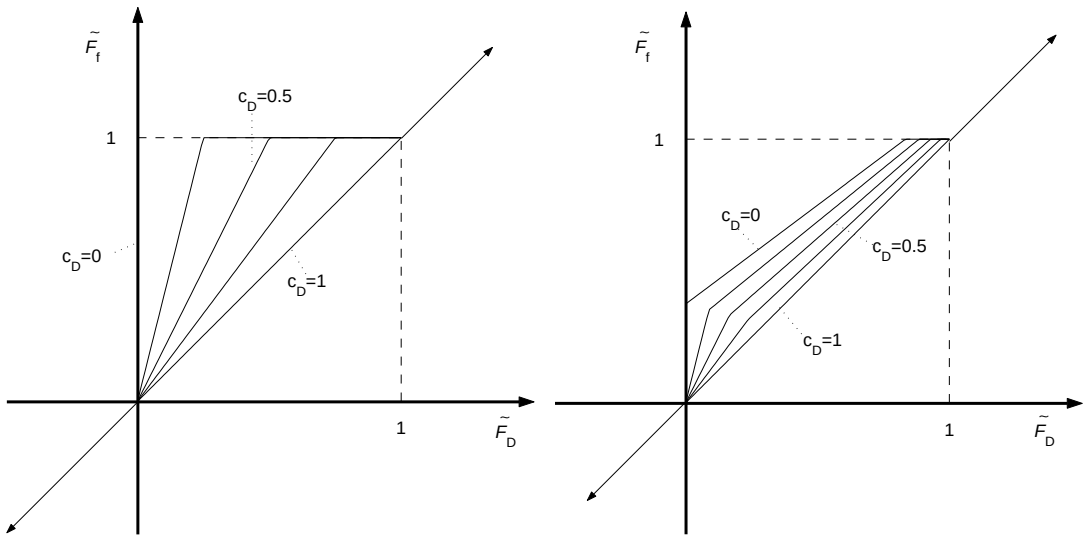

(a) CBC (b) ULTIMATE-QUICKEST

Figure 2.6: Normalized Variable Diagram of the binding schemes of CICSAM.

in which the weighting factor is given as

$$\gamma_{\mathrm{f}} = \min\left\{k_\gamma \frac{\cos(2\alpha_\gamma)+1}{2}, 1\right\}, \tag{2.67}$$

where k_γ is a constant introduced to control the dominance of the different schemes and the recommended value is $k_\gamma = 1$, α_γ is the angle between the vector normal to the interface and the vector which convects the centres of donor and acceptor cells.

The final expression for the face value of F is

$$F_{\mathrm{f}} = (1-\beta_{\mathrm{f}})F_{\mathrm{D}} + \beta_{\mathrm{f}} F_{\mathrm{A}}, \tag{2.68}$$

where the weight factor β_{f} is obtained by

$$\beta_{\mathrm{f}} = \frac{\tilde{F}_{\mathrm{f}} - \tilde{F}_{\mathrm{D}}}{1-\tilde{F}_{\mathrm{D}}}. \tag{2.69}$$

It is noted that the normalized variable in (2.63) will be divided by zero if

the volume fraction F has the same value in the acceptor and upwind cell. In the numerical implementation, the numerator and denominator of the weighting factor in (2.69) are multiplied by $(F_{\mathrm{A}} - F_{\mathrm{U}})$, resulting a modified expression of the normalized variable on the face (not shown here), to avoid the singularity in the computation.

2.10 Implementation of Boundary Conditions

2.10.1 Inlet Boundary Condition

Generally, water waves can be generated with a specified boundary condition at the inlet, with an internal wave maker via a source term (Lin & Liu, 1999) or with a moving wave maker at the inlet.

When the analytical solutions of the water particle kinematics are given, different types of water waves can be generated from the inlet boundary by specifying the value at the current time step as

$$[\boldsymbol{u}]_{\mathrm{inlet}}^{n+1} = B_1(\boldsymbol{u}_{\mathrm{wave}}^{n+1}), \tag{2.70}$$

$$[F]_{\mathrm{inlet}}^{n+1} = B_2(\eta_{\mathrm{wave}}^{n+1}). \tag{2.71}$$

The detail of the expressions for the sinusoidal wave, solitary wave, conoidal wave and Stokes wave can be found in Dean & Dalrymple (1984) as well as in the following chapters.

2.10.2 Open or Radiative Boundary Condition

The discretization of the Sommerfeld radiation condition is obtained by the explicit scheme as

$$\begin{aligned} \phi_{\mathrm{imax}}^{n+1} &= \phi_{\mathrm{imax}}^{n} + C_0 \Delta t \left(\frac{\partial \phi}{\partial x} \right)_{\mathrm{imax}}^{n} \\ &= \phi_{\mathrm{imax}}^{n} + C_0 \Delta t \frac{\phi_{\mathrm{imax}}^{n} - \phi_{\mathrm{imax}-1}^{n}}{\Delta x}, \end{aligned} \tag{2.72}$$

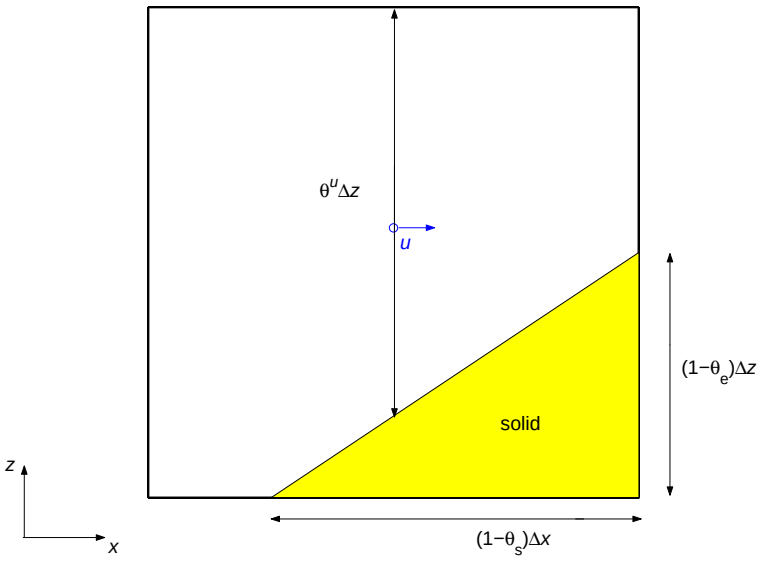

Figure 2.7: Boundary treatment in a cut cell for the u momentum equation in 2D Cartesian grid.

where the subscript imax denotes the value at the outlet in the x direction of wave propagation and C_0 is the characteristic velocity of water waves.

2.10.3 Wall Boundary Condition

Momentum equations

When the control volume is a cut cell, special attention has to be paid to the spatial discretization. When the face of a momentum control volume is on the wall, the diffusion flux is obtained as

$$\iint_S \Gamma \frac{\partial \phi}{\partial n} \mathrm{d}S = \sum_{\mathrm{f}} \Gamma_{\mathrm{f}} \frac{\partial \phi}{\partial n} (\theta A)_{\mathrm{f}} + \tau_{\mathrm{w}} [(1-\theta)A]_{\mathrm{f}}, \tag{2.73}$$

where $\frac{\partial \phi}{\partial n}$ is calculated by the finite difference approach in (2.39) and τ_{w} is the shear stress on the face of the control volume. For example, in the case of the control volume for u momentum equation in 2D (see figure 2.7), the shear stress on the south face is

$$\tau_{\mathrm{w}} = -\Gamma_{\mathrm{s}} \frac{u_{\mathrm{P}} - u_{\mathrm{solid}}}{0.5(\theta^u \Delta z)}, \tag{2.74}$$

where u_{solid} is the velocity on the solid boundary.

The mass flux has also to be modified by the θ function on the boundary. If $\theta = 0$, there is no mass flux through the face and the convective flux is obtained as

$$m_{\text{f}} = 0. \tag{2.75}$$

Boundary condition for the pressure correction equation

If the normal fluid velocity at the boundary is specified, there is no need to correct the velocity at the boundary, namely

$$\boldsymbol{u}'_{\text{f}} = 0, \tag{2.76}$$

and according to equation (2.54) which leads to

$$\frac{\partial p'}{\partial n} = 0, \tag{2.77}$$

and therefore on the boundary we can set the normal derivative of the pressure correction to be zero. Sometimes, having Neumann conditions on all boundaries makes the pressure correction equation singular. To obtain the unique solution, it is usual to take the pressure at one reference point to be fixed, so all corrected pressures are subtracted by the pressure correction calculated at the reference point (Ferziger & Peric, 2002).

2.11 Solution Techniques for Systems of Linear Algebraic Equations

In this study, the ADI (Alternating Direction Implicit) method with TDMA (Tridiagonal Matrix Algorithm) is used the solve the algebraic equations in the 2D model since it is very efficient and easy to implement at the early stage of the code development. However, it becomes inefficient with increasing number of nodes. Thus in the 3D model, the iterative procedures used to solve the algebraic equations are the 3D version SIP (Strongly Implicit Procedure) method or Bi-CGSTAB (Bi-Conjugate Gradients Stablized) Method proposed by van der

Vorst (1992). A comprehensive description of the solution techniques for linear algebraic equations is presented in Chapter 5 of Ferziger & Peric (2002) and will not be discussed here.

2.12 Concluding Remarks

In this chapter, the mathematical model and numerical implementation have been presented. The finite volume discretization for the governing equations and pressure-velocity coupling have been described in detail. After briefly reviewing the technique for interface calculations, we introduced the CICSAM scheme which we found to do a good job for interface capturing. The wave generation for numerical simulations as well as the radiative boundary condition for reducing the computational domain were also discussed. This code has the capability of studying various free surface flow problems. It is worth remarking that although only the Navier–Stokes equations are discussed in this chapter, the numerical methods are also applicable to other governing equations described in later chapters.

Chapter 3

RANS Modelling of Two-Dimensional Breaking Waves

Most flows in breaking waves are turbulent and therefore need different treatment for the turbulence. The most accurate and straightforward approach is direct numerical simulation (DNS), which solves the Navier–Stokes equations directly without any modification. All detailed features in the turbulent flow are captured in DNS, so the grid size must be no larger than the Kolmogorov scale (Ferziger & Peric, 2002). Due to the high demand of the number of grid points (which is proportional to $Re^{9/4}$ in 3D, where Re is the Reynolds number), it has been mostly used for low Reynolds number flows and it is only applicable to the high Reynolds flow calculation in a small domain for current computational powers.

In many engineering practices, just a few quantitative properties of the turbulent flow are of interest. Therefore the Reynolds-averaged Navier–Stokes (RANS) equations are usually solved, in which all of the unsteadiness is averaged out and considered as part of the turbulence, which is modelled by different approximations. Compared to DNS, the RANS model requires less computational effort and can be solved in a relatively coarse grid, so the RANS model is employed in this study to investigate two-dimensional breaking waves.

In this chapter, after briefly introducing the RANS model and the $k-\epsilon$ turbulence model, we discuss the initial and boundary conditions for the RANS model

and present the special numerical implementation for the $k-\epsilon$ turbulence model near the wall. After that, two cases of 2D overturning waves with experimental measurements are used to validate the model.

3.1 Reynolds-Averaged Navier–Stokes Equations

3.1.1 Reynolds Averaging

In the RANS model, every variable ϕ can be represented by the sum of the averaged value and the fluctuating part as (Ferziger & Peric, 2002)

$$\phi(x_i,t) = \langle\phi(x_i)\rangle + \phi'(x_i,t). \tag{3.1}$$

In a steady flow, the time averaging is used to obtain the mean value

$$\langle\phi(x_i)\rangle = \lim_{T\to\infty}\frac{1}{T}\int_0^T \phi(x_i,t)\mathrm{d}t, \tag{3.2}$$

while ensemble averaging is used in unsteady flow

$$\langle\phi(x_i,t)\rangle = \lim_{N_\phi\to\infty}\frac{1}{N_\phi}\sum_{n=1}^{N_\phi}\phi(x_i,t), \tag{3.3}$$

where N_ϕ is the total number of the ensemble values.

The RANS model has following fundamental properties:

(i). $$\langle\langle\phi\rangle\rangle = \langle\phi\rangle\,, \langle\phi'\rangle = 0; \tag{3.4}$$

(ii). $$\langle a\phi + b\psi\rangle = a\langle\phi\rangle + b\langle\psi\rangle\,, a \text{ and } b \text{ are constants}; \tag{3.5}$$

(iii). $$\langle\phi\psi\rangle = \langle(\langle\phi\rangle+\phi')(\langle\psi\rangle+\psi')\rangle = \langle\phi\rangle\langle\psi\rangle + \langle\phi'\psi'\rangle\,; \tag{3.6}$$

(iv). $$\left\langle\frac{\partial\phi}{\partial t}\right\rangle = \frac{\partial\langle\phi\rangle}{\partial t}, \left\langle\frac{\partial\phi}{\partial x_i}\right\rangle = \frac{\partial\langle\phi\rangle}{\partial x_i}. \tag{3.7}$$

Applying the averaging processes to the Navier–Stokes equations (2.8–2.9), we can obtain the RANS equations

$$\frac{\partial \langle u_i \rangle}{\partial x_i} = 0, \tag{3.8}$$

$$\frac{\partial(\rho \langle u_i \rangle)}{\partial t} + \frac{\partial(\rho \langle u_j \rangle \langle u_i \rangle)}{\partial x_j} = -\frac{\partial \langle p \rangle}{\partial x_i} + \frac{\partial}{\partial x_j}\left[\mu\left(\frac{\partial \langle u_i \rangle}{\partial x_j} + \frac{\partial \langle u_j \rangle}{\partial x_i}\right) - \rho \left\langle u_i' u_j' \right\rangle\right] + \rho \langle g_i \rangle, \tag{3.9}$$

where the velocity-velocity correlation terms $RS = -\rho \left\langle u_i' u_j' \right\rangle$ are called the *Reynolds stresses*.

The above RANS equations can also be rewritten in vector form as

$$\boldsymbol{\nabla} \cdot \langle \boldsymbol{u} \rangle = 0, \tag{3.10}$$

$$\frac{\partial(\rho \langle \boldsymbol{u} \rangle)}{\partial t} + \boldsymbol{\nabla} \cdot (\rho \langle \boldsymbol{u} \rangle \otimes \langle \boldsymbol{u} \rangle) = -\boldsymbol{\nabla} \langle p \rangle + \boldsymbol{\nabla} \cdot [\mu(\boldsymbol{\nabla} \langle \boldsymbol{u} \rangle + \boldsymbol{\nabla}^{\mathrm{T}} \langle \boldsymbol{u} \rangle) + RS] + \rho \langle \boldsymbol{g} \rangle. \tag{3.11}$$

3.1.2 Turbulence Models

In RANS modelling, attention is focused on the mean flow and the effects of turbulence on mean flow properties. Extra terms ($-\rho \left\langle u_i' u_j' \right\rangle$) appear in the Reynolds-averaged flow equations due to the interactions between various turbulent fluctuations. The governing equations are not closed, namely, the unknown variables are more than the number of equations, thus, we have to use closure or turbulence models to close the governing equations.

Eddy viscosity model

The eddy viscosity model relates the Reynolds stresses to the mean velocity gradients as

$$-\rho \left\langle u_i' u_j' \right\rangle = \mu_t \left(\frac{\partial \langle u_i \rangle}{\partial x_j} + \frac{\partial \langle u_j \rangle}{\partial x_i}\right) - \frac{2}{3}\rho \delta_{ij} k, \tag{3.12}$$

where δ_{ij} is the Kronecker delta

$$\delta_{ij} = \begin{cases} 1, & \text{if } i = j; \\ 0, & \text{if } i \neq j, \end{cases} \tag{3.13}$$

k is the turbulent kinetic energy defined as

$$k = \frac{1}{2}\langle u_i' u_i' \rangle = \frac{1}{2}(\langle u'u' \rangle + \langle v'v' \rangle + \langle w'w' \rangle), \tag{3.14}$$

and μ_t is the turbulent eddy viscosity, namely,

$$\mu_t = C_\mu \rho L_t V_t, \tag{3.15}$$

where L_t is the turbulent length scale and V_t is the turbulent velocity scale. C_μ is a dimensionless constant whose value will be given later. The eddy viscosity model contains a number of different turbulence models with varying degree of complexity, see Versteeg & Malalasekera (2007) for a discussion.

3.1.3 The $k - \epsilon$ Model

The $k-\epsilon$ model is the most widely used model among two-equation eddy viscosity models. It has been tested over a large variety of flow situations and therefore its limitations, as well as its successes, have become well understood. The standard high-Reynolds-number $k-\epsilon$ turbulence model (Launder & Spalding, 1974) is used in this study where

$$\frac{\partial(\rho k)}{\partial t} + \boldsymbol{\nabla} \cdot (\rho \boldsymbol{u} k) = \boldsymbol{\nabla} \cdot [(\mu + \frac{\mu_t}{\sigma_k})\boldsymbol{\nabla} k] + P_k - \rho\epsilon, \tag{3.16}$$

$$\frac{\partial(\rho \epsilon)}{\partial t} + \boldsymbol{\nabla} \cdot (\rho \boldsymbol{u} \epsilon) = \boldsymbol{\nabla} \cdot [(\mu + \frac{\mu_t}{\sigma_\epsilon})\boldsymbol{\nabla} \epsilon] + C_{1\epsilon}\frac{\epsilon}{k}P_k - C_{2\epsilon}\rho\frac{\epsilon^2}{k}, \tag{3.17}$$

in which P_k is the turbulent production term, and the turbulent length scale and turbulent velocity scale for the $k - \epsilon$ model are

$$V_t = k^{\frac{1}{2}}, \tag{3.18}$$

$$L_t = \frac{k^{\frac{3}{2}}}{\epsilon}. \tag{3.19}$$

Thus, the turbulent eddy viscosity μ_t can be obtained from equation (3.15) as

$$\mu_t = \rho C_\mu \frac{k^2}{\epsilon}, \tag{3.20}$$

where the empirical coefficients C_μ, σ_k, σ_ϵ, $C_{1\epsilon}$ and $C_{2\epsilon}$ are given in table 3.1.

Table 3.1: Empirical coefficients in the $k-\epsilon$ turbulence model (Launder & Spalding, 1974)

C_μ	σ_k	σ_ϵ	$C_{1\epsilon}$	$C_{2\epsilon}$
0.09	1.0	1.3	1.44	1.92

3.2 Initial and Boundary Conditions

Initial and boundary conditions for the continuity and momentum equations are the same as in § 2.2, so only the conditions for the $k-\epsilon$ model are presented here.

3.2.1 Boundary Conditions for the $k-\epsilon$ Model

Inlet boundary condition

Similar to the method of Lin (1998), at the inlet, the turbulent kinetic energy is obtained as $k = \frac{1}{2}(I \times C)^2$, where C is the wave phase speed and I is the turbulent intensity. The turbulent eddy dissipation $\epsilon = \rho C_\mu k^2/(I_\epsilon \times \mu)$ is adjusted so the turbulent eddy viscosity is I_ϵ times the dynamic viscosity of each fluid at the inlet. Unless stated otherwise $I = 0.005$ and $I_\epsilon = 10$ are used in this study.

Open boundary condition

On the open boundary, the zero gradient boundary condition is usually applied for the turbulence and dissipation, so

$$\left[\frac{\partial k}{\partial n}\right]_{\text{open}} = 0, \quad \left[\frac{\partial \epsilon}{\partial n}\right]_{\text{open}} = 0. \tag{3.21}$$

Wall functions for the $k-\epsilon$ model

In high Reynolds number flows, the viscous sublayer is so thin that it will need very fine mesh in the near wall region to resolve it. To alleviate this, wall functions are used in the present study, which are based on the empirical near-wall velocity profile of a turbulent boundary layer

$$u^+ = \frac{u_t}{u_\tau} = \begin{cases} n^+, & n^+ \leq 11.225; \\ \dfrac{1}{\kappa}\ln\left(E^+ n^+\right), & n^+ > 11.225, \end{cases} \tag{3.22}$$

where $\kappa = 0.4187$ is von Kármán's constant, $E^+ = 9.7393$ is the coefficient for a smooth wall, n^+ is the dimensionless distance from the wall (also known as 'near wall Reynolds number') as

$$n^+ = \frac{\rho u_\tau n}{\mu}, \tag{3.23}$$

where n is the distance to the wall and u_τ is the friction velocity defined as

$$u_\tau = \sqrt{\frac{\tau_{\text{w}}}{\rho}}. \tag{3.24}$$

Spalding (1961) found that the turbulent viscosity is a cubic function of n^+ or u^+ in the viscous and buffer layers but in the logarithmic layer the viscosity is an exponential function of u^+. By matching these two functions, and assuming that the shear stress is constant very near to the wall, he derived the following universal formula for the law of the wall

$$n^+ = u^+ + \frac{1}{E^+}\left[e^{\kappa u^+} - 1 - \kappa u^+ - \frac{(\kappa u^+)^2}{2!} - \frac{(\kappa u^+)^3}{3!}\right]. \tag{3.25}$$

Generally, the wall functions are usually applied at the first grid point above

the wall. The shear stress on the wall is calculated from the velocity u_t by employing the law of the wall.

From the definition of the shear velocity we have

$$u^+ = \frac{u_t}{u_\tau} \quad \Longrightarrow \quad u_\tau = \sqrt{\frac{\tau_\mathrm{w}}{\rho}} \quad \Longrightarrow \quad \tau_\mathrm{w} = \frac{\sqrt{\rho\tau_\mathrm{w}}u_t}{u^+}. \tag{3.26}$$

In the fully developed boundary layer (local equilibrium), we have

$$\tau_\mathrm{w}^2 = C_\mu \rho^2 k^2 \quad \Longrightarrow \quad \sqrt{\rho\tau_\mathrm{w}} = \rho C_\mu^{\frac{1}{4}} k^{\frac{1}{2}}. \tag{3.27}$$

Thus, substitute equations (3.27) and (3.22) into (3.26), we can obtain the shear stress at the first grid point as

$$\tau_\mathrm{w} = \begin{cases} \mu\dfrac{u_t}{n}, & n^+ \leq 11.225; \\ \dfrac{\rho C_\mu^{\frac{1}{4}} k^{\frac{1}{2}} u_t}{\dfrac{1}{\kappa}\ln\left(E^+ n^+\right)}, & n^+ > 11.225. \end{cases} \tag{3.28}$$

The turbulent eddy dissipation is obtained as

$$\epsilon = C_\mu^{\frac{3}{4}} \frac{k^{\frac{3}{2}}}{\kappa n}. \tag{3.29}$$

The turbulent production in the wall region is calculated as

$$P_k = \tau_\mathrm{w} \frac{\partial u_t}{\partial n}, \tag{3.30}$$

and the velocity gradient can be obtained from

$$\tau_\mathrm{w} = \mu_t \frac{\partial u_t}{\partial n} \quad \Longrightarrow \quad \frac{\partial u_t}{\partial n} = \frac{\tau_\mathrm{w}}{\mu_t}, \tag{3.31}$$

thus, the production term is rewritten as

$$P_k = \frac{\tau_\mathrm{w}^2}{\mu_t}. \tag{3.32}$$

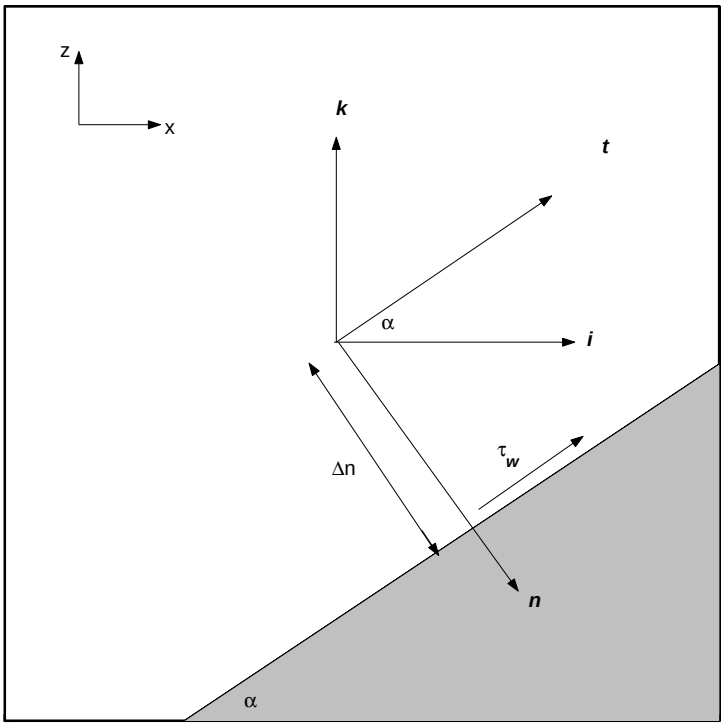

Figure 3.1: Wall function treatment for a sloping wall and air-water interface with angle α to the horizontal.

Wall functions for a sloping wall and air-water interface

In the present study, the wall functions are extended for a sloping wall and air-water interface. Figure 3.1 shows a typical control volume containing a wall or air-water interface at an angle of α to the horizontal and the distance from the grid point to the interface is Δn. It can be seen from figure 3.1 that the normal unit vector $\boldsymbol{n}$ and tangential unit vector $\boldsymbol{t}$ can be expressed in terms of the unit vectors in the x and z directions, $\boldsymbol{i}$ and $\boldsymbol{k}$ as

$$\boldsymbol{n} = \boldsymbol{i} \sin\alpha - \boldsymbol{k} \cos\alpha, \tag{3.33}$$

$$\boldsymbol{t} = \boldsymbol{i} \cos\alpha + \boldsymbol{k} \sin\alpha. \tag{3.34}$$

The tangential velocity relative to the wall or air-water interface can be ob-

tained as

$$\begin{aligned}\boldsymbol{u_t} &= [(\boldsymbol{u}-\boldsymbol{u}_{\mathrm{w}})\cdot\boldsymbol{t}]\,\boldsymbol{t}\\ &= [(u-u_{\mathrm{w}})\cos\alpha+(w-w_{\mathrm{w}})\sin\alpha]\,\boldsymbol{t}\\ &= [(u-u_{\mathrm{w}})\cos\alpha+(w-w_{\mathrm{w}})\sin\alpha]\cos\alpha\boldsymbol{i}+\\ &\quad [(u-u_{\mathrm{w}})\cos\alpha+(w-w_{\mathrm{w}})\sin\alpha]\sin\alpha\boldsymbol{k},\end{aligned} \tag{3.35}$$

where $\boldsymbol{u}_{\mathrm{w}}$ is the velocity vector for the solid wall or the first point just below the air-water interface.

Substituting the tangential velocity (3.35) into the shear stress (3.28), the shear stress along the x and z directions can be obtained as

$$\tau_{\mathrm{w}}^{x}=\begin{cases}\mu\dfrac{[(u-u_{\mathrm{w}})\cos\alpha+(w-w_{\mathrm{w}})\sin\alpha]\cos\alpha}{\Delta n}, & \Delta n^{+}\leq 11.225;\\ \dfrac{\rho C_{\mu}^{\frac{1}{4}}k^{\frac{1}{2}}\,[(u-u_{\mathrm{w}})\cos\alpha+(w-w_{\mathrm{w}})\sin\alpha]\cos\alpha}{\dfrac{1}{\kappa}\ln\left(E^{+}\Delta n^{+}\right)}, & \Delta n^{+}>11.225.\end{cases} \tag{3.36}$$

$$\tau_{\mathrm{w}}^{z}=\begin{cases}\mu\dfrac{[(u-u_{\mathrm{w}})\cos\alpha+(w-w_{\mathrm{w}})\sin\alpha]\sin\alpha}{\Delta n}, & \Delta n^{+}\leq 11.225;\\ \dfrac{\rho C_{\mu}^{\frac{1}{4}}k^{\frac{1}{2}}\,[(u-u_{\mathrm{w}})\cos\alpha+(w-w_{\mathrm{w}})\sin\alpha]\sin\alpha}{\dfrac{1}{\kappa}\ln\left(E^{+}\Delta n^{+}\right)}, & \Delta n^{+}>11.225.\end{cases} \tag{3.37}$$

The wall function used for the air-water interface during the calculation here is similar to the wall function for the solid wall. The wall function for the water surface is applied at the first point in the air above the water surface. It is worth remarking that the boundary layer in water generated by wind (Tsanis, 1989; Wu & Tsanis, 1995) or without wind (Cotton *et al.*, 2005) is ignored in this study and we assume there is no surface boundary layer in water. After obtain the shear stress in the air $\boldsymbol{\tau}_{\mathrm{w}}^{\mathrm{a}}$, the condition $\boldsymbol{\tau}_{\mathrm{w}}^{\mathrm{w}}=\boldsymbol{\tau}_{\mathrm{w}}^{\mathrm{a}}$ is applied at the interface for water. This calculated shear stress across the interface is used for discretization of the momentum equation and turbulence model during the computation. The wall function for the air-water interface is neglected for the cut cells on the slope where run-up depth is very small.

3.2.2 Initial Conditions for the $k-\epsilon$ Model

When the RANS model is employed, the turbulence fields for k and ϵ are initialized to the same value as the boundary conditions at the inlet.

3.3 Special Numerical Implementation

3.3.1 Numerical Discretization

Table 3.2 shows the various values of ϕ, Γ and Q_ϕ^{S} in the general integral formulation (see § 2.3.2) to represent the Reynolds-averaged Navier–Stokes equations. The same numerical discretization used in Chapter 2 is employed here for the RANS model.

Table 3.2: Values of ϕ, Γ and Q_ϕ^{S} in the general integral formulation to represent the Reynolds-averaged Navier–Stokes equations.

Equation	ϕ	Γ	Q_ϕ^{S}
Continuity	1	0	0
Momentum	$\langle \boldsymbol{u} \rangle$	$\mu + \mu_t$	$-\boldsymbol{\nabla} \langle p \rangle + \rho \langle \boldsymbol{g} \rangle$
k	k	$\mu + \frac{\mu_t}{\sigma_k}$	$P_k - \rho\epsilon$
ϵ	ϵ	$\mu + \frac{\mu_t}{\sigma_\epsilon}$	$C_{1\epsilon}\frac{\epsilon}{k}P_k - C_{2\epsilon}\rho\frac{\epsilon^2}{k}$

3.3.2 Source Term Linearization for the $k-\epsilon$ Model

Using the source term linearization described in § 2.5.3, the finite volume discretization of the source term in k equation is obtained as

$$\begin{aligned} Q_k^{\mathrm{S}} &= P_k - \rho\epsilon \\ &= P_k - C_\mu \frac{\rho^2 k}{\mu_t} k \\ &= Q_k^{\mathrm{S0}} + Q_k^{\mathrm{S1}} k, \end{aligned} \tag{3.38}$$

where

$$Q_k^{\mathrm{S0}} = P_k, \quad Q_k^{\mathrm{S1}} = -C_\mu \frac{\rho^2 k}{\mu_t}. \tag{3.39}$$

Similarly, the finite volume discretization of the source term in ϵ equation is obtained as

$$\begin{aligned} Q_\epsilon^{\mathrm{S}} &= C_{1\epsilon}\frac{\epsilon}{k}P_k - C_{2\epsilon}\rho\frac{\epsilon^2}{k} \\ &= C_{1\epsilon}\frac{\epsilon}{k}P_k - C_{2\epsilon}\rho\frac{\epsilon}{k}\epsilon \\ &= Q_\epsilon^{\mathrm{S0}} + Q_\epsilon^{\mathrm{S1}}\epsilon, \end{aligned} \tag{3.40}$$

where

$$Q_\epsilon^{\mathrm{S0}} = C_{1\epsilon}\frac{\epsilon}{k}P_k, \quad Q_\epsilon^{\mathrm{S1}} = -C_{2\epsilon}\rho\frac{\epsilon}{k}. \tag{3.41}$$

3.3.3 Wall Boundary Condition

Momentum equations

When the face of a momentum control volume is on the wall, the diffusion flux on the wall is obtained as

$$\iint_S \Gamma\frac{\partial\phi}{\partial n}\mathrm{d}S = \Gamma_{\mathrm{f}}\frac{\partial\phi}{\partial n}(\theta A)_{\mathrm{f}} + \tau_{\mathrm{w}}[(1-\theta)A]_{\mathrm{f}}. \tag{3.42}$$

The $k-\epsilon$ model

In the first grid point near the wall, the turbulent eddy dissipation is obtained as

$$\epsilon = C_\mu^{\frac{3}{4}}\frac{k^{\frac{3}{2}}}{\kappa n}, \tag{3.43}$$

and the turbulent production term is obtained from

$$P_k = \frac{\tau_{\mathrm{w}}^2}{\mu_t}. \tag{3.44}$$

3.4 2D Overturning Waves on a Sloping Beach

3.4.1 Introduction

Prior to attempting numerical simulation of breaking waves, several validation checks of the proposed code for dam break and regular wave tests were performed. In order to test the code for overturning waves, we simulate a two-dimensional overturning solitary wave and compare with the experiment by Li (2000) for a breaking solitary wave splash-up on a 1:15 sloping beach. The processes for wave breaking and splash-up in the experiment are shown in figure 3.2. The wave surface profiles in space were captured using a high-speed video camera in the experiment, thus this is considered as a benchmark problem to simulate breaking waves over a slope.

In the past, Grilli *et al.* (1997) investigated the breaking criterion and characteristics for solitary waves on slopes. Several cases for different slopes and wave steepnesses were studied and detailed information for breaking waves was presented up to the point at which the plunging jet of breaking waves impinged on the free surface. Li & Raichlen (1998) compared the experimental data against the potential flow model of Grilli *et al.* (1997) and found that there is a phase shift of the wave shape due to the energy dissipation which is not taken into account in the potential flow model. In order to simulate post-breaking waves with the BEM (Boundary Element Method) and save computational efforts in the VOF model, the coupling between the BEM and VOF methods is developed by using the 'weak coupling method', in which the VOF model is initialized from the BEM results (Guignard *et al.*, 1999), or the 'strong coupling method', in which the BEM and VOF models are fully coupled and constantly exchanging information with each other (Lachaume *et al.*, 2003). Recently, meshless particle methods have been advanced to simulate breaking waves and wave impacts on structures. Khayyer *et al.* (2008) developed the CISPH (Corrected Incompressible SPH) method to investigate breaking solitary waves, and both qualitative and quantitative comparisons were made with experimental data. More recently, Ma & Zhou (2009) developed the MLPG_R (Meshless Local Petrov-Galerkin method based on Rankine source solution) method for 2D breaking waves and quite good

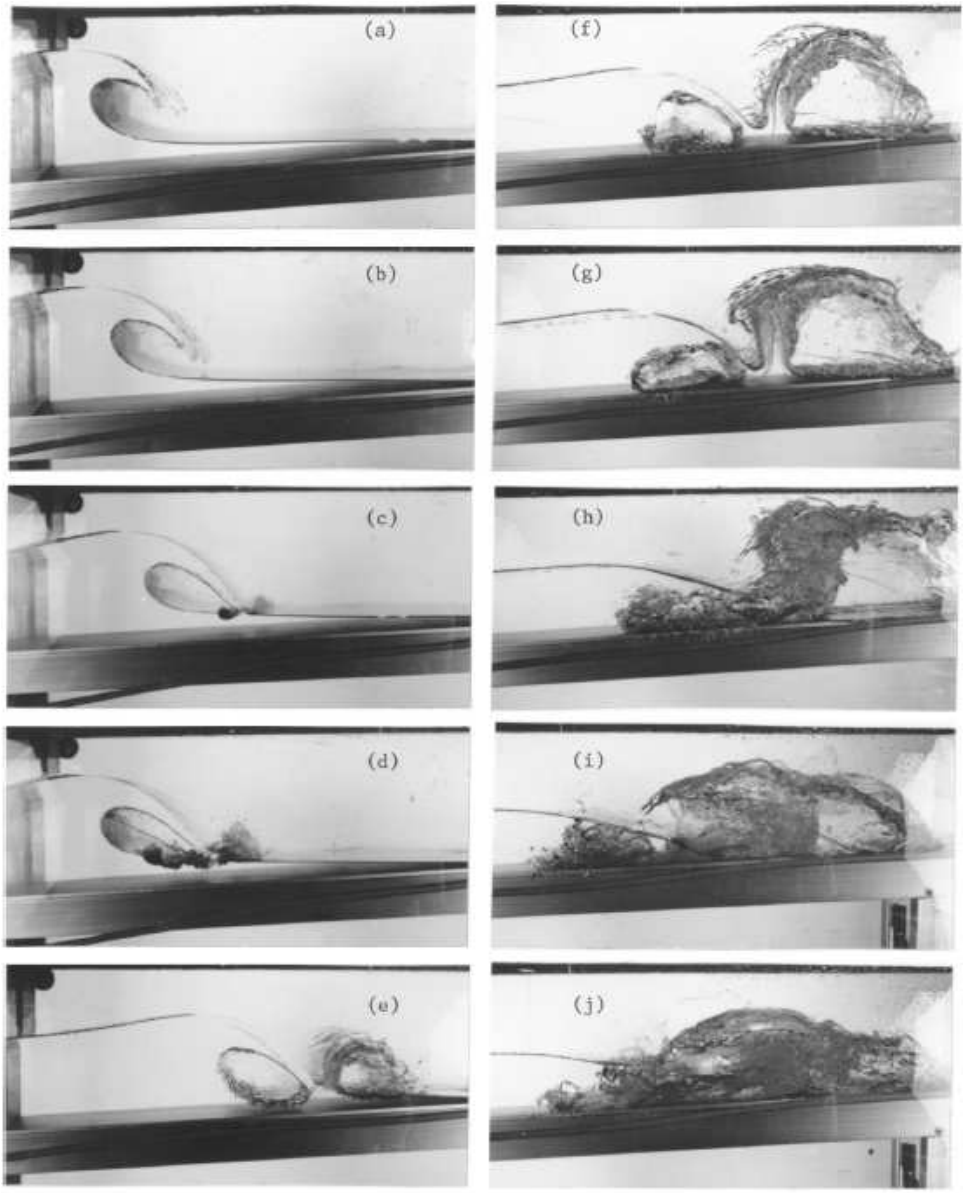

Figure 3.2: Solitary wave splash-up on a 1:15 slope for an incident wave $H/D = 0.40$ from Li & Raichlen (2003).

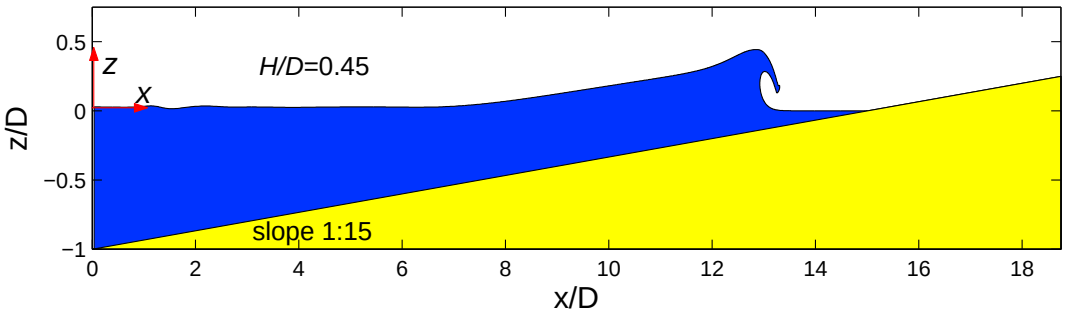

Figure 3.3: Schematic of an incident $H/D = 0.45$ solitary wave breaking on a 1:15 sloping beach (not scaled).

agreement with experimental data for the wave surface profiles during wave overturning was obtained. It is worth noting that only the numerical results in Grilli *et al.* (1997) and Ma & Zhou (2009) have compared the wave surface profiles in space with experimental data.

3.4.2 Computational Setup

Computational parameters

In the simulation, the computational setup is the same as the laboratory setup except that we use the analytical solution to generate the solitary wave at the inlet. The schematic of the run-up of a breaking solitary wave is shown in figure 3.3, where the origin of the coordinate system is on the still water level above the toe of the beach, x and z are the horizontal and vertical coordinates respectively, D is the still water depth, H is the solitary wave height. The slope of the beach $\tan(\beta) = 1 : 15$, the still water depth is $D = 0.3048$ m and we calculate the case for the incident solitary wave with the ratio of wave height to still water depth, $H/D = 0.45$. The computational domain starts from the toe of the beach and extends to the location beyond the maximum run-up point $18.75D$. The height of the computational domain is $1.75D$ and it is discretized by a 1800×140 nonuniform grid with minimum meshes $\Delta x/D = 0.005$ and $\Delta z/D = 0.005$ in the breaking region. The CPU time is approximately 72h on a PC (Intel® Pentium® D CPU 3.40GHz, 2GB RAM).

Boundary conditions

At the inlet, the solitary wave is generated by giving the water surface profile and the water particle velocities based on the analytical solution (Dean & Dalrymple, 1984) as

$$\begin{aligned}
\eta(x,t) &= H\mathrm{sech}^2\left[\sqrt{\frac{3H}{4D^3}}X\right], \\
X &= x - Ct - x_L, \\
u(x,z,t) &= C\left\{\left[\frac{H}{D}+3\left(\frac{H}{D}\right)^2\left(\frac{1}{6}-\frac{1}{2}\left(\frac{z+D}{D}\right)^2\right)\right]\frac{\eta}{H}-\left(\frac{H}{D}\right)^2\left(\frac{7}{4}-\frac{9}{4}\left(\frac{z+D}{D}\right)^2\right)\left(\frac{\eta}{H}\right)^2\right\}, \\
w(x,z,t) &= C\sqrt{\frac{3H}{D}}\frac{z+D}{D}\frac{\eta}{D}\tanh\left(\sqrt{\frac{3H}{4D^3}}X\right)\left\{1+\frac{H}{2D}\left[1-7\frac{\eta}{H}-\left(\frac{z+D}{D}\right)^2\left(1-\frac{3\eta}{H}\right)\right]\right\}.
\end{aligned} \tag{3.45}$$

The no-slip wall boundary condition is applied at the sloping beach and open boundary conditions are applied at the top and outlet of the computational domain.

Similar to the method in Lin & Liu (1998*a*), the turbulent kinetic energy is obtained as $k = \frac{1}{2}(I \times C)^2$, where C is the wave phase speed and $I = 0.005$ is the turbulent intensity. The turbulent eddy dissipation is adjusted so the turbulent eddy viscosity is ten times the dynamic viscosity of each fluid at the inlet.

Initial conditions

At $t = 0$, the water velocities and water surface are given by the results of the analytical solution of a solitary wave (3.45), the velocity in the air is initialized as zero, the pressure distribution in the whole domain is hydrostatic and the turbulence fields for k and ϵ are initialized to the same value as the boundary conditions at the inlet.

3.4.3 Results and Discussion

Comparison of wave surface profiles

In figure 3.4, the profiles of the overturning wave are compared with the experimental data (Li, 2000) at $t\sqrt{g/D} = 9.29, 9.87, 10.35, 10.73$ along with the recently published results of Ma & Zhou (2009) using the MLPG_R method. At $t\sqrt{g/D} = 9.29$ before wave breaking, it can be seen that the wave crest becomes steep due to the shoaling effect. At $t\sqrt{g/D} = 9.87$ during wave breaking, the wave has passed the breaking point, which is defined as when the front of the wave becomes vertical, and starts to overturn. At $t\sqrt{g/D} = 10.35$ during wave overturning, a plunging jet is formed in front of the wave. At $t\sqrt{g/D} = 10.73$ during wave curling down, the plunging jet will impinge the water surface ahead and generate the splash-up. Numerical results are only presented up to this stage because the water surface profiles are not available after the wave touches down. It can be seen from figure 3.4 that the computational results agree well with experimental measurements and MLPG_R results in terms of the wave shape and location before wave curling down, and there is only a slight difference in the size of the cavity enclosed by the plunging jet. The slight discrepancy may be caused by the solitary wave at the inlet generated from the analytical solution differing slightly from the experiment (as indicated by Lee *et al.*, 1982).

A detailed comparison of the plunging jet, at the time of jet impingement, with the experimental and the BEM results are shown in figure 3.5. Both numerical results (VOF and BEM) agree reasonably with experimental data. The slight difference is that the jet obtained from the VOF model has a similar size to that obtained from the BEM model and both are thicker than their experimental counterpart as discussed by Li & Raichlen (1998). Nevertheless, since the numerical model cannot get the exact initial condition used in the experiment, any small difference will lead to the change of the plunging jet, thus we do not expect to match everything between the experiment and computation. In an overall sense, the present code well predicts the overturning wave and a good agreement with experimental data is obtained.

The overturning jet of breaking waves has been investigated mathematically by Longuet-Higgins (1982), New (1983) and Greenhow (1983). New has found

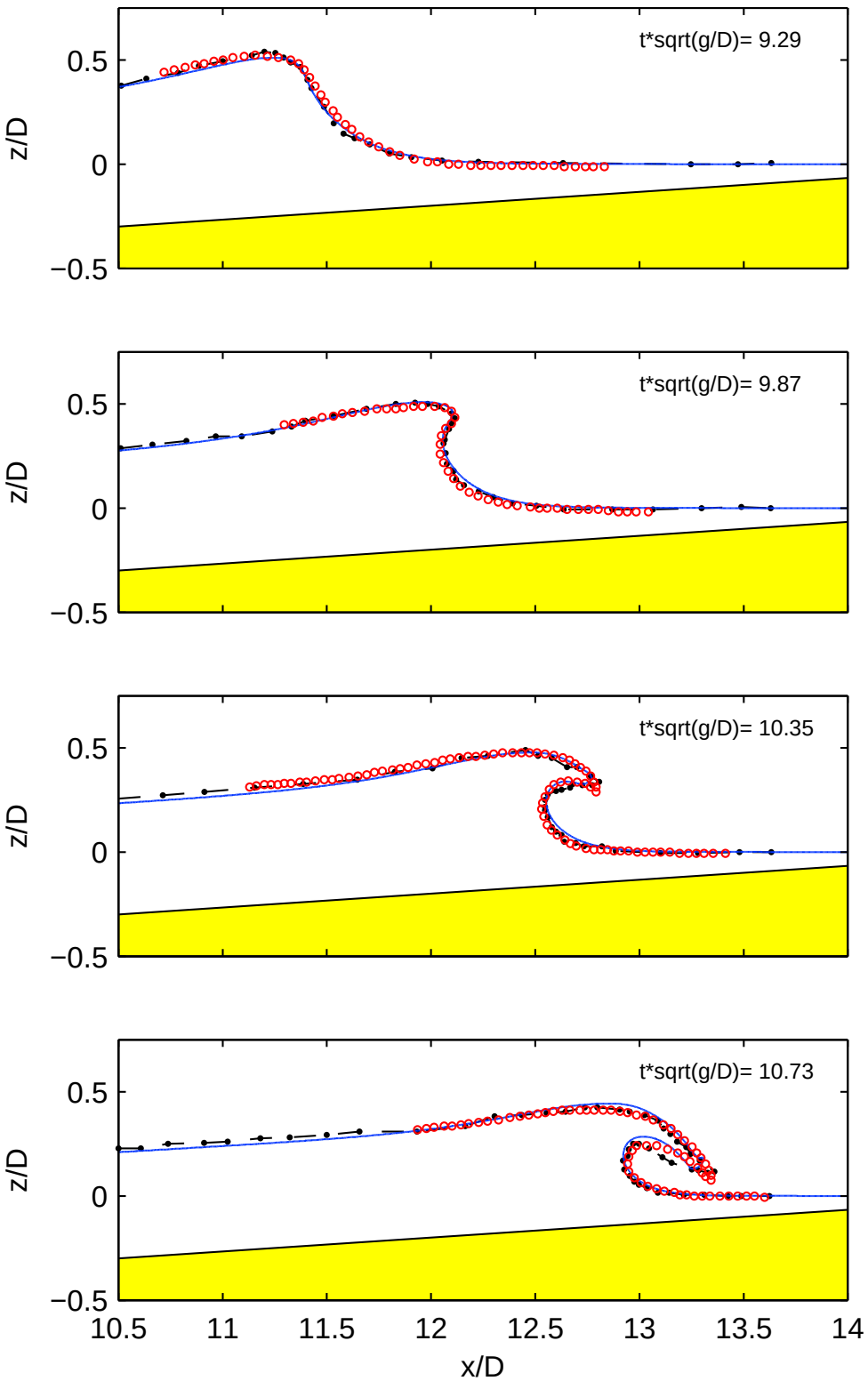

Figure 3.4: Comparison of wave surface profiles during wave overturning on a sloping beach. Blue solid line: present results; red circles: experimental data (Li, 2000); black dashed line: results obtained by the MLPG_R method (Ma & Zhou, 2009).

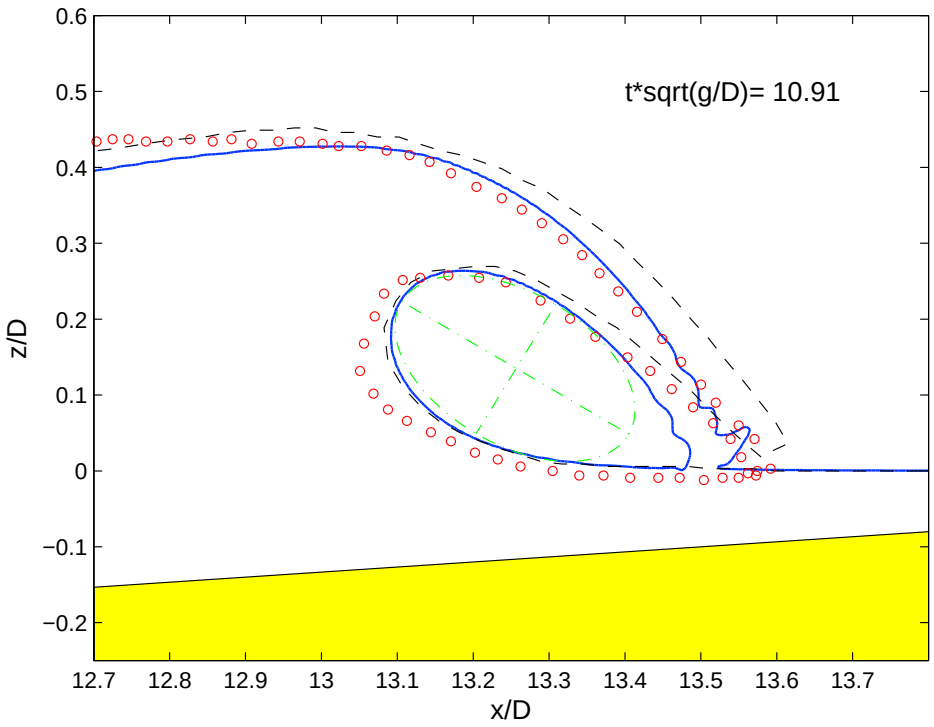

Figure 3.5: Detailed comparison of the plunging jet. Blue solid line: present results; red circles: experimental data (Li, 2000); black dashed line: profile at $t\sqrt{g/D} = 10.73$ obtained by the BEM (Grilli *et al.*, 1997); green dash-dotted line is a $\sqrt{3}$ aspect-ratio ellipse.

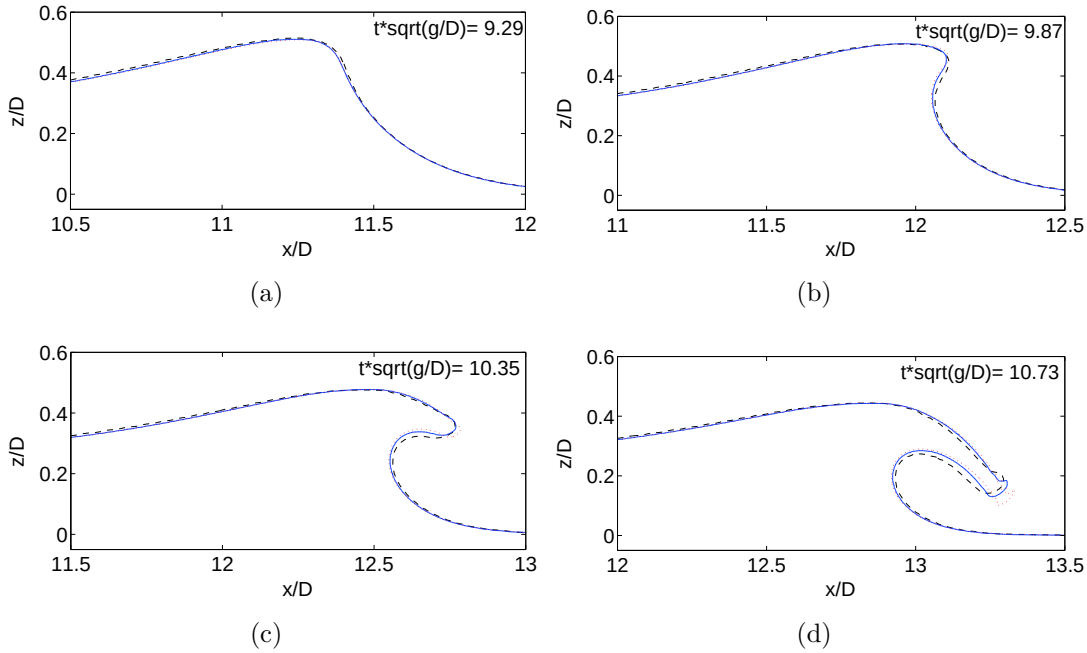

Figure 3.6: Comparison of the profiles of the overturning wave obtained by different meshes. Coarse mesh (900×90): black dashed line; medium mesh (1800×140): blue solid line; fine mesh (2600 × 240): red dotted line.

that a certain section of the wave profile beneath overturning waves, in both deep and shallow water, can be closely approximated by a $\sqrt{3}$ aspect-ratio ellipse. The best fitted $\sqrt{3}$ aspect-ratio ellipse for the curve beneath the plunging jet obtained from the present model is also shown in figure 3.5 with $-30°$ orientation relative to the x direction. It can be seen that the plunging jet follows New's theory and similar results have also been observed for deep-water breaking waves in the numerical simulations by Chen *et al.* (1999) and Hendrickson (2005).

Convergence study

To investigate the convergence of the method, another two sets of mesh, a coarse mesh (900×90) with minimum meshes $\Delta x/D = 0.01$ and $\Delta z/D = 0.01$ and a fine mesh (2600 × 240) with minimum meshes $\Delta x/D = 0.0025$ and $\Delta z/D = 0.0025$, are used to simulate the overturning wave. The comparison of the profiles of the overturning wave is shown in figure 3.6. It is found that the results are convergent

and grid-independent results are obtained for the medium and fine meshes. The finer mesh produces sharper plunging jet during wave overturning but it requires more computational effort.

Velocity fields during wave overturning

Figure 3.7 shows the velocity fields during wave overturning. At $t\sqrt{g/D} = 9.29$ before wave breaking, the wave becomes steep and the velocity in the water increases from the bottom to the water surface. The velocity and the water surface profile all suggest the wave is in the pre-breaking region, which is classified as $u < C$ before wave breaking. At $t\sqrt{g/D} = 9.87$ during wave breaking, the maximum velocity in the water is greater than the phase speed C, is nearly horizontal and is located at the front face of the wave. Large velocity vectors are produced in the air ahead of the front face of the wave due to the pushing of the wave. At $t\sqrt{g/D} = 9.87$ during wave overturning, the velocity in the plunging jet increases. At $t\sqrt{g/D} = 10.73$ during wave curling down, the maximum velocity in the water is located at the tip of the plunging jet and large velocities beneath the plunging jet are observed as the entrapped air tries to escape from the enclosed cavity. It is worth noting that the air above the crest of the wave tries to follow the water surface and the recirculation of air can be clearly observed above the wave crest during wave breaking. These results are more detailed than experimental measurements which cannot give velocities there. They are physically realistic so support the model to simulate breaking waves.

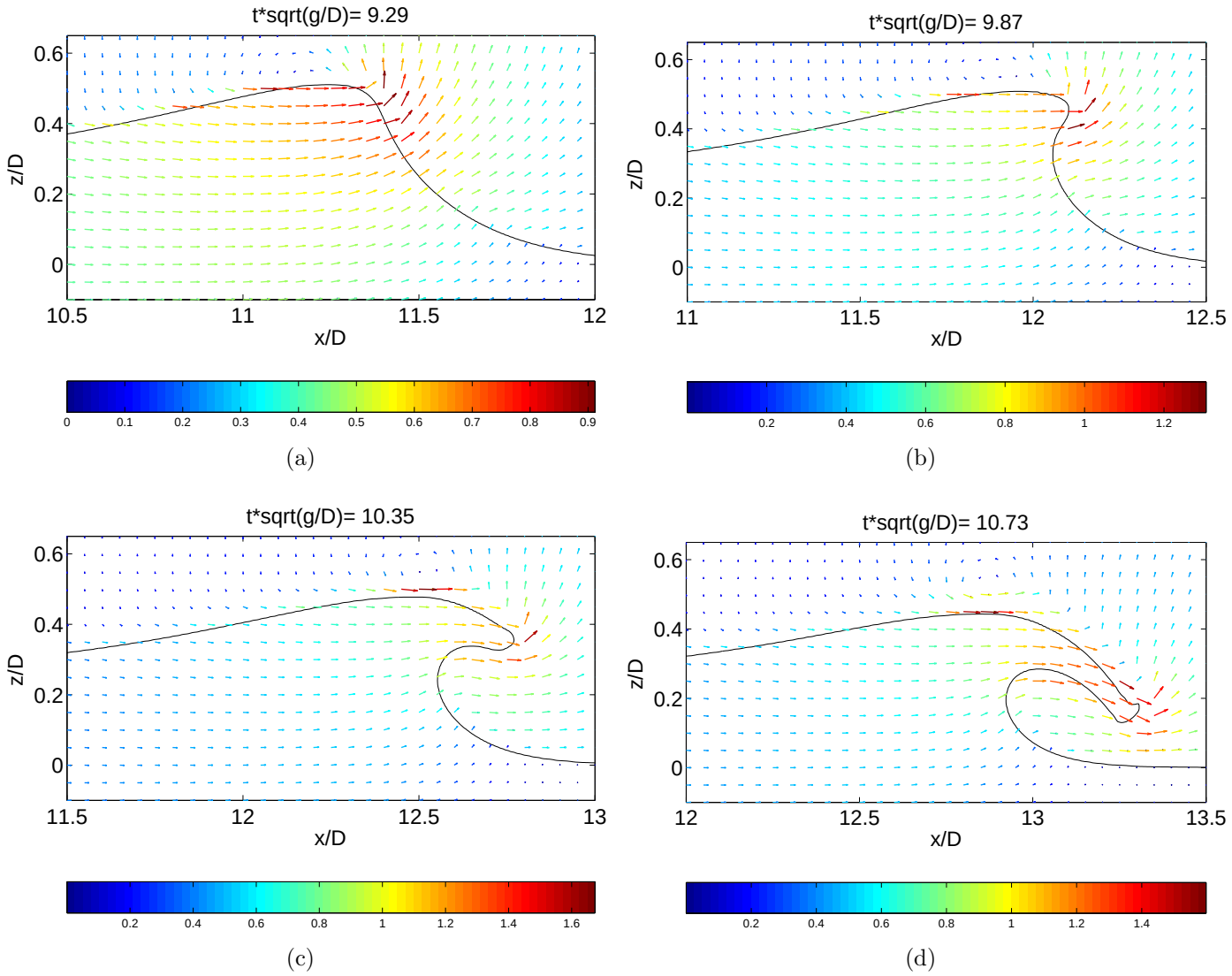

Figure 3.7: Velocity fields during wave overturning on a sloping beach. Velocities are normalized by the wave phase speed C and the color bar represents the magnitude of the velocity.

3.5 2D Overturning Waves over a Reef

3.5.1 Introduction

It is worth pointing out that several researchers in Helluy *et al.* (2005) have used the overturning of a solitary wave over a reef (Yasuda *et al.*, 1997) to validate their models, in which only the time series of water surface profiles at fixed gauges are compared against experimental data. In order to compare the model with others, we present our numerical results here for completeness.

3.5.2 Computational Setup

We use a similar computational setup to Helluy *et al.* (2005). The detail of the experimental setup can be found in Yasuda *et al.* (1997). The schematic of the overturning of a solitary wave over a reef is shown in figure 3.8, where the origin of the coordinate system is on the still water level above the toe of the reef, x and z are the horizontal and vertical coordinates respectively. $D = 0.31$ m is the still water depth, $H = 0.1314$ m is the solitary wave height, $R = 0.263$ m is the height of the reef. The computational domain is 6 m long and 0.8 m high and it is discretized by a 1500×200 uniform grid. The no-slip boundary conditions are used for all boundaries and the solitary wave is initialized similar to that in the previous section, but the centre is located at $x = -2$ m. The CPU time is approximately 18h on a PC (Intel® Pentium® D CPU 3.40GHz, 2GB RAM).

3.5.3 Results and Discussion

Comparison of numerical results and experimental data

Figure 3.9 shows the comparison of wave elevations between numerical results and experimental data for the wave gauges P2-P4. At gauge P2 ($x = 0$ m), the wave profile is similar to the initial solitary wave, but the wave steepness is higher than that for the initial wave ($H/D = 0.424$). When the wave propagates on the reef, the wave profile becomes asymmetrical (see from P3 and P4) and the front of the wave becomes steeper during wave breaking. It is shown that the computed water surface profiles agree well with the experimental measurements

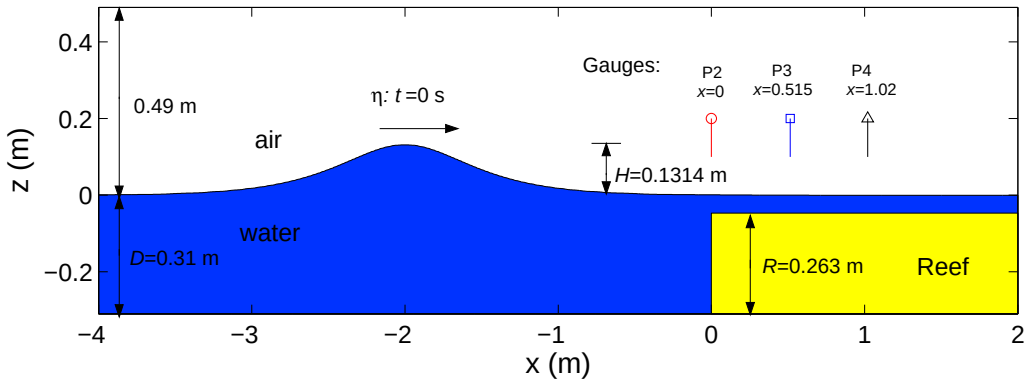

Figure 3.8: Schematic of the overturning of a solitary wave over a reef.

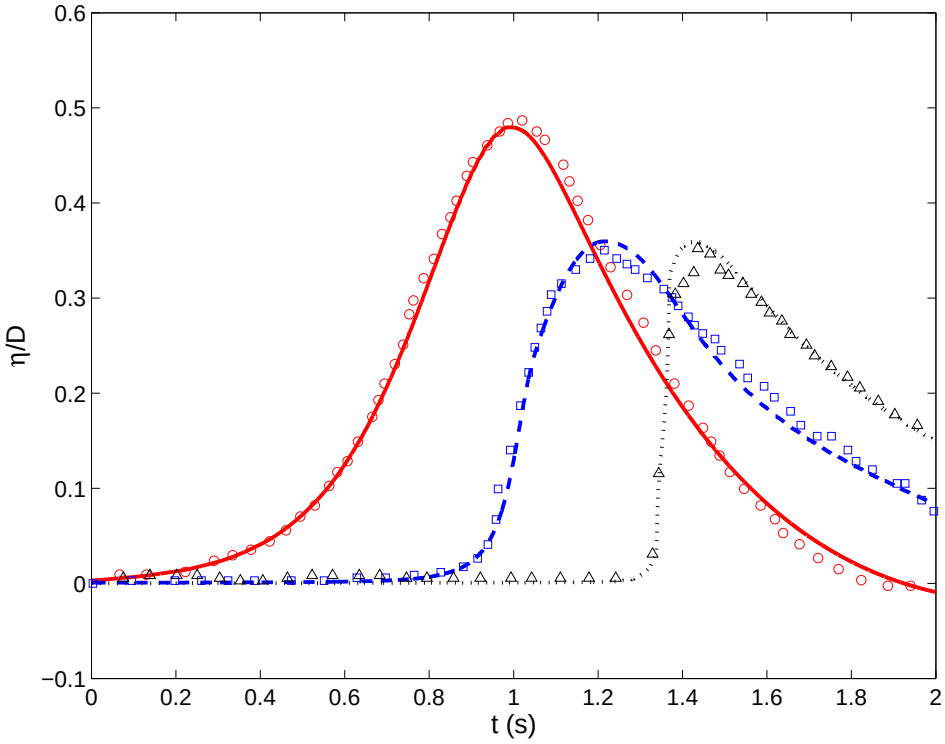

Figure 3.9: Comparison of wave elevations between numerical results (lines) and experimental data (marks). Wave gauges P2 (red), P3 (blue) and P4 (black). As the wave starts at a different location between the experiment and calculation, all experimental data are shifted with a same period of time to match the wave elevation in the first gauge P2.

(Yasuda *et al.*, 1997), and similar to the results obtained in previous numerical studies (Helluy *et al.*, 2005; Lin, 2007; Ma & Zhou, 2009).

Evolution of overturning waves

At the beginning of the solitary wave propagating towards the reef, there is little change in the wave shape. As the solitary wave approaches the toe of the reef, a small part of the wave is reflected back, whereas the main part of the wave propagates on the reef. Since the top of the wave moves faster than the bottom of the wave, the front of wave is steepened and the wave starts to overturn. Figure 3.10 shows the evolution of water surface profiles during wave overturning. At the onset of wave breaking ($t = 1.2$ s), the wave front becomes near vertical. The plunging jet is observed during wave overturning ($t = 1.3$ s and $t = 1.4$ s). The plunging jet impinges the water surface ahead to generate the secondary jet ($t = 1.6$ s) and the jet-splash cycles are developed afterwards ($t = 1.8$ s). The wave profiles at the breaking point and the jet-fall initiation, measured with a high-speed video camera in Yasuda *et al.* (1997), are plotted in figure 3.10 as well for comparison. It is noted that the shape of the computed wave profiles agree reasonably with the experimental measurements, however, there is a phase shift between the numerical results and experimental data, which has also been observed in Lubin (2004). This might be attributed to the small domain used in the simulation, whereas a much longer domain was used in the experiment. Overall, the present model is capable of simulating the wave overturning, air entrainment and splash-up processes.

3.6 Concluding Remarks

In this chapter, the 2D RANS model with the $k - \epsilon$ turbulence model has been described to simulate 2D overturning waves. It is shown that good agreement between numerical simulations and experimental measurements is obtained using the RANS model presented here. The overturning jet, air entrainment and splash-up during wave breaking have been captured by the two-phase flow model, which demonstrates the capability of the model to simulate free surface flow and wave

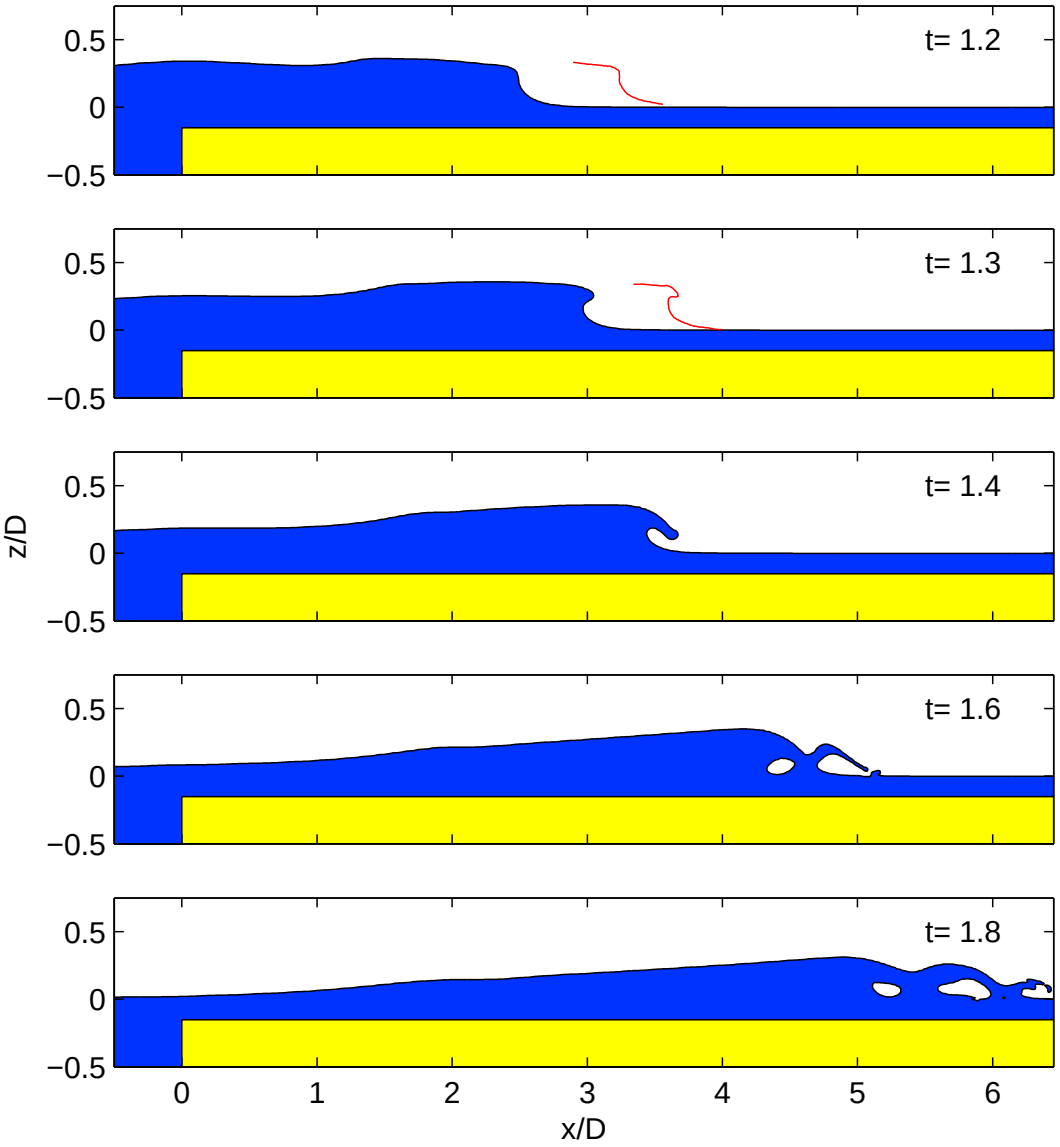

Figure 3.10: The evolution of water surface profiles during wave overturning over a reef. The experimental water surface profiles measured with the high-speed video camera during the overturning process are plotted in red lines (only two profiles at the breaking point and jet fall initiation are available in the experiment (Yasuda *et al.*, 1997)).

breaking problems. Hence, the RANS model is utilized to further study two-dimensional breaking solitary waves in Chapter 4 and periodic breaking waves in Chapter 5.

Chapter 4

Two-Dimensional Breaking Solitary Waves

The solitary wave was first discovered by John Scott Russell in 1834 while carrying out experiments to determine the most efficient design for canal boats (Russell, 1844). The solitary wave, which can represent many characteristics of water waves and tsunamis, is often used to study nearshore wave propagation and coastal effects of tsunamis (Synolakis & Bernard, 2006).

This chapter begins with introduction of some relevant experimental and numerical studies of breaking solitary waves. The RANS model is then employed here to study breaking solitary waves on a sloping beach. The numerical results are compared with experimental measurements in the absence of wind, and then detailed wind effects on breaking solitary waves are presented and discussed.

4.1 Introduction

Many experimental investigations of breaking solitary waves have been performed, which have important implications in understanding the run-up height of tsunamis on shores and their hydrodynamic loads on coastal structures. Synolakis (1986) carried out laboratory measurements to study the run-up of non-breaking and breaking solitary waves on a 1:19.85 sloping beach. The empirical run-up relations for non-breaking waves were derived and improved our understanding of

the run-up process. Water surface profiles were presented during the wave run-up process and it was found that the maximum run-up of the incident wave depends on its breaking characteristics. Yasuda *et al.* (1997) performed laboratory measurements to study the overturning of a solitary wave over a reef. The shoaling effect of wave breaking was investigated by reefs instead of slopes and it was found that the size of the overturning jet changes, depending on the relative height of the submerged reef. Li (2000) experimentally investigated the splash-up of breaking solitary waves on a 1:15 sloping beach and vertical walls. Detailed profiles for the overturning jet and subsequent splash-up were presented in that study. Two different wave breaking types were found from the experiments. If the plunging jet impinges on a dry slope, no splash-up occurs and the breaking wave simply collapses. If the plunging jet impinges on a water surface, the splash-up is observed and a reflected jet is generated with both clockwise and counterclockwise vortices. Jensen *et al.* (2003) performed an experimental study of solitary wave run-up at a steep beach and attention was paid to the dynamics of the early stages of the run-up. It was found that the steepening wave front neither develops into plunging nor spilling breakers due to the steep beach. Jensen *et al.* (2005) investigated the velocity and acceleration patterns of a collapsing breaker through PIV measurements and the VOF computation. Good agreement between experiments and simulations was obtained and it was found that the jet is mainly formed at the crest of the wave in plunging breakers whereas the jet is formed over the whole height of the wave in collapsing breakers.

Non-breaking and breaking solitary wave run-up has been studied intensively by different numerical models, such as the shallow water equations (Li & Raichlen, 2002; Titov & Synolakis, 1995), Boussinesq equations (Zelt, 1991), shallow water equations with the incorporation of Boussinesq terms (Borthwick *et al.*, 2006; Stansby, 2003), fully nonlinear potential flow (Grilli *et al.*, 1997), single phase Navier–Stokes model (Lin *et al.*, 1999; Lo & Shao, 2002) and two-phase Navier–Stokes model (Guignard *et al.*, 2001). The depth-averaged models like the shallow water and Boussinesq equations are able to model the general characteristics of the run-up, but they only provide depth-averaged velocities and cannot model the water surface profile during wave overturning and breaking. The discrepancy is due to the hydrostatic pressure assumption and the lack of the treatment for

the bottom friction effect as discussed by Lin *et al.* (1999) and Li & Raichlen (2002). The fully nonlinear potential flow can simulate the physics of wave shoaling on the beach and provide detailed information like the shape of plunging jet, breaking index and velocity field during wave breaking, but it is not able to calculate the maximum run-up and energy dissipation as the computation terminates when the plunging jet impinges on the water surface. In the single phase Navier–Stokes models by the VOF (Lin *et al.*, 1999) and SPH (Lo & Shao, 2002) methods, the water surface profile and velocity distribution agreed with the experiment, but the detailed information during wave breaking, such as the development of the plunging jet and splash-up phenomena, were neglected. Guignard *et al.* (2001) presented a two-dimensional DNS study of breaking solitary waves on sloping beaches using the two-phase flow model. The pseudo-compressibility method is employed to solve the Navier–Stokes equations and the SL-VOF (Segment Lagrangian- VOF) method is used to track the interface. The overturning jet during wave breaking and the splash-up were obtained and compared with experimental measurements. It was suggested that the velocity and pressure fields exhibit a highly non-hydrostatic flow near breaking, which cannot be predicted by hydrostatic models.

It is worth noting that the effect of wind is neglected in all the above computations. Therefore, the objective of this chapter is to investigate wind effects on breaking solitary waves and provide more detailed information during wave breaking. We calculate breaking solitary waves on a 1:19.85 sloping beach as detailed water surface profiles and run-up in the absence of wind are provided in the experiment (Synolakis, 1986), which is also considered as a 2D benchmark problem for breaking solitary waves (Synolakis *et al.*, 2008).

4.2 Computational Setup

4.2.1 Geometry

Wind effects on a two-dimensional breaking solitary wave running up a uniform sloping beach of angle β are considered in this chapter. The schematic of this problem is shown in figure 4.1, where the origin of the coordinate system is where

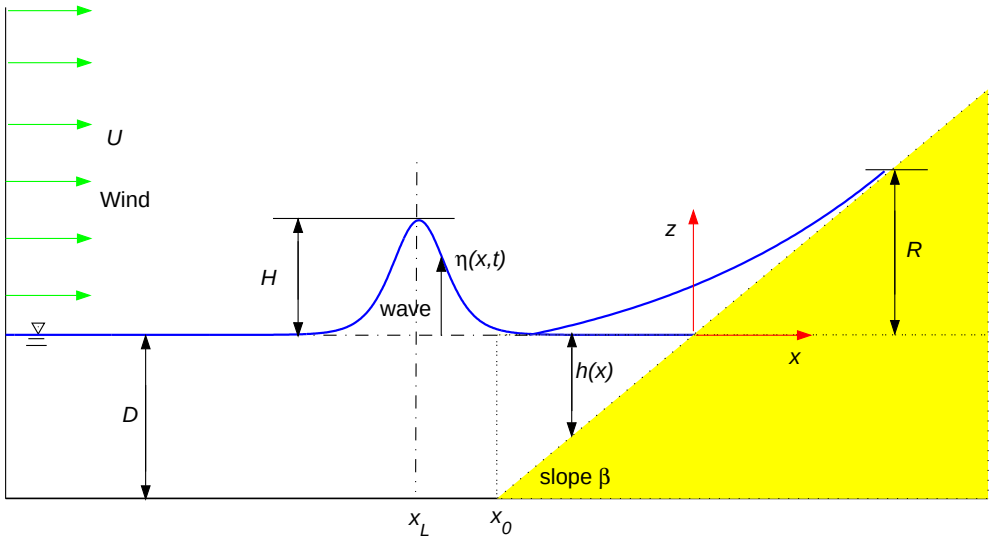

Figure 4.1: Sketch of wind effects on a two-dimensional breaking solitary wave run-up on a uniform sloping beach.

the still water surface meets the beach slope, x and z are the horizontal and vertical coordinates respectively, D is the still water depth, H is the solitary wave height, $\eta(x,t)$ is the solitary wave profile, t is time, and x_L is the initial centre of the solitary wave. x_0 is the toe location of the beach, $h(x)$ is the local still water depth, U is the wind speed and R is maximum run-up, which is defined as the highest position the wave can reach on the slope.

4.2.2 Governing Equations

The governing equations used for this study are the Reynolds-averaged Navier–Stokes equations (as discussed in § 3.1) and the standard $k-\epsilon$ model (3.16-3.17).

4.2.3 Computational Parameters

The detailed laboratory setup for breaking solitary waves can be found in Synolakis (1986) and only the important parameters used in this study are summarized here. The slope of the beach $\tan(\beta) = 1 : 19.85$ and only the case for breaking solitary waves is considered in this study, that is a solitary wave

with the ratio of wave height to still water depth, $H/D = 0.28$, generated in the experiment. In this study, the still water depth $D = 0.2116$ m is used and the wave phase speed $C = \sqrt{g(D+H)} = 1.6292$ m/s. The computational domain starts from the toe of the beach and extends to the location beyond the maximum run-up point $35.44D$. The height of the computational domain is $2D$ and it is discretized by a 550×100 nonuniform grid. Minimum meshes with $\Delta x/D = 0.025$ and $\Delta z/D = 0.01$ are uniformly distributed in the breaking region where $x/D \in [-5, 0]$ and $z/D \in [0, 0.3]$, and other meshes increase linearly to the boundary. The CPU time is approximately 3h on a PC (Intel® Pentium® D CPU 3.40GHz, 2GB RAM).

4.2.4 Initial and Boundary Conditions

Boundary conditions

At the inlet, the solitary wave is generated by specifying the water surface elevation and velocity fields based on the analytical solutions (3.45). The effect of wind is obtained by specifying different uniform wind speed above the water surface. As the water surface elevation changes with time at the inlet, the lowest point of wind forcing also changes with the movement of the water surface at a distance about $h^{\mathrm{a}}/D = 0.05$, where h^{a} is the height of the lowest point of wind forcing above the water surface at the inlet. If the wind forcing is too close to the water surface, the solitary wave profile may be changed during its generation at high wind speeds, therefore we choose a distance about five minimum meshes in the vertical direction away from the water surface based on our experience. It is worth noting that the flux of the wind at the inlet is not a constant and has a minimum value when the crest of the wave arrives at the inlet. A key parameter for this problem is the ratio of wind speed U to wave phase speed C. Only the onshore wind U/C in the range of 0 to 3 is considered in this study although the offshore wind effect can be obtained in a similar way. We assume development time for the boundary layer is negligible and for the sake of simplicity, only uniform wind profiles are considered here although other more physically realistic wind profiles can also be studied. For the turbulence field, the turbulent kinetic energy is obtained as $k = \frac{1}{2}(I \times C)^2$, where $I = 0.005$ is the turbulent intensity

and the turbulent eddy dissipation is adjusted so the turbulent eddy viscosity is ten times the dynamic viscosity of each fluid at the inlet.

The no-slip boundary condition is specified on the bottom and top of the domain and along the sloping beach. The log law of the wall function for the turbulence is applied at the no-slip boundaries (see § 3.2.1).

The zero gradient boundary conditions on the mean flow and turbulence are applied at the outlet.

Near the air-water interface, the log law of the wall function for the turbulence model on the water surface (see § 3.2.1) is employed in this study and the boundary layer in water generated by wind (Tsanis, 1989; Wu & Tsanis, 1995) is ignored here. Without using the wall function, when we calculate the turbulent air flow over calm water (not shown here), the flow in the air would behave like a laminar flow similar to a laminar flow near a solid wall.

Initial conditions

At $t = 0$, the water velocities and water surface are given by the results of the analytical solution of a solitary wave (3.45), the velocity in the air is initialized as zero, the pressure distribution in the whole domain is hydrostatic and the turbulence field is initialized to the same value as the boundary conditions at the inlet.

4.3 Comparison of Numerical Results and Experimental Data Without Wind

In order to study the effect of wind on breaking solitary waves, we first simulate breaking solitary waves in the absence of wind ($U/C = 0$) and compare with experimental measurements in terms of water surface profiles and the evolution of maximum wave height. The results obtained here will be used to compare with results in the presence of wind in the next section.

4.3.1 Water Surface Profiles

Figure 4.2 shows the comparison of the computational results with the experimental measurements in terms of the water surface profiles. Figure 4.2(a-b) shows the wave shoaling process. As the water depth decreases, the wave height increases and the wave shape becomes asymmetrical. The front of the wave is steepening and nearly vertical in figure 4.2(b). Figure 4.2(c) shows the wave breaking process, it can be seen that the wave starts to break when the critical ratio of wave height to water depth is achieved and that air entrainment is observed during wave breaking. After wave breaking, the wave continues to run up the beach as seen in figure 4.2(d). After reaching the maximum run-up shown in figure 4.2(e), the wave starts to run down the beach. The shoreline movement during wave run-up agrees well with the experimental data.

It is shown from figure 4.2 that the computational results agree with the experimental measurements in terms of the shape and location of the wave during wave shoaling, breaking and the run-up processes. The favourable agreement provides additional validation of this model for simulating breaking waves.

4.3.2 The Evolution of Maximum Wave Amplitude

In the absence of wind ($U/C = 0$), Synolakis & Skjelbreia (1993) studied the evolution of the maximum amplitude of solitary waves on a 1:19.85 sloping beach and found that breaking solitary waves are in the gradual shoaling zone, where the amplitude variation can be identified as similar to Green's law (Lamb, 1932): $\eta_{\max} \sim 1/h^{1/4}$.

Figure 4.3 shows the comparison of evolution of maximum wave amplitude in the absence of wind ($U/C = 0$) between the numerical simulation, experiment and Green's law. In the shoaling region where $0.3 < h(x)/D < 1$, the numerical results are underestimated compared to experimental measurements and Green's law. This might be caused by the incident wave generated in the simulation differed slightly from the incoming wave in the experiment. However in the breaking region where $0.1 < h(x)/D < 0.3$, a good agreement with the experiment of Synolakis & Skjelbreia (1993) is obtained. As Synolakis & Skjelbreia (1993)

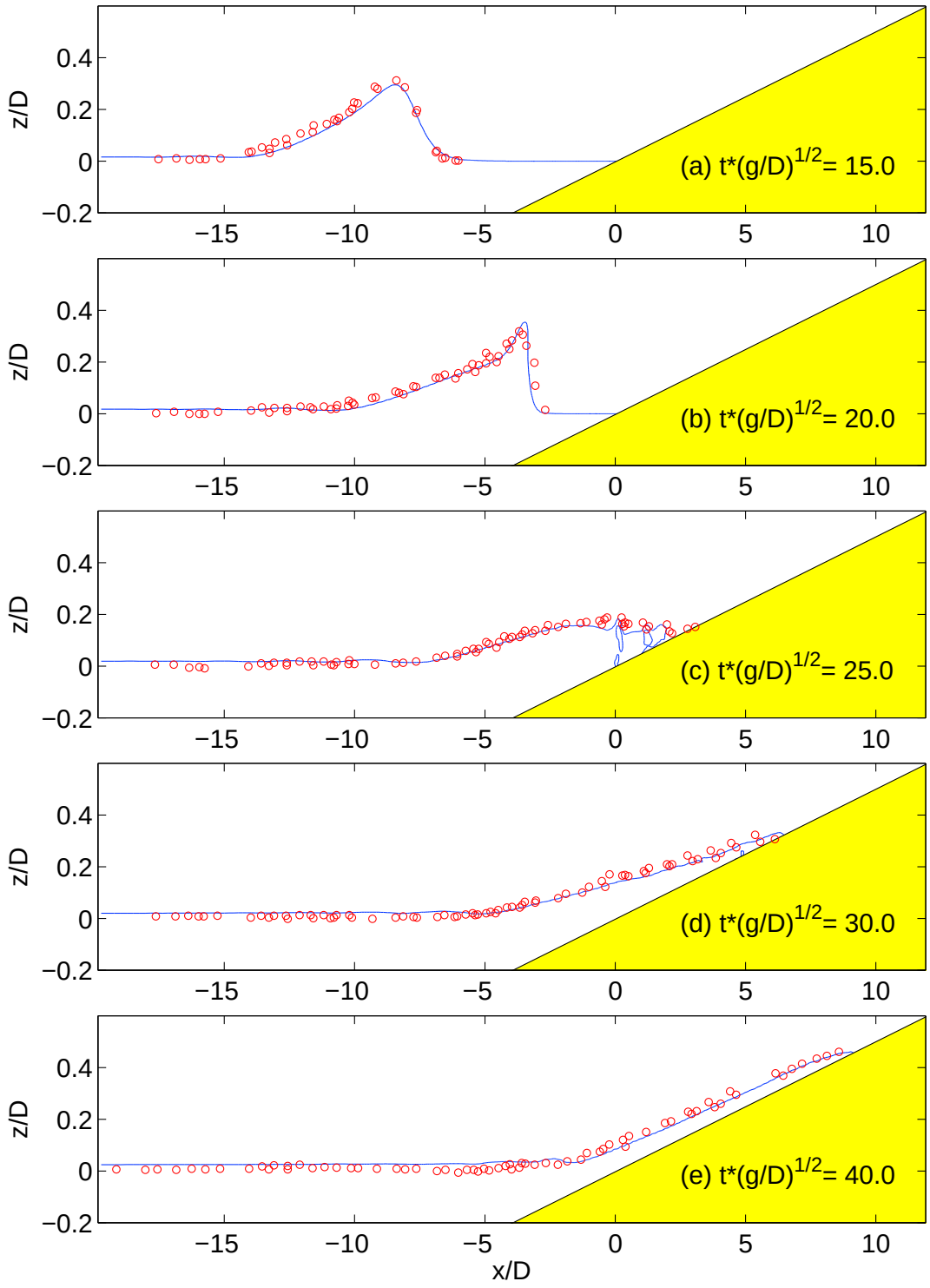

Figure 4.2: Comparison of numerical results of breaking solitary wave run-up in the absence of wind ($U/C = 0$) with experimental data, blue solid line: numerical results; red circles: experimental data (Synolakis, 1986). The vertical scale is exaggerated by a factor of 10.

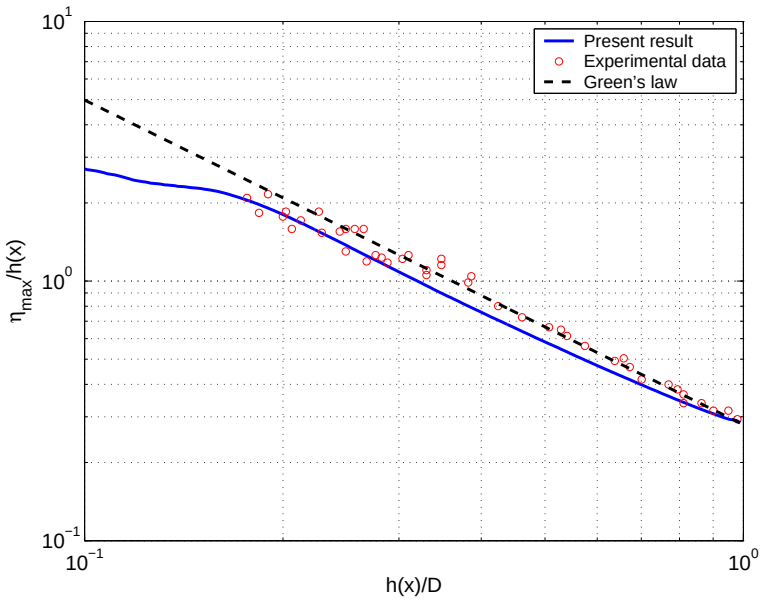

Figure 4.3: Comparison of the evolution of maximum wave amplitude up the beach in the absence of wind ($U/C = 0$) with the experiment of Synolakis & Skjelbreia (1993) and Green's law (Lamb, 1932).

indicated, Green's law overestimates the amplitude during wave breaking as it can be seen from figure 4.3.

4.4 Wind Effects on Breaking Solitary Waves

In this section we present the results of wind effects on breaking solitary waves, with a focus on the effects during wave breaking. Numerical results are based on the comparison of the cases between different wind speeds as well as the case in the absence of wind.

4.4.1 Water Surface Profiles

In this section, we study the effect of wind on water surface profiles. As the scope of the present study is breaking waves, only those results during wave breaking are shown here.

Figure 4.4 shows the evolution of the water surface profiles during wave breaking at $t\sqrt{g/D} = 20.0 - 21.0$ for different wind speeds $U/C = 0 - 3$. At a fixed

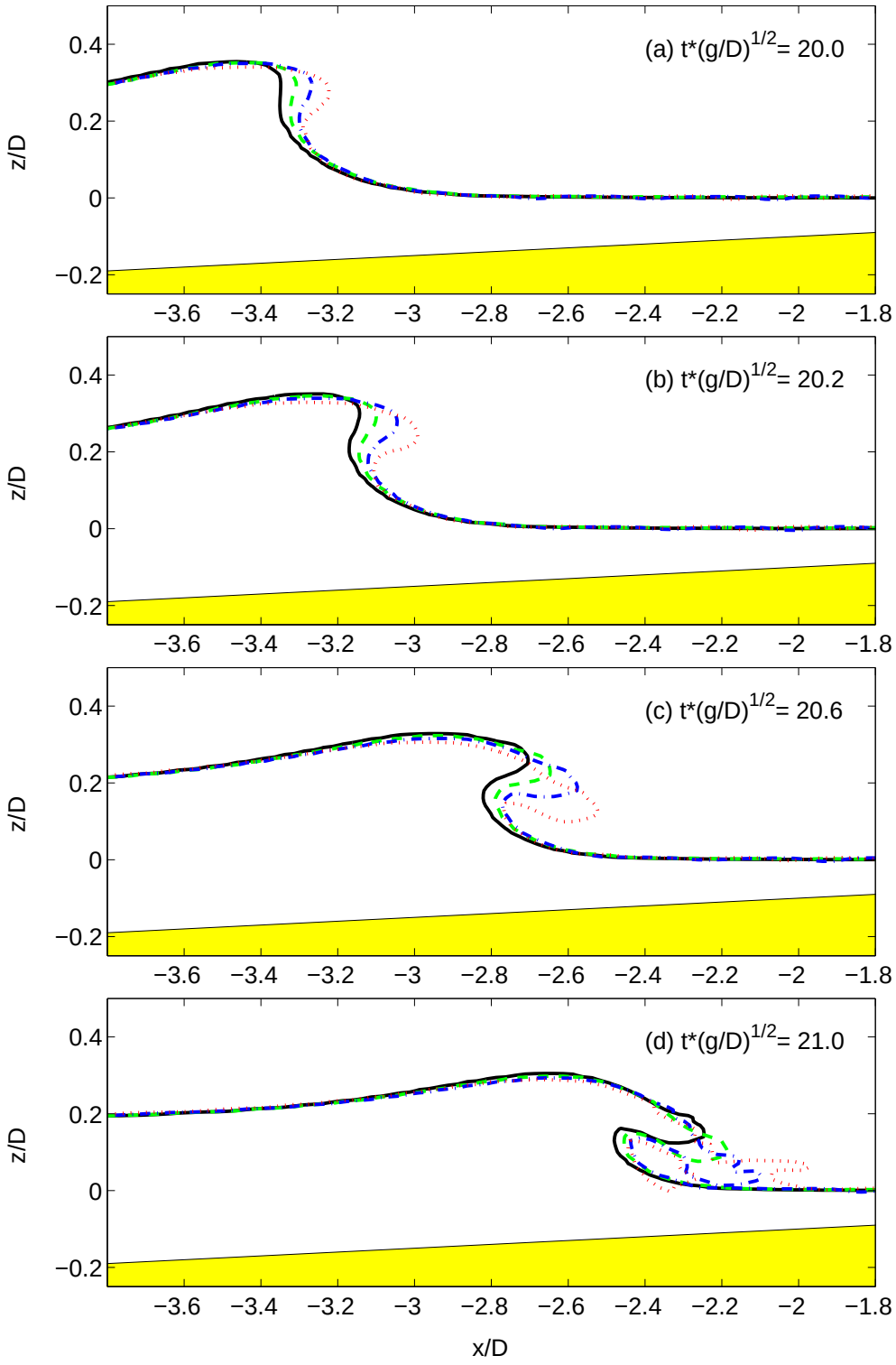

Figure 4.4: The evolution of water surface profiles during wave breaking for different wind speeds: $U/C = 0$: black solid line; $U/C = 1$: green dashed line; $U/C = 2$: blue dash-dotted line; $U/C = 3$: red dotted line.

time $t\sqrt{g/D} = 20.0$ in figure 4.4(a), the solitary wave with $U/C = 0$ is just at the breaking point while the ones with $U/C = 1 - 3$ have passed the breaking point, which is defined as the point where the front of the wave becomes vertical. The wave front moves faster as U/C increases. When $t\sqrt{g/D} = 20.2$ in figure 4.4(b), the wave for $U/C = 3$ starts to curl down but others ($U/C = 0-2$) are still in the overturning process. Figure 4.4(c) shows the plunging jets of breaking solitary waves and we observe that the distance between the front of each wave increases as U/C increases. At $t\sqrt{g/D} = 21.0$ in figure 4.4(d), the plunging jet for $U/C = 3$ first begins to strike the water surface and the splash-up is developed.

It is shown from figure 4.4 that the wind affects the wave breaking process and the shape of the plunging jet. The wind has a significant effect on the front face of the wave but a little effect on the rear face. As the wave receives the energy from the wind, the distance between the front face of each wave with different U/C increases monotonically with time. It can be seen from figure 4.4 that the wave moves faster as the wind speed increases, and this causes the wave to break earlier which is consistent with the previous laboratory investigation by Douglass (1990).

4.4.2 Velocity Fields

In this section, we investigate the effect of wind on the velocity fields under breaking waves. Figure 4.5 shows the evolution of the velocity vectors during wave breaking for different wind speeds. For clarity (due to the large difference in velocity between the air and water for higher wind speeds), only the velocity fields for $U/C = 0$ (left figures) and $U/C = 2$ (right figures) are presented here.

Figure 4.5(a) shows the velocity field at $t\sqrt{g/D} = 20.0$ before wave breaking. When $U/C = 0$ in the left figure, the air above the crest of the wave tries to follow the water surface and the recirculation of air can be clearly observed above the wave crest. The velocity in the water increases from the bottom to the water surface with the maximum velocity in the water $u_{\max} = 0.88C$. The velocity and the water surface profile are consistent with the wave in the pre-breaking region, which is usually classified as $u < C$ everywhere. When $U/C = 2$ in the right figure, the recirculation of air doesn't exist due to the presence of the wind.

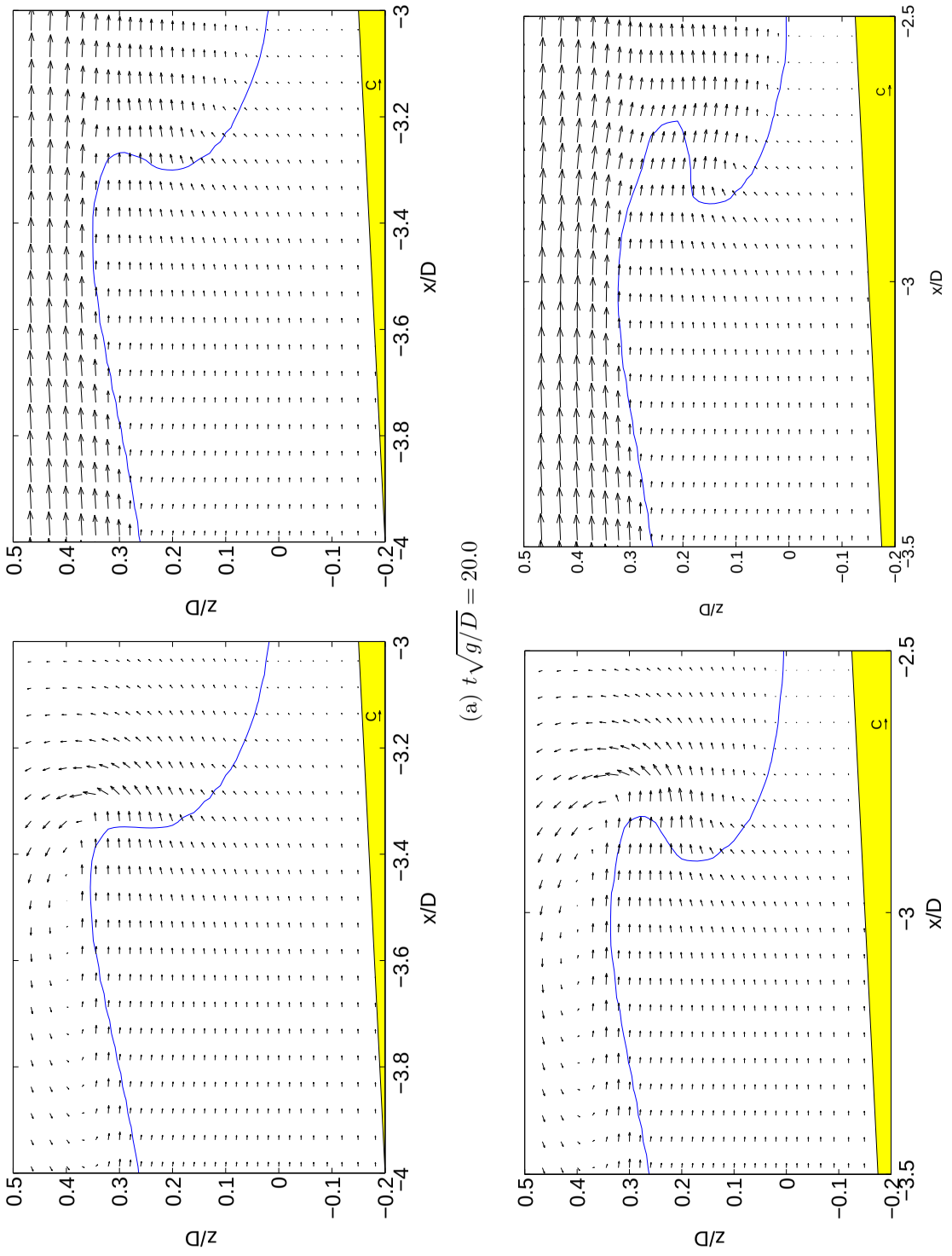

(a) $t\sqrt{g/D} = 20.0$

(b) $t\sqrt{g/D} = 20.5$

Figure 4.5: For caption see facing page.

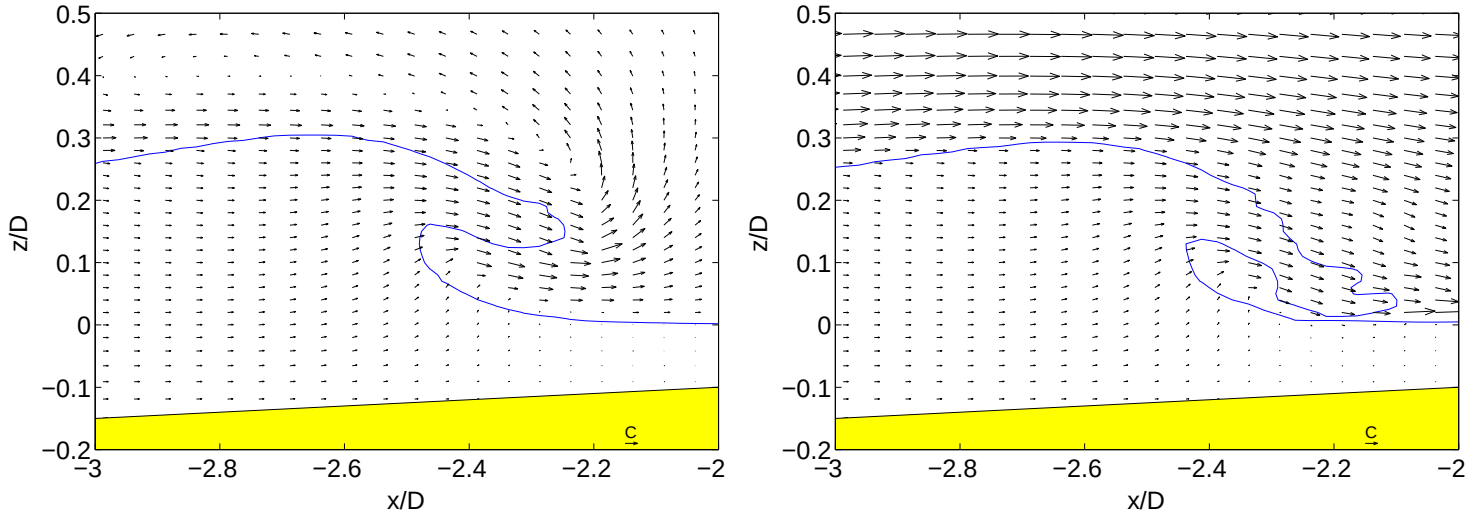

(c) $t\sqrt{g/D} = 21.0$

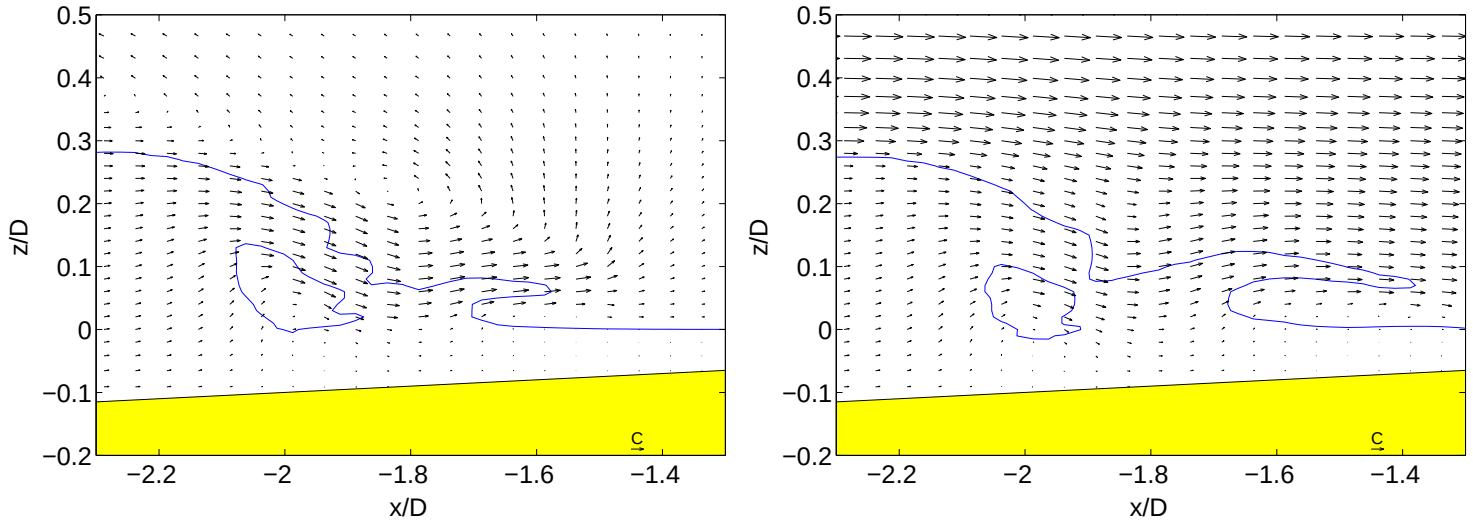

(d) $t\sqrt{g/D} = 21.5$

Figure 4.5: The evolution of velocity vectors during wave breaking for $U/C = 0$ (left of pair) and $U/C = 2$ (right of pair). The velocity vectors have been normalized by C. The bold line is the water surface.

Above the crest of the wave, air flow separation can be observed downstream of the front face of the wave. It is noted that the air is driven by the wave when $U/C = 0$ and the wave is driven by the wind when the value of U/C is high, respectively.

Figure 4.5(b) shows the velocity field at $t\sqrt{g/D} = 20.5$ during wave breaking. When $U/C = 0$ in the left figure, the maximum velocity in the water is $u_{\max} = 1.01C$, and thus causes the wave to break. The maximum velocity vector at the front face of the wave is nearly horizontal and large velocities are produced in the air ahead of the wave. When $U/C = 2$ in the right figure, the wave is breaking, similar to the case in the absence of wind, except for the separation of the air flow above the crest of the wave.

In figure 4.5(c), the forming of the plunging jet at the front face of the wave is presented for both cases at $t\sqrt{g/D} = 21.0$ during wave overturning. It can be seen that the plunging jet is more advanced in the $U/C = 2$ case due to the wind forcing. During wave overturning, large velocities below the plunging jet are observed as the entrapped air tries to escape from the cavity for both cases.

Figure 4.5(d) depicts the splash-up phenomenon at $t\sqrt{g/D} = 21.5$ after wave breaking. When $U/C = 0$, the plunging jet impinges on the water surface ahead and reaches the maximum velocity during wave breaking. A secondary jet is generated during the splash-up and an air cavity is enclosed by the plunging jet. When $U/C = 2$, the second jet is more advanced due to the wind effects. The wind may affect the splash-up process as the generated secondary jet obtains energy from the wind, which affects the shape and height of the subsequent splash-up.

As discussed above, it is shown that the water particle velocity increases during wave overturning, reaches a maximum when the plunging jet strikes the water surface and decreases during the splash-up, which is consistent with the experimental investigation of overturning waves by Chang & Liu (1998). The onshore wind does have an effect on the velocity field of the water during wave breaking as the wind assists the development of water particle velocity towards the wave phase speed to initiate an earlier breaking. Hence, the higher the wind speed, the earlier the wave breaks. This can be easily seen from figure 4.5(a–d) when compared the water surface profiles between $U/C = 0$ (left figures) and

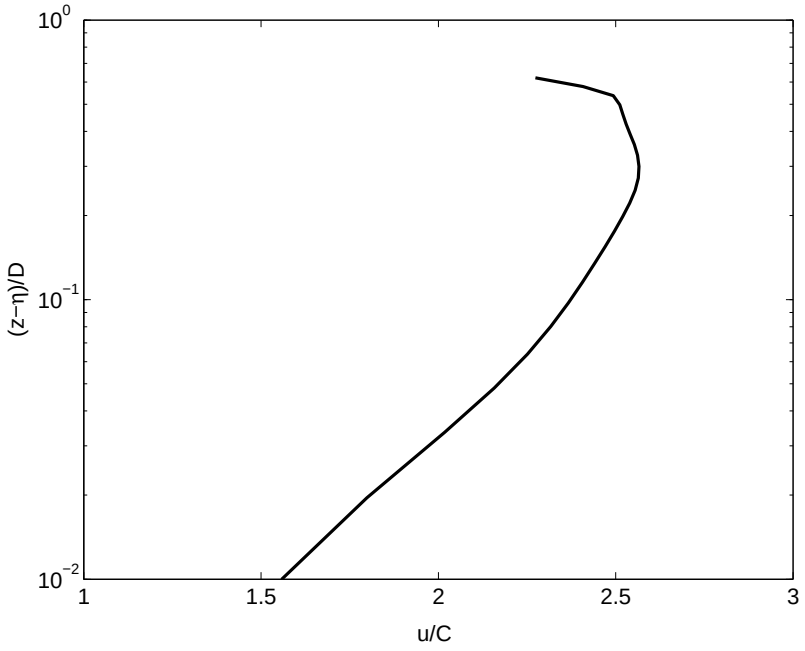

Figure 4.6: The logarithmic profile of the velocity u at $x/D = -3.4$ above the crest of the wave for $U/C = 2$ during wave breaking at $t\sqrt{g/D} = 20.0$.

$U/C = 2$ (right figures). The same effects are also observed in the cases for $U/C = 1$ and $U/C = 3$ (not shown here).

Banner (1990) experimentally investigated the wind-wave interactions and found the logarithmic wind profile over breaking waves. In the presence of wind $U/C = 2$, the detailed velocity profile at $x/D = -3.4$ above the crest of the wave in the right part of figure 4.5(a) is depicted in figure 4.6. It can be seen that the turbulent velocity distribution above the water surface is obtained due to the use of the wall function for the air-water interface and it follows logarithmic profiles (Banner, 1990). Without using the wall function, we cannot capture the turbulent shear layer above the wave and the velocity profile above the air-water interface would behave like a laminar flow near a solid wall.

4.4.3 Pressure Distributions and Drag Force

The pressure distributions in the air and water have a significant effect on wave breaking. The air pressure distribution on the water surface has important implications for the momentum and energy transfer at the air-water interface and the

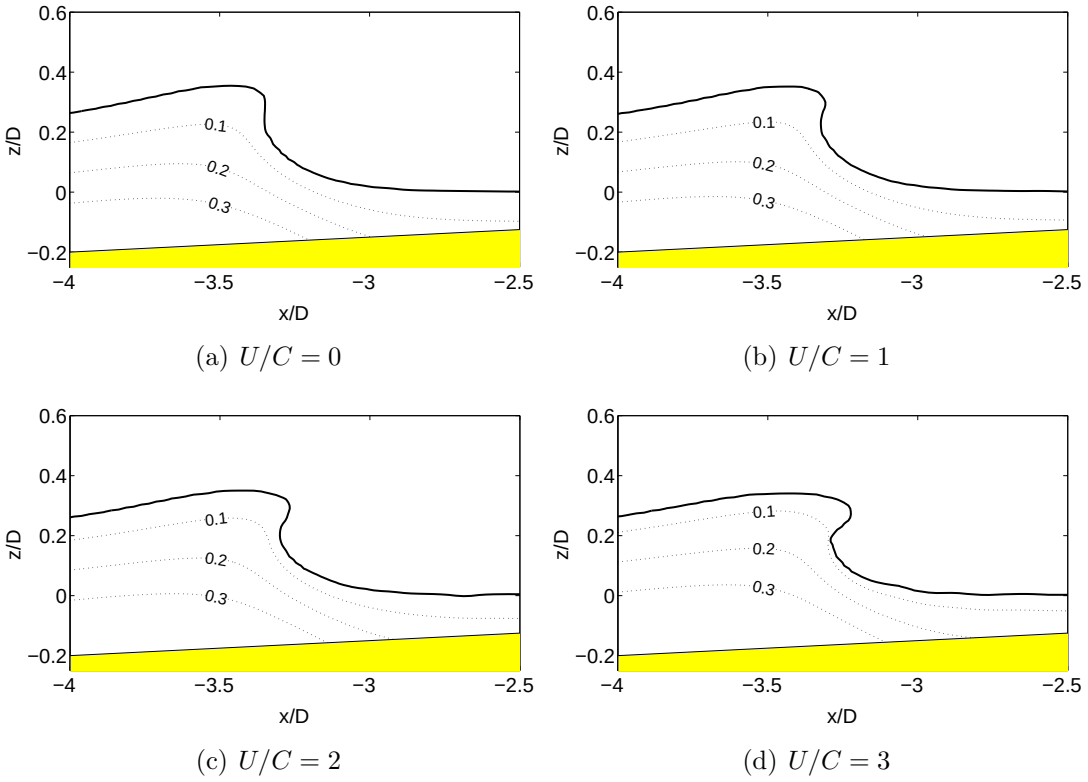

(a) $U/C = 0$ (b) $U/C = 1$

(c) $U/C = 2$ (d) $U/C = 3$

Figure 4.7: The contours of the pressure in the water during wave breaking for different wind speeds $U/C = 0 - 3$ at $t\sqrt{g/D} = 20.0$. The reference pressure is at the top of outlet and the pressure has been normalized by $\rho g D$. The bold line is the water surface.

form drag (Banner, 1990), and the water pressure distribution is the main contribution of the force and wave loads on marine structures. Thus, in this section, we investigate the effect of wind on the pressure field and drag force for breaking solitary waves.

Figure 4.7 shows the pressure distribution in the water during wave breaking for different wind speeds $U/C = 0 - 3$ at a representative time $t\sqrt{g/D} = 20.0$. It is shown that the pressure distribution changes slightly in the presence of wind. The effect of wind on the pressure of the water is small due to the large density of water.

In the vicinity of the water surface, the pressure may be changed in the presence of wind, which has important consequence of the wind stress and associated

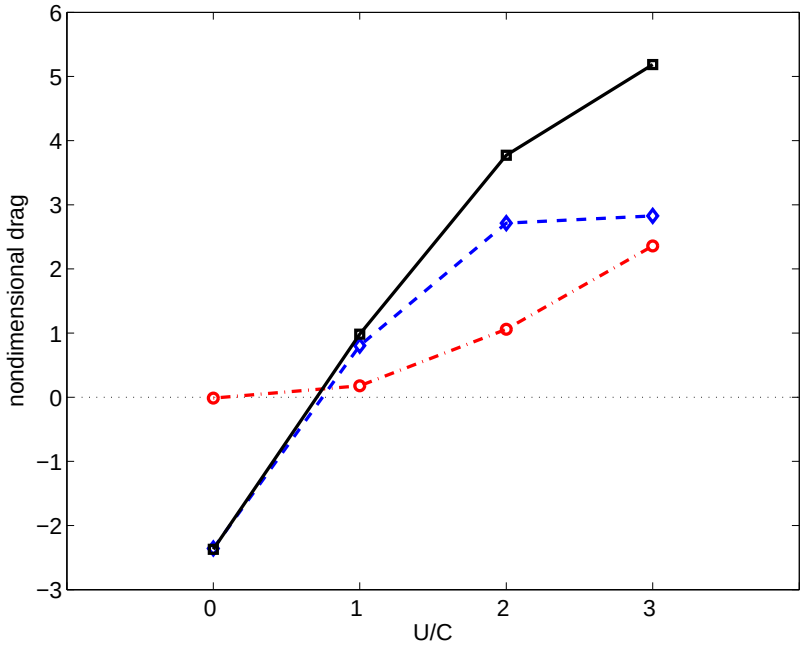

Figure 4.8: Comparison of the drag coefficients for different wind speeds $U/C = 0-3$ at $t\sqrt{g/D} = 20.0$. Form drag C_p: diamond dashed line; friction drag C_τ: circle dash-dotted line; total drag $C_t = C_p + C_\tau$: square solid line.

form drag. The form drag D_p and friction drag D_τ along the water surface are calculated as

$$D_p = \int_\eta -p\boldsymbol{i}\cdot\boldsymbol{n}\mathrm{d}S, \tag{4.1}$$

$$D_\tau = \int_\eta (\tau_{xx}\boldsymbol{i}\cdot\boldsymbol{n} + \tau_{xz}\boldsymbol{k}\cdot\boldsymbol{n})\mathrm{d}S, \tag{4.2}$$

where τ_{xx} and τ_{xz} are turbulent stresses discussed in § 4.4.5. The drag coefficients for the form drag C_p, friction drag C_τ and total drag C_t are obtained as

$$\begin{aligned} C_p &= \frac{D_p}{\frac{1}{2}\rho^{\mathrm{a}}C^2H}, \\ C_\tau &= \frac{D_\tau}{\frac{1}{2}\rho^{\mathrm{a}}C^2H}, \\ C_t &= C_p + C_\tau. \end{aligned} \tag{4.3}$$

Figure 4.8 gives the comparison of the drag coefficients for different wind

speeds during wave breaking at $t\sqrt{g/D} = 20.0$. It can be seen that the drag forces have a relation with the wind speed relative to wave speed and the variation for the form drag is larger than that for the friction drag.

We first investigate the form drag due to pressure. In the absence of wind ($U/C = 0$), the wave creates a relative headwind with a speed equal to that of the wave phase speed during wave propagation (as can be seen from the velocity field in the left figure in figure 4.5(a)), thus the form drag is negative which means that there is air resistance in front of the wave and it resists the wave moving forwards. In the presence of wind ($U/C = 1$), where the wind speed equals to the wave phase speed, as the water particle velocities in most part of the wave are less than the wave phase speed, therefore the wind pushes the wave forwards. The form drag has been changed dramatically with its sign from negative to positive in the direction of the wave propagation. For higher wind speeds ($U/C = 2, 3$), the stronger wind forcing changes the pressure distribution and the associated form drag significantly. The form drag is a way in which the wind can transfer energy to waves (Banner, 1990) and this is one reason why we can see the wave breaks earlier in the presence of wind. It is noted that only the form drag during the early stage of wave breaking at $t\sqrt{g/D} = 20.0$ is calculated here. The form drag depends on the wave shape and differs during wave propagation. The wave becomes steeper in the forward face and flatter in the rear face before wave breaking, thus the form drag is affected by the changed wave shape and the associated pressure distribution.

We next study the wind effects on the friction drag. In the absence of wind ($U/C = 0$), the friction drag has very small negative value due to no wind forcing. In the presence of wind ($U/C = 1$), the friction drag increases slightly and pushes the wave forwards. For high wind speeds ($U/C = 2, 3$), the variation for the friction drag is relatively larger when compared with low wind speeds ($U/C = 1$).

The total drag varies dramatically for different wind speeds. It is negative in the absence of wind ($U/C = 0$) and positive in the presence of wind ($U/C = 1-3$). It is worth remarking that there is a wind speed between $U/C = 0$ and $U/C = 1$, at which the total drag is zero. At this wind speed, the wind forcing is balanced by the air resistance in front of the wave. It is shown from figure 4.8 that the drag force increases monotonically in the direction of the wave propagation as U/C

increases. It is noted that the drag force is the main effect of wind on breaking solitary waves. This is the reason for the increase of the water particle velocities in § 4.4.2 and the change of water surface profiles by the wind in § 4.4.1.

4.4.4 Vorticity Generation

Wave breaking plays an important role in the generation of vorticity, turbulence and air entrainment. In this section we analyze the generation of vorticity, which is defined as

$$\omega = \frac{\partial w}{\partial x} - \frac{\partial u}{\partial z}. \tag{4.4}$$

Figure 4.9 shows the evolution of the vorticity field during wave breaking for different wind speeds $U/C = 0 - 3$ from $t\sqrt{g/D} = 20.0$ to $t\sqrt{g/D} = 21.0$. Through our numerical simulation, it is seen that the vorticity fields are totally different for different wind speeds and the wind has a significant effect on the generation of vorticity.

In the absence of wind ($U/C = 0$) shown in figure 4.9(a), the vorticity in the water has a smaller value in comparison with the vorticity in the air. In the air above the crest of the wave and plunging jet, there is a large positive vorticity region due to the shear and the recirculation of air flow above the wave, which is consistent with the velocity vectors shown in the left figure of figure 4.5(a). For $t\sqrt{g/D} = 21.0$ shown in the right figure of figure 4.9(a), beneath the plunging jet and in the thin region above the water surface, there are strong vortices because the air is trapped by the plunging jet and it tries to escape from the cavity. This is in agreement with the numerical results by Hendrickson (2005), who used DNS to study steep breaking water waves with a coupled air-water interface in the absence of wind.

In the presence of wind ($U/C = 1 - 3$) shown in figure 4.9(b–d), the vorticity field is totally different from the case without wind in figure 4.9(a). There is no recirculation of air flow and the wind pushes the wave moving forwards. For $U/C = 1$ in figure 4.9(b), since the wind speed is close to the wave phase speed, the region of positive vorticity becomes thicker, smaller and closer to the tip of the plunging jet when compared to the case for $U/C = 0$. When the wind is blowing, there is a region of negative vorticity formed just above most of the water

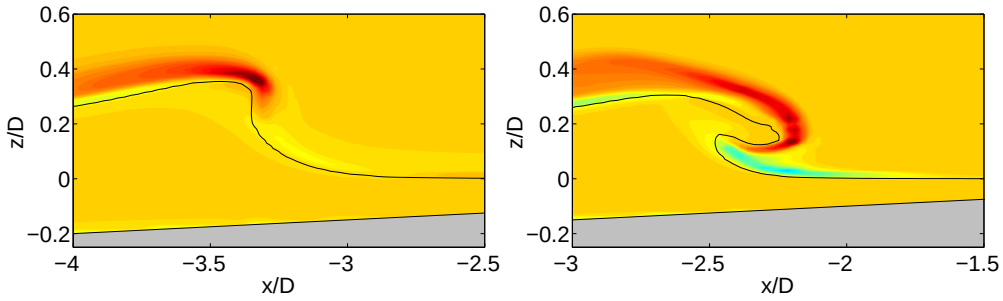

(a) $U/C = 0$

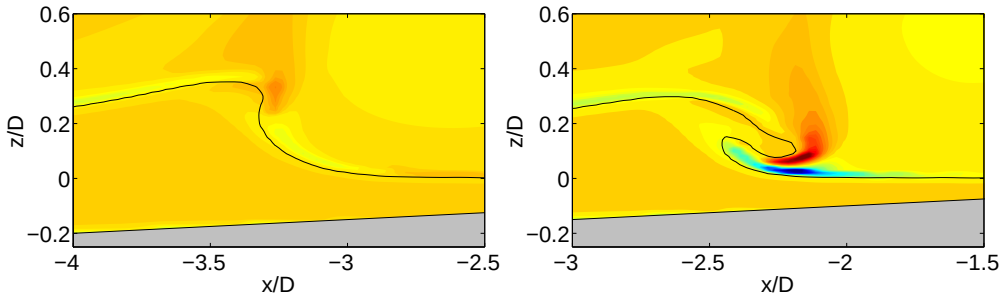

(b) $U/C = 1$

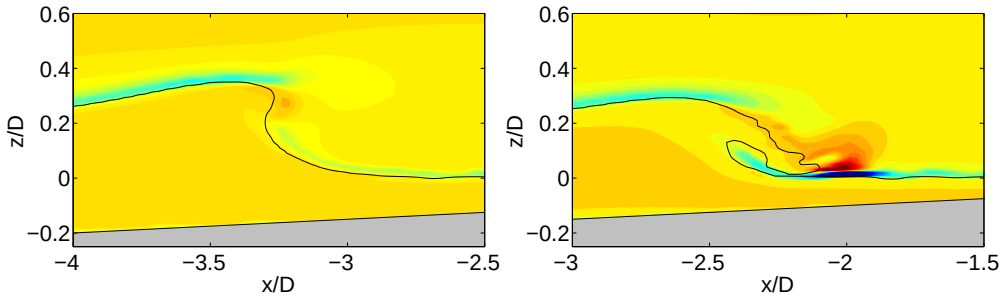

(c) $U/C = 2$

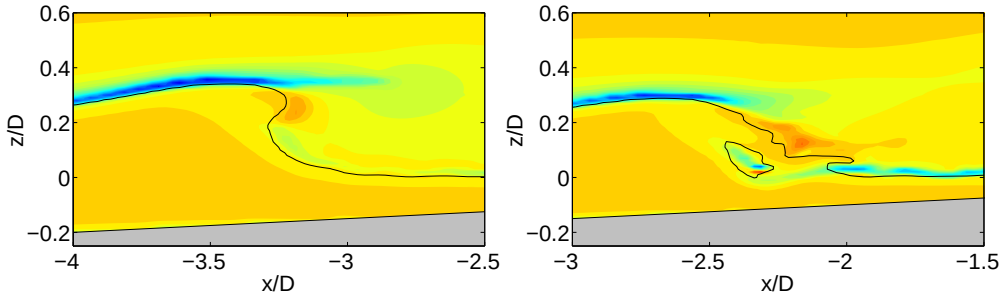

(d) $U/C = 3$

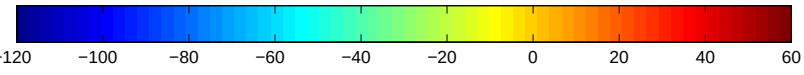

Figure 4.9: The contours of the vorticity during the wave breaking for different wind speeds $U/C = 0 - 3$ at $t\sqrt{g/D} = 20.0$ (left of pair) and $t\sqrt{g/D} = 21.0$ (right of pair). The bold line is the water surface and the vorticity has been normalized by $\sqrt{g/(D+H)}$.

surface, which means that there is a shear in the wind profile. With increased wind speeds $U/C = 2, 3$ in figure 4.9(c,d), the region of positive vorticity becomes even smaller while the region of the wind induced negative vorticity becomes thicker and larger. From this, it is shown that wind plays an important role in the generation of vorticity in the vicinity of the water surface.

In the right figure of figure 4.9(d), the vorticity for the splash-up process for $U/C = 3$ at $t\sqrt{g/D} = 21.0$ is shown, in which the plunging jet strikes the water surface and generates a secondary jet. There are three vortices during the splash-up process. Two clockwise vortices form before and after the impingement point. One of them is caused by the incident plunging jet and reverse flow under the jet, and the other is formed by the reflected jet. Another counter-clockwise vortex is formed above the jet of the splash-up. The splash-up obtained by the numerical simulation is consistent with previous theory (Basco, 1985; Peregrine, 1983) and experiments (Bonmarin, 1989; Li, 2000) in the absence of wind. In the presence of wind, another clockwise vortex is generated by the wind above the crest of the wave for higher wind speeds (shown in the right figure of figure 4.9(d)). This is due to shear associated with flow separation ahead of the wave.

4.4.5 Turbulent Stress

In this section, we investigate wind effects on the turbulent shear stress in the turbulence closure which is defined as

$$\tau_{xz} = (\mu + \mu_t)(\frac{\partial u}{\partial z} + \frac{\partial w}{\partial x}). \tag{4.5}$$

Figure 4.10 shows the comparison of the turbulent stress τ_{xz} during wave breaking at a representative time $t\sqrt{g/D} = 20.0$ for different wind speeds $U/C = 0 - 3$. The turbulent stress τ_{xz} changes dramatically for different wind speed. In the absence of wind ($U/C = 0$), the large shear stress τ_{xz} is mainly located at the front face of the wave and near the bottom of the wave. In the presence of wind ($U/C = 1$), the shear stress τ_{xz} increases slightly as the wind is blowing at the same speed as the water wave. For $U/C = 2, 3$, the shear stress τ_{xz} at the crest of the wave increases significantly as the wind speed increases. The shear stress near the air-water interface is much higher than that in the water. With

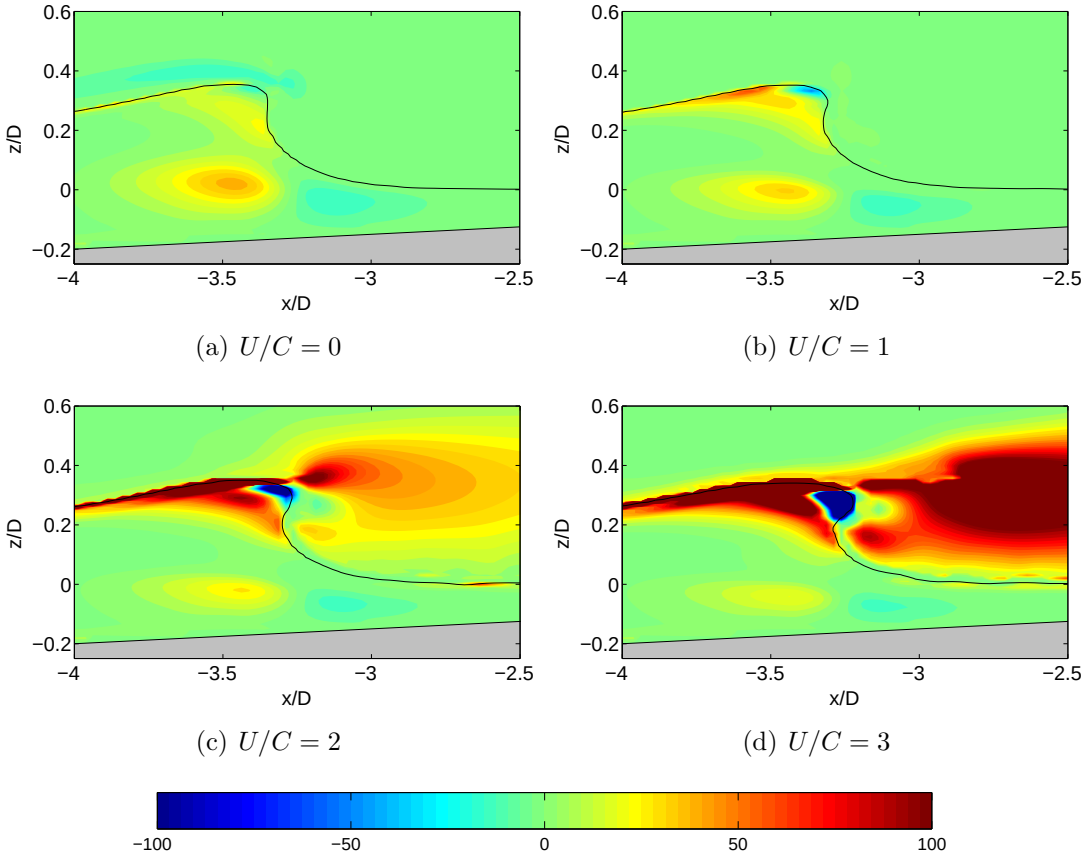

(a) $U/C = 0$ (b) $U/C = 1$

(c) $U/C = 2$ (d) $U/C = 3$

Figure 4.10: The contours of the turbulent stress τ_{xz} during wave breaking for different wind speeds $U/C = 0 - 3$ at $t\sqrt{g/D} = 20.0$. The bold line is the water surface and the turbulent stress has been normalized by $\mu^{\mathrm{w}}\sqrt{g/(D+H)}$.

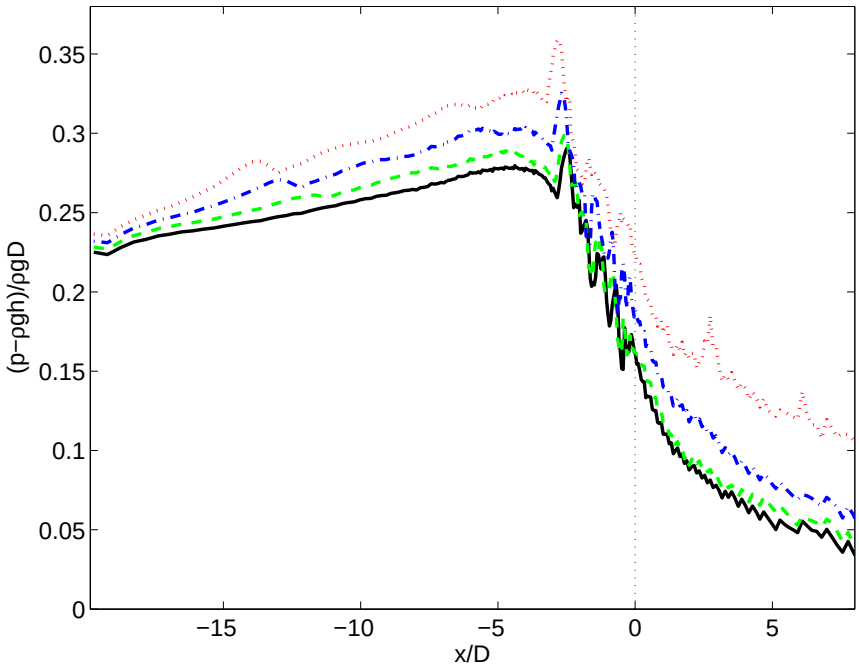

Figure 4.11: The evolution of maximum normalized wave induced pressure $(p - \rho gh)/\rho gD$ along the beach for different wind speeds: $U/C = 0$: black solid line; $U/C = 1$: green dashed line; $U/C = 2$: blue dash-dotted line; $U/C = 3$: red dotted line.

the increasing wind speed, there is a large shear layer near the air-water interface on the top of the crest of the wave as well as in the region downstream of the front of the wave. A wake is created downstream of the wave crest for high wind speeds ($U/C = 2, 3$). It can be seen from figure 4.10 that the wind has a large effect on the turbulent stress near the water surface and this accelerates the water particle velocities, generates surface currents and thus causes the wave to break earlier, which is consistent with the velocity field shown in the right column of figure 4.5 for $U/C = 2$.

4.4.6 Wave Induced Pressure Distributions On the Beach

When water waves break, they place large hydrodynamic loads on sea walls, breakwaters and other coastal structures (Peregrine, 2003). In this section, we analyze the wave induced pressure distribution on the beach, which is relevant to hydrodynamic loads and sediment transport on the beach.

Figure 4.11 shows the evolution of maximum normalized wave induced pressure $(p-\rho gh)/\rho gD$ along the beach during breaking solitary wave run-up. When compared with the water surface profiles in § 4.4.1, it can be seen that the maximum pressure occurs in the breaking region ($-5 \leq x/D \leq 0$) and located below the still water level. The higher the wind speed, the higher the maximum pressure is on the beach. With increased wind speed, the maximum wave induced pressure moves offshore, which is consistent with foregoing discussion for the water surface profile in § 4.4.1 that the wind causes the wave to break earlier and move offshore. Above the still water level, the wave induced pressure is increased by the wind due to the wind pushing breaking water waves up the beach.

4.4.7 Maximum Run-up Height

To accurately predict the maximum run-up height plays an important role in determining the design height of coastal structures (Ward *et al.*, 1998) and studying coastal effects of tsunamis (Synolakis, 1987). Previous empirical expressions for the maximum run-up height are based on the incident wave steepness H/D and the angle of the beach β, in which there is no relation with the effect of wind. In this section, we investigate the effect of wind on the maximum run-up height for breaking solitary waves.

Figure 4.12 shows the numerical results of the maximum run-up height for different wind speeds $U/C = 0 - 3$. The numerical result for the maximum run-up height when $U/C = 0$ is 0.52, which is very close to the experimental value of 0.5287 obtained by Synolakis (1986). For $U/C = 1$, the maximum run-up height increases slightly due to a weak effect of wind. For higher wind speed ($U/C = 2, 3$), the maximum run-up height increases due to increased form drag and the shear layer formed near the water surface by the wind, which is consistent with the experimental investigation of the run-up under the influence of onshore wind by Ward *et al.* (1998). The current results for the maximum run-up height nearly linearly increase with wind speeds U/C. Figure 4.12 shows that the wind has a significant effect on the maximum run-up height for solitary waves and it is suggested that the effects of wind should be taken into account in the current maximum run-up expressions in practical applications to better predict its value

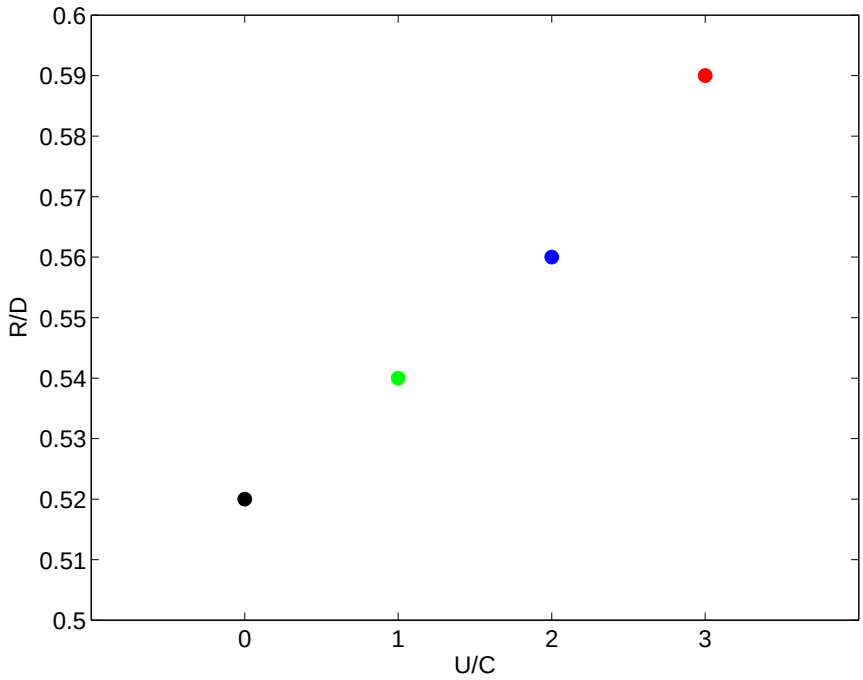

Figure 4.12: The numerical results of the maximum run-up height for different wind speeds U/C.

when the wind is present. More general relations for the maximum run-up height under the influence of wind should be studied by taking various different values for the incident wave steepness H/D, the angle of the beach β and the wind speed U/C. This relation is of much interest and it is beyond the scope of the present study.

4.4.8 The Evolution of Maximum Wave Amplitude

The evolution of maximum wave amplitude during wave shoaling is essential for nearshore hydrodynamics and has important implications for the design of coastal structures and prediction of beach morphodynamic processes. Here, we analyze the effect of wind on wave shoaling.

Figure 4.13 shows the comparison of the evolution of maximum wave amplitude for different wind speeds $U/C = 0 - 3$. In the absence of wind ($U/C = 0$), the maximum wave amplitude increases before the breaking point and decreases after the breaking point, which agrees with the experimental measurement (Syn-

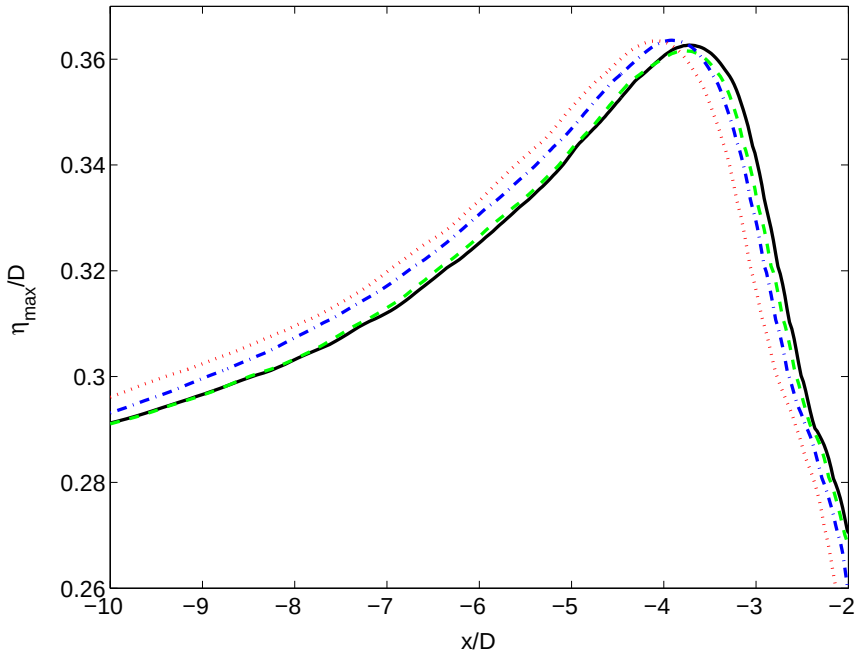

Figure 4.13: Comparison of the evolution of maximum wave amplitude for different wind speeds: $U/C = 0$: black solid line; $U/C = 1$: green dashed line; $U/C = 2$: blue dash-dotted line; $U/C = 3$: red dotted line. It is worth noting that this is the profile of the maximum wave height along the beach rather than a snapshot of the free surface profile.

olakis & Skjelbreia, 1993). In the presence of wind ($U/C = 1 - 3$), the evolution of the maximum wave amplitude changes slightly when compared with the case for $U/C = 0$. There is a phase shift for the wave amplitude transformation along the beach in figure 4.13 because the wind affects the wave shoaling and breaking processes. Higher winds lead to earlier breaking and hence the maximum wave height is located further off shore. The maximum wave height reduces slightly for $U/C = 1$ and increases slightly for $U/C = 2, 3$, thus the effect of wind on the maximum wave height is small. It is shown from figure 4.13 that the evolution of the maximum wave amplitude is altered by the presence of the wind and the obtained results for wind effects on wave shoaling are consistent with previous experiments (Douglass, 1990; Feddersen & Veron, 2005) as discussed in § 1.3.

4.4.9 Energy Dissipation

Energy loss and transfer during wave breaking play an important role in air-sea interaction and nearshore hydrodynamics. Therefore, better understanding of the energy dissipation due to wave breaking will provide more information for practical applications. In this section, we investigate the effect of wind on the energy dissipation during wave shoaling, breaking, run-up and run-down processes.

We use the kinetic energy (KE) and potential energy (PE) in the water to study the total energy (TE) dissipation. The PE considered here is the difference between the potential energy with the wave present and with no wave present. The KE, PE and TE are calculated from the whole computational domain for the wave and obtained as (Dean & Dalrymple, 1984)

$$\mathrm{KE} = \iint_{F\neq 0} \rho \frac{(u^2+w^2)}{2} \mathrm{d}z\mathrm{d}x, \tag{4.6}$$

$$\mathrm{PE} = \iint_{F\neq 0} \rho g z \mathrm{d}z\mathrm{d}x - \left[\iint_{F\neq 0} \rho g z \mathrm{d}z\mathrm{d}x\right]^{t=0}, \tag{4.7}$$

$$\mathrm{TE} = \mathrm{PE} + \mathrm{KE}. \tag{4.8}$$

Figure 4.14 shows the time history of the normalized energy for the breaking solitary wave run-up on the beach as a function of normalized time for different wind speeds $U/C = 0 - 3$. Once the solitary wave has completely entered the computational domain ($t\sqrt{g/D} = 8.0$), the volume of water is constant during the wave breaking, run-up and run-down, which means that mass is conserved during the calculation for all cases $U/C = 0 - 3$ considered here.

In the absence of wind ($U/C = 0$), it is shown from figure 4.14 that from the beginning to $t\sqrt{g/D} = 8.0$, the total energy increases as the solitary wave enters the computational domain. The total energy contribution from the kinetic energy decreases and potential energy increases as the solitary wave begins to run up the beach. From $t\sqrt{g/D} = 8.0$ to $t\sqrt{g/D} = 20.0$ before wave breaking, KE, PE and TE decrease with time as the wave shoals due to the viscous dissipation. During wave breaking from $t\sqrt{g/D} = 20.0$ to $t\sqrt{g/D} = 25.0$, the total energy decreases dramatically due to the generation of vorticity, production of turbulence and air entrainment during wave breaking. During this time, the potential energy

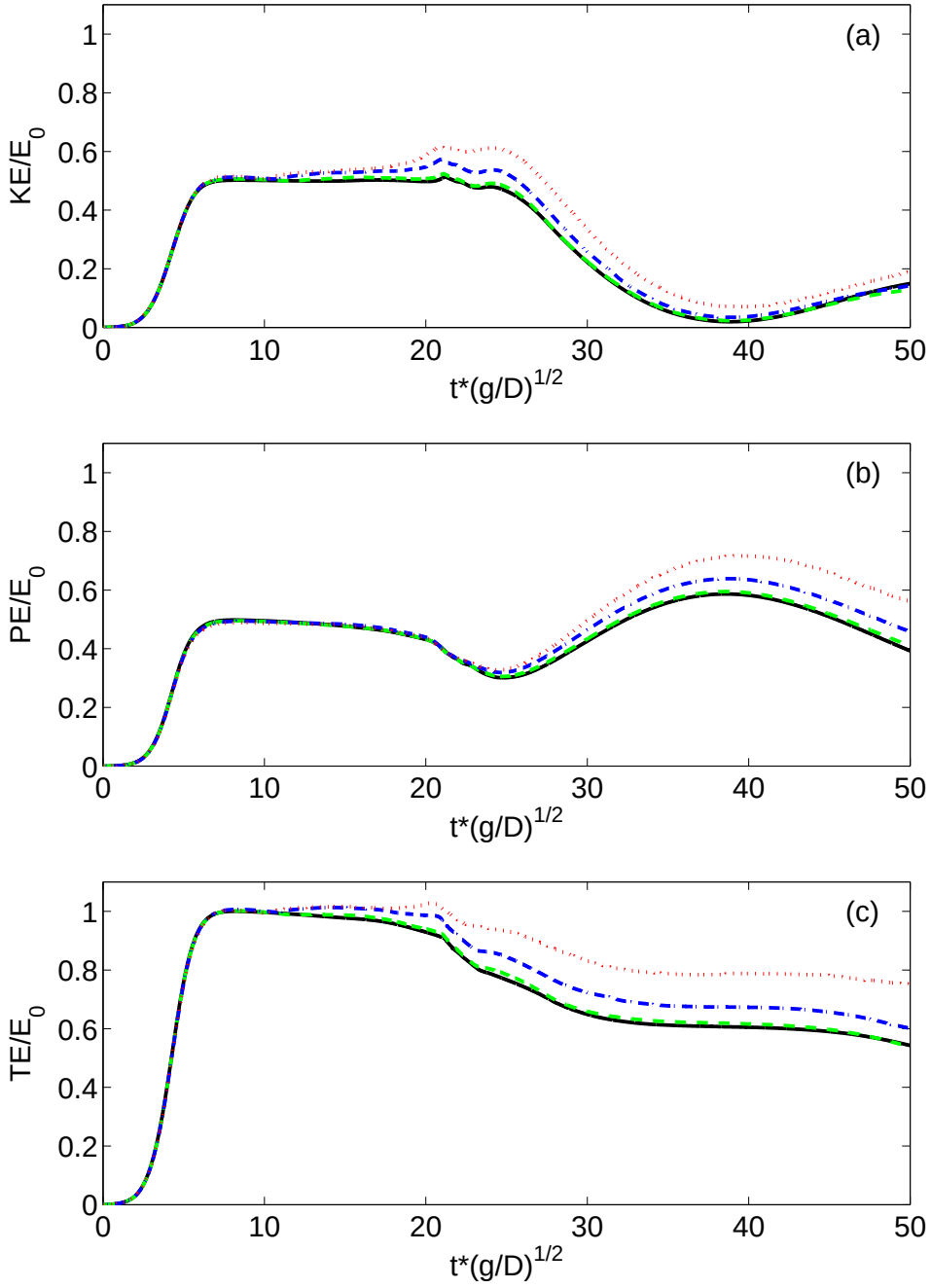

Figure 4.14: The time history of the normalized energy for the breaking solitary wave run-up on the beach as a function of normalized time for different wind speeds: $U/C = 0$: black solid line; $U/C = 1$: green dashed line; $U/C = 2$: blue dash-dotted line; $U/C = 3$: red dotted line. (a) KE, (b) PE and (c) TE. The energy has been normalized by the total energy $E_0 = [\mathrm{TE}]_{U/C=0}$ in the absence of wind ($U/C = 0$) at $t\sqrt{g/D} = 8.0$ when the solitary wave nearly completely enters the computational domain.

decreases as it has been transformed to the kinetic energy and the kinetic energy increases. After wave breaking, the wave starts to run up the beach and the total energy decreases due to the effect of viscosity and bottom friction. The kinetic energy decreases and potential energy increases as the wave runs up the beach. When the wave reaches the maximum run-up position around $t\sqrt{g/D} = 39.0$, the potential energy reaches its maximum value and the kinetic energy reaches its minimum value. After this point, the wave starts to run down and potential energy is converted back to kinetic energy. Li & Raichlen (2002) investigated a breaking solitary wave run-up with $H/D = 0.30$ on a 1:15 slope using the shallow water equations. The present result of energy dissipation for $U/C = 0$ is similar to their results (see figure 14 in Li & Raichlen, 2002).

It can be seen from figure 4.14 that the wind has a significant effect on the energy dissipation and transformation. The kinetic energy KE (see figure 4.14(a)), from the beginning to $t\sqrt{g/D} = 8.0$, has little dependence on the wind speeds U/C as the solitary wave just completely enters the computational domain. From $t\sqrt{g/D} = 8.0$ to $t\sqrt{g/D} = 20.0$ during wave shoaling, the KE decreases with time for $U/C = 0, 1$ due to the viscous dissipation. As the wind speed increases to $U/C = 2, 3$, the KE increases with time during wave shoaling. This is mainly caused by the wind induced surface currents and shear layer near the water surface. From $t\sqrt{g/D} = 20.0$ to $t\sqrt{g/D} = 25.0$ during wave breaking, the KE for all cases U/C reaches its maximum value when the plunging jet strikes the water surface. After that, the KE decreases. It is worth pointing out that the maximum value occurs earlier as U/C increases, as the wind causes the wave to break earlier. Up to this stage, the difference in KE between different wind speeds U/C is largest and we can see that the wind affects the KE significantly during wave shoaling and breaking. During wave run-up and run-down (after $t\sqrt{g/D} = 25.0$), the difference in KE between different wind speeds U/C becomes smaller and the KE for all cases U/C reaches its minimum value at the maximum run-up. After that, the KE increases as the PE is converted back to the KE during run-down.

The potential energy PE (see figure 4.14(b)), from the beginning to $t\sqrt{g/D} = 8.0$, has little dependence on the wind speeds U/C, which is similar to the KE. From $t\sqrt{g/D} = 8.0$ to $t\sqrt{g/D} = 20.0$ during wave shoaling, the PE decreases with time due to the viscous dissipation. From $t\sqrt{g/D} = 20.0$ to $t\sqrt{g/D} = 25.0$

during wave breaking, the PE decreases and reaches its minimum value for all cases U/C. It is worth pointing out that the PE for all wind speeds U/C comes to a common minimum value after the plunging jet strikes the water surface. This may be attributed to the similarity of the plunging breakers which means that the wind has only a small effect on the shape of breaking waves. After that minimum value, the difference in PE between different wind speeds U/C becomes bigger. During wave run-up and run-down (after $t\sqrt{g/D} = 25.0$), it can be clearly seen from figure 4.14(b) that the wind has a significant effect on the PE and the difference in PE between different wind speeds U/C increases with time. The PE for all cases U/C reaches its maximum value at the maximum run-up and then decreases as the wave runs down the beach.

It is shown in figure 4.14(a,b) that in the presence of wind, both the kinetic energy and the potential energy increase monotonically as U/C increases. The energy transformation between the kinetic energy and potential energy is similar to the case in the absence of wind. However, the kinetic energy increases more than the potential energy during wave shoaling and breaking because wind inputs energy to the wave through increasing KE to accelerate the water, and the potential energy increases more than the kinetic energy during wave run-up and run-down because there is more KE converted back to PE and there is some small additional acceleration by the form drag. In the whole process, compared to the value in the absence of wind, the total energy TE (see figure 4.14(c)) increases about 2%, 6% and 12% due to the presence of the wind for $U/C = 1$, $U/C = 2$ and $U/C = 3$, respectively.

4.5 Concluding Remarks

Previous studies have not considered the effect of wind on breaking solitary waves and not presented such detailed results, in this chapter the RANS model is utilized to investigate 2D breaking solitary waves on a sloping beach. In the absence of wind, the computed water surface profiles are in agreement with previous experiments.

Later, breaking solitary waves under the influence of wind are investigated. All detailed information for water surface profiles, velocity distributions, pressure

distributions and drag force, vorticity generation, turbulent stress, wave induced pressure distributions on the beach, maximum run-up, evolution of maximum wave height and energy dissipation are presented and discussed.

Chapter 5

Two-Dimensional Periodic Breaking Waves

In the nearshore region and engineering applications, most waves are irregular breaking waves, classified as spilling or plunging breakers. These waves play an important role in sediment transport in the surf zone and hence are the subject of this chapter.

In this chapter, different models and numerical methods for simulating periodic breaking waves in the surf zone are discussed first. The RANS model is then further used to study spilling and plunging breakers on a sloping beach. In the absence of wind, the numerical results are compared with experimental measurements, as well as other previous numerical studies. After that, detailed wind effects on periodic breaking waves are presented and discussed.

5.1 Introduction

Several experimental investigations of periodic breaking waves in the surf zone (shown in figure 5.1) have been carried out (as discussed in § 1.2.2). Both spilling and plunging breakers were investigated on a 1:35 sloping beach and the details of the water surface elevation, mean flow field and turbulence were presented in Ting & Kirby (1994, 1995, 1996). They found that the turbulence level and vertical variations of undertow and turbulence intensity are different for spilling and plunging breakers, which are associated with the mechanism for sediment

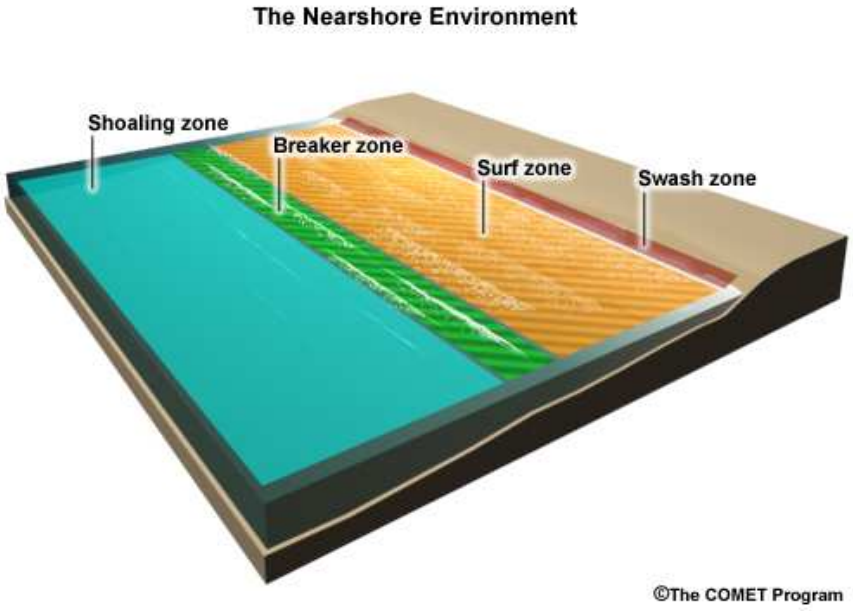

Figure 5.1: Illustration of the nearshore environment. (The source of this material is the COMET® Website at http://meted.ucar.edu/ of the University Corporation for Atmospheric Research (UCAR), sponsored in part through cooperative agreement(s) with the National Oceanic and Atmospheric Administration (NOAA), U.S. Department of Commerce (DOC). ©1997-2010 University Corporation for Atmospheric Research. All Rights Reserved.)

transport in the surf zone. As all detailed flow information was provided, this laboratory study is considered as a benchmark problem to test the models for simulating breaking waves and turbulence in the surf zone and we will study this case in this chapter.

Many numerical models have been developed to simulate periodic breaking waves in the surf zone. One of these is the Boussinesq-type model (Lynett, 2006; Madsen *et al.*, 1997; Veeramony & Svendsen, 2000), which is widely used in the nearshore wave modelling. With developments of CFD and increases in computer power, recent models for studying free surface flows, including breaking waves, solve the Navier-Stokes equations coupled with a free surface calculation. Lemos (1992) presented the RANS model, which is based on the SOLA-VOF[1] code (Nichols *et al.*, 1980) with the standard $k-\epsilon$ turbulence model. Breaking

[1]a solution algorithm for transient fluid flow with multiple free boundaries

solitary waves and periodic breaking waves on a sloping beach were simulated, however, the numerical results were not compared to experimental data and the overturning wave was not shown in the simulations. Takikawa *et al.* (1997) investigated a plunging breaker on a slope. The RANS equations were solved by a modified SMAC (Simplified Marker and Cell) method (Amsden & Harlow, 1970) and the calculation was initialized from the FEM result to model the wave breaking process. A useful numerical model to study breaking waves in the surf zone was the COBRAS (COrnell BReaking waves And Structures) model developed by Lin & Liu (1998*a*,*b*), who combined the modification of the RIPPLE[1] code (Kothe *et al.*, 1991) with implementation of the algebraic Reynolds stress $k-\epsilon$ turbulence model. The RANS equations are solved by the two-step projection method (Chorin, 1968) in the finite difference form and the VOF method is employed to capture the water surface. Periodic breaking waves on a sloping beach were investigated and compared with the experimental measurements (Ting & Kirby, 1994, 1995, 1996). Good agreement between numerical results and experimental data was obtained in terms of water surface profiles, mean velocities and turbulent kinetic energy. The plunging jet of an overturning wave on constant water depth was computed in Lin & Liu (1998*b*). Since then, several investigations have been performed to study breaking waves in the experiment of Ting & Kirby (1994, 1995, 1996). Bradford (2000) utilized the commercial software FLOW-3D to investigate spilling and plunging breaking waves in the surf zone and compared with the experimental measurements (Ting & Kirby, 1994, 1995, 1996). A comparison of the numerical results obtained by different turbulence models was made, and detailed water surface elevation, time averaged fields for the velocities and turbulence were analyzed. It was found that the location of initial wave breaking is sensitive to the representation of waves from the inlet boundary. In addition, the model has difficulty in capturing the plunging jet, which may be attributed to a lack of spatial resolution or the VOF scheme used. Comparison between different turbulence models indicated that a one equation turbulence model is inadequate to get good results, and the RNG (Re-Normalized Group) turbulence model predicts lower turbulence intensities in the outer surf zone compared to the $k-\epsilon$ model. Mayer & Madsen (2000) investigated spilling

[1] a computer program for incompressible flows with free surfaces

breakers (Ting & Kirby, 1996) by solving the RANS equations with the $k-\omega$ turbulence model. A surface tracking approach and a VOF method were employed to model the interface and it was shown that the VOF method gives better results. Zhao *et al.* (2004) performed a numerical simulation of periodic breaking waves. The space filtered Navier–Stokes equations with a multi-scale turbulence model were proposed and solved by the finite difference approach. Improved agreement with experimental measurements was obtained in terms of water surface elevations, wave height distribution and mean velocities when compared to the RANS models (Bradford, 2000; Lin & Liu, 1998*a*). In addition, it was found that turbulent production is mainly located at the front of the wave whereas turbulent dissipation is mainly located at the rear face of the wave. Similar to Bradford (2000), the plunging jet was not captured in the plunging breaker case because the air entrainment was not taken into account as indicated by Zhao *et al.*, but the plunging jet of an overturning wave was presented in that paper. Shao (2006) presented the simulation of both spilling and plunging breaking waves by the SPH method coupled with the $k-\epsilon$ model and later extended with the LES Smagorinsky model (Shao & Ji, 2006). The curling forward of the plunging jet was captured by the SPH method and it was shown that the SPH method provides a useful tool to investigate surf zone dynamics. Hsieh *et al.* (2008) solved the RANS model with the VOF and embedding methods to simulate spilling breaking waves. More recently, Bakhtyar *et al.* (2009) employed the RANS equations with the standard $k-\epsilon$ turbulence model to investigate the turbulent flow in the surf and swash zones. Good agreement for the undertow between numerical results and experimental data was obtained for spilling and plunging breakers, however, the obtained turbulence intensity was much higher than experimental measurements and the plunging jet was not shown. It is worth remarking that all the models discussed above are based on one-phase flow, in which only the flow in the water is considered in the computation. In order to take the air into account for wave breaking, two-phase flow models are developed, in which both flows in the air and the water are solved. Hieu *et al.* (2004) developed a two-phase flow model to investigate two-dimensional breaking waves in the surf zone. The sub-grid scale Smagorinsky model, which is similar to the large eddy simulation, is employed to get the turbulent eddy viscosity. Spilling breaking waves

are considered in that paper and compared with the experiment of Ting & Kirby (1996). Wang *et al.* (2009*b*) performed a two-dimensional DNS study of spilling breaking waves in the surf zone. A mass conservative level set method was used for capturing the air-water interface and the solver was based on a curvilinear coordinate system. There are also some attempts for 3D large eddy simulation of breaking waves (Christensen & Deigaard, 2001; Lubin *et al.*, 2006; Watanabe *et al.*, 2005), and Christensen (2006) presented the 3D simulation of spilling and plunging breakers in the surf zone. It was found that the modelled mean velocity field is in good agreement with experimental data of Ting & Kirby (1994, 1995, 1996) but the model predicts higher turbulence intensities. Earlier breaking in spilling breakers and later breaking in plunging breakers were found in the simulation when compared to experimental measurements. Christensen indicated that the reason might be due to the coarse resolution or the effect of the air.

However, wind effects on periodic breaking waves in the surf zone have received less attention in previous studies. Therefore, the objective of this chapter is to investigate wind effects on periodic breaking waves. First, we calculate spilling and plunging breaking waves on a 1:35 sloping beach in the absence of wind, and compare with the experimental measurements (Ting & Kirby, 1994, 1995, 1996) and other published results. Then, computational results for breaking waves under the influence of wind are presented and discussed.

5.2 Computational Setup

5.2.1 Geometry

A sketch of the laboratory setup (Ting & Kirby, 1994) and the computational domain are shown in figure 5.2, where the origin of the coordinates is located at the still water level at which the local still water depth is 0.38 m, x and z are the horizontal and vertical coordinates respectively, H is the wave height, $d_0 = 0.4$ m is the water depth in the horizontal region, $\zeta(x)$ is the water surface elevation, $\overline{\zeta}(x)$ is the mean water surface elevation, $d(x)$ is the local still water depth, and $h(x) = d(x) + \overline{\zeta}(x)$ is the local mean water depth.

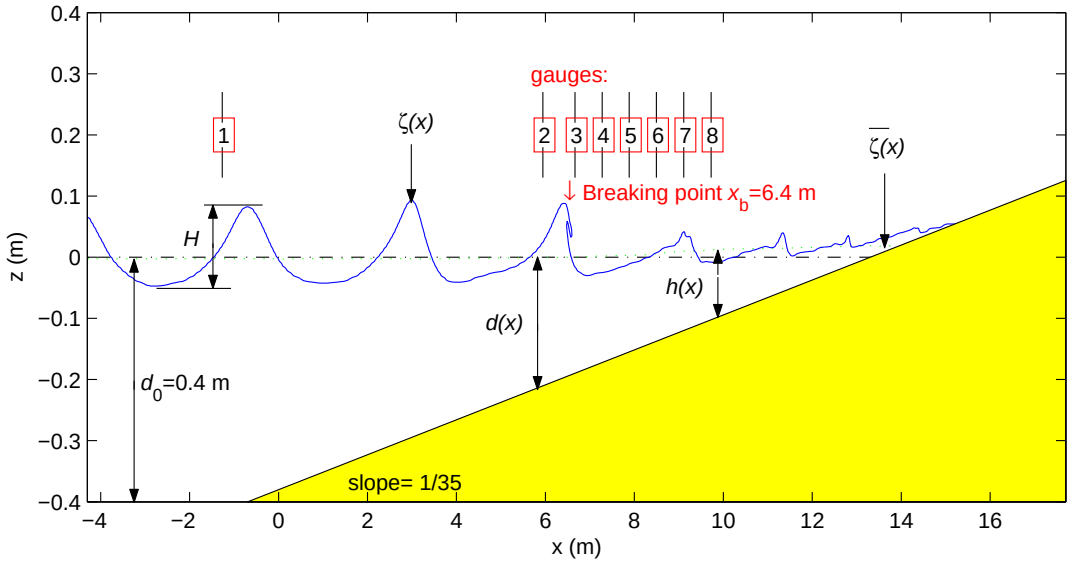

(a) spilling breaking waves

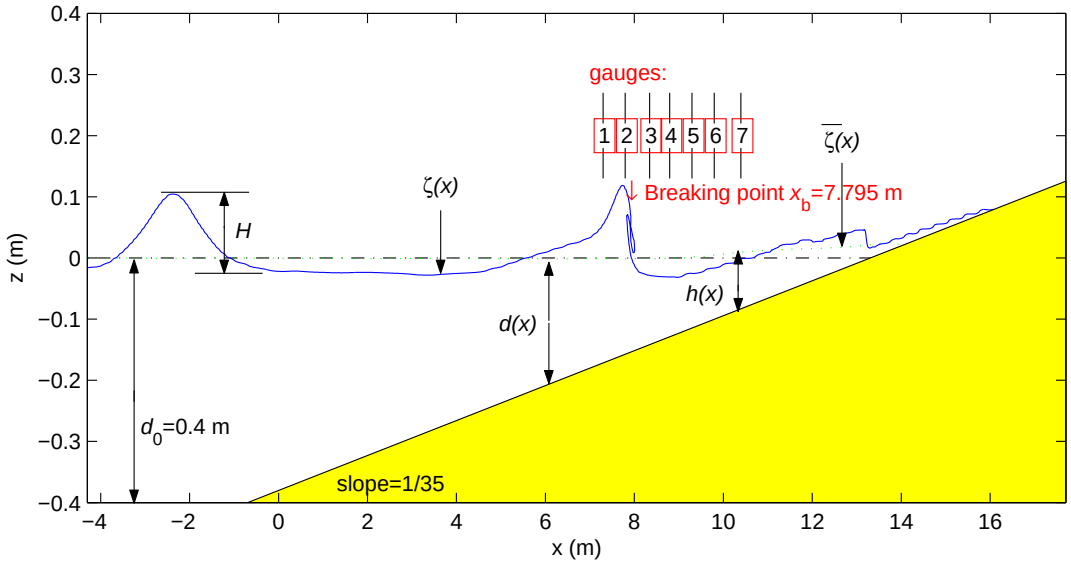

(b) plunging breaking waves

Figure 5.2: Sketch of experimental setup and computational domain for periodic breaking waves in the surf zone. The boxes are the location of wave gauges in the experiment.

5.2.2 Governing Equations

The governing equations used for this study are the Reynolds-averaged Navier–Stokes equations (as discussed in § 3.1) and the standard $k-\epsilon$ turbulence model (3.16-3.17).

5.2.3 Computational Parameters

In the simulation, the computational setup is the same as the laboratory setup, except that we use the analytical solution to generate the cnoidal wave at the inlet. The computational domain (started from $x = -4.3$ m) is 22 m long and 0.8 m high, and it is discretized by a uniform grid with $\Delta x = 0.02$ m and $\Delta z = 0.008$ m, which is similar to that of Zhao *et al.* (2004) and Bradford (2000). The computation is run up to 50 s for spilling breakers and 60 s for plunging breakers, and the period of the last five waves are used to obtain the mean value for the analysis. The CPU time is approximately 10h on a PC (Intel® Pentium® D CPU 3.40GHz, 2GB RAM). Table 5.1 shows the wave conditions for the spilling and plunging breakers in the experiment, where T is the wave period, H_0 and L_0 are the wave height and wave length in deep water, and x_b and d_b are the location and water depth of wave breaking.

Table 5.1: Wave conditions in the experiment of Ting & Kirby (1994)

Breaker type	H_0 (m)	H (m)	T (s)	H_0/L_0	x_b (m)	d_b (m)
Spilling	0.127	0.125	2.0	0.02	6.400	0.196
Plunging	0.089	0.128	5.0	0.0023	7.795	0.156

the subscripts 0 and b denote deep water and breaking point

5.2.4 Initial and Boundary Conditions

Boundary conditions

At the inlet, the cnoidal wave is generated by specifying the water surface elevation and water particle velocities based on the third-order cnoidal wave theory

(Horikawa, 1988) as

$$\begin{aligned}
\zeta(x,t) &= d_0 \sum_{n=0}^{3} A_n \mathrm{cn}^{2n}\left[2K\left(\frac{x}{L}-\frac{t}{T}\right)\right], \\
u(x,z,t) &= \sqrt{gd_0}\sum_{n=0}^{3}\sum_{m=0}^{2} B_{nm}\left(\frac{d_0+z}{d_0}\right)^{2m} \mathrm{cn}^{2n}\left[2K\left(\frac{x}{L}-\frac{t}{T}\right)\right], \\
w(x,z,t) &= \sqrt{gd_0}\cdot \mathrm{sn}\left[2K\left(\frac{x}{L}-\frac{t}{T}\right)\right]\cdot \mathrm{dn}\left[2K\left(\frac{x}{L}-\frac{t}{T}\right)\right] \\
&\quad \times \frac{4Kd_0}{L}\sum_{n=1}^{3}\sum_{m=0}^{2}\frac{n}{2m+1}B_{nm}\left(\frac{d_0+z}{d_0}\right)^{2m+1} \mathrm{cn}^{2n-1}\left[2K\left(\frac{x}{L}-\frac{t}{T}\right)\right].
\end{aligned} \tag{5.1}$$

In the above equations, cn, sn, and dn are Jacobian elliptic functions, and K is the complete elliptic integrals of the first kind. The details of the coefficients A_n and B_{nm} are given in Appendix A.

The effect of wind is obtained by specifying an uniform wind speed above $z = 0.1$ m at the inlet. For clarity, only the onshore wind $U/C = 2$ is considered to investigate the wind effects on periodic breaking waves in this study.

Following Lin & Liu (1998*a*), the turbulent kinetic energy is obtained as $k = \frac{1}{2}(I \times C)^2$, where $I = 0.0025$ is the turbulent intensity and the turbulent eddy dissipation is adjusted so the turbulent eddy viscosity is ten percent of the dynamic viscosity of each fluid at the inlet.

The no-slip wall boundary condition is applied at the sloping beach and the top of the domain, while open boundary conditions are applied at the outlet of the computational domain (described in § 3.2.1).

Initial conditions

At $t = 0$, the water surface is given as the initial still water depth, the velocity field is initialized as zero, the pressure distribution in the whole domain is hydrostatic and the turbulence field is initialized to the same value as the boundary conditions at the inlet.

5.3 2D Spilling Breaking Waves

5.3.1 Comparison of Experimental Data and Numerical Results Without Wind

Figure 5.3 shows the comparison of the computational and experimental distribution of wave amplitudes and mean water level for the spilling breaker case. The modelled results by Bradford (2000), Zhao *et al.* (2004) and Shao (2006) are also plotted in figure 5.3 for comparison. It is shown that the minimum water surface elevation is well simulated by all models when compared to experimental data. The present model predicts the mean water level accurately while Bradford (2000) slightly overestimates the wave set-up after wave breaking. In the outer surf zone, all models predict similar results for the maximum water surface elevation. In the breaking and inner surf zone, the maximum water surface elevation is well computed by the present model. However, during wave breaking, the maximum water surface elevation is underestimated by the present model when compared to experimental data, which is also observed in other RANS models (Bradford, 2000; Lin & Liu, 1998*a*). On the contrary, it is noticed that the maximum water surface elevation is slightly overestimated in the breaking and inner surf zone by the multi-scale turbulence model of Zhao *et al.* (2004). The SPH method (Shao, 2006) predicts the shape of maximum water surface elevation well, but with a slight phase shift which predicts the breaking point later.

In the surf zone, since waves have shoreward net volume flux, then according to mass conservation there must also be a seaward going current, which is called the undertow (Svendsen, 2005). Figure 5.4(a) shows the comparison of the computational and experimental variation of time-mean horizontal velocity with depth. After wave breaking ($x = 6.665 - 8.495$ m), the present model reasonably predicts the vertical structure of the undertow in comparison with the experimental data. It is noticed that Bradford (2000) generally underestimated the undertow after wave breaking compared to experimental data. Shao (2006) obtained improved results for the vertical structure of the undertow. Zhao *et al.* (2004) got better results near the trough level but slightly underestimated the undertow near the bottom while the present model predicts better results near

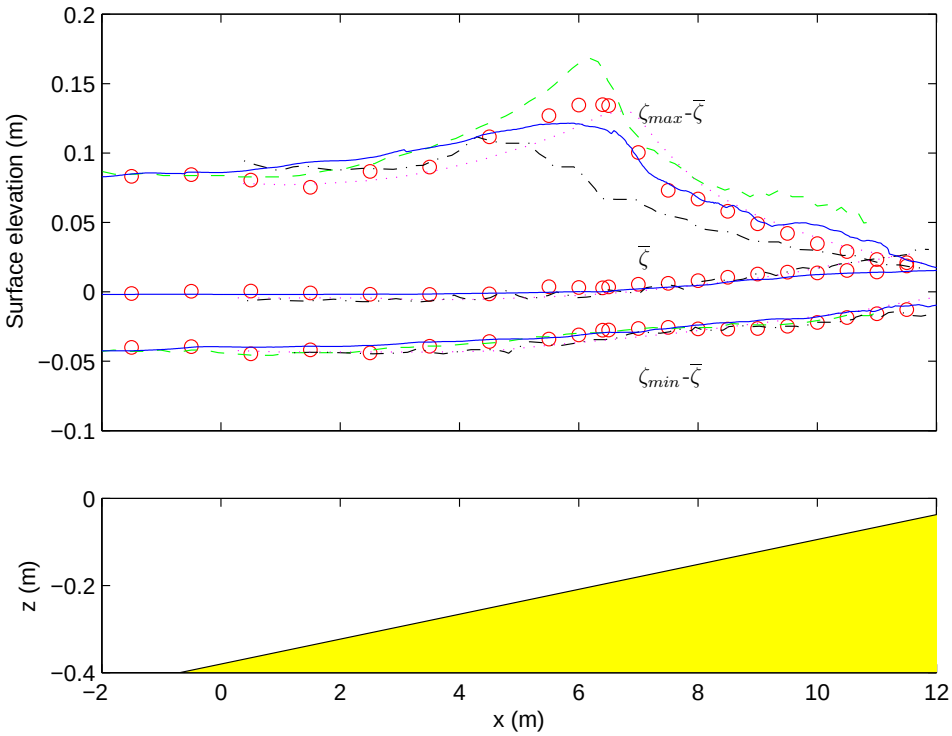

Figure 5.3: Comparison of the computational and experimental distribution of wave amplitudes and mean water level for the spilling breaker case. Red circles are experimental data (Ting & Kirby, 1994); blue solid lines are the present results; green dashed lines are the results by Zhao *et al.* (2004); black dash-dotted lines are the results by Bradford (2000); magenta dotted lines are the results by Shao (2006).

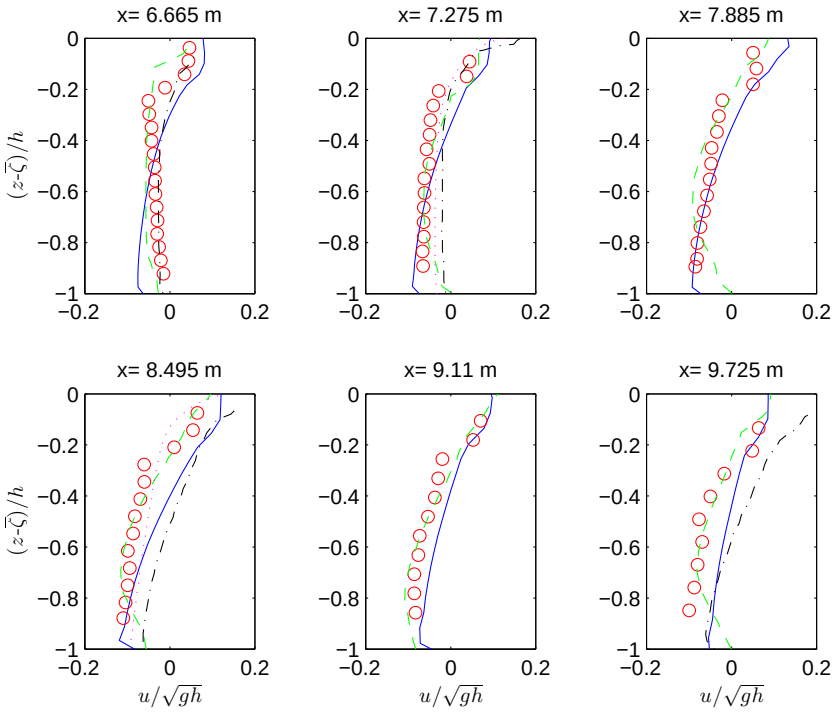

(a) undertow

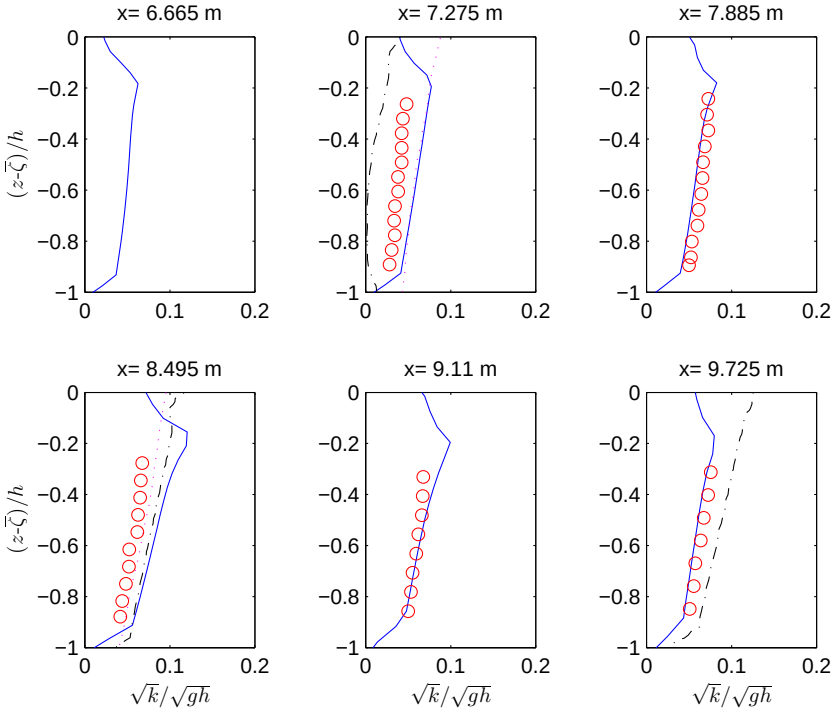

(b) turbulence intensity

Figure 5.4: Comparison of the undertow and turbulence intensity with experimental measurements and other models for the spilling breaker case. For caption see figure 5.3.

the bottom but slightly underestimates the undertow near the trough level when compared to experimental data. After wave breaking, there is air entrainment near the trough and also some bubbles, this strong mixing of two-phase flow could be one reason why our model slightly underestimates the undertow structure. In the bore region ($x = 9.11 - 9.725$ m), all models slightly underestimate the undertow near the bottom while Zhao *et al.* (2004) predicted better results near the water surface. Overall, the present model predicts reasonable vertical structure of the undertow in comparison with the experimental data and is also similar to previous numerical studies.

Figure 5.4(b) shows the comparison of the computational and experimental variation of time-mean turbulent kinetic energy with depth. It is worth remarking that only the computed turbulent kinetic energy in the water is considered here, which is the turbulent kinetic energy times the corresponding value of the volume fraction. As the turbulence was not presented in Zhao *et al.* (2004), only the results in Bradford (2000) and Shao (2006) are included for comparison. The turbulence is weak in the outer surf zone as the turbulence is primarily originated from the breaker. Once the wave breaks, the turbulence intensities increase gradually in the onshore direction and vary slowly with the water depth which is consistent with experimental measurements (Ting & Kirby, 1994). After wave breaking ($x = 7.275$ m), the present model matches with most part of SPH results by Shao (2006) and both slightly overestimate the turbulence level, while the RNG model in Bradford (2000) underestimated the value when compared to experimental data. At $x = 7.885$ m, the present model predicts the turbulence intensity well. At $x = 8.495$ m, all models slightly overestimate the turbulence level and the SPH method provides the best result. In the bore region ($x = 9.11 - 9.725$ m), good agreement between the present model and experimental measurements is obtained while Bradford (2000) slightly overestimated the turbulence level. In general, the present model predicts reasonable turbulence intensities in comparison with the experimental data, and is similar to previous numerical investigations.

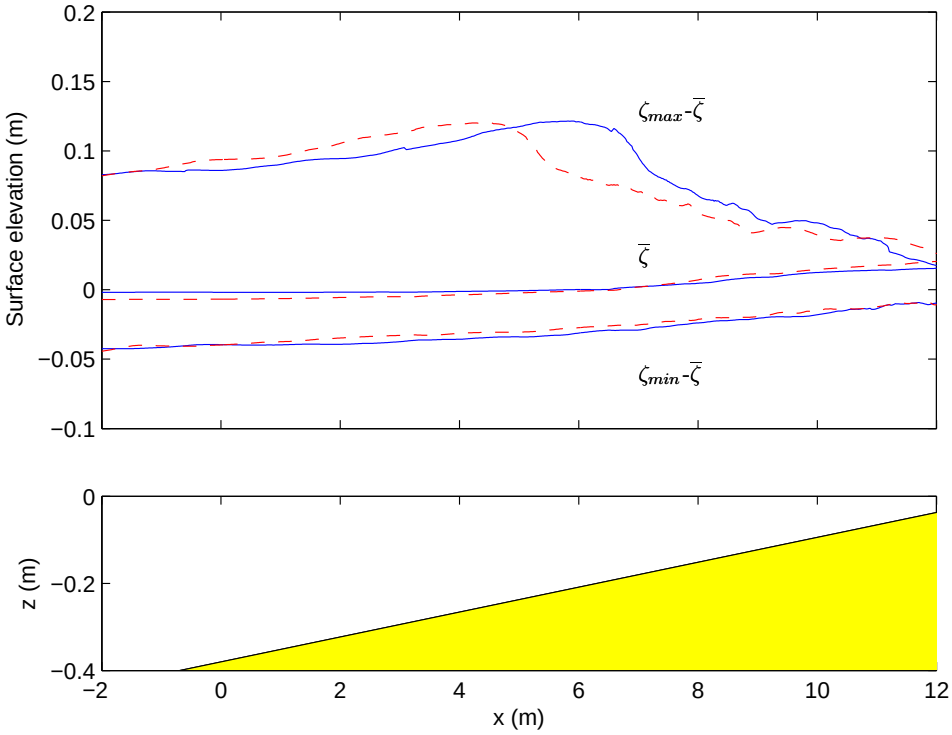

Figure 5.5: Wind effects on the distribution of wave amplitudes and mean water level for the spilling breaker case. Blue solid lines: $U/C = 0$; red dashed lines: $U/C = 2$.

5.3.2 Spilling Breaking Waves under the Influence of Wind

In this study, the effect of the onshore wind with speed $U/C = 2$ on spilling breaking waves is investigated although the offshore wind effect can be obtained in a similar way. The simulations are run up to 50 s and the result in the last wave period is used for the analysis and comparison.

Figure 5.5 shows the wind effects on the distribution of wave amplitudes and mean water level. During wave shoaling, the maximum wave elevation increases in the presence of wind while there is a slight change of the slope for the minimum wave elevation. In the presence of wind, the wind transfers energy to the waves by means of wind-induced form drag and shear stress, which are the contribution for the increase of the maximum wave elevation. During wave breaking, it can be seen from figure 5.5 that the wave breaks earlier and further from shore in

the presence of wind, which is consistent with the previous laboratory studies by Douglass (1990) and King & Baker (1996). This is attributed to the direct push of the wind and the increased kinetic energy obtained from the wind in water waves. The water particle velocity is increased by the wind and thus the wave breaks earlier. This phenomenon is also observed in the study of wind effects on breaking solitary waves in Chapter 4. After wave breaking in the bore region, the wind has little effect on the crest and trough level of the wave. It is shown from figure 5.5 that the mean water level has been changed by the wind. In the surf zone, the radiation stress (Longuet-Higgins & Stewart, 1962) increases before the breaking point due to the decreasing water depth, and decreases after the breaking point due to the energy dissipation. Therefore, through the horizontal momentum flux balance, the slope of the mean water level, namely, the wave set-up and set-down, are related to the change of radiation stress across the surf zone (Sorensen, 2006). In the presence of wind, the slope of the mean water level increases in comparison with the case in the absence of wind, which is attributed to wind forcing.

Figure 5.6 shows the velocity fields for the spilling breaker when $U/C = 0$ in one wave period at $t/T = 0.0, 0.1, 0.2, 0.4$, where $t/T = 0.0$ corresponding to when the wave is close to the breaking point. At $t/T = 0.0$, the front of the wave becomes nearly vertical and the velocity in the water is slightly smaller than the wave phase speed. A recirculation of air flow can be easily seen on the top of the wave as the air is driven by the wave motion. During wave breaking at $t/T = 0.1$, an overturning jet is formed at the front face of the wave with increasing velocity in the water. It is shown that the maximum velocity in the water is nearly horizontal and located on the tip of the overturning jet. During wave curling down at $t/T = 0.2$, large velocities are produced in front of the overturning jet as the air is pushed by the wave. At $t/T = 0.4$, it can be seen that the overturning jet spills down the front face of the wave and large velocities are observed in that region. It is noted that the present model is capable of producing the spilling breaker which has rarely been shown in previous studies.

Figure 5.7 shows the velocity fields for the spilling breaker when $U/C = 2$ in one wave period at $t/T = 0.0, 0.1, 0.2, 0.4$. The air flow has been changed significantly due to wind forcing. The recirculation of air flow does not exist with

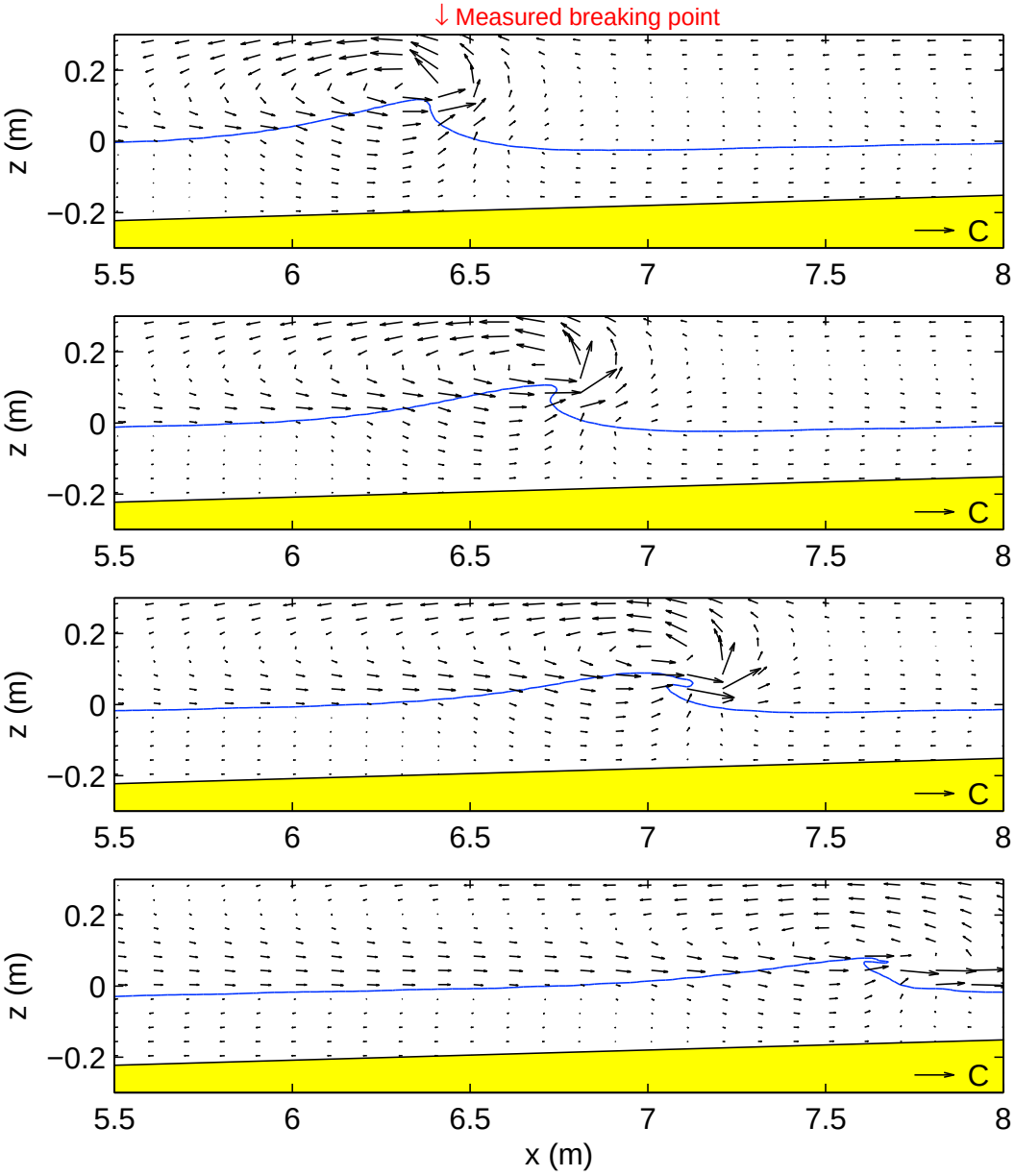

Figure 5.6: Velocity fields during wave breaking for the spilling breaker case when $U/C = 0$ at $t/T = 0.0, 0.1, 0.2, 0.4$. Velocities are normalized by the wave phase speed C.

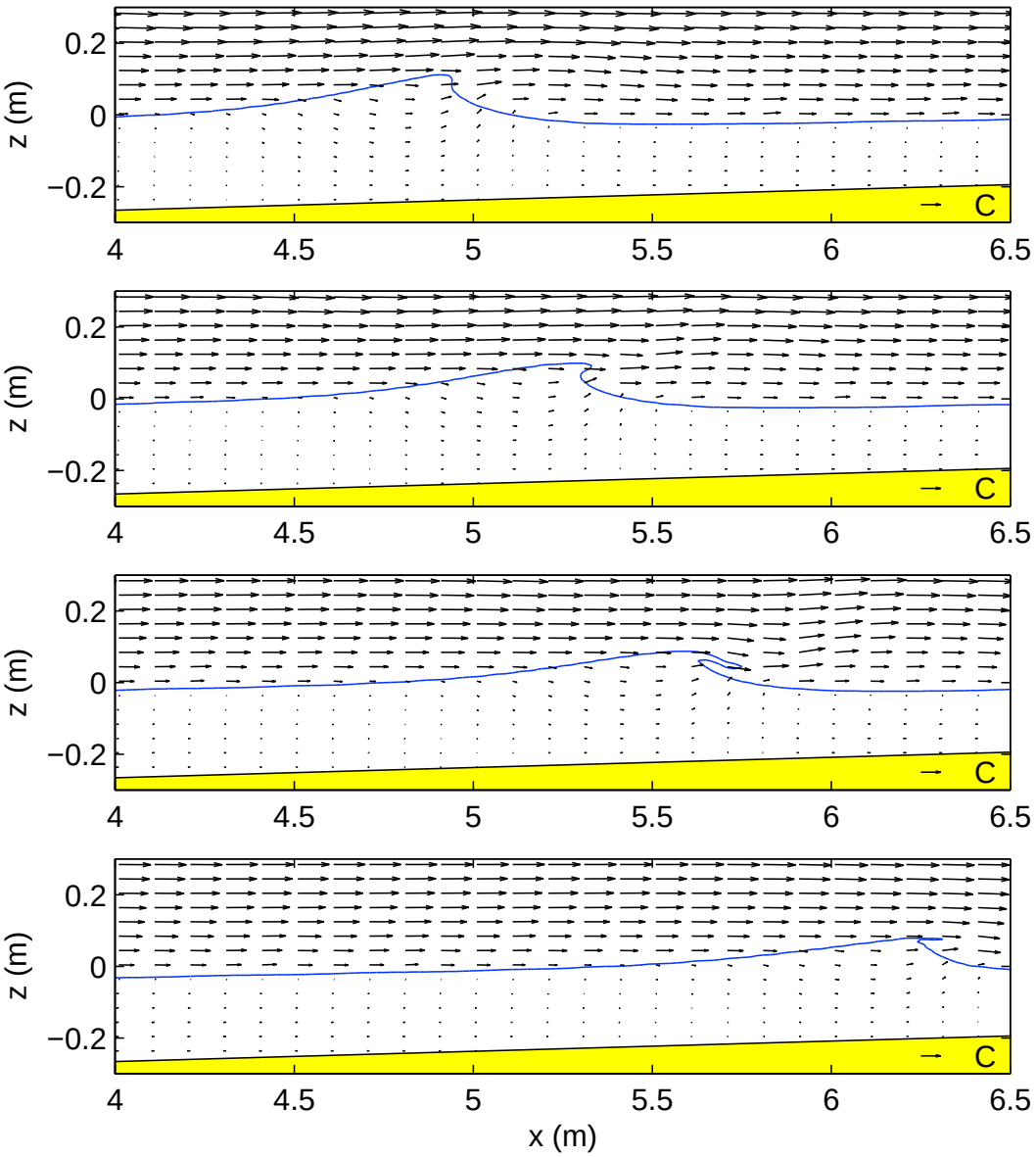

Figure 5.7: Velocity fields during wave breaking for the spilling breaker case when $U/C = 2$ at $t/T = 0.0, 0.1, 0.2, 0.4$. Velocities are normalized by the wave phase speed C.

all air moving onshore instead. It is worth remarking that the wave is driven by the wind when $U/C = 2$ while the air is driven by the wave when $U/C = 0$. The wave breaking process is similar to the case for $U/C = 0$, but the location of the breaking point has been changed significantly. The breaking point is about $x_b = 6.4$ m for $U/C = 0$ but $x_b = 4.95$ m for $U/C = 2$. It is shown that under the influence of wind, the wave breaks in deeper water and further from shore which is consistent with the previous laboratory studies by Douglass (1990) and King & Baker (1996).

Figure 5.8 shows the mean vorticity fields for the spilling breaker when $U/C = 0$ in one wave period at $t/T = 0.0, 0.1, 0.2, 0.4$. The vorticity in the water has a smaller value in comparison with the vorticity in the air. Close to wave breaking ($t = 0.0$), only small negative vorticity is observed near the front face of the wave, which is consistent with experiment where the vortices are initially generated in the wave front due to surface rollers (Ting & Kirby, 1994). Large positive vorticity can be seen above the wave crest due to the recirculation of air flow. During wave breaking ($t/T = 0.1 - 0.4$), the region of negative vorticity in the water increases and spreads above the trough region of the breaker. The vorticity is confined to the region near the water surface and the bottom which means that the vertical mixing is weak in spilling breakers. In the air, the region of positive vorticity is moving forward and a region of negative vorticity is produced near the water surface in front of the wave. This is attributed to the air flow induced by the breaking wave.

Figure 5.9 shows the mean vorticity fields for the spilling breaker when $U/C = 2$ in one wave period at $t/T = 0.0, 0.1, 0.2, 0.4$. In the air, the vorticity field is totally different from that for $U/C = 0$. There is no positive vorticity above the wave crest as the wind is moving onshore. Large negative vorticity is generated in the vicinity of the water surface due to the wind-induced shear. A small region of positive vorticity appears in front of the wave during wave breaking as the air tries to escape from the cavity. In the water, the vorticity generation during wave breaking is similar to that for $U/C = 0$, except that the wave breaks in a deeper region.

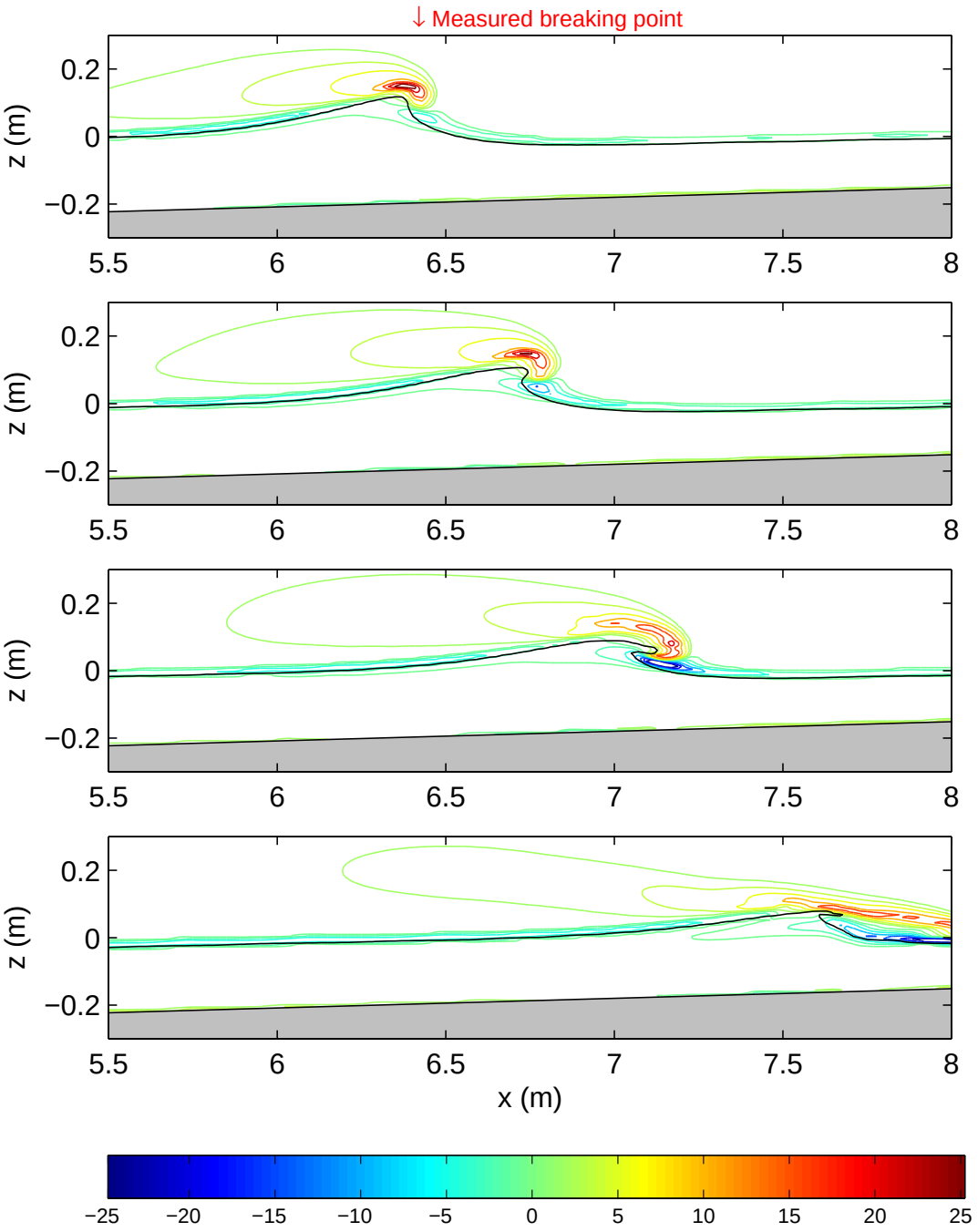

Figure 5.8: Mean vorticity fields during wave breaking for the spilling breaker case when $U/C = 0$ at $t/T = 0.0, 0.1, 0.2, 0.4$. The vorticity has been normalized by $\sqrt{g/(d_0 + a)}$ and the contours are shown for $\pm[1, 2.5, 5, 10, 15, 20, 25]$.

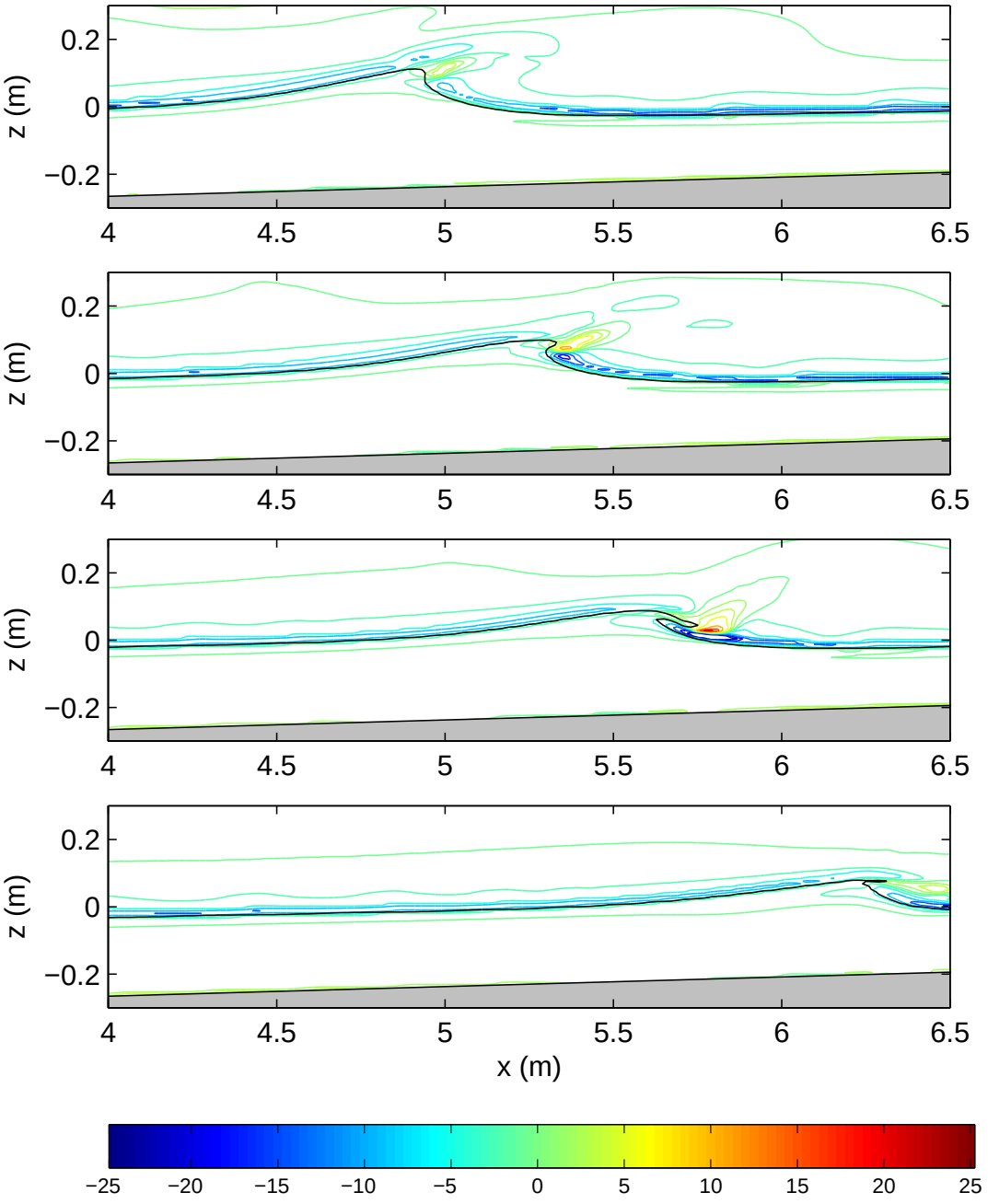

Figure 5.9: Mean vorticity fields during wave breaking for the spilling breaker case when $U/C = 2$ at $t/T = 0.0, 0.1, 0.2, 0.4$. The vorticity has been normalized by $\sqrt{g/(d_0 + a)}$ and the contours are shown for $\pm[1, 2.5, 5, 10, 15, 20, 25]$.

5.4 2D Plunging Breaking Waves

5.4.1 Comparison of Experimental Data and Numerical Results Without Wind

Figure 5.10 shows the comparison of the computational and experimental distribution of wave amplitudes and mean water level for the plunging breaker case. It is shown that the mean water level is well simulated by all models when compared to experimental data. However, differences are found in all the models considered here for the maximum and minimum water surface elevations. The present model predicts the minimum water surface elevation accurately and similar results are found in Zhao *et al.* (2004). Higher and lower trough levels when compared to the experimental data are found in Bradford (2000) and Shao (2006), respectively. In the shoaling zone, all models well predict the maximum water surface elevation, except Bradford (2000) which slightly overestimates the value. In the breaking and inner surf zone, unlike the spilling breaker case in which all models predict earlier or later breaking, it is surprising that all models predict earlier breaking in the plunging breaker case when compared to experimental measurements. The reason is unknown yet and one possibility is that there is a slight difference between the laboratory and computational setup, which will slightly change the transformation of the wave during its propagation. The maximum wave height during wave breaking is overestimated slightly in Zhao *et al.* (2004) and underestimated slightly in all other models. In the bore region, similar results are found in all models except Bradford (2000) which slightly overestimates the maximum water surface elevation after wave breaking. In general, the distribution of wave amplitudes and mean water level are reasonably predicted in the present model when compared to experimental measurements and are comparable and sometimes better than other modelling studies.

Figure 5.11(a) shows the comparison of the computational and experimental variation of time-mean horizontal velocity with depth. After wave breaking ($x = 7.795 - 8.795$ m), the present model slightly overestimates the undertow near the bottom of the beach at $x = 7.795$ m and 8.345 m and predicts the value well at $x = 8.795$ m. This is attributed to the earlier wave breaking that is predicted in

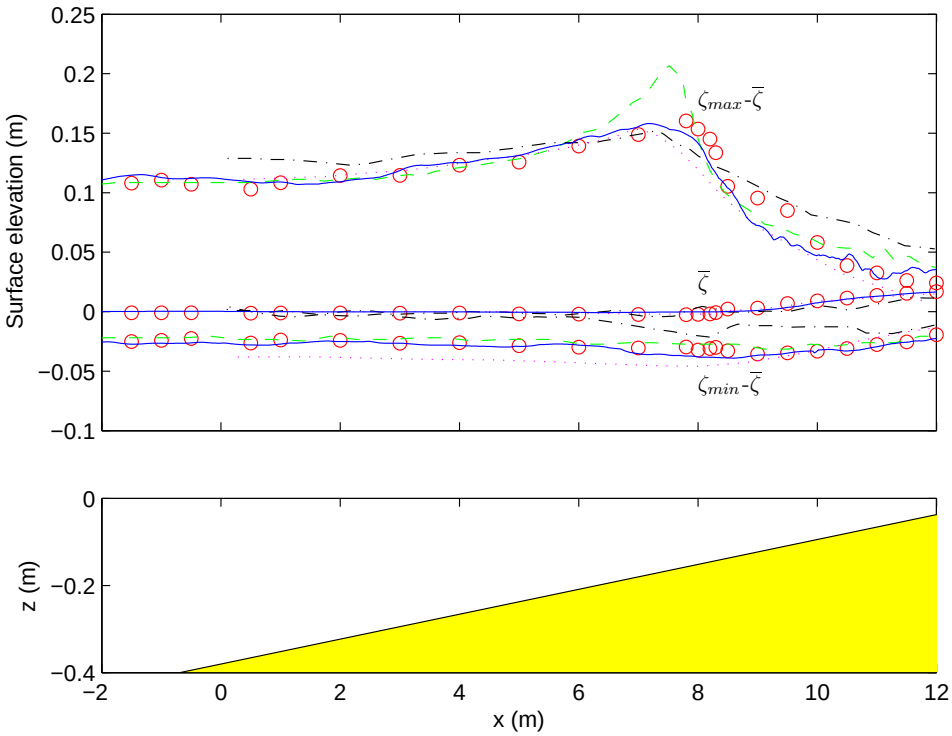

Figure 5.10: Comparison of the computational and experimental distribution of wave amplitudes and mean water level for the plunging breaker case. Red circles are experimental data (Ting & Kirby, 1994); blue solid lines are the present results; green dashed lines are the results by Zhao *et al.* (2004); black dash-dotted lines are the results by Bradford (2000); magenta dotted lines are the results by Shao (2006).

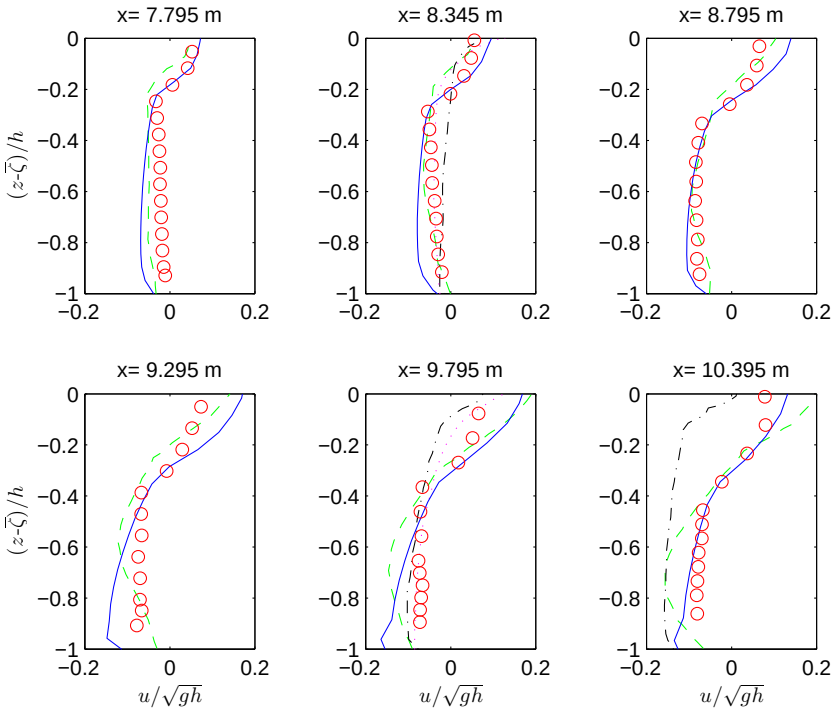

(a) undertow

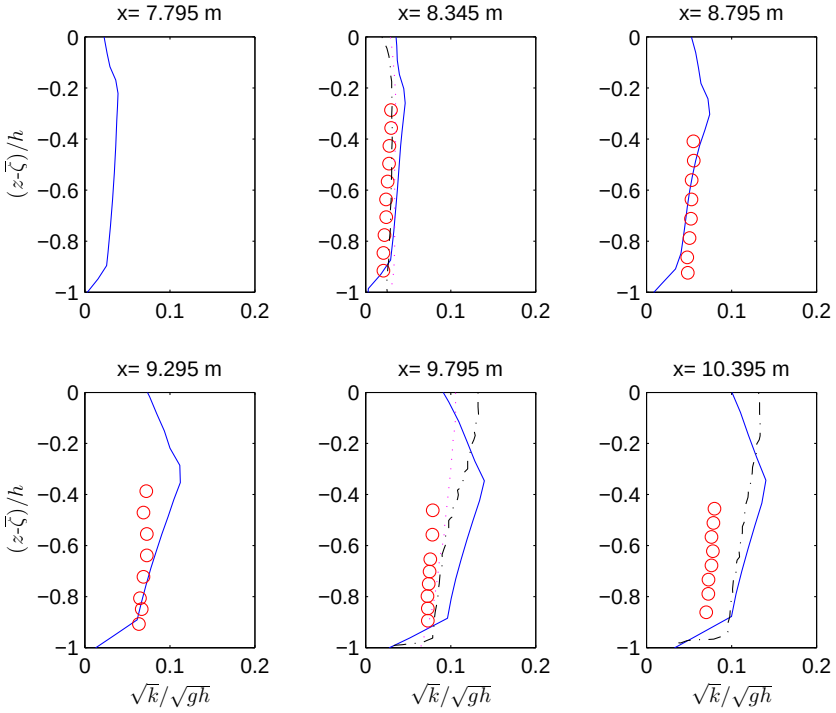

(b) turbulence intensity

Figure 5.11: Comparison of the undertow and turbulence intensity with experimental measurements and other models for the plunging breaker case. For caption see figure 5.10.

the present model, which gives higher onshore velocity near the wave trough and thus has a higher offshore velocity near the beach. It is noticed that Bradford (2000) slightly underestimated the undertow at $x = 8.345$ m. Zhao *et al.* (2004) and Shao (2006) obtained better results for the vertical structure of the undertow when compared to experimental data. In the inner surf zone ($x = 9.295$ m and 9.795 m), both the present model and Zhao *et al.* (2004) overestimate the undertow in the lower part of water. Bradford (2000) and Shao (2006) did a good job in this area after wave breaking. In the bore region ($x = 10.395$ m), the present model well predicts the structure of the undertow whereas the undertow profile was overestimated in Bradford (2000) and Zhao *et al.* (2004). In general, the present model predicts reasonable undertow in comparison with experimental data and is also similar to previous numerical studies.

Figure 5.11(b) shows the comparison of the computational and experimental variation of time-mean turbulent kinetic energy with depth. Compared to spilling breakers shown in figure 5.4(b), the vertical variation of turbulence intensity is smaller in plunging breakers as the plunging wave can penetrate into a deeper region in the water and has stronger vertical mixing, which is consistent with experimental measurements (Ting & Kirby, 1994). Just after wave breaking ($x = 8.345$ m), the present model slightly overestimates the turbulence level due to the predicted earlier breaking, while the RNG turbulence model (Bradford, 2000) and the SPH model (Shao, 2006) well predict the value. Better results are obtained by the present model at $x = 8.795$ m. In the inner surf zone and bore region ($x = 9.295 - 10.395$ m), all models overestimate the turbulence level and better results were obtained by Shao (2006) and Bradford (2000) at $x = 9.795$ m. In this region, higher turbulence intensities in comparison with experimental measurements are found in many 2D (Bakhtyar *et al.*, 2009; Bradford, 2000; Lin, 1998; Shao, 2006) and 3D (Christensen, 2006) simulations. Lin (1998) and Shao (2006) indicated the primary reason for overestimating the turbulence level near the breaking point is that the coefficients used in the turbulence model are derived from quasi-steady turbulent flows rather than oscillatory flows. Lin also discussed that this discrepancy is due to the uncertainty of the initial and inflow boundary conditions for the turbulence field, and the limitation of numerical solution, as the overturning jet is not captured during wave breaking. Christensen

et al. (2002) indicated that the overpredicted turbulence intensities are due to the stronger mixing, as the effect of air is not taken into account in their model and a large part of the production and dissipation take place in the mixture of air and water before the impingement of the overturning jet. In the present model, the turbulence intensities near the breaking point are reasonably predicted as the overturning jet is captured during wave breaking. However, the turbulence intensities are significantly overestimated in the bore region. The reason is that the turbulence production during jet-splash cycles is complicated, and the strong two-phase flow mixing and the generation of bubbles are not able to be captured in the present turbulence model, therefore the improvement of the turbulence model after wave breaking, especially during jet-splash cycles which are not considered here, is needed in the future research.

5.4.2 Plunging Breaking Waves under the Influence of Wind

Figure 5.12 shows the wind effects on the distribution of wave amplitudes and mean water level. In the whole region, there is nearly no difference for the evolution of minimum wave elevation between these two cases, while the evolution of maximum wave elevation has been changed significantly in the presence of wind, which is similar to the case for spilling breakers. It is shown from figure 5.12 that the mean water level has been changed slightly by the wind. In the presence of wind, the mean water level decreases in the shoaling region and increases in the bore region when compared to the case in the absence of wind. The driving mechanism for the change of the slope of the mean water level is similar to that discussed in the spilling breaker case (see § 5.3.2).

Figure 5.13 shows the velocity fields for the plunging breaker when $U/C = 0$ in one wave period at $t/T = 0.0, 0.05, 0.1, 0.2$, where $t/T = 0.0$ corresponding to when the wave is close to the breaking point. Compared to the spilling breaker, the flow in the air is similar as the recirculation of air flow is also observed above the wave crest. However, the flow in the water is slightly different due to the stronger breaking in the plunging breaker. At $t/T = 0.0$, the front of the wave becomes vertical and an overturning jet is formed when the wave passes the

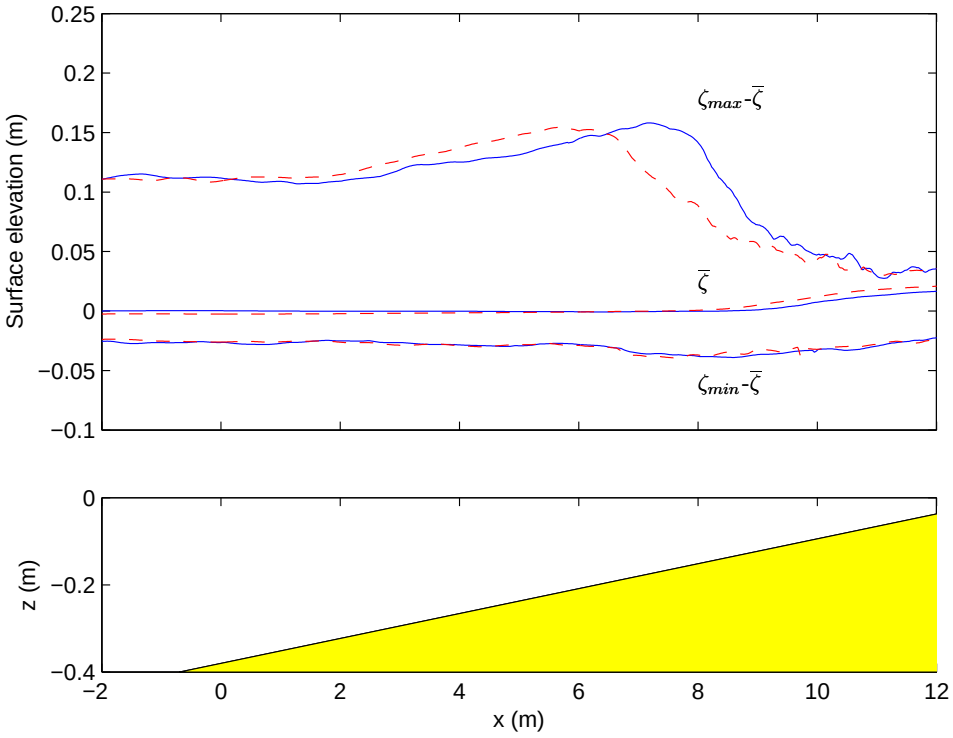

Figure 5.12: Wind effects on the distribution of wave amplitudes and mean water level for the plunging breaker case. Blue solid lines: $U/C = 0$; red dashed lines: $U/C = 2$.

breaking point at $t/T = 0.05$. It is shown that the maximum velocity in the water is nearly horizontal and located on the tip of the overturning jet, and the air beneath the overturning jet moves fast and tries to escape from the enclosed cavity. During the splash-up at $t/T = 0.1$, the overturning jet curls down and impinges on the water surface ahead to generate a secondary wave, where large velocities are found. It can be seen that the first plunging point, which is before $x = 8.795$ m in the experiment (Ting & Kirby, 1995), is reproduced in the simulation. During the jet-splash cycles at $t/T = 0.2$, the jet generated during wave splash-up propagates with the wave and strikes the water ahead to generate another jet, which is consistent with the laboratory observation (Ting & Kirby, 1994). It can be seen that the velocity in the water decreases after the first

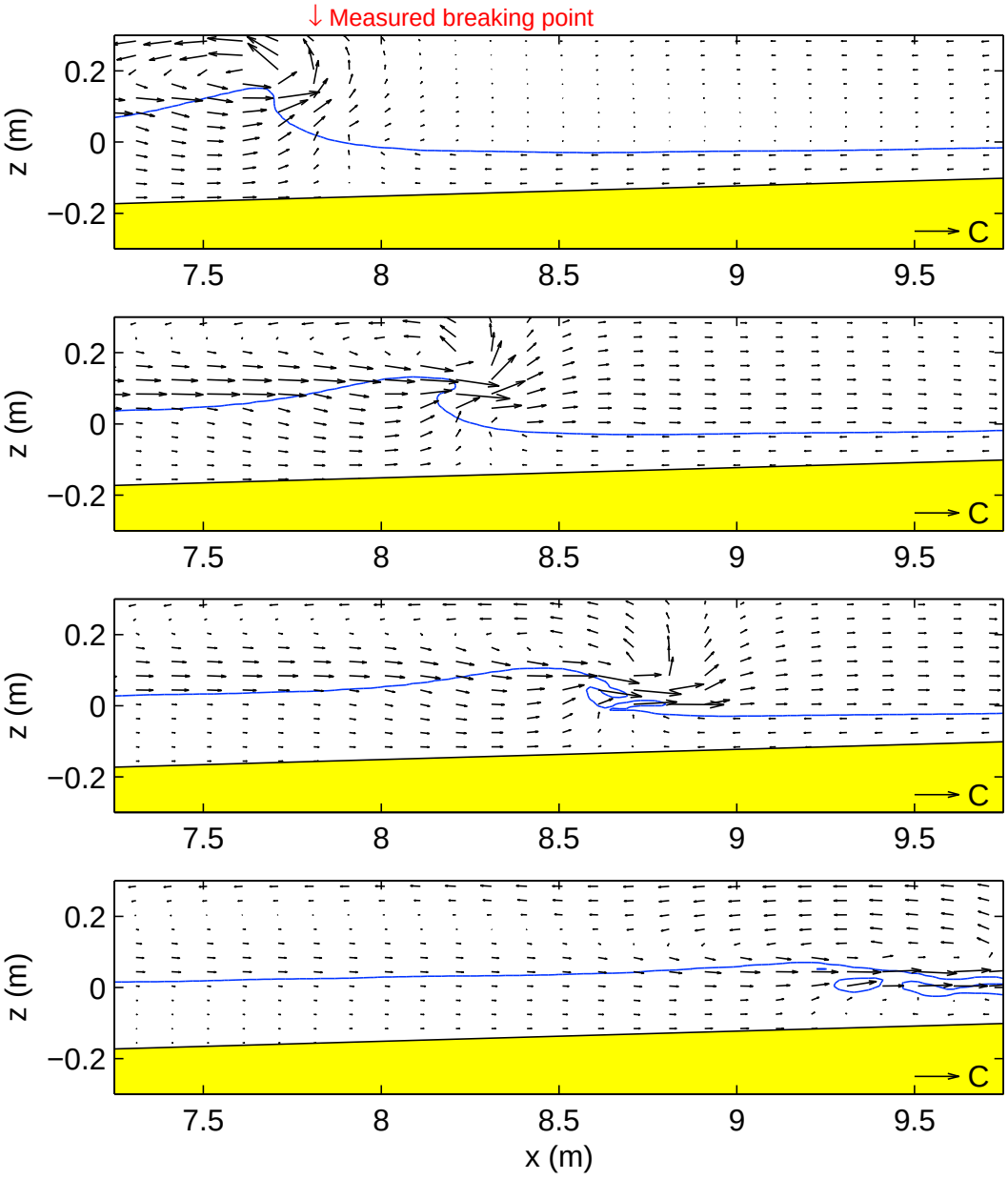

Figure 5.13: Velocity fields during wave breaking for the plunging breaker case when $U/C = 0$ at $t/T = 0.0, 0.05, 0.1, 0.2$. Velocities are normalized by the wave phase speed C.

splash-up. It is worth noting that the overturning jet curls down and impinges on the water ahead to generate the splash-up in plunging breakers, whereas the overturning jet only spills down the front face of the wave during wave breaking in spilling breakers. The jet-splash cycles only occur in the plunging breaker case.

It it worth remarking that with similar spatial resolution as used in previous studies, the present model is able to capture the overturning jet during wave breaking. Bradford (2000) discussed this problem and he stated that the model used in Bradford (2000) has difficulty in capturing the overturning jet, even when increasing the grid resolution. However, the detailed wave breaking processes are captured here for both spilling and plunging breakers due to the use of two-phase flow model and the sophisticated interface capturing scheme.

Figure 5.14 shows the velocity fields for the plunging breaker when $U/C = 2$ in one wave period at $t/T = 0.0, 0.05, 0.1, 0.2$. Similar to the spilling breaker, the air flow has been changed significantly due to wind forcing and the breaking point has been moved seaward. The breaking point is about $x_b = 7.7$ m for $U/C = 0$ while $x_b = 6.25$ m for $U/C = 2$. It is noted that the breaking point has been shifted about 1.5 m seaward in both spilling and plunging breakers. This is attributed to the fixed wind speed ($U/C = 2$) used here. It can be seen that the evolution of the wave shape has been slightly changed under the influence of wind. The wind also affects the shape of the overturning jet and the subsequent splash-up.

Figure 5.15 shows the mean vorticity fields for the plunging breaker when $U/C = 0$ in one wave period at $t/T = 0.0, 0.05, 0.1, 0.2$. The vorticity fields in the air are similar to the spilling breaker case, but there is much difference in the water. Close to wave breaking at $t = 0.0$, only small negative vorticity is observed near the front face of the wave. During wave breaking at $t/T = 0.05$, the region of negative vorticity in the water increases and spreads to the rear face of the wave. Both positive and negative vorticities with large magnitude are observed in the air beneath the overturning jet. During wave curling down at $t/T = 0.1$, large negative vorticity is generated in the vicinity of the plunging point, and the region of negative vorticity in the water becomes even larger. During the jet-splash cycles at $t/T = 0.2$, strong vortex motions are generated and it can be seen that the negative vorticity is spread downward close to the bottom in the

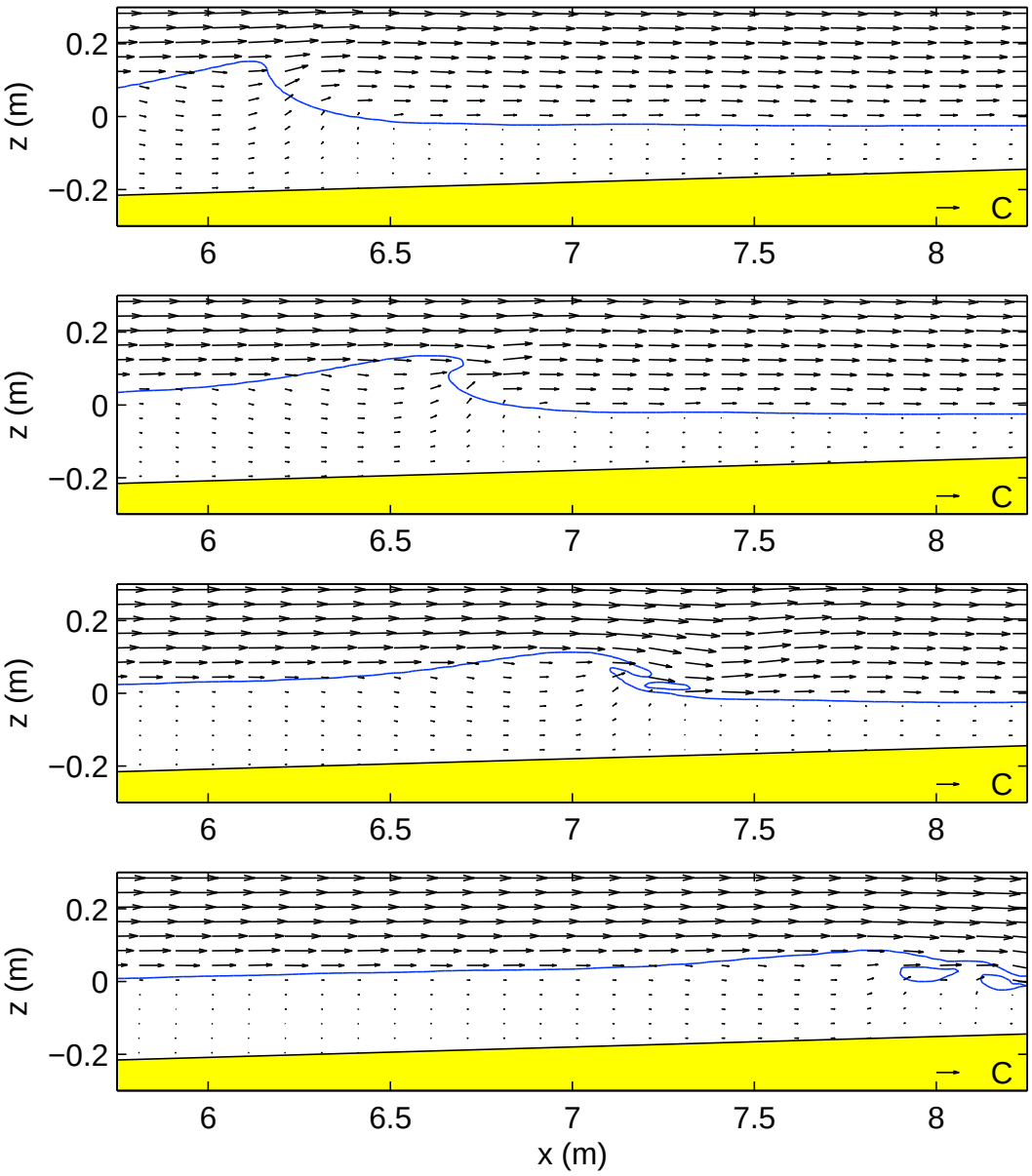

Figure 5.14: Velocity fields during wave breaking for the plunging breaker case when $U/C = 2$ at $t/T = 0.0, 0.05, 0.1, 0.2$. Velocities are normalized by the wave phase speed C.

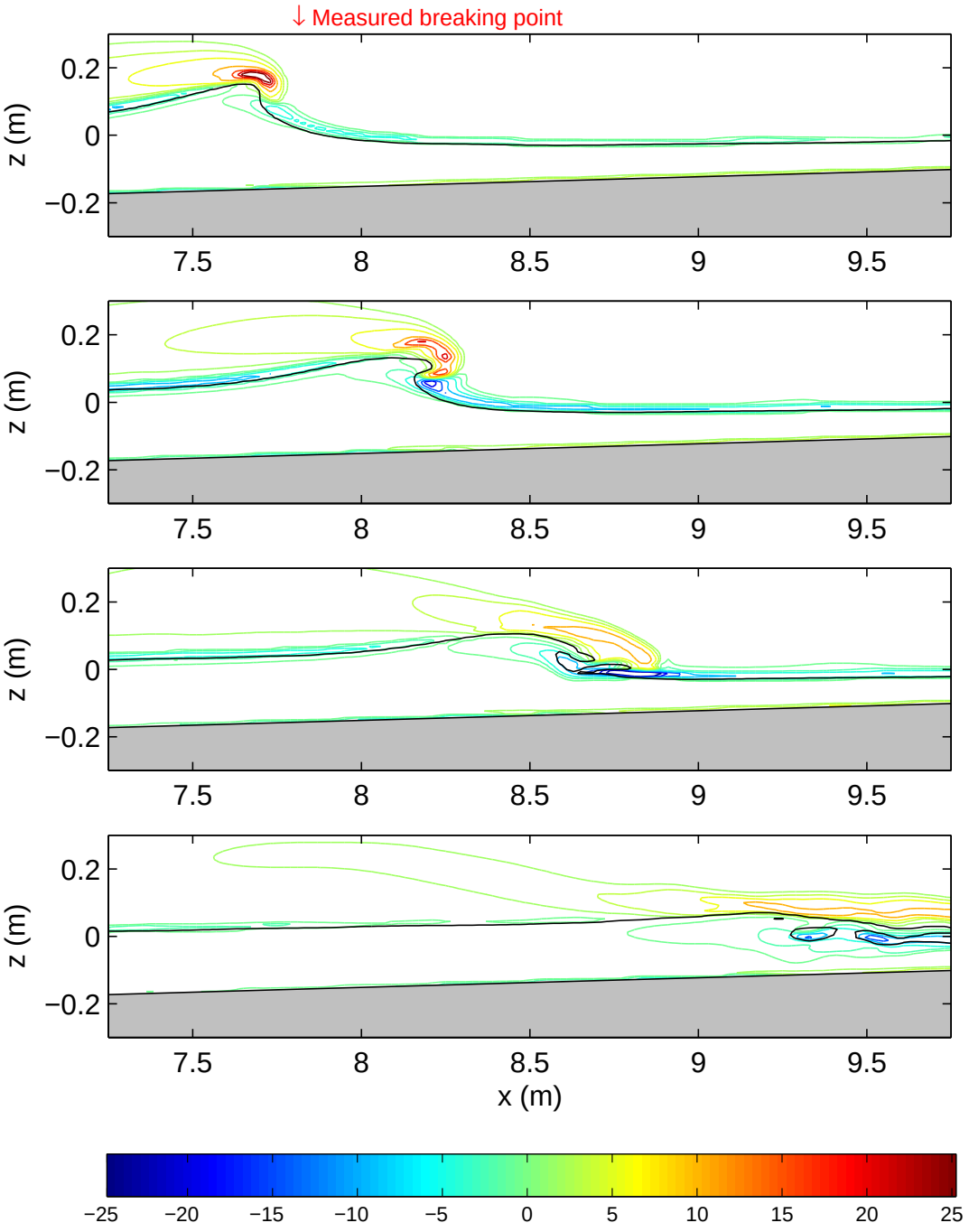

Figure 5.15: Mean vorticity fields during wave breaking for the plunging breaker case when $U/C = 0$ at $t/T = 0.0, 0.05, 0.1, 0.2$. The vorticity has been normalized by $\sqrt{g/(d_0 + a)}$ and the contours are shown for $\pm[1, 2.5, 5, 10, 15, 20, 25]$.

whole region underneath the wave front, whereas the vorticity is only confined to the region near the water surface in spilling breakers. It is shown that vorticity generation is much stronger in the plunging breaker than that in the spilling breaker.

Figure 5.16 shows the mean vorticity fields for the plunging breaker when $U/C = 2$ in one wave period at $t/T = 0.0, 0.05, 0.1, 0.2$. In the air, similar to the spilling breaker, large negative vorticity is generated in the vicinity of the water surface due to the wind shear compared to the case for $U/C = 0$. There is only negative vorticity in the air before wave breaking, whereas both the positive and negative vorticities coexist in front of the overturning jet after wave breaking. In the water, small negative vorticity is observed just underneath the water surface. However, the vorticity generation has been weakened in comparison with the case for $U/C = 0$ as the region of negative vorticity becomes thinner and moves upward. This is because the wind affects the wave to break earlier in a deeper water, which leads to the change of the vortex motion after wave breaking. Also there is reduced shear due to the wind and hence less vorticity.

5.5 Concluding Remarks

In this chapter, the RANS model is utilized to simulate 2D periodic breaking waves in the surf zone. Both spilling and plunging breakers in Ting & Kirby (1994) have been investigated, and numerical results of the distribution of wave amplitudes, vertical variations of the undertow and turbulence field have been compared with the experimental data and previous numerical studies in the absence of wind.

Later, wind effects on periodic breaking waves are investigated, which has not been considered in previous studies. Comparisons are made for the results between $U/C = 0$ and $U/C = 2$ in terms of water surface profiles, velocity and vorticity fields. It is worth remarking that the overturning jet in both spilling and plunging breakers, which are rarely shown in previous studies, have been reproduced in the simulations for both cases.

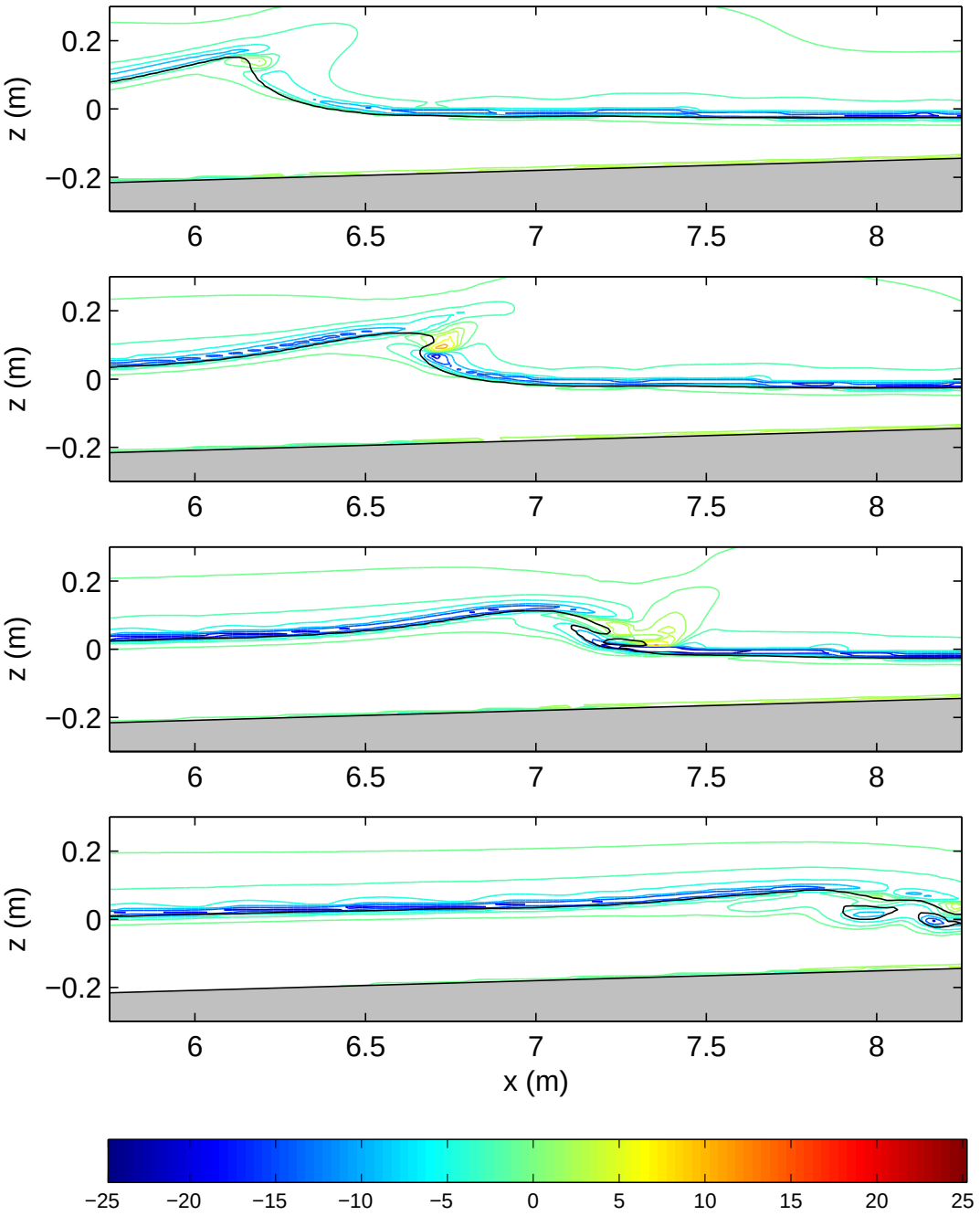

Figure 5.16: Mean vorticity fields during wave breaking for the plunging breaker case when $U/C = 2$ at $t/T = 0.0, 0.05, 0.1, 0.2$. The vorticity has been normalized by $\sqrt{g/(d_0 + a)}$ and the contours are shown for $\pm[1, 2.5, 5, 10, 15, 20, 25]$.

Chapter 6

Large Eddy Simulation of Three-Dimensional Breaking Waves

It is shown from pervious chapters that the RANS model is capable of simulating two-dimensional breaking waves. However, most water waves in nature break in a three-dimensional (3D) feature (see figure 6.1 for a 3D nearshore breaking wave). In order to simulate three-dimensional breaking waves, we cannot use direct numerical simulation due to high computational requirements and hence large eddy simulation is employed in this study.

This chapter is devoted to the kinematics and dynamics of three-dimensional breaking waves. After reviewing previous numerical studies for 3D breaking waves, the mathematical model and numerical implementation are briefly described, and then the benchmark problem of a solitary wave run-up on a conical island is used to validate the 3D model. Afterwards, three-dimensional overturning waves are investigated and discussed in detail.

6.1 Introduction

Several potential flow models have been developed to study three-dimensional overturning waves in deep or shallow water (as discussed in § 1.2.3), which provide much insight into the characteristics of breaking waves up to impingement. With

Figure 6.1: Breaking waves on St Andrews beach, Scotland, UK (photograph by Z. Xie).

increases in computational power and developments of numerical methods, some attempts have been made to investigate three-dimensional breaking waves using direct numerical simulation (DNS) or large eddy simulation (LES).

Miyata *et al.* (1996) performed a DNS study of three-dimensional breaking waves around bodies. The Navier–Stokes equations are solved by the MAC-type algorithm and the density function is employed to capture the interface. Several cases for ship waves and flow over a cylinder were simulated and it was shown that the model can predict qualitatively realistic nonlinear free surface phenomena when compared to experimental photos. This model was later used in a 3D viscous numerical wave tank for wave-structure interaction by Park *et al.* (1999).

Hodges & Street (1999) performed a three-dimensional large eddy simulation of finite-amplitude waves in a turbulent channel flow. The governing equations are discretized in curvilinear coordinates and solved by the fractional step method, and a dynamic model is employed to model subgrid-scale turbulence effects. The free surface is tracked by the boundary-fitted grid that moves in each time step. The interaction between nonlinear non-breaking surface waves and a turbulent current was investigated in a periodic space domain, and it was indicated that this method can be further modified to simulate overturning waves.

Watanabe & Saeki (1999) carried out a three-dimensional large eddy simulation of breaking waves. The Navier–Stokes equations are solved by the fractional step method, a modified Smagorinsky model is used in the subgrid-scale model and the density function is employed to capture the interface. The overturning wave and subsequent splash-up were investigated and qualitatively compared with experiments. The velocity field after wave breaking and the three-dimensional vortex structures under spilling and plunging breaking waves were further explored in Watanabe & Saeki (2002) and Watanabe *et al.* (2005), respectively.

Christensen & Deigaard (2001) presented a three-dimensional large eddy simulation of breaking waves. The governing equations are solved by the SOLA-VOF (Nichols *et al.*, 1980) procedure, the Smagorinsky model is employed as the subgrid-scale model, and the surface markers method is used to track the interface. Several different types of breaking waves on a sloping beach were investigated and the velocity field during wave breaking was shown in that paper. It was found that the obliquely descending eddies can be seen from the velocity fields in two longitudinal sections. Later, Christensen (2006) used the Navier–Stokes solver (Mayer *et al.*, 1998) to further investigate the detail of breaking waves in the surf zone. Two different approaches, the Smagorinsky model and a model based on the k-equation, are implemented for the subgrid-scale turbulence. The VOF method is utilized to capture the interface. Both spilling and plunging breakers in the surf zone were investigated and compared with experimental measurements (Ting & Kirby, 1994, 1995, 1996). Although a rather coarse mesh was used in the simulation, satisfactory results for the wave setup and undertow were obtained, but turbulence intensities were overpredicted as the effect of air was not taken into account.

Wu (2004) developed a three-dimensional finite volume solver, based on the TRUCHAS[1] code (Kothe *et al.*, 1997) developed in Los Alamos National Laboratory (LANL), to study breaking waves and turbulence effects. Both 3D RANS and LES models were proposed in that study. The governing equations are solved by the two-step projection method and the VOF method is employed to capture the interface. The spilling breaker case in 2D (Ting & Kirby, 1996) was investigated and the details of the turbulence effect of a dam-break flow over a square

[1] http://telluride.lanl.gov/

cylinder were analyzed. A moving solid algorithm was implemented in the model and applied to investigate the run-up from three-dimensional sliding masses (Liu *et al.*, 2005), in which good agreement with the experimental measurements was obtained.

In contrast to other methods which often use numerical schemes to discretize the governing equations, there are some studies for breaking waves using the finite analytic method (Chen *et al.*, 1981), in which local analytical solutions to the PDEs are used for discretization. Wang (2007) developed a 3D viscous numerical wave tank and performed a DNS study of the propagation of a solitary wave and periodic waves over 3D breakwaters with the MAC method to treat the 3D free surface. The SIMPLER method is employed to couple the velocity and pressure.

Few attempts have been made in the development of 3D two-phase flow model to study three-dimensional breaking waves. Mutsuda & Yasuda (2000) investigated the turbulent air-water mixing layer of a breaking solitary wave over a double reef by LES. The compressibility is taken into account in the governing equations with a dynamic subgrid-scale model, and the density function is used to capture the interface. The development of the overturning jet and the splash-up were presented along with the velocity field. It was found that the water surface profile and the motion of air bubbles develop quickly into three-dimensional turbulent flow during jet-splash cycles, and the strongest turbulence intensity is generated when the overturning jet impinges on the water surface.

Lubin *et al.* (2006) performed a three-dimensional LES of air entrainment under plunging breaking waves. The governing equations are solved by the augmented Lagrangian method. A dynamics subgrid-scale model is employed and an explicit Lax-Wendroff TVD scheme is used for the VOF equation to capture the interface. The overturning wave, leading from a planar Stokes wave, was investigated in a periodic space domain. The plunging jet, splash-up cycles, vorticity generation and energy dissipation were analyzed in detail. It was found that three-dimensional turbulence is more dissipative than the two-dimensional turbulence obtained by Chen *et al.* (1999).

Liovic & Lakehal (2007) developed a finite difference MFVOF-3D (multi-fluid VOF in 3D) code for turbulent interfacial flows. The governing equations are

solved by the two-step projection method and a VOF method, resolved on a twice-as-fine sub-mesh nested within the underlying solver mesh, is employed to capture the interface. A damping function, based on the normalized distance to the interface in the air side, was introduced in the modified Smagorinsky model. Periodic breaking waves on a slope, similar to Christensen & Deigaard (2001), were investigated. Some qualitative results were presented and special attention was given to resolve the sublayer near the air-water interface. It was shown that the proposed approach is capable of providing more detailed information for near interface multi-physics treatment.

Recently, Yang & Stern (2009) presented a 3D LES two-phase flow model for ship hydrodynamics. The sharp interface immersed boundary method and a level set/ghost-fluid method were employed to deal with the solid-fluid and fluid-fluid interface, respectively. The Navier–Stokes equations are solved by a four-step fractional-step method and a Lagrangian dynamic Smagorinsky model is used to solve the subgrid-scale turbulence. A variety of application cases were well simulated by the model, such as the bubble dynamics, water entry and exit of a cylinder, landside-generated waves (Liu *et al.*, 2005), and three ship flow cases.

Some hybrid models are developed to reduce the computational effort in 3D computations. Biausser *et al.* (2004) carried out a DNS study of the internal kinematics and dynamics of a three-dimensional overturning solitary wave on slopes. The governing equations are based on the coupling between potential flow equations, solved by high order BEM, and Euler equations, solved by the pseudo-compressibility method with the VOF method for interface capturing. The plunging jet during wave overturning was observed and detailed analysis of the velocity field was shown in the study. It was found that overturning waves were more dissipative in VOF simulations than the BEM.

It is worth remarking that only planar waves are considered in most previous 3D models. Hence, the present study is devoted to the kinematics and dynamics of three-dimensional breaking waves.

6.2 Large Eddy Simulation

6.2.1 Spatial Filtering

In LES, scales are separated by applying a low-pass filter and the filtered variable is defined as

$$\overline{\phi}(x) = \int \phi(x')G(x,x')\mathrm{d}x', \tag{6.1}$$

where $G(x,x')$ is the filter kernel, which is associated with a cutoff length scale $\overline{\Delta}$. In general, eddies of size larger than $\overline{\Delta}$ are explicitly modelled large eddies while those smaller than $\overline{\Delta}$ are small eddies, which need to be parameterized.

The filter has following fundamental properties (Sagaut, 2002):

(i). $$\overline{a} = a, \quad a \text{ is a constant} \tag{6.2}$$

(ii). $$\overline{\phi + \psi} = \overline{\phi} + \overline{\psi} \tag{6.3}$$

(iii). $$\overline{\frac{\partial \phi}{\partial t}} = \frac{\partial \overline{\phi}}{\partial t}, \quad \overline{\frac{\partial \phi}{\partial x_i}} = \frac{\partial \overline{\phi}}{\partial x_i} \tag{6.4}$$

In the FVM, the top-hat filter is usually used and the one-dimensional case is written as

$$G(x,x') = \begin{cases} 1, & \text{if } |x'-x| \leq \dfrac{\overline{\Delta}}{2}; \\ 0, & \text{otherwise.} \end{cases} \tag{6.5}$$

6.2.2 Filtered Navier–Stokes Equations

Applying the filter to the Navier–Stokes equations (2.8–2.9), we can obtain

$$\frac{\partial \overline{u}_i}{\partial x_i} = 0, \tag{6.6}$$

$$\frac{\partial (\rho \overline{u}_i)}{\partial t} + \frac{\partial (\rho \overline{u}_i \overline{u}_j)}{\partial x_j} = -\frac{\partial \overline{p}}{\partial x_i} + \frac{\partial}{\partial x_j}\left[\mu\left(\frac{\partial \overline{u}_i}{\partial x_j} + \frac{\partial \overline{u}_j}{\partial x_i}\right)\right] + \rho g_i + \frac{\partial \tau_{ij}^{SGS}}{\partial x_j}. \tag{6.7}$$

It is worth noting that

$$\overline{u_i u_j} \neq \overline{u}_i \overline{u}_j, \tag{6.8}$$

and the difference between this inequality is

$$\tau_{ij}^{SGS} = -\rho(\overline{u_i u_j} - \overline{u}_i \overline{u}_j), \tag{6.9}$$

which is defined as subgrid-scale Reynolds stress in LES.

6.2.3 Subgrid Scale Models

Similar to the RANS equations, the governing equations are not closed, and subgrid-scale models have to be introduced to solve the filtered Navier–Stokes equations. In general, there are two modelling strategies (Sagaut, 2002):

Functional modelling

The subgrid terms are modelled based on the resolved quantity $\overline{\boldsymbol{u}}$ not the tensor τ^{SGS} itself. The modelling assumption is based on the form $\boldsymbol{\nabla} \cdot \tau^{SGS} = \mathbb{H}(\overline{\boldsymbol{u}})$, where $\mathbb{H}$ is an arbitrary function.

Structural modelling

Contrary to functional modelling, the tensor τ^{SGS} is solved and approximated by the evaluation of the resolved quantity $\overline{\boldsymbol{u}}$ or a formal series expansion. The closure hypothesis consists in using the relation $\tau^{SGS} = \mathbb{H}(\overline{\boldsymbol{u}})$ or $\boldsymbol{u}' = \mathbb{H}(\overline{\boldsymbol{u}})$.

In the present study, we focus on the conventional LES modelling with a Smagorinsky subgrid-scale closure scheme. Various other subgrid-scale models are presented and discussed in Sagaut (2002).

6.2.4 Smagorinsky Model

The earliest and most commonly used subgrid-scale model in LES is the one developed by Smagorinsky (1963). It is based on the subgrid viscosity concept, and similar to the eddy viscosity model in RANS modelling, the subgrid-scale Reynolds stress can be expressed as

$$\tau_{ij}^{SGS} - \frac{1}{3}\tau_{ij}^{SGS}\delta_{ij} = \mu^{SGS}\left(\frac{\partial \overline{u}_i}{\partial x_j} + \frac{\partial \overline{u}_j}{\partial x_i}\right) = 2\mu^{SGS}\overline{S}_{ij}, \tag{6.10}$$

where μ^{SGS} is the subgrid-scale eddy viscosity and $\overline{S}_{ij}$ is the strain rate of the resolved field.

Based on the dimensional analysis, the subgrid-scale eddy viscosity can be obtained as

$$\mu^{SGS} = \rho L_S^2 \left|\overline{S}\right| = \rho(C_S\overline{\Delta})^2 \left|\overline{S}\right|, \tag{6.11}$$

in which

$$\left|\overline{S}\right| = \left(2\overline{S}_{ij}\overline{S}_{ij}\right)^{1/2}, \tag{6.12}$$

and $L_S = C_S\overline{\Delta}$ is the Smagorinsky length scale, in which C_S is the Smagorinsky coefficient and the cut-off length scale $\overline{\Delta}$ in the present study is defined as

$$\overline{\Delta} = (\Delta x \Delta y \Delta z)^{1/3}, \tag{6.13}$$

where Δx, Δy and Δz are the grid lengths in the x, y and z directions in a control volume, respectively.

It is noted that different values of the Smagorinsky coefficient ($0.1 \sim 0.2$) have been employed in different flow simulations, and in the present study, $C_S = 0.1$ is used in the simulation.

6.3 Initial and Boundary Conditions

Initial and boundary conditions for the continuity and momentum equations are the same as in § 2.2, so only the near-wall treatment for large eddy simulation is presented here.

In the near-wall region, the characteristic length scale has to be reduced, which corresponds to a reduction in the subgrid-scale viscosity (Sagaut, 2002). One commonly used technique is employing the von Driest's damping function (van Driest, 1956). The usual relation:

$$L_S = C_S\overline{\Delta}, \tag{6.14}$$

is replaced by

$$L_S = C_S\overline{\Delta}d_{\mathrm{w}}(n^+), \tag{6.15}$$

where $d_{\mathrm{w}}(n^+)$ is the damping function, n^+ is the nondimensionalized distance from the wall (similar to the wall function in the RANS model) and from van Driest (1956) we obtain

$$d_{\mathrm{w}}(n^+) = 1 - e^{-n^+/A^+}, \tag{6.16}$$

in which A^+ is a constant usually equal to 25. However, it is suggested that the subgrid-scale model should depend solely on the local properties of the flow field and it is difficult to justify how the distance affects the subgrid model (Ferziger & Peric, 2002).

The structure of the boundary layer in the near-well region has certain characteristics and therefore special attention has to be paid in LES modelling. There are two possible approaches to deal with the near-wall dynamics (Sagaut, 2002):

- Resolving the near-wall dynamics directly. In this approach, very fine grids, the first grid in the zone ($0 \leq n^+ \leq 1$), are required to represent the near-wall turbulence, and thus limit the LES application for high Reynolds number flows.

- Modelling the near-wall dynamics. In this approach, a special subgrid-scale model called a wall model, is used to represent the near-wall turbulence at the first grid point outside the wall (similar to the wall function used in the RANS model), and thus a relatively coarse mesh can be used in the near-wall region which gives us much advantage in LES modelling.

In the present study, the second approach is employed with the wall model proposed by Cabot & Moin (2000). The subgrid eddy viscosity at the first grid point off the wall is obtained by a RANS type mixing-length eddy viscosity as

$$\frac{\mu^{\mathrm{SGS}}}{\mu} = \kappa n^+ \left(1 - e^{-n^+/A^+}\right)^2, \tag{6.17}$$

with $n^+ = \dfrac{\rho u_\tau n}{\mu}$ and $A^+ = 19$. In Cabot & Moin's model, the empirical velocity profile in the logarithmic region is used to approximate the friction velocity u_τ from the instantaneous tangential velocity u_t as

$$\frac{u_t}{u_\tau} = \frac{1}{\kappa} \ln\left(E^+ \frac{\rho u_\tau n}{\mu}\right), \tag{6.18}$$

where $E^+ = 9.7393$ is the coefficient for a smooth wall. In order to take all regions in the turbulent boundary layer into account, the Spaldings' universal formula (3.25) is used here.

6.4 Special Numerical Implementation

6.4.1 Numerical Discretization

Table 6.1 shows the various values of ϕ, Γ and Q_ϕ^{S} in the general integral formulation (see § 2.3.2) to represent the filtered Navier–Stokes equations. The same numerical discretization used in Chapter 2 is employed here for the LES model.

Table 6.1: Values of ϕ, Γ and Q_ϕ^{S} in the general integral formulation to represent the filtered Navier–Stokes equations.

Equation	ϕ	Γ	Q_ϕ^{S}
Continuity	1	0	0
Momentum	$\overline{\boldsymbol{u}}$	$\mu + \mu^{SGS}$	$-\boldsymbol{\nabla}\overline{p} + \rho\boldsymbol{g}$

6.4.2 Near-wall Treatment in LES

The friction velocity u_τ is needed to get the subgrid eddy viscosity at the first grid point off the wall in (6.17). In this study, the Spaldings' universal formula (3.25)

$$n^+ = u^+ + \frac{1}{E^+}\left[e^{\kappa u^+} - 1 - \kappa u^+ - \frac{(\kappa u^+)^2}{2!} - \frac{(\kappa u^+)^3}{3!}\right], \tag{6.19}$$

is used to approximate the friction velocity u_τ, where

$$n^+ = \frac{\rho u_\tau n}{\mu}, \quad u^+ = \frac{u_t}{u_\tau}. \tag{6.20}$$

Since u_τ is nonlinear in Spaldings' universal formula, it can be solved iteratively via the Newton-Raphson method as

$$u_\tau^{\mathrm{ni}} = u_\tau^{\mathrm{ni}-1} + \frac{X}{X'}, \tag{6.21}$$

where ni is the number of iteration and X and X' are

$$X = -n^+ + u^+ + \frac{1}{E^+}\left[e^{\kappa u^+} - 1 - \kappa u^+ - \frac{(\kappa u^+)^2}{2!} - \frac{(\kappa u^+)^3}{3!}\right],$$
$$X' = \frac{\partial X}{\partial u_\tau} = \frac{1}{u_\tau}\left\{-n^+ - u^+ + \frac{1}{E^+}\left[-\kappa u^+ e^{\kappa u^+} + \kappa u^+ + (\kappa u^+)^2 + \frac{(\kappa u^+)^3}{2}\right]\right\}. \tag{6.22}$$

6.5 Solitary Wave Run-up on a Conical Island

6.5.1 Introduction

For three-dimensional breaking solitary waves, a laboratory experiment was carried out by Briggs *et al.* (1995) for the run-up of solitary waves on a conical island, which was motivated by the tsunamis which happened in Babi island of Flores (Indonesia) and Okushiri island (Japan). Liu *et al.* (1995) presented an early numerical study of a solitary wave run-up over a conical island based on the two-dimensional shallow water wave equations, and good agreement between the numerical model and the laboratory data for the water surface displacement and maximum run-up heights was obtained. Later, Kanoglu & Synolakis (1998) presented an analytical method for determining the wave evolution for piecewise linear topographies and also calculated the run-up of solitary waves on a conical island. Since then, this experiment is considered as a benchmark problem for validating several numerical models for free surface flows, such as shallow water equations (Bradford & Sanders, 2002; Hubbard & Dodd, 2002; Titov & Synolakis, 1998; Valiani & Begnudelli, 2006; Wei *et al.*, 2006), Boussinesq-type equations (Chen *et al.*, 2000; Fuhrman & Madsen, 2008; Lynett *et al.*, 2002), depth-integrated non-hydrostatic model (Yamazaki *et al.*, 2009), three-dimensional hydrodynamic model (Chen, 2004), and the commercial CFD code FLOW-3D (Choi *et al.*, 2007).

6.5.2 Experimental and Computational Setup

Physical model studies for a solitary wave run-up on a conical island were conducted at the coastal and hydraulic laboratory, engineer research and develop-

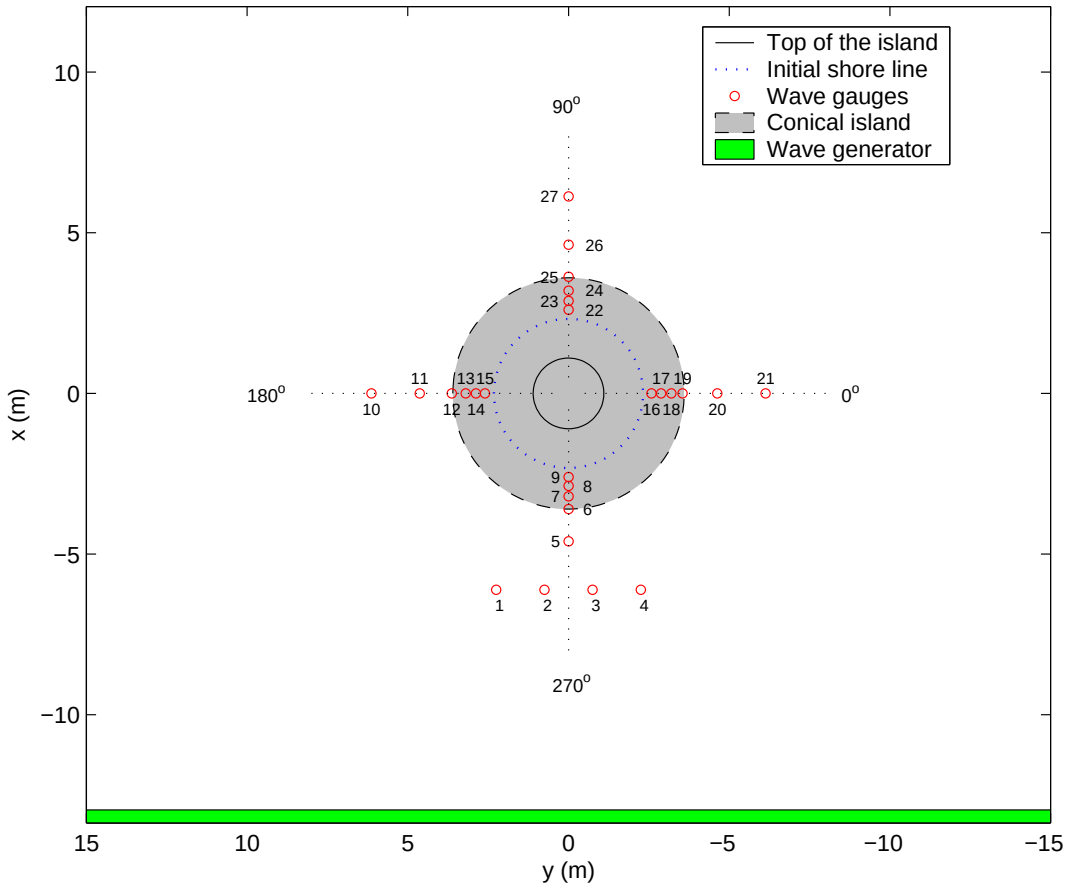

(a) top view

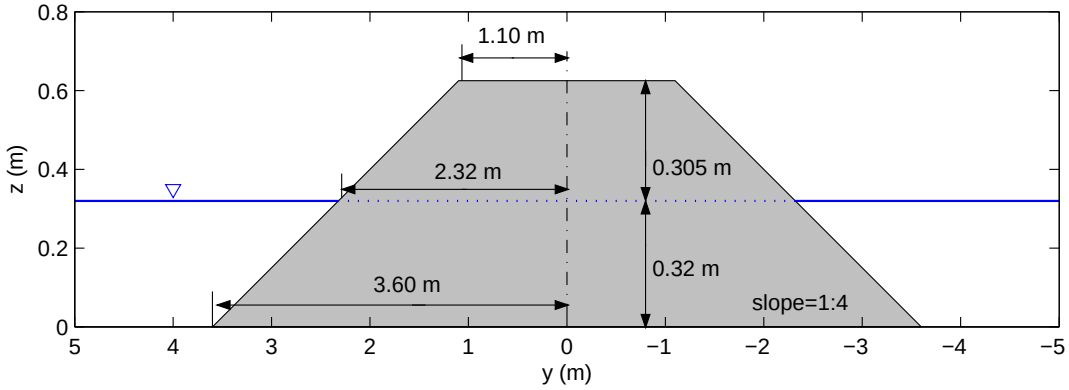

(b) enlarged side view, the vertical scale is exaggerated by a factor of 4

Figure 6.2: Sketch of experimental setup and computational domain for a solitary wave run-up on a conical island.

ment center, U.S. Army Corps of Engineers (Briggs *et al.*, 1995). Figure 6.2 shows the schematic of the laboratory setup, where a conical island was constructed in the centre of a 25 m long and 30 m wide wave basin. The conical island is 0.625 m high with diameters of 7.2 m at the toe and 2.2 m at the crest, and the slope is 1:4. 27 capacitance wave gages were used to measure the water surface elevations and the maximum run-up heights were recorded in 20 locations around the perimeter of the island. The details of the experiment can be found in Briggs *et al.* (1995) and Liu *et al.* (1995).

Three incident wave cases for $H/D = 0.05, 0.1, 0.2$ with the water depth $D = 0.32$ m are considered in the present study, but only the results for the steepest wave case $H/D = 0.2$ are presented here for the sake of brevity. The computational domain is discretized by a $250 \times 250 \times 30$ nonuniform grid, with minimum meshes of $\Delta x = \Delta y = 0.072$ m uniformly distributed in the island region and $\Delta z = 0.01$ m in the vicinity of the water surface. It is noted that this grid resolution is sufficient to give representative flow features in comparison with other researchers although the mesh is not refined for validated LES and further refinement is necessary. The initial time step is $\Delta t = 0.01$ s and changed with the CFL condition due to the interface capture scheme. The computation is run up to 20 s which is similar to previous studies.

In the simulation, the solitary wave is generated at the inlet by specifying the water surface elevation and velocity field based on the analytical solution (3.45) similar to the 2D simulations in Chapter 4. The no-slip boundary condition (2.17) is specified on the bottom, top and both side walls of the domain and along the island. The radiative boundary condition (2.16) is applied at the outlet to let the wave propagate out of the computational domain. This work was undertaken on the White Rose Grid and the CPU time was approximately 30h.

6.5.3 Results and Discussion

Comparisons between laboratory measurements and numerical results

Figure 6.3 shows the comparison of the wave run-up on the lee side of the island between the experiment and numerical simulation. The wave paddles can

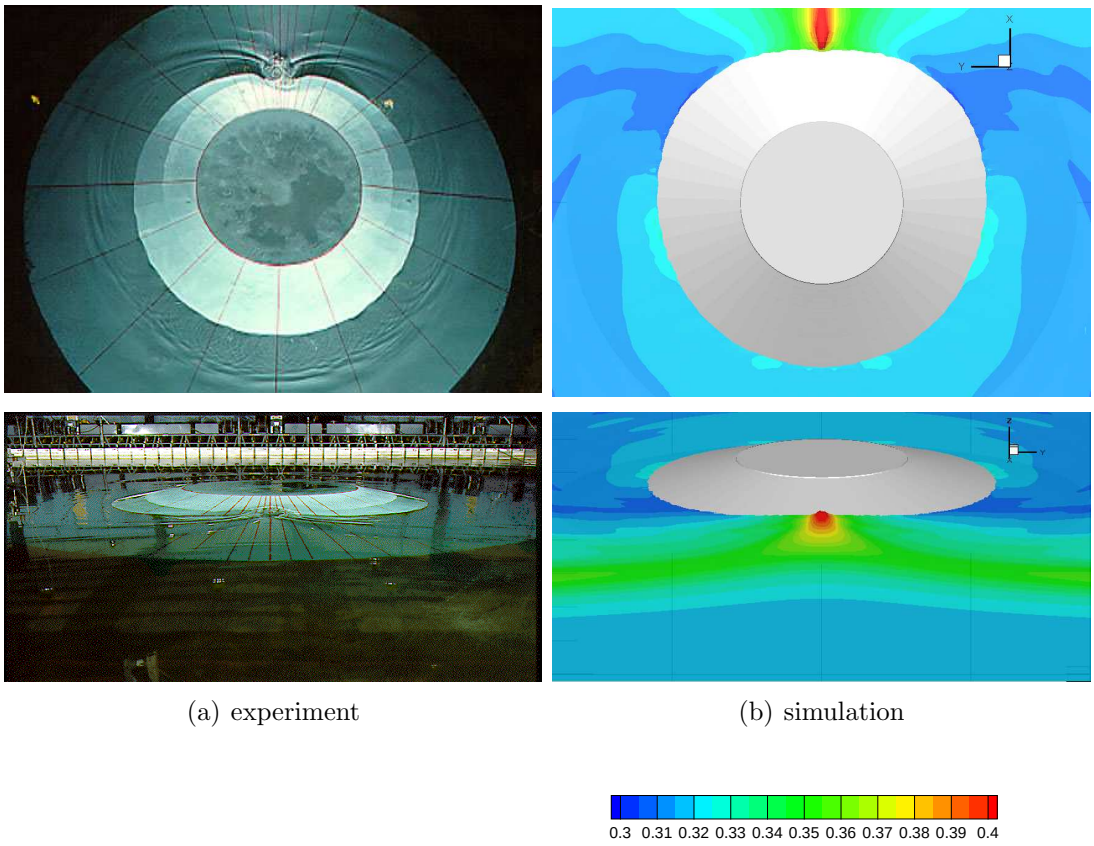

(a) experiment (b) simulation

Figure 6.3: Comparison of the wave run-up on the lee side of the island between the experiment and simulation. Top figures are the top view and bottom figures are the back view. The computed water surfaces are colored based on local values of wave height z. The experimental photos are obtained from `http://chl.erdc.usace.army.mil/chl.aspx?p=s&a=Projects;35`.

be seen from the experimental photo and it is shown that the run-up height increases due to the collision of two trapped waves on the lee side of the island. In general, acceptable agreement between the experiment and numerical simulation is obtained.

Figure 6.4(a) shows the comparison of the computed wave surface displacement against experimental measurements at five representative gauges. Gauge 3 is located half a wave length upstream from the toe of the island, gauge 6 is located on the front side of the toe of the island, and gauges 9, 16 and 22 are on the front, side and rear face of the island near the still water shoreline (see figure 6.2 for the location of wave gauges). The primary wave height and shape are well predicted by the present model, however, the secondary depression wave is slightly underestimated compared to the experimental measurements. It is noted that wave breaking is observed during the experiment on the lee side of the island due to the collision of two trapped waves for $H/D = 0.2$, some previous numerical models overestimated the wave height at this region as the wave breaking process was not taken into account, but it is shown that good agreement of the wave height is obtained for gauge 22 in the present model. It is worth remarking that there is a slight phase difference for the wave surface displacement on the lee side of the island gauge 22, which predicts later wave arrival in comparison to the experiment and this has also been found in all previous numerical studies.

Figure 6.4(b) presents the comparison of the locations of computed maximum run-up heights against experimental measurements, where the local coordinate 270^o corresponding to the front face of the island (see figure 6.2(a)). The vertical run-up heights (using a minimum shoreline depth as 0.002 m) are converted to the horizontal directions and normalized by the radius of the initial shore line. It is shown that good agreement between numerical simulations and experimental measurements is obtained. It is observed that the run-up height is higher on the front side of the island and decreases as the wave bends towards the lee side of the island. Compared to other cases for $H/D = 0.05, 0.1$ (not shown here), the higher incident wave ($H/D = 0.2$) produces higher run-up height on the front side of the island as more kinetic energy contained in the higher incident wave has been converted to the potential energy associated with the run-up height.

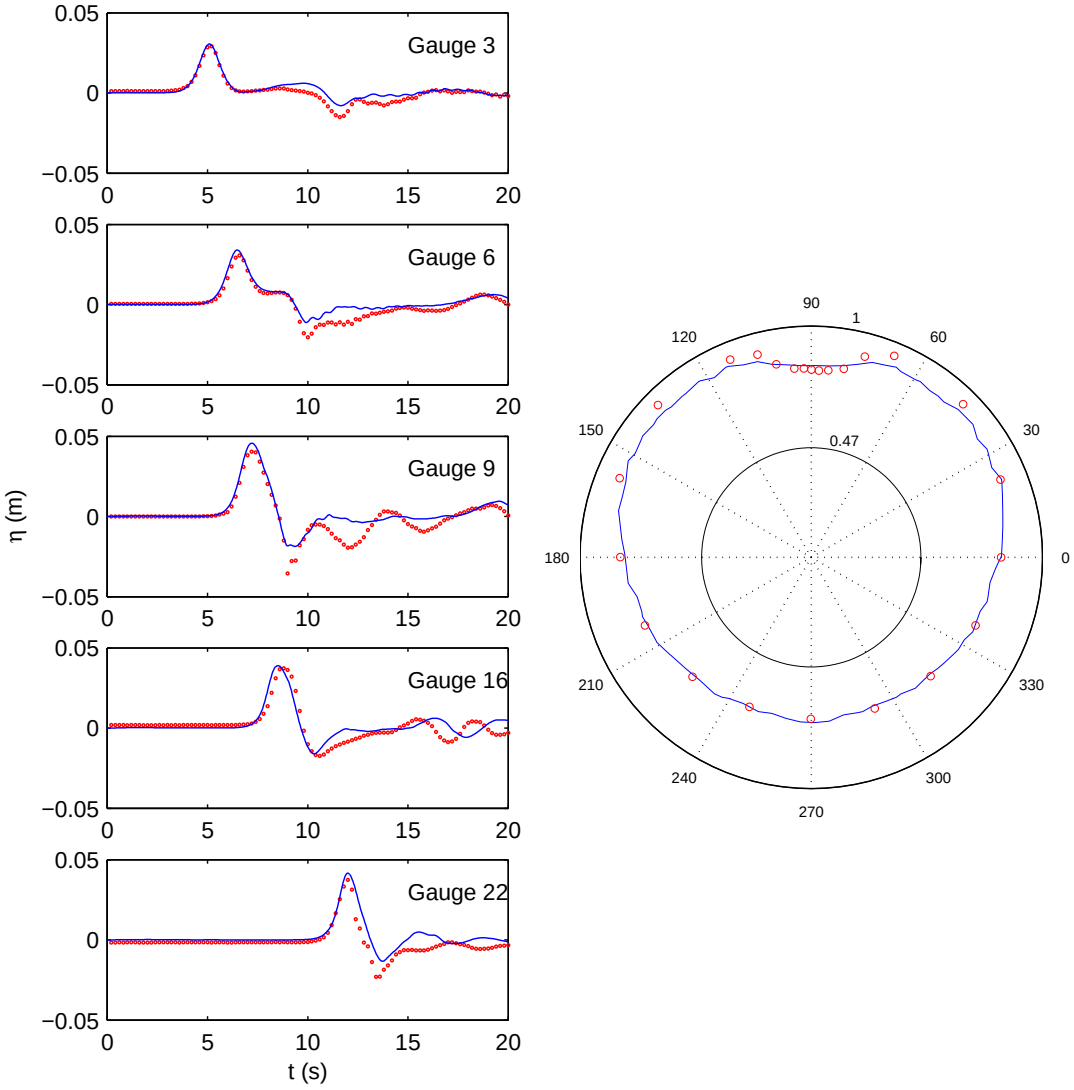

(a) wave surface displacement (b) maximum run-up heights

Figure 6.4: Comparison of numerical results against experimental measurements for $H/D = 0.2$. Blue solid lines are numerical results and red circles are experimental data. In (b), the inner black solid line is the crest of the island and the outer black solid line is the initial shoreline.

Snapshots of water surface profiles

Figure 6.5 presents the snapshots of water surface profiles for the incident wave case $H/D = 0.2$ when the solitary wave is in the vicinity of the conical island. The crest line is nearly parallel to the wave generation before reaching the island. Once the wave approaches the island, the crest line bends due to the wave shoaling and scattering by the island. When the wave reaches the maximum run-up height on the front face of the island (figure 6.5(a)), it can be seen that the wave is highest in the middle of the shoreline. After that, two trapped waves are formed and propagate along both sides of the shoreline around the island (figure 6.5(b)). As the wave moves faster due to greater depth, it is shown that when the incident wave in the offshore region reaches the middle of the island, the wave on the island shore is left behind with a slower speed. After the wave runs up the front face of the island, the wave starts to run down and generates a cylindrical wave pattern (figure 6.5(c)), which is similar to Liu *et al.* (1995). The two trapped waves wrap around the island and move towards the lee side. Eventually, the two trapped waves collide with each other on the lee side of the island and high run-up height is observed (figure 6.5(d)), which is consistent with the experimental measurements (Briggs *et al.*, 1995) and tsunamis which happened in Babi island (Yeh *et al.*, 1994). At this moment, the incident wave is moving offshore while the trapped waves are moving alongshore. The depression wave during wave running down the island can also be observed in figure 6.5(d).

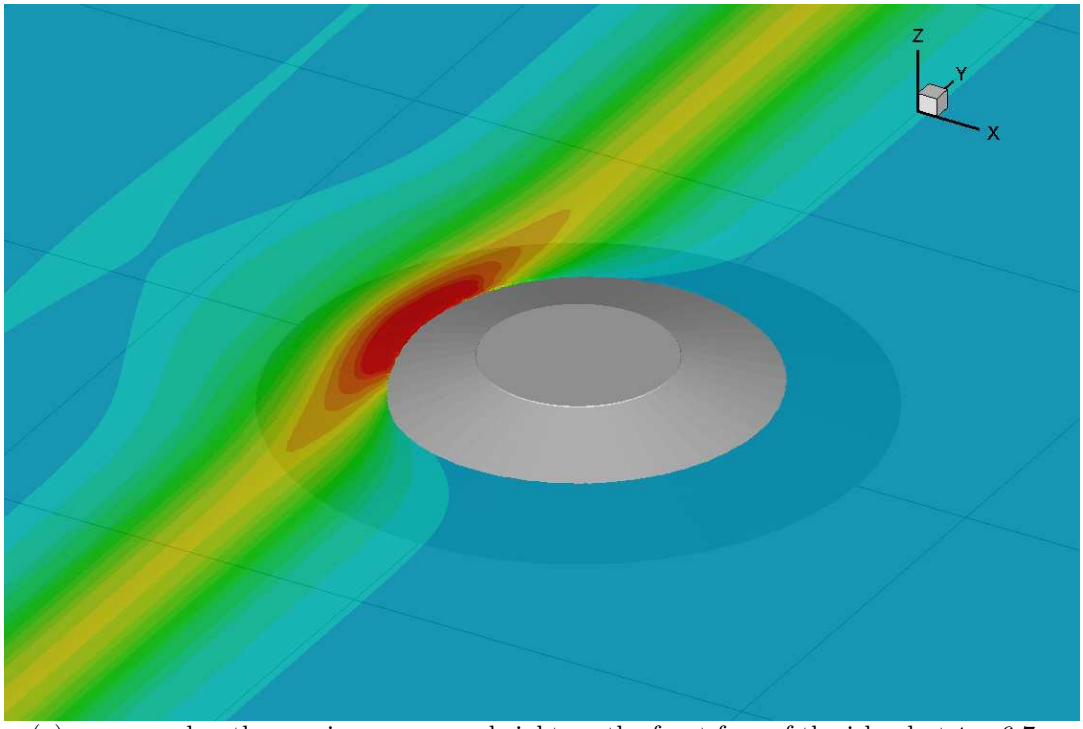

(a) wave reaches the maximum run-up height on the front face of the island at $t = 6.7$ s

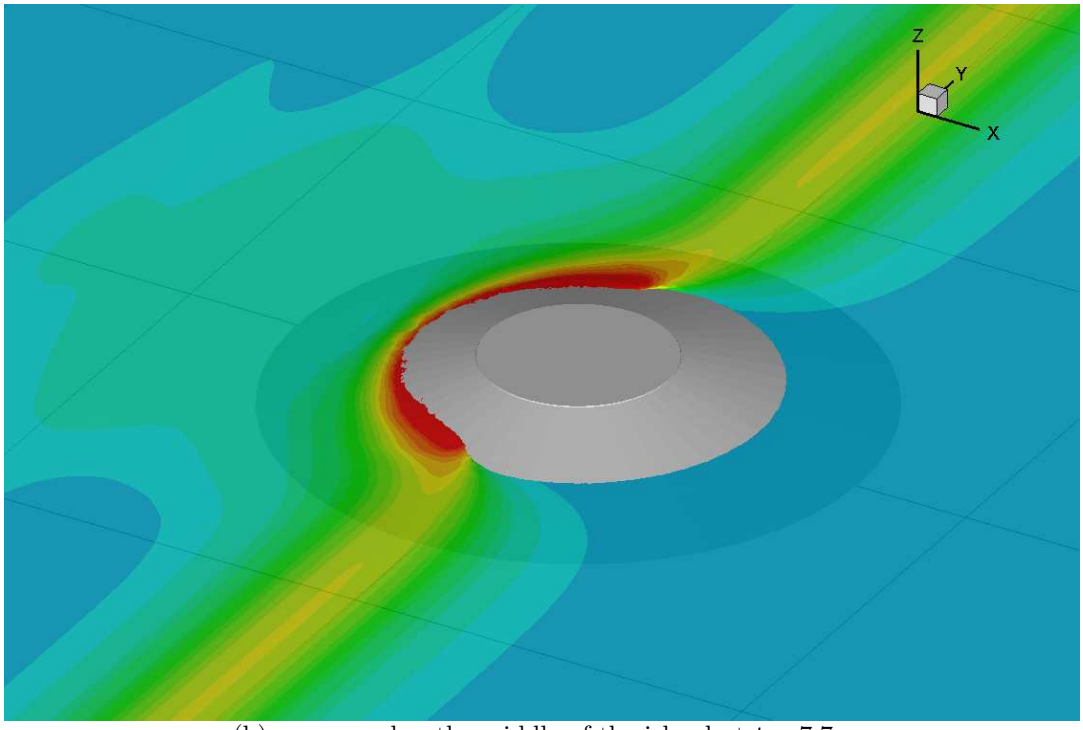

(b) wave reaches the middle of the island at $t = 7.7$ s

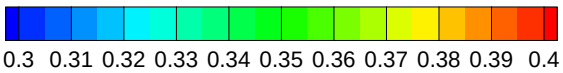

Figure 6.5: For caption see facing page.

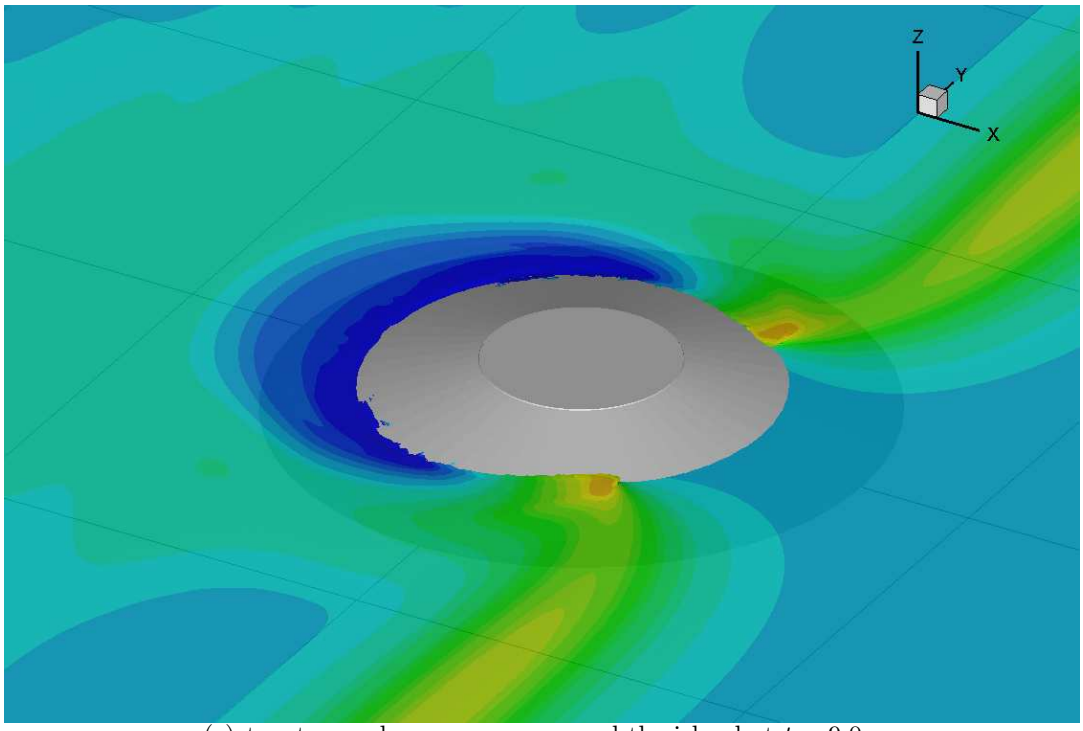

(c) two trapped waves wrap around the island at $t = 9.0$ s

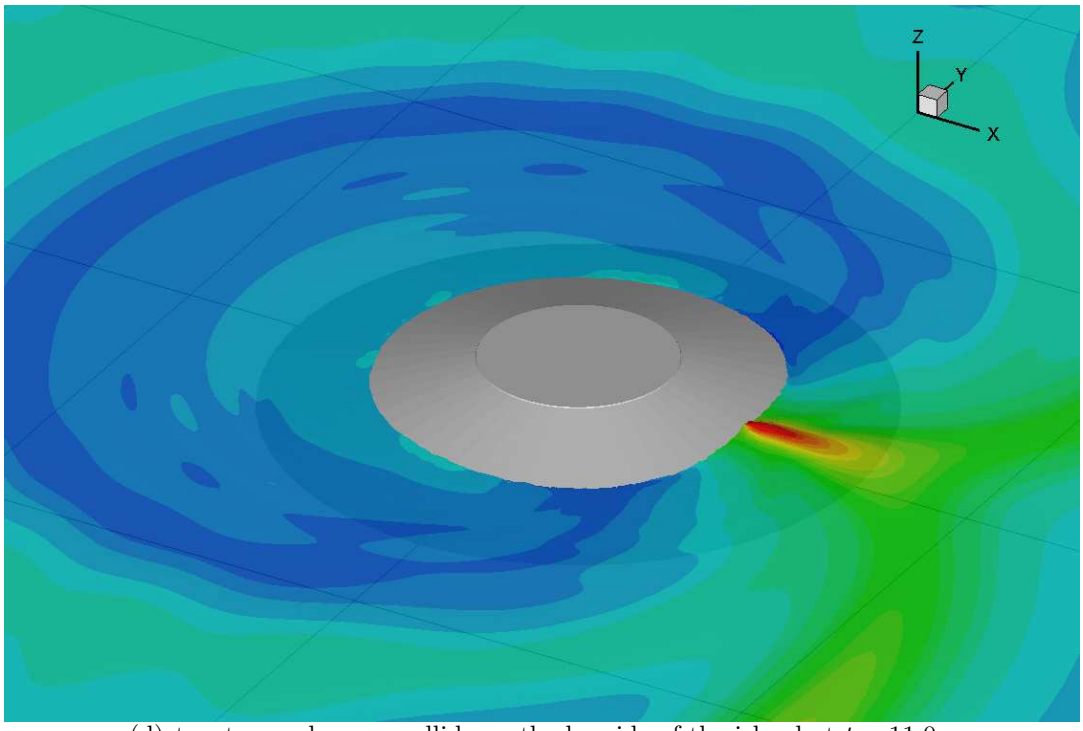

(d) two trapped waves collide on the lee side of the island at $t = 11.0$ s

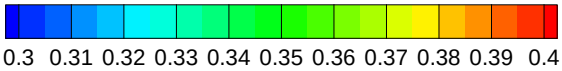

Figure 6.5: Snapshots of water surfaces during the run-up of the solitary wave on a conical island. The water surfaces are colored based on local values of wave height z. Four images at different times are shown for different stages.

6.6 3D Overturning Waves Over a Submerged Conical Island

6.6.1 Introduction

The numerical results for the solitary wave run-up on a conical island are shown in the previous section, however, due to the relatively low wave steepness, the overturning jet of the breaking wave (like figure 6.1) is not observed in the numerical computation. Apart from the study for water waves, similar research has been performed for shallow water flow around conical islands (Lloyd & Stansby, 1997*a*,*b*). Both laboratory experiments and numerical simulations were carried out when the conical island was surface piercing or submerged. It was found that vortex shedding occurs in the wake of conical islands and the slope of the island has little effect on the island wakes. As the water depth increases for submerged islands, the shedding becomes weaker and eventually stops. In this section, in order to study the kinematics and dynamics of three-dimensional breaking waves, we investigate 3D overturning waves over a submerged conical island, which have not been studied elsewhere to the best of our knowledge.

6.6.2 Computational Setup

In the simulation, the computational setup is similar to that in § 6.5, but for a smaller conical island with the same slope (1:4) submerged in the water. Figure 6.6 shows the schematic of the computational setup, where the origin of the coordinates is located at the still water level in the centre of the conical island and all lengths are normalized by the water depth $D = 0.32$ m. The conical island is $0.8D$ high with diameters of $8.0D$ at the toe and $1.6D$ at the crest, and the slope is 1:4. The incident planar solitary wave with $H/D = 0.5$ is considered here. The computational domain, which has a length of $14.0D$, width of $8.0D$, and height of $2.0D$, is discretized by a $350 \times 80 \times 70$ grid in the normalized streamwise (X), spanwise (Y) and vertical (Z) directions, respectively. The grid is uniform in the x and y directions, and nonuniform (finer meshes in the vicinity of the water surface) in the z direction, with minimum meshes of $\Delta x/D = 0.04$, $\Delta y/D = 0.1$

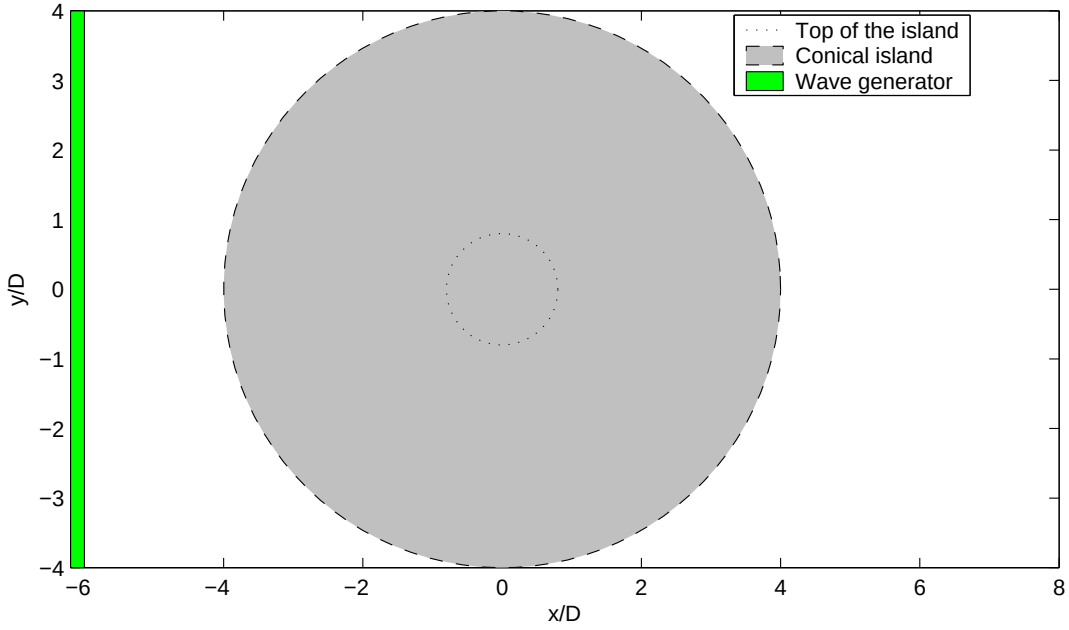

(a) top view

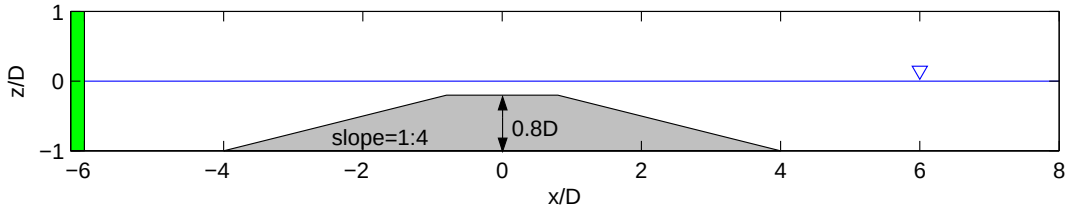

(b) side view

Figure 6.6: Sketch of computational domain for overturning waves over a submerged conical island.

and $\Delta z/D = 0.02$. This work was undertaken on the White Rose Grid and the CPU time was approximately 30h.

6.6.3 Water Surface Profiles and Kinematics

Figures 6.7-6.10 show a sequence of snapshots of water surface profiles during wave overturning over a submerged conical island. The color contour on the water surface represents the distribution of normalized velocity components u, v and w, respectively.

When the wave approaches the submerged island at $t = 1.0$ s (figure 6.7), there is only a small change in the shape of the incident planar wave, and the crest line is nearly straight and parallel to the spanwise direction. The velocity component u has similar magnitude on the front and rear face of the wave, with higher value in the vicinity of the wave crest. The velocity component w is nearly symmetrical with respect to the crest line, which follows the elliptical water particle trajectory. Both u and w velocities resemble the feature of 3D planar waves, however, the velocity component v is still small compared to u and w. Due to the change of bottom topography and wave scattering by the submerged island, it can be seen that the water moves towards both sides in front of the island whereas it moves towards the central plane in the rear side of the island. It is noted that the spanwise velocity is higher on the rear side than that on the front side of the island.

When the wave arrives at the crest of the submerged island at $t = 1.4$ s (figure 6.8), there is a significant change in the wave shape which leads to a three-dimensional wave profile. The wave profile is nonuniform in the spanwise direction and the crest line becomes a curve instead. The streamwise velocity u is highest in the central plane and gradually decreases at both sides, and the maximum value increases from $0.4C$ ($t = 1.0$ s) to $0.6C$ ($t = 1.4$ s). The vertical velocity w becomes asymmetrical and the magnitude in the positive direction is twice that in the negative direction. The highest vertical velocity is located in the central plane similar to the streamwise velocity. The spanwise velocity v increases from $0.02C$ ($t = 1.0$ s) to $0.1C$ ($t = 1.4$ s) during wave passing the island, which

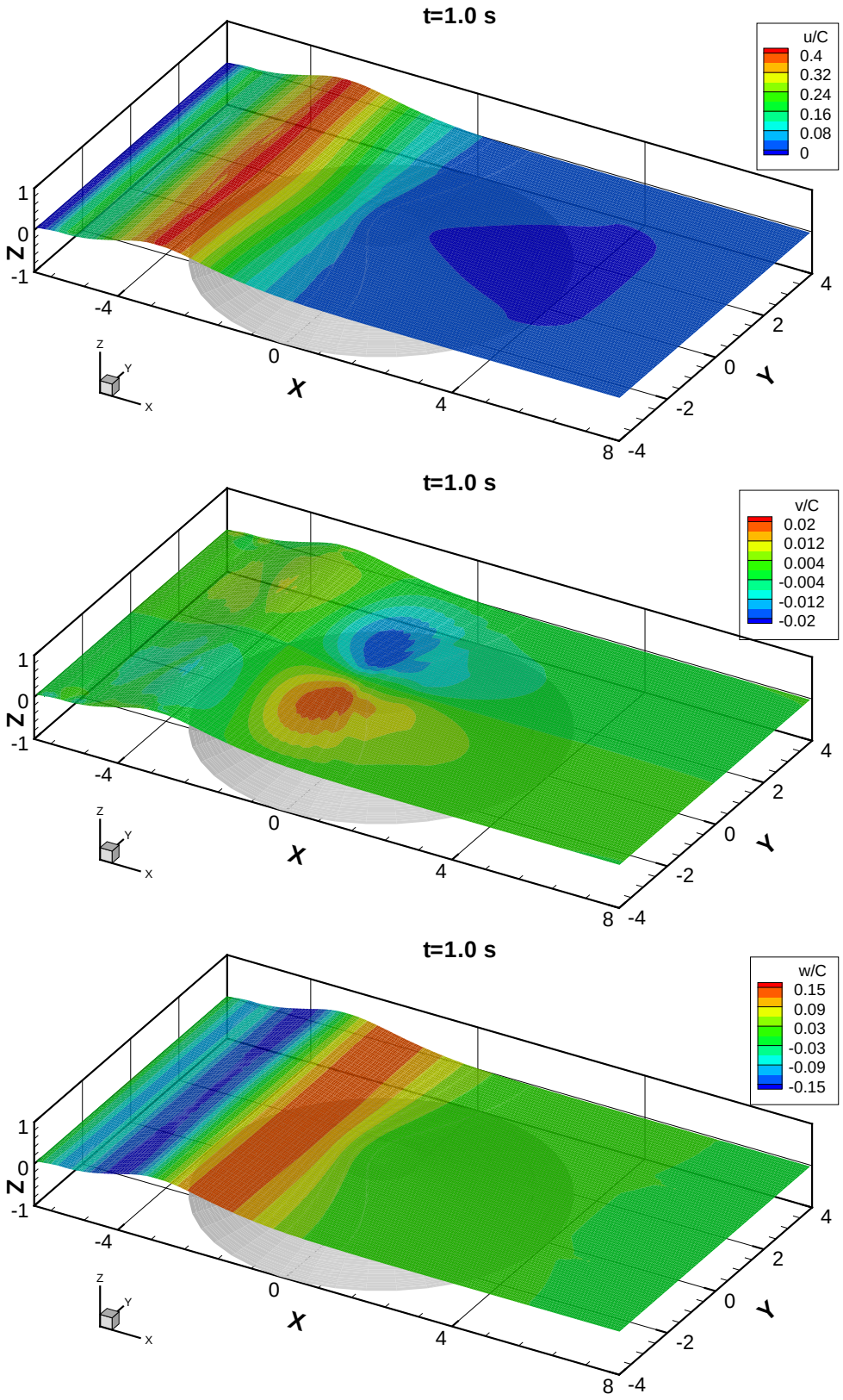

Figure 6.7: Snapshots of water surfaces during wave overturning over a submerged conical island at $t = 1.0$ s. The water surfaces are colored based on local values of normalized velocity component u/C (top), v/C (middle) and w/C (bottom), respectively.

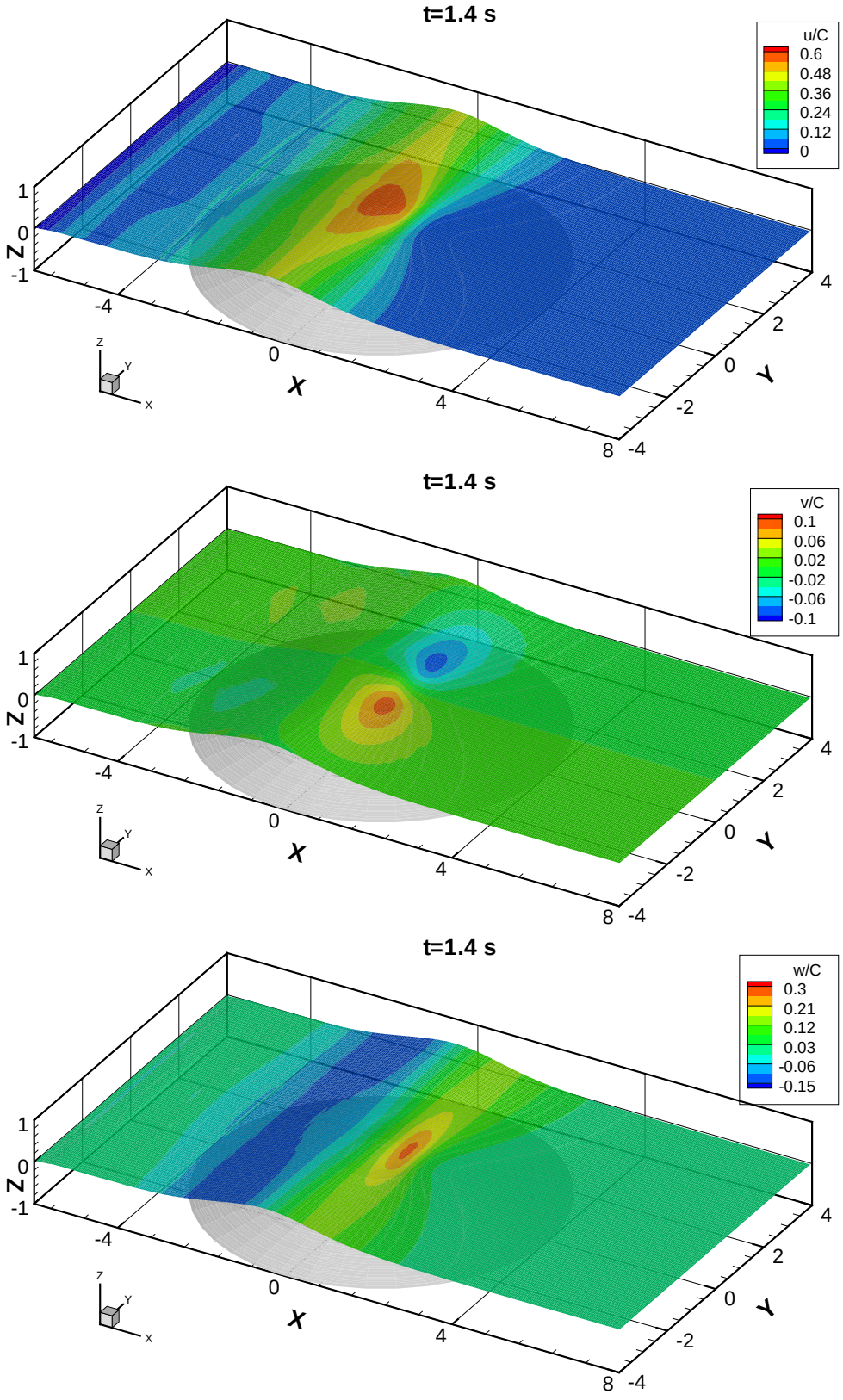

Figure 6.8: As in figure 6.7, but at $t = 1.4$ s.

can be clearly seen on the front face of the wave. All these phenomena are related to focusing of the wave over the submerged island.

Because the wave in the central plane propagates faster due to wave focusing after the island, the wave crest plunges forward to overturn when passing the crest of the submerged island at $t = 1.8$ s. A three-dimensional overturning wave can be easily seen in figure 6.9. During wave overturning, it is shown that the streamwise velocity u in the plunging jet is higher than the wave phase speed C, which is consistent with the common sense criterion that $u/C \geq 1$ during wave breaking. Far from the central plane, the streamwise velocity is less than the wave phase speed C and the wave propagates forward without breaking. The vertical velocity w is positive on the front face of the wave and negative on the rear face and the tip of the plunging jet. At this moment, the overturning wave starts to curl down as it can be seen from the sign of the vertical velocity. During wave overturning, the spanwise velocity v in the plunging jet is very small and the highest spanwise velocity is located near the toe of the plunging jet on both sides.

At $t = 2.0$ s (figure 6.10), the plunging jet curls down and impinges on the water surface ahead to generate the splash-up, and an air cavity is enclosed beneath the overturning jet. During the wave splash-up, breaking region gets wider as time increases when more of the wave plunges forward and it is apparent that $u/C \geq 1$ is observed in the plunging jet and the subsequent splash-up. The vertical velocity w is different from that during wave overturning, as the plunging jet moves downward before the plunging point and upward after the plunging point. Contrast to the spanwise velocity v in the plunging jet during wave overturning, it changes significantly during wave splash-up. The shoulders of the plunging jet move away from the tip whereas the top of the plunging jet moves towards the central plane. Wave scattering by the island can also be observed from the spanwise velocity on the back face of the wave.

By comparing the velocity components u, v and w from the stage when the wave approaches the island to the overturning stage, it is shown that there is a significant change in surface velocities within the crest of the submerged island near the central plane. The maximum u velocity is tripled during wave overturning which means that the strongest motion is in the longitudinal direction. For

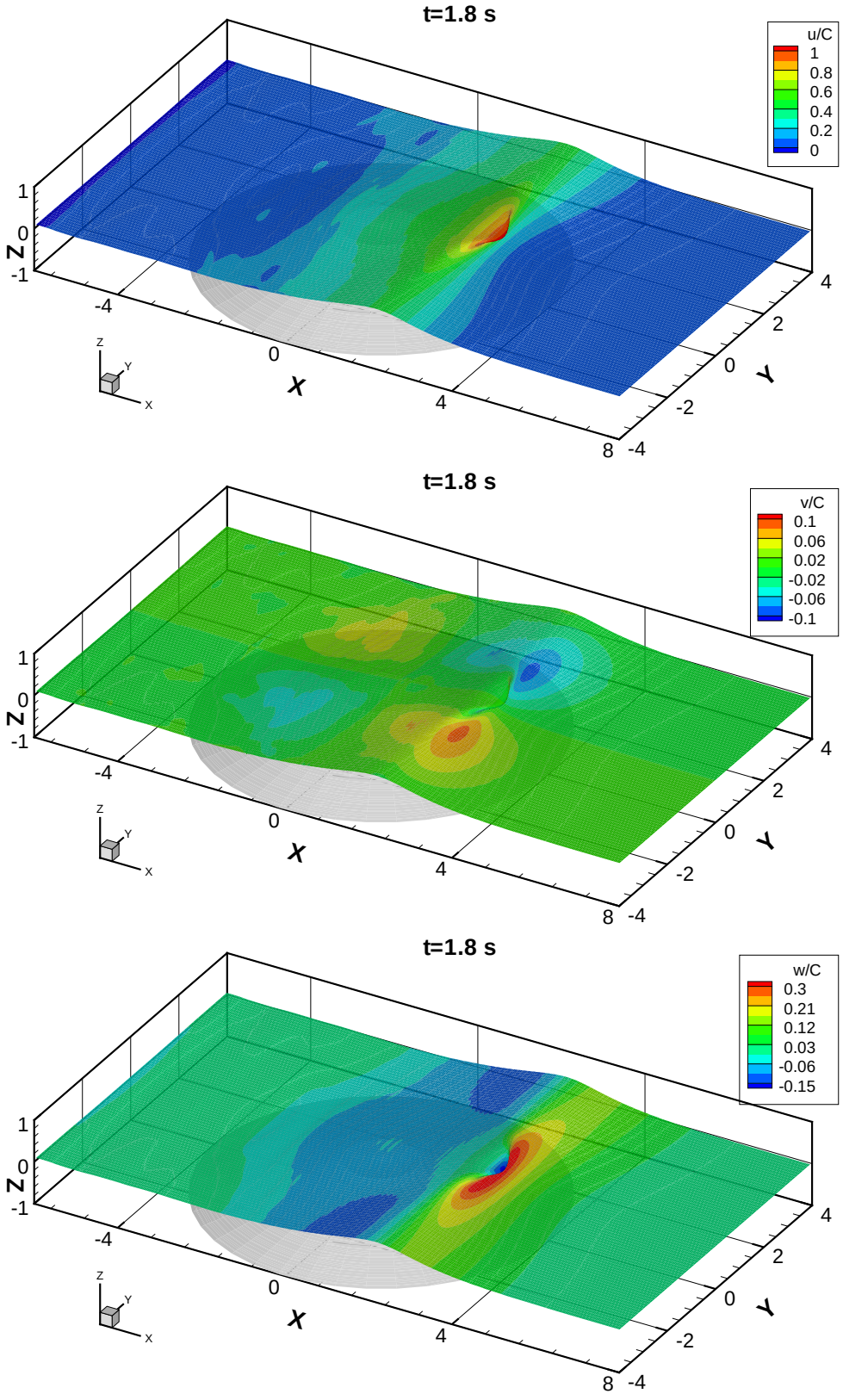

Figure 6.9: As in figure 6.7, but at $t = 1.8$ s.

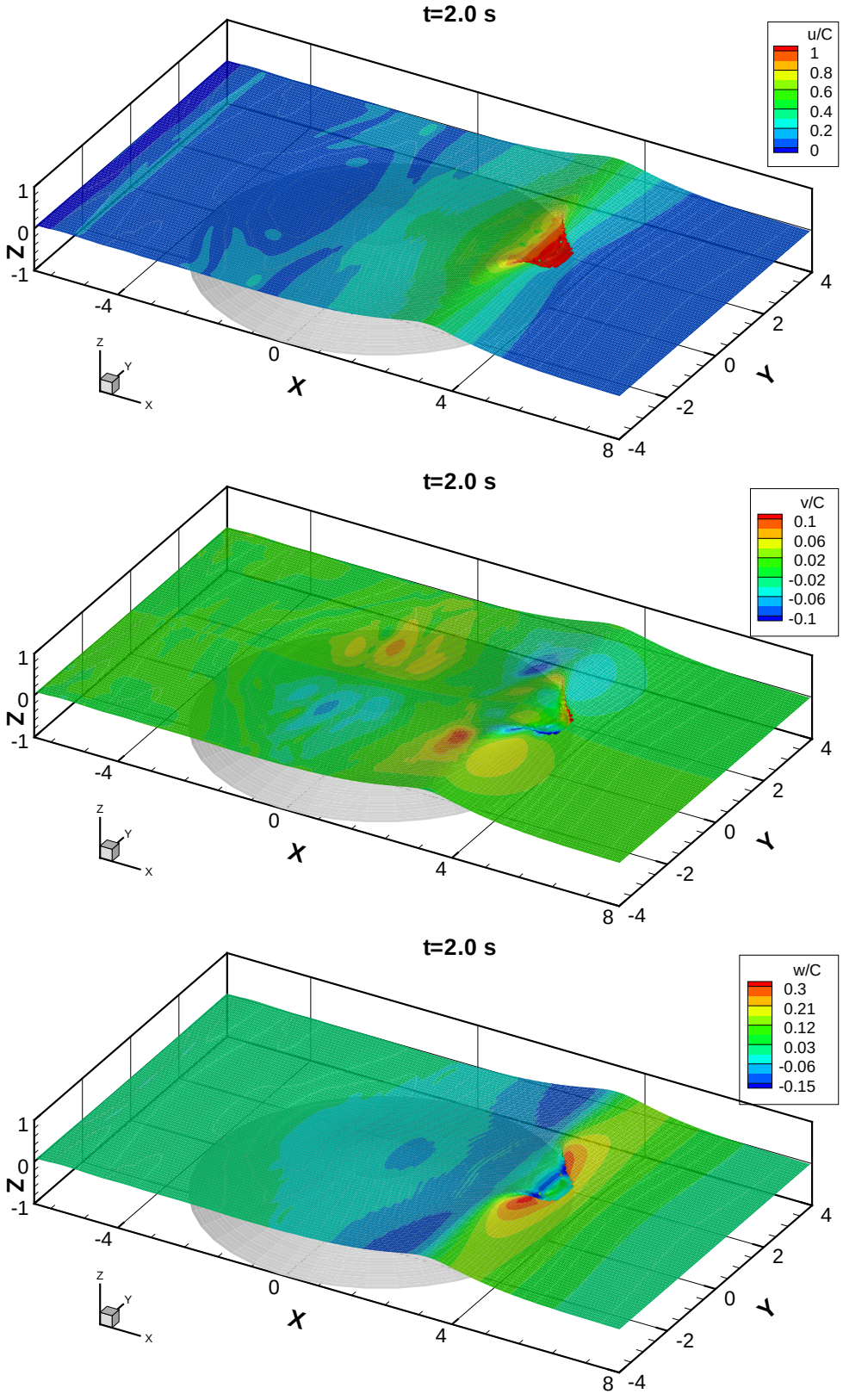

Figure 6.10: As in figure 6.7, but at $t = 2.0$ s.

the magnitude of vertical velocity w, the positive w on the front face of the wave is doubled, whereas the negative w on the back face of the wave is nearly unchanged. The spanwise velocity v is initially zero and gradually increases when the wave passes the submerged island. The region of large v values increases significantly when the plunging jet impinges on the water surface ahead. But in general, the spanwise motion of the wave, which is important in generating convergence and enhancing flow near the centreline, is weakest compared to the longitudinal and vertical motions.

Figure 6.11 shows detailed views of the overturning wave during and after wave breaking. Perspective, side and front views are shown in the top, bottom left and bottom right, respectively. A typical three-dimensional overturning jet can be seen in figure 6.11(a) during wave breaking and the width of the overturning jet is about half of the crest diameter of the submerged island. A tube is formed beneath the overturning wave during the splash-up shown in figure 6.11(b) and the width of the overturning jet increases as more of the wave plunges forward. It is worth remarking that the overturning waves are different between 2D and 3D simulations. In 2D, the air is enclosed by the overturning jet, but in 3D, the air in the tube can escape in the spanwise direction.

6.6.4 Velocity Fields

3D velocity vectors

Figure 6.12 shows a sequence of three-dimensional velocity vectors corresponding to the water surface profiles shown in § 6.6.3 for $t = 1.0$ s and $t = 1.8$ s. All velocity vectors are normalized by the wave phase speed $C = 2.17$ m/s and only velocity vectors in the water are shown for clarity. It is shown that the velocities increase from the bottom to the water surface and large velocity vectors are located under the crest of the wave. It is apparent that the wave is dominated by the longitudinal motion and the spanwise motion is very weak. The velocity is highest near the central plane and maximum velocity vector is observed during wave overturning.

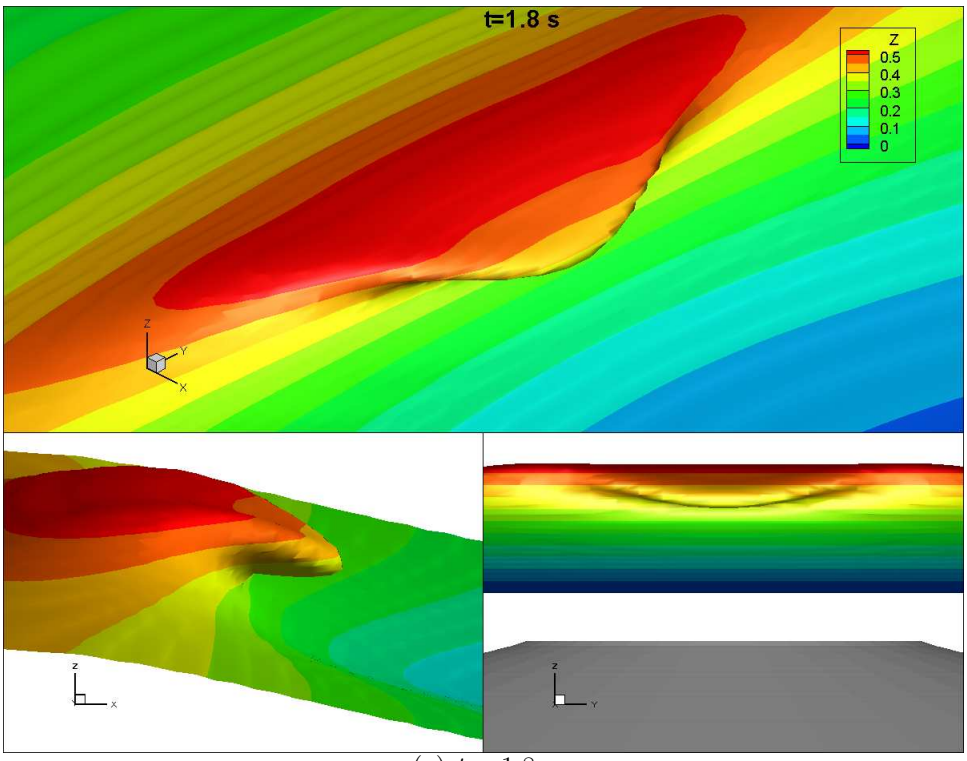

(a) $t = 1.8$ s

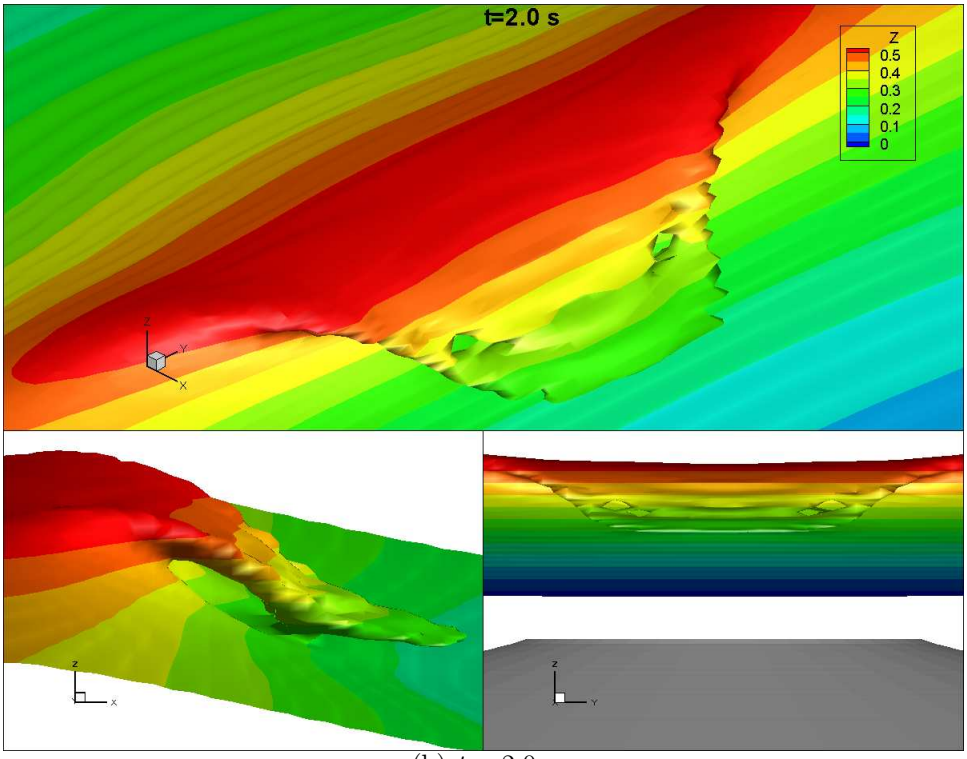

(b) $t = 2.0$ s

Figure 6.11: Detailed views of the overturning wave from different angles during (a) and after (b) wave breaking. The water surfaces are colored based on local values of z/D.

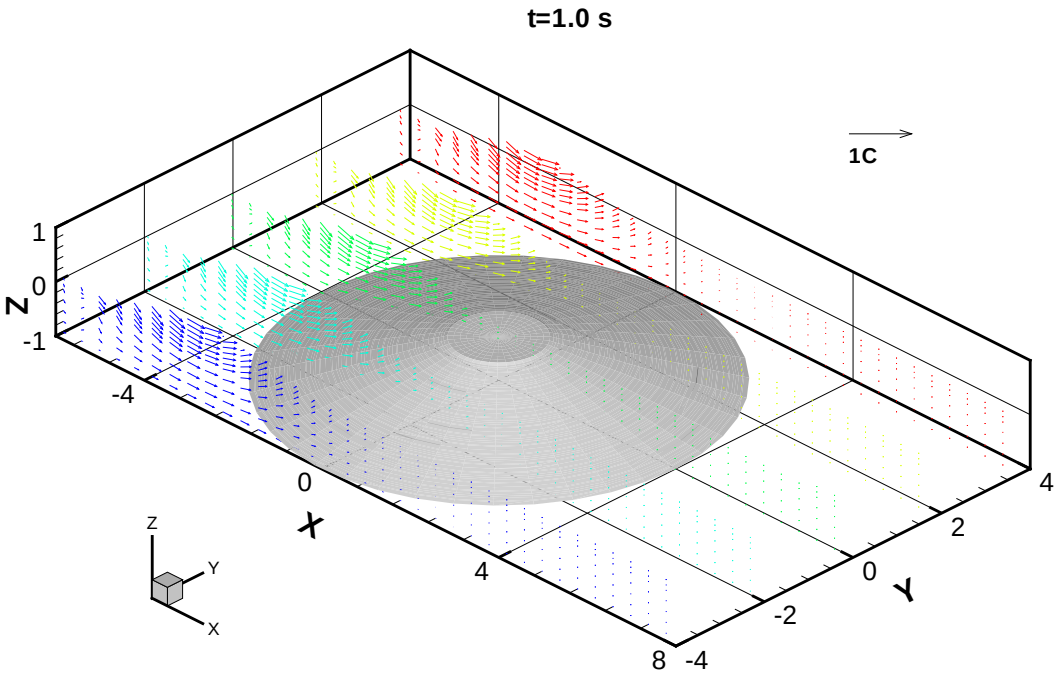

(a)

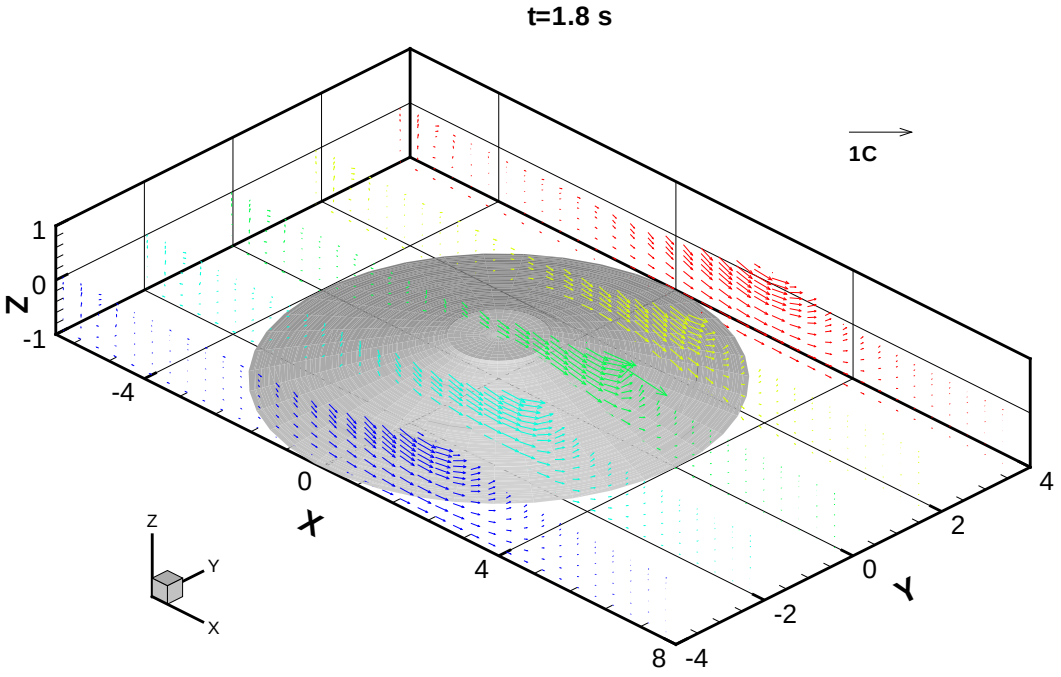

(b)

Figure 6.12: Snapshots of 3D velocity field during wave overturning over a submerged conical island.

Evolution of velocity vectors in Y-planes

Figure 6.13 shows the evolution of the velocity vectors in the vertical Y-planes. The velocities in the central plane ($Y = 0$) are shown on the top, whereas the velocities near the edge of the computational domain ($Y = -3.9$) are presented on the bottom. When the wave approaches the submerged island (figures 6.13(a)), there is nearly no change of the water surface between the centre and edge, and thus the flow patterns in two planes are very similar, apart from the area near the island. Recirculation of air flow can be clearly seen above the crest of the wave as the air is driven by the water. When the wave arrives at the crest of the island (figure 6.13(b)), due to wave focusing after the island, the wave in the central plane moves faster and this is evident by comparing the water surface profiles and the velocities near the centre of the island. Up to this stage, there is no significant change in the flow pattern near the edge plane. During wave overturning over the submerged conical island (figure 6.13(c)), large velocity vectors are observed beneath the plunging jet as the air tries to escape from the enclosed cavity. The velocity vectors in the wave crest are nearly horizontal during wave breaking. In contrast to the central plane, the wave near the edge plane is moving with lower speed without wave breaking.

Velocity vectors in Z-planes

Figure 6.14 shows the velocity vectors of the horizontal Z-planes in the water. Two instantaneous results when the wave approaches the island ($t = 1.0$ s) and when the wave passes the island ($t = 1.8$ s) are presented, respectively. Three Z-planes corresponding to the bottom ($z/D = 0.02$), middle ($z/D = 0.14$) and top ($z/D = 0.30$) layers of the water are shown. It is apparent that the wave is scattered by the submerged island as the water moves towards both sides in front of the island and towards the central plane in the lee side of the island. It is worth noting that the horizontal velocities increase from the bottom to the top layer of the water, which is inconsistent with the uniform horizontal velocity assumptions in depth-integrated models.

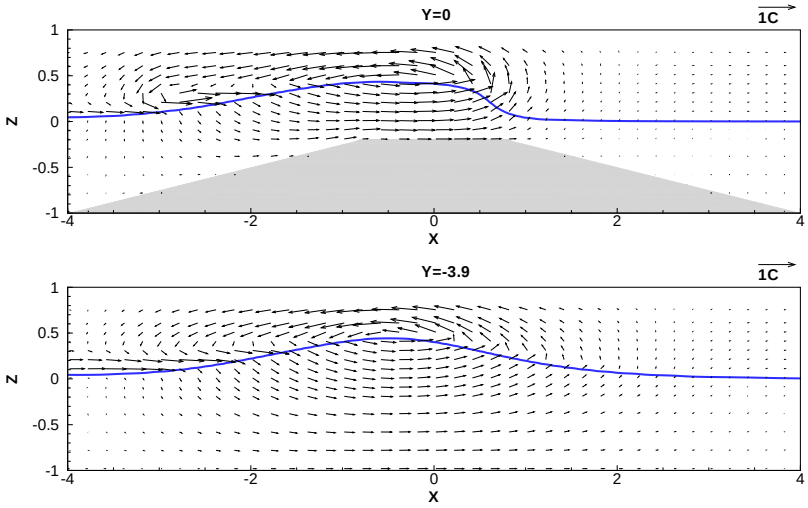

(a) $t = 1.0$ s

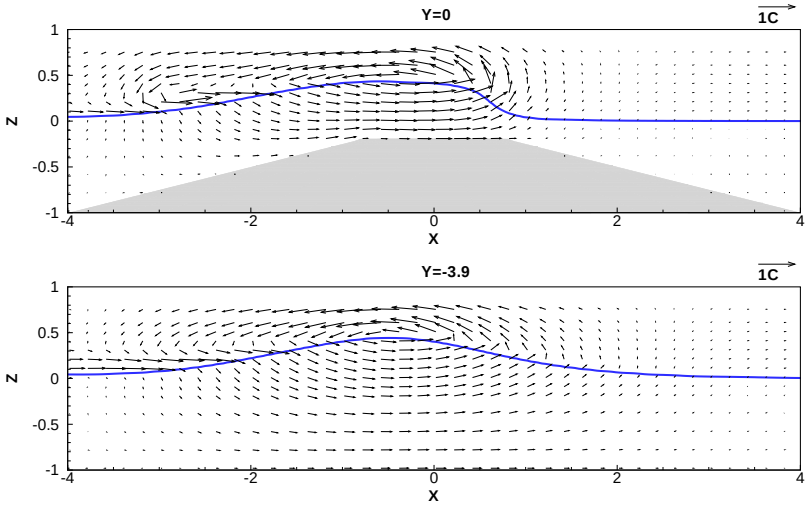

(b) $t = 1.4$ s

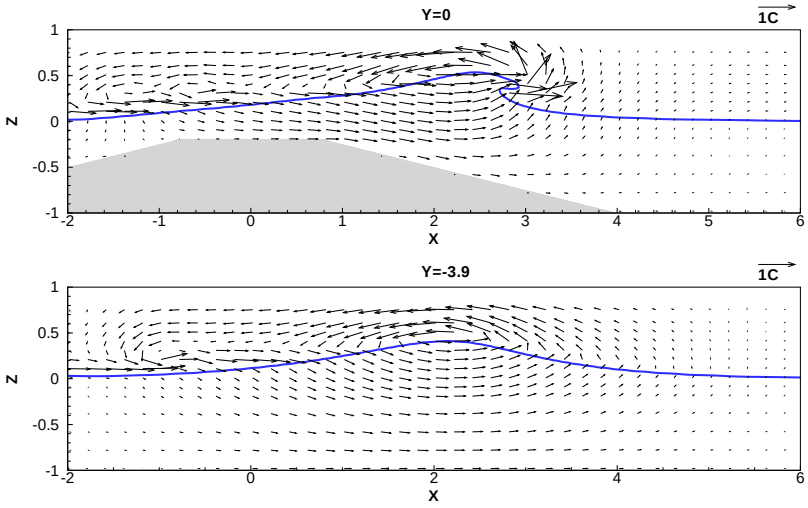

(c) $t = 1.8$ s

Figure 6.13: Evolution of the velocity vectors in the vertical Y-planes at different times. Top is in the centre and bottom is near the sidewall.

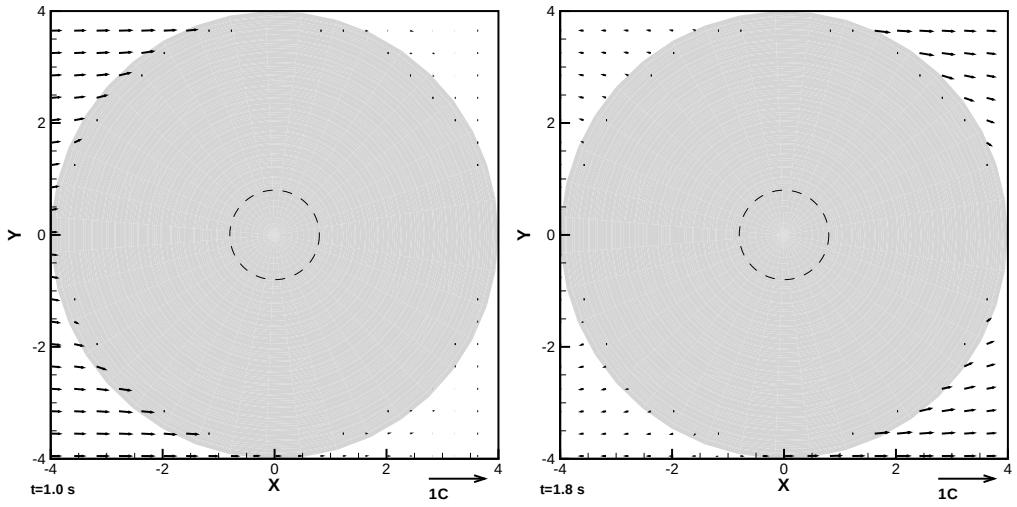

(a) bottom

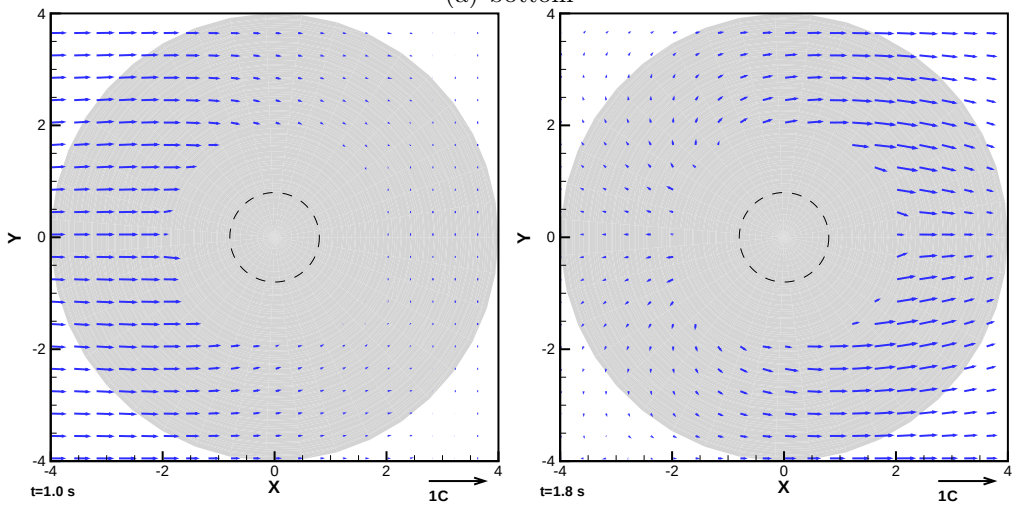

(b) middle

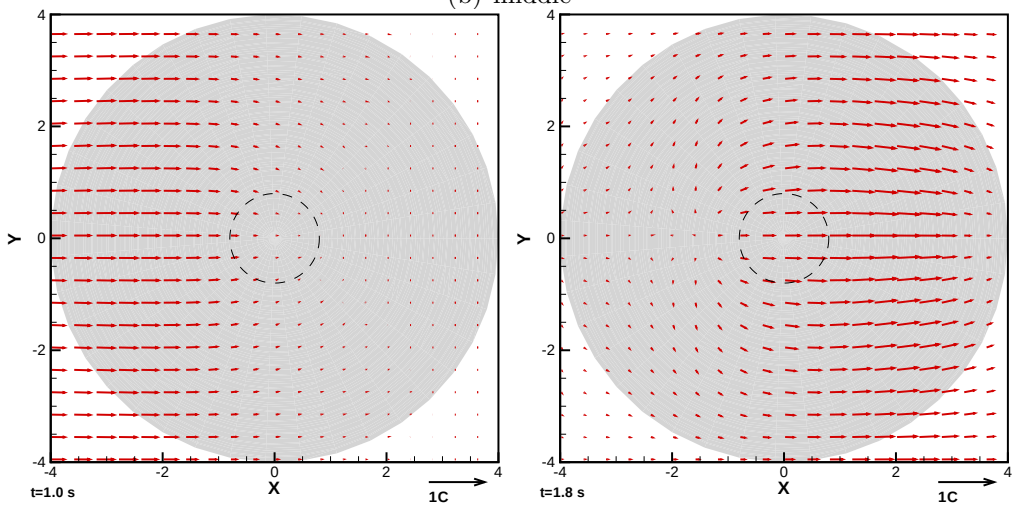

(c) top

Figure 6.14: Velocity vectors of the horizontal Z-planes in the water. Left column is when $t = 1.0$ s and right column is when $t = 1.8$ s.

Velocity vectors in X-planes

Figure 6.15 shows velocity vectors of vertical X-planes, from the front edge ($X = -4$) to the rear edge ($X = 4$) of the island, during wave breaking at $t = 1.8$ s. It is observed that the wave moves away from the island on the front side of the island ($X = -4$ to $X = 0$) due to wave scattering, whereas the wave moves towards the island on the rear side of the island ($X = 2$ and $X = 4$) due to wave focusing. $X = 2$ plane is near the crest of the wave and it is shown that large velocity vectors are located near the water surface as the wave overturns and curls down. It is noted that the water moves upward on the front face of the wave ($X = 4$), whereas the water moves downward on the back face of the wave ($X = -4$ to $X = 2$).

6.6.5 Vorticity

In this section we analyze the generation of three-dimensional vorticity under breaking waves. The streamwise, spanwise and vertical vorticities are defined as

$$\omega_x = \frac{\partial w}{\partial y} - \frac{\partial v}{\partial z}, \tag{6.23}$$

$$\omega_y = \frac{\partial u}{\partial z} - \frac{\partial w}{\partial x}, \tag{6.24}$$

$$\omega_z = \frac{\partial v}{\partial x} - \frac{\partial u}{\partial y}. \tag{6.25}$$

The vorticities are normalized by $\sqrt{g/(H+D)}$ in the following analysis.

Figure 6.16 shows the isosurfaces of the streamwise, spanwise and vertical vorticities in the water, as well as the water surface profile. Due to wave scattering by the island, the counter-rotating streamwise vorticities are generated on the back face of the wave. Large negative spanwise vorticities are observed on the tip of the overturning jet. Counter-rotating streamwise and vertical vorticities arise surrounding the overturning jet, generating a three-dimensional vorticity field, which is consistent with the previous numerical study of three-dimensional vortex structures under breaking waves (Watanabe *et al.*, 2005).

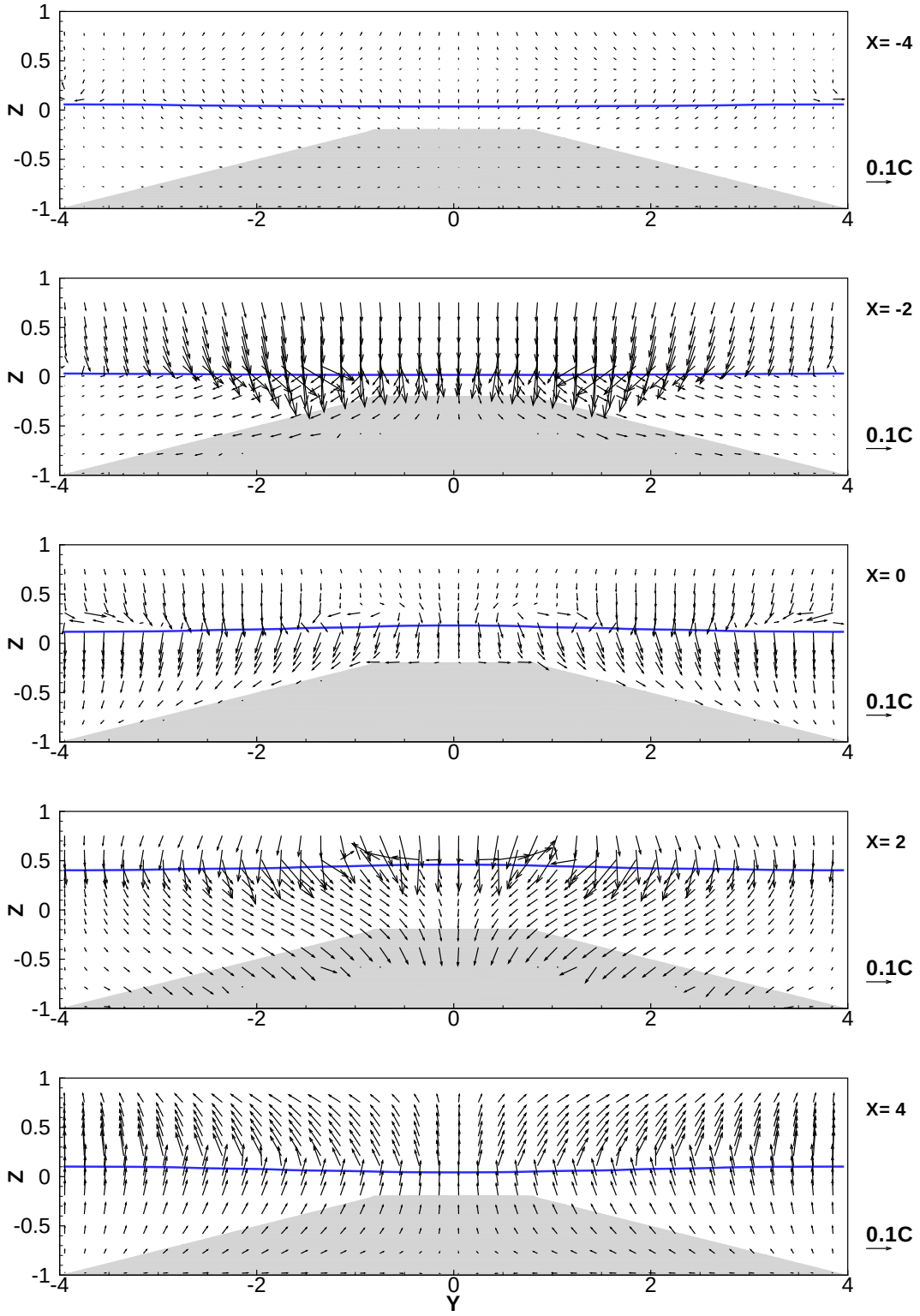

Figure 6.15: Velocity vectors of the vertical X-planes during wave breaking at $t = 1.8$ s.

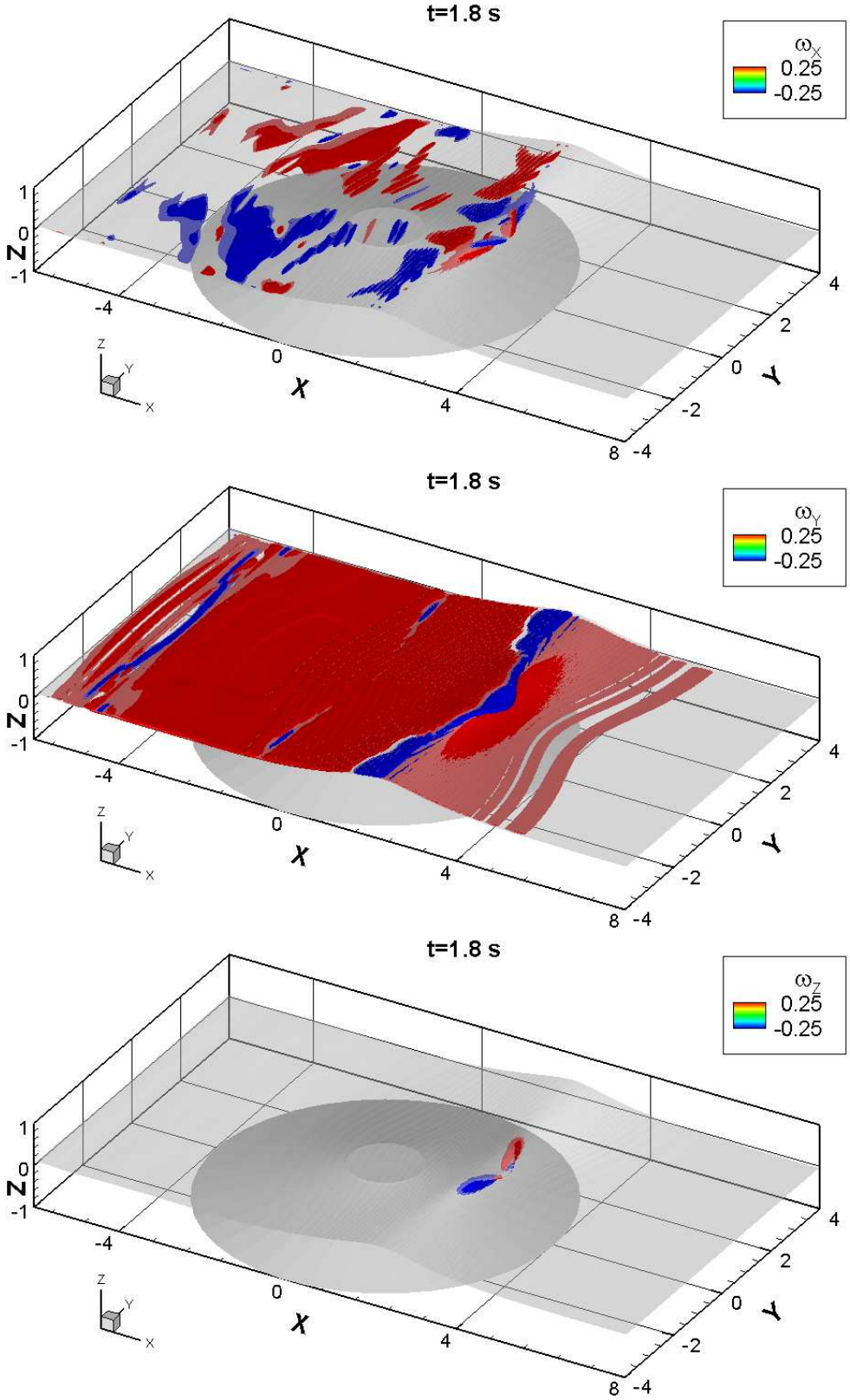

Figure 6.16: Isosurfaces of the streamwise (top), spanwise (middle) and vertical (bottom) vorticity during wave breaking at $t = 1.8$ s. Isosurfaces are only shown for the value ± 0.25.

6.6.6 Energy Dissipation and Transformation

Here, the energy dissipation and transformation for the overturning wave over the submerged conical island is studied. It is worth emphasizing that the energy defined here is calculated in the whole computational domain, rather than in a fixed volume of water in one wave length. The kinetic energy (KE), potential energy (PE) and total energy (TE) are obtained as (Dean & Dalrymple, 1984)

$$\mathrm{KE} = \iiint_{F\neq 0} \rho \frac{(u^2+v^2+w^2)}{2} \mathrm{d}z\mathrm{d}x\mathrm{d}y, \tag{6.26}$$

$$\mathrm{PE} = \iiint_{F\neq 0} \rho g z \mathrm{d}z\mathrm{d}x\mathrm{d}y - \left[\iiint_{F\neq 0} \rho g z \mathrm{d}z\mathrm{d}x\mathrm{d}y\right]^{t=0}, \tag{6.27}$$

$$\mathrm{TE} = \mathrm{PE} + \mathrm{KE}. \tag{6.28}$$

In order to study the effect of the submerged island on water waves, another simulation is performed for the flat bottom case. Figure 6.17 shows the time history of normalized energy for the overturning wave over the submerged conical island, together with the corresponding energy when there is no island. All energies increase up to $t = 1.0$ s as the wave propagates into the computational domain and decrease after $t = 2.0$ s as the wave leaves the domain.

When there is no island, it is shown that the energies decrease slightly due to the viscous dissipation and there is no significant energy transformation between the kinetic and potential energies. When the submerged island is present, there is more energy dissipation compared to the case in the absence of island as the wave breaks. Due to the bathymetry of the island, the kinetic energy is converted to the potential energy when the wave approaches the island. When the wave arrives at the crest of the island, the potential energy is converted back to the kinetic energy, which attains its maximum value during wave breaking. After wave breaking, the kinetic energy decreases and potential energy increases slightly during the jet-splash cycles.

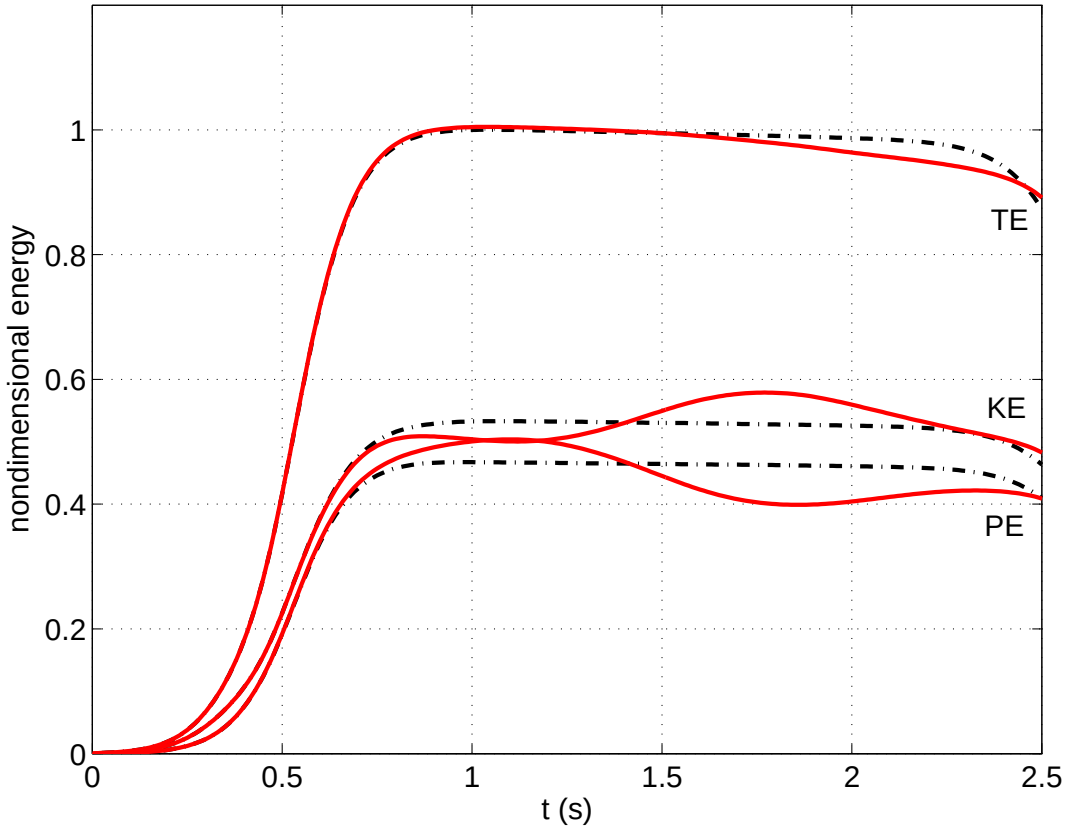

Figure 6.17: The time history of the normalized energy for the overturning wave over a submerged conical island (red solid lines) and a flat bottom (black dash-dotted lines). The energies have been normalized by the total energy $E_0 = [\text{TE}]$ for the flat bottom case at $t = 1.0$ s when the solitary wave nearly completely enters the computational domain.

6.7 3D Overturning Waves under the Influence of Wind

6.7.1 Introduction

In the previous section (§ 6.6), three-dimensional overturning waves over a submerged conical island are studied. In this section, 3D overturning waves under the influence of wind are going to be investigated and discussed. Since there are many similarities for the breaking waves if the wind is present or absent, we focus on the wind effects on overturning waves and differences between these two cases.

6.7.2 Computational Setup

The computational setup is the same as that in § 6.6, except that a uniform wind speed $U/C = 2$ is specified at the inlet.

6.7.3 Water Surface Profiles and Kinematics

Figures 6.18–6.21 show a sequence of snapshots of water surface profiles for 3D overturning waves under the influence of wind over a submerged conical island. The color contour on the water surface represents the distribution of normalized velocity components u, v and w, respectively. It is shown that water surface profiles and wave kinematics are very similar to those shown in figures 6.7–6.10 where the wind speed is $U/C = 0$ due to the short upstream fetch considered in this study. In contrast to the surface velocities u, v and w when $U/C = 0$, it is apparent that there is a significant change of the surface velocities on the back face of the wave and there is a slight change on the front side of the wave. The spanwise velocity v is strengthened whereas the vertical velocity w is weaken under the influence of wind. The streamwise velocity u on the back face of the wave increases due to wind forcing and a larger region with $u/C \geq 1$ is observed in the overturning jet. The wave breaks earlier and closer to the submerged island due to the wind pushing.

Figure 6.22 shows the evolution of water surface profiles in the central plane for different wind speeds. There is not much difference before wave breaking and

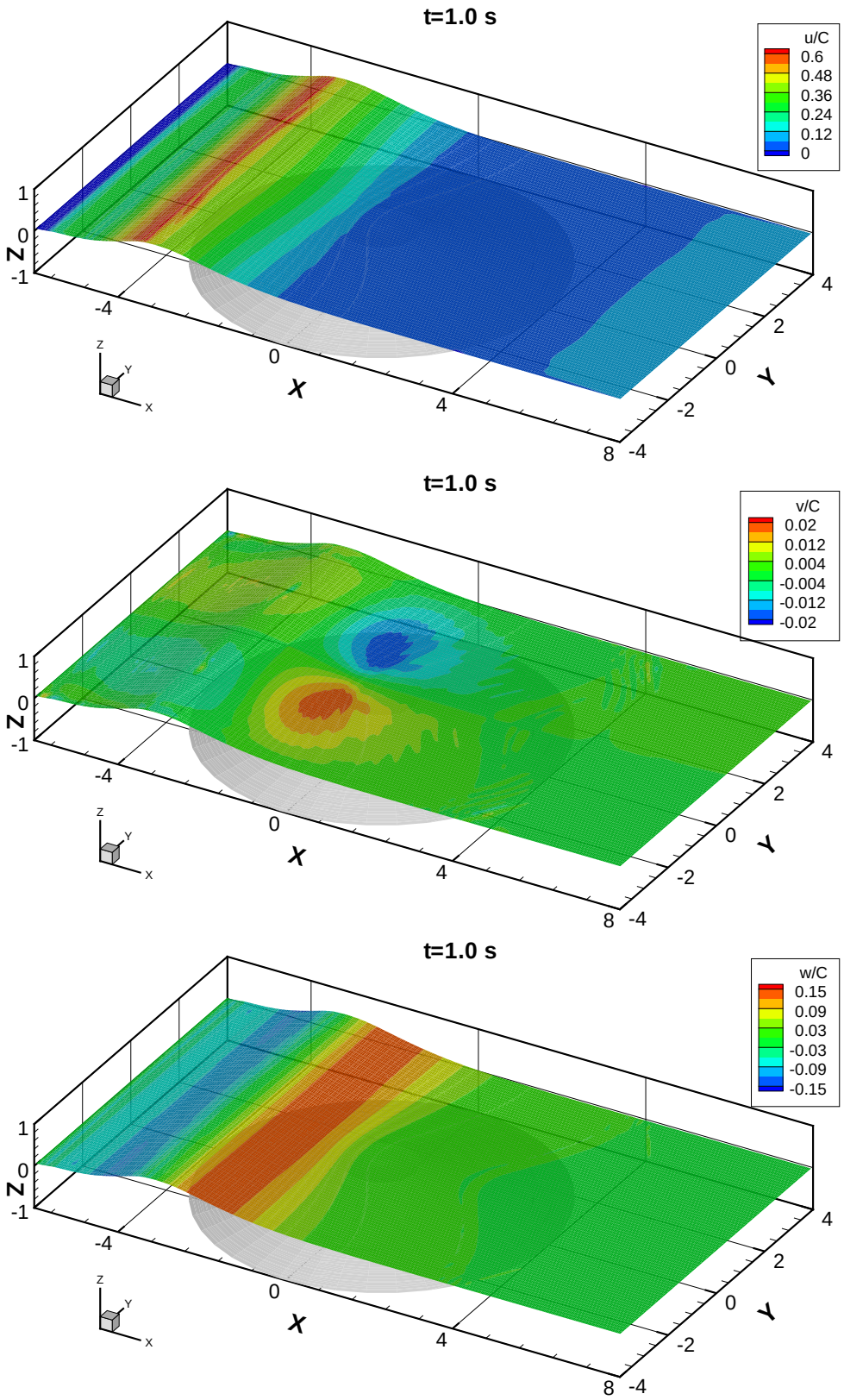

Figure 6.18: Snapshots of water surfaces during wave overturning under the influence of wind $U/C = 2$ over a submerged conical island at $t = 1.0$ s. The water surfaces are colored based on local values of normalized velocity component u/C (top), v/C (middle) and w/C (bottom), respectively.

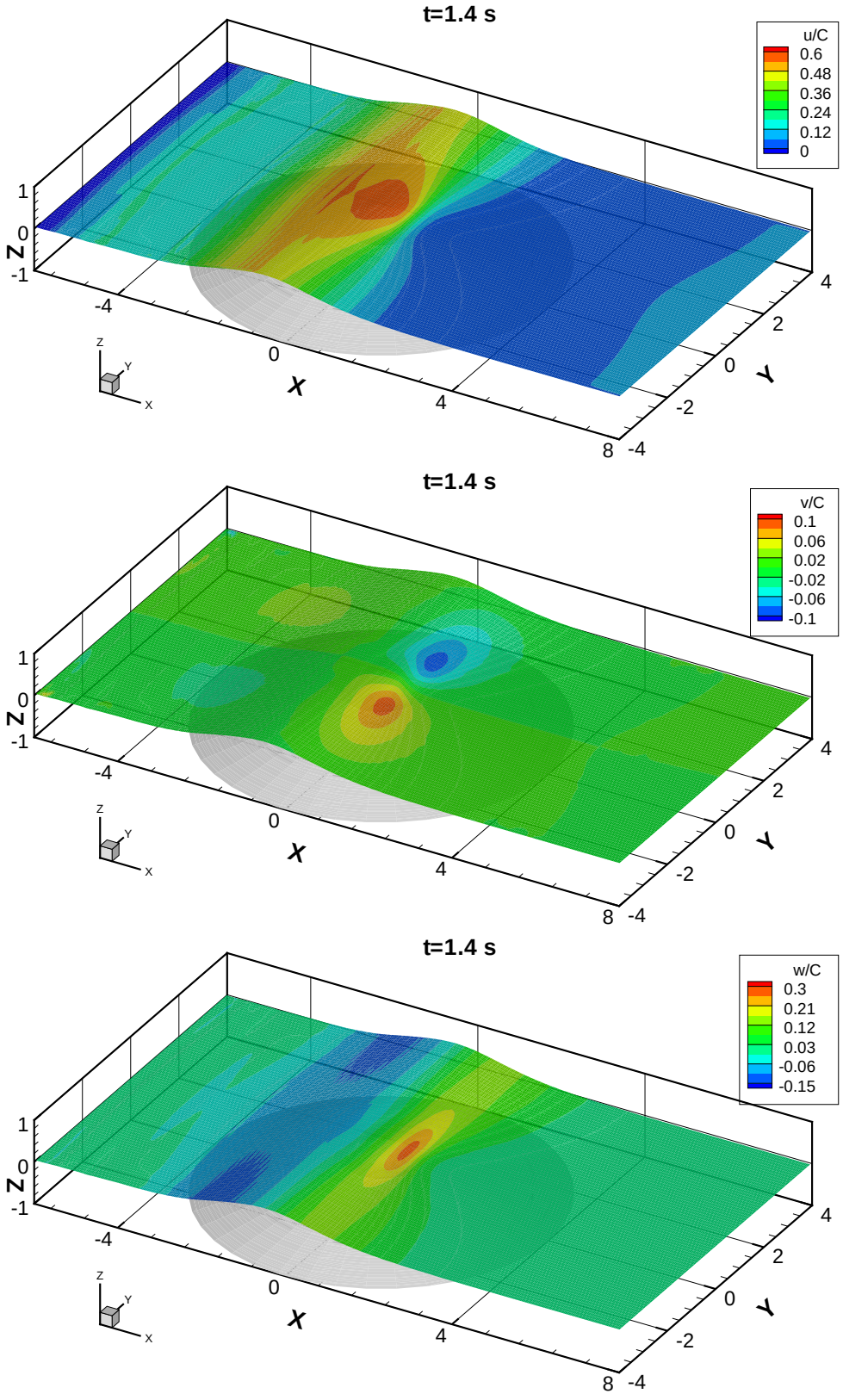

Figure 6.19: As in figure 6.18, but at $t = 1.4$ s.

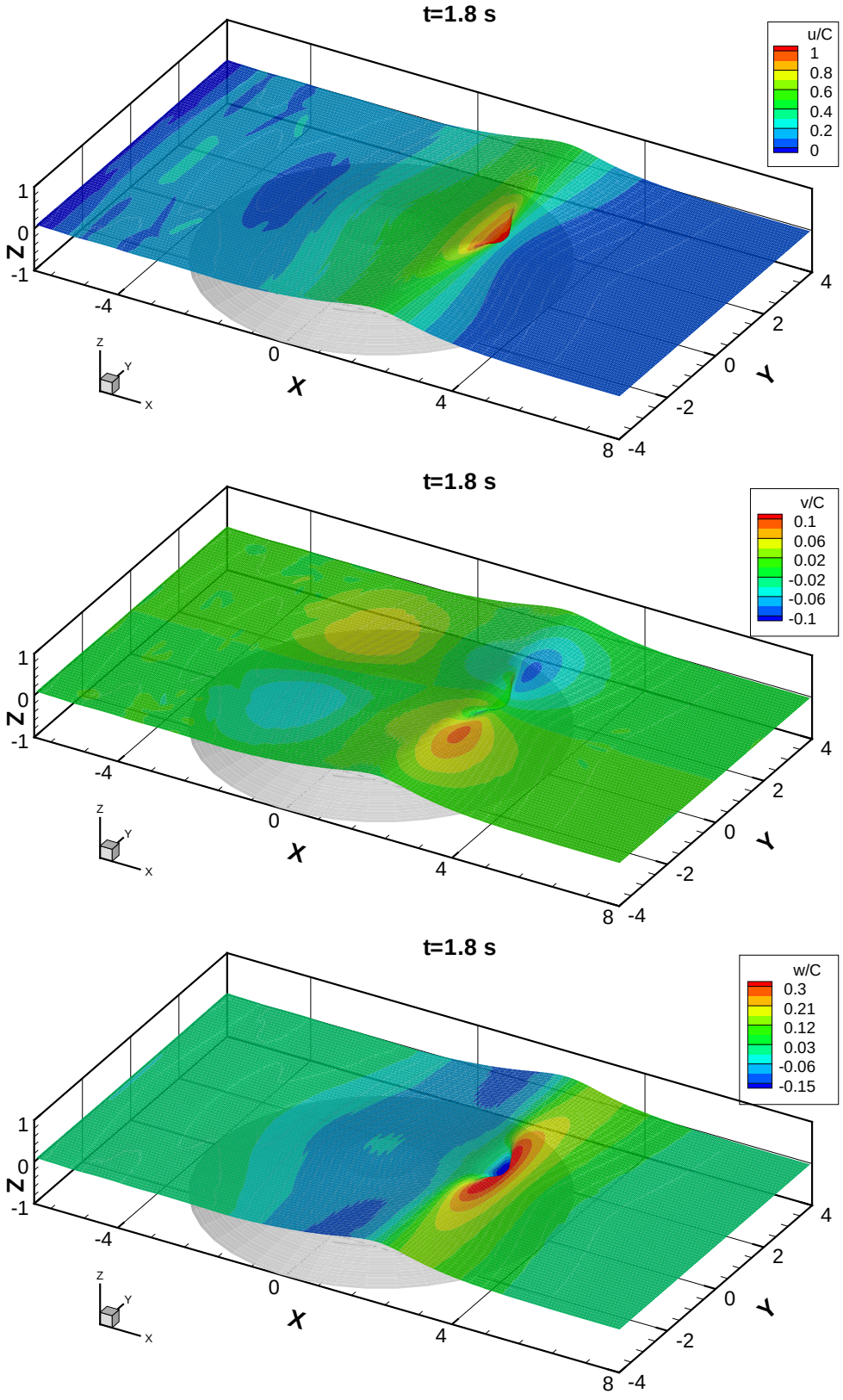

Figure 6.20: As in figure 6.18, but at $t = 1.8$ s.

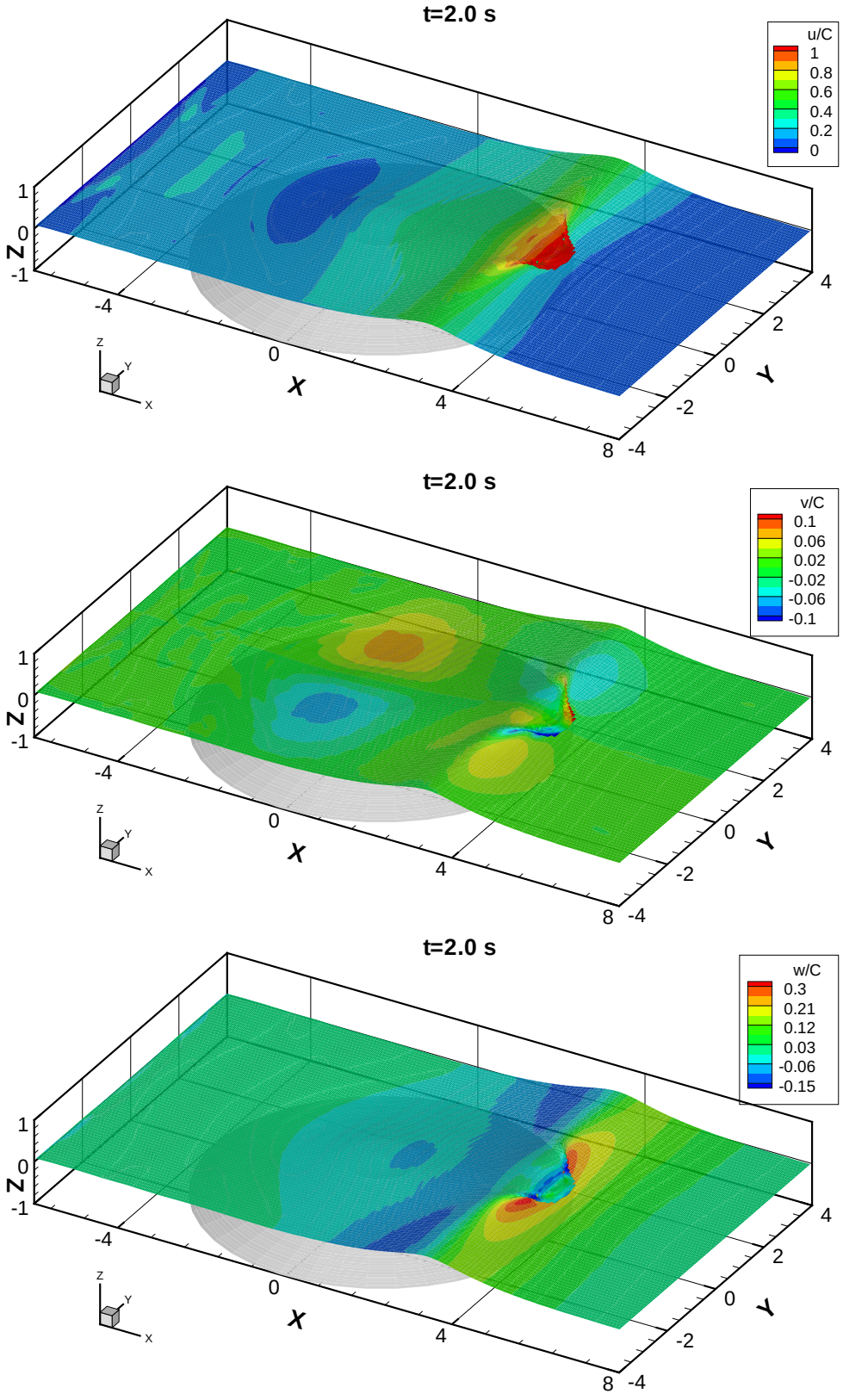

Figure 6.21: As in figure 6.18, but at $t = 2.0$ s.

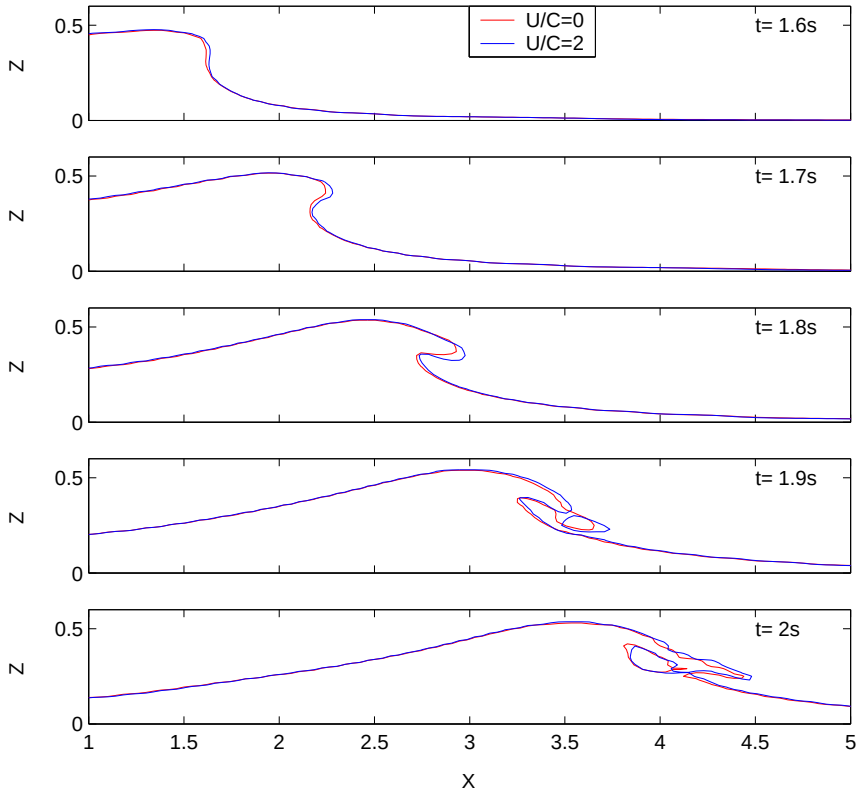

Figure 6.22: The evolution of water surface profiles between $t = 1.6 - 2.0$ s for different wind speeds: $U/C = 0$: red lines; $U/C = 2$: blue lines.

only the water surface profiles during wave overturning are shown for clarity. It is apparent that as the streamwise velocity u increases due to wind forcing, the wave moves faster and breaks earlier under the influence of wind. The wind also affects the shape of the enclosed cavity during the jet-splash cycles.

Figure 6.23 shows the time history of the maximum velocities in the wave for different wind speeds. It is apparent that the longitudinal motion is strongest and the spanwise motion is weakest which is consistent with foregoing discussion in §6.6.3. The effect of wind on the wave is dominated by its wind direction and the effect on other perpendicular directions is weak. Compared to the case $U/C = 0$, the maximum streamwise velocity increases when the wave passes the island under the influence of wind. The maximum spanwise velocity increases before wave breaking and decreases afterwards. The maximum vertical velocity

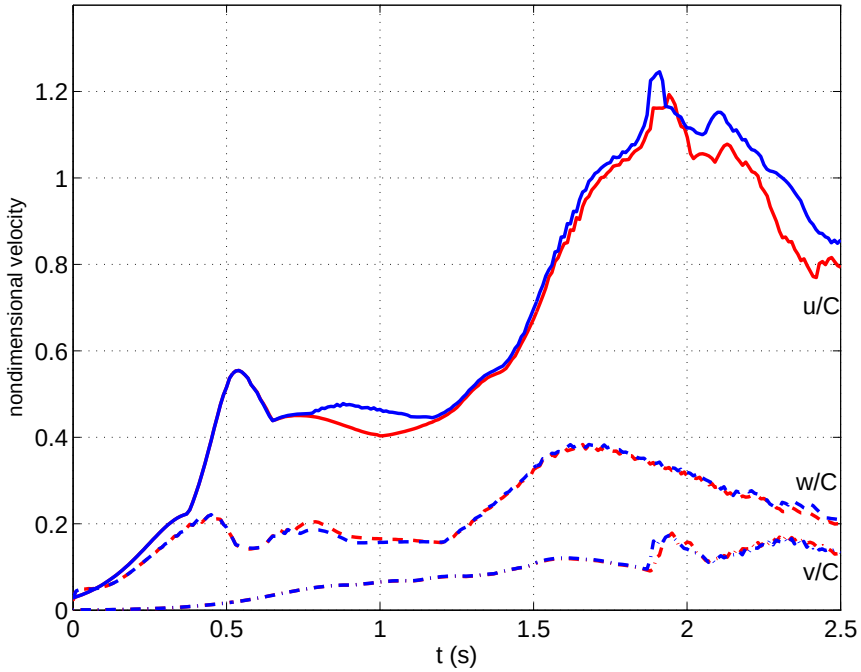

Figure 6.23: The time history of the maximum velocities in the wave for different wind speeds: $U/C = 0$: red lines; $U/C = 2$: blue lines.

decreases before the wave reaches the crest of the island and increases afterwards. There is a phase difference for the peak value of the maximum velocities between the two cases which indicates that the waves break at different times.

6.7.4 Velocity Fields

Evolution of velocity vectors in the vertical central plane

Figure 6.24 shows the evolution of the velocity vectors in the vertical central plane for the case $U/C = 2$. Compared to the case $U/C = 0$, the water surface profiles and velocities in the water are very similar. However, there is significant difference in the air flow as the recirculation of air above the wave crest does not exist when the wind is present. It is worth remarking that the air is driven by the wave when $U/C = 0$, whereas the wave is driven by the wind when $U/C = 2$. It is apparent that the air flow structure ahead of the wave front is very complex and changes gradually during wave overturning.

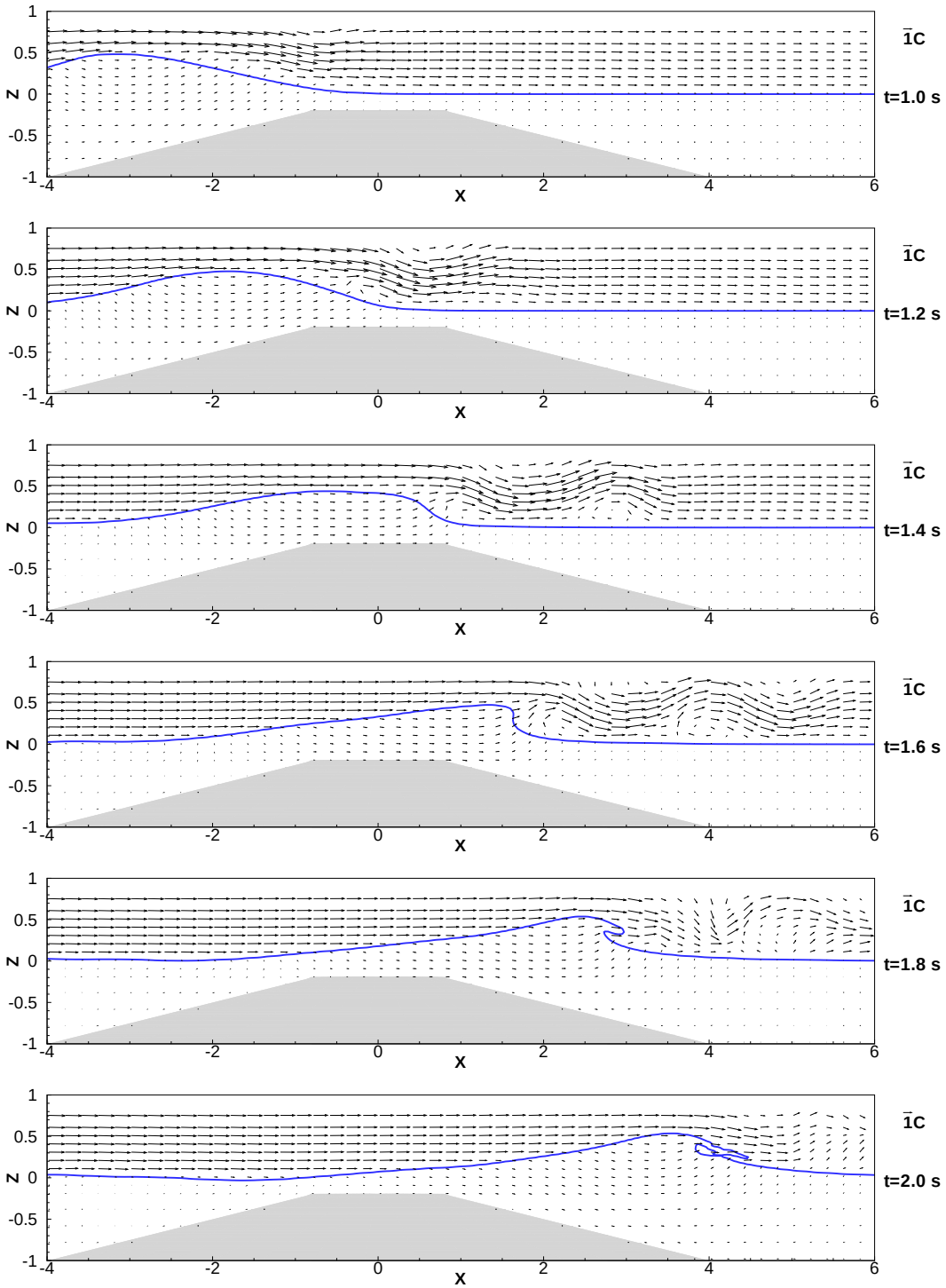

Figure 6.24: Evolution of the velocity vectors in the vertical central plane at different times for $U/C = 2$.

Cross sections

In order to investigate wind effects on the velocity fields in different planes, we present the results at a representative time $t = 1.8$ s during wave overturning under the influence of wind $U/C = 2$. Since the results are close to those for $U/C = 0$, only the differences are discussed here.

Figure 6.25 shows the velocity vectors of the vertical X-planes. The velocity vectors in the air are totally different from those for $U/C = 0$. On the back face of the wave, the wave goes downward whereas the air goes upward due to wind forcing. Recirculation of air flow with large velocity vectors is observed in front of the overturning jet.

Figure 6.26 shows the velocity vectors of the vertical Y-planes. It is shown that the air flow structure is similar on the back face of the wave with decreasing velocity magnitude towards the side wall. However, the air flow structure is different on the front face of the wave and the vertical motion is strongest in the central plane due to the shape of the overturning wave.

Figure 6.27 shows the velocity vectors of the horizontal Z-planes. It is apparent that the velocity in the water increases from the bottom to the top layer. Higher velocity vectors are observed in the air and the spanwise motion is strengthened ahead of the overturning wave.

6.7.5 Vorticity

Figure 6.28 shows the isosurfaces of the streamwise, spanwise and vertical vorticities in the water, together with the water surface profile for $U/C = 2$. By comparing the isosurfaces in figure 6.16, it is apparent that the structure of the streamwise vorticity has been modified by the wind, the spanwise vorticity is strengthened due to the surface shear, and there is little change of the vertical vorticity.

6.7.6 Energy Dissipation and Transformation

Figure 6.29 shows the comparison of the time history of normalized energy for the overturning wave over the submerged conical island between $U/C = 0$ and

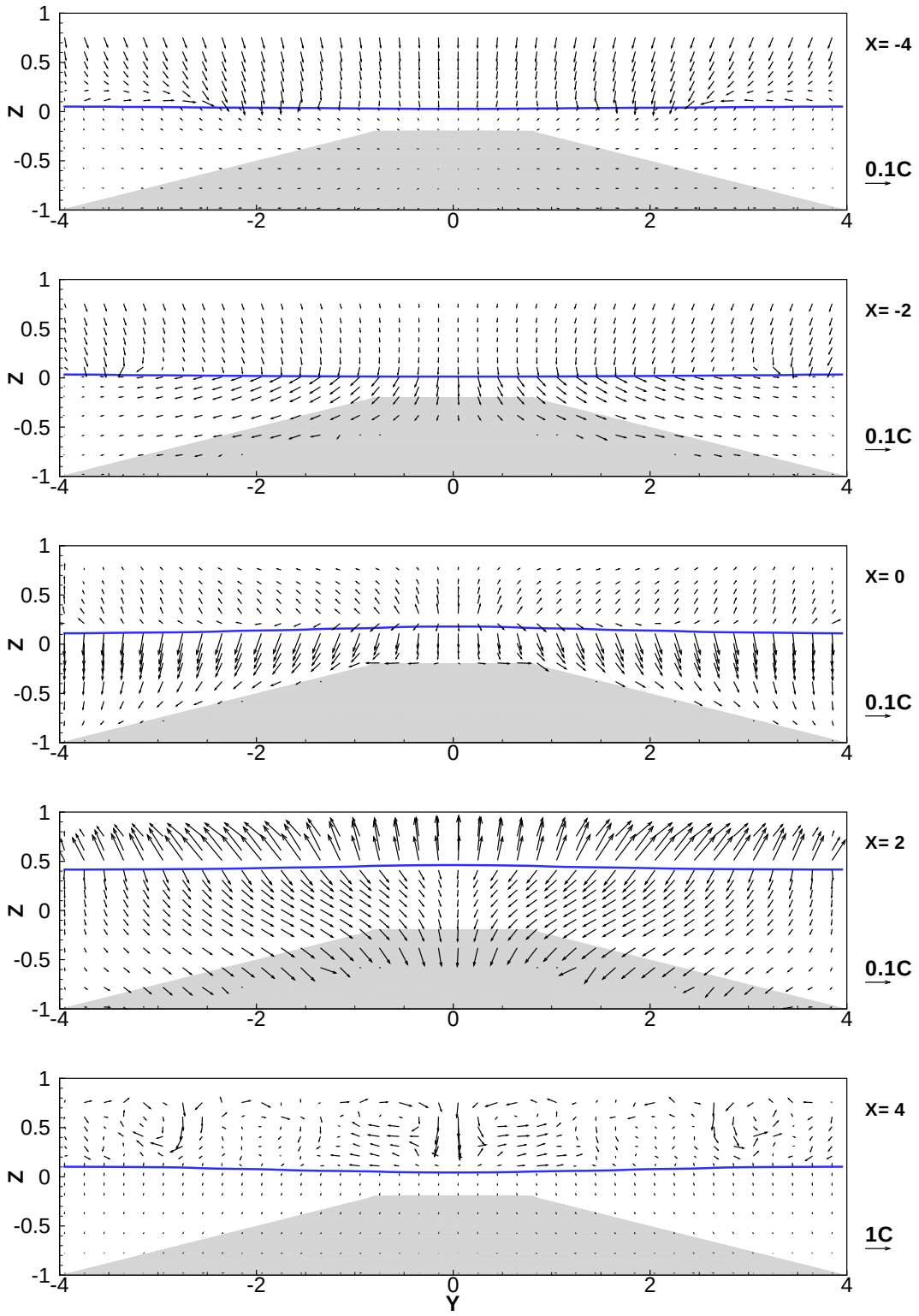

Figure 6.25: Velocity vectors of the vertical X-planes during wave breaking under the influence of wind $U/C = 2$ at $t = 1.8$ s. It is noted that different length scale is used for $X = 4$.

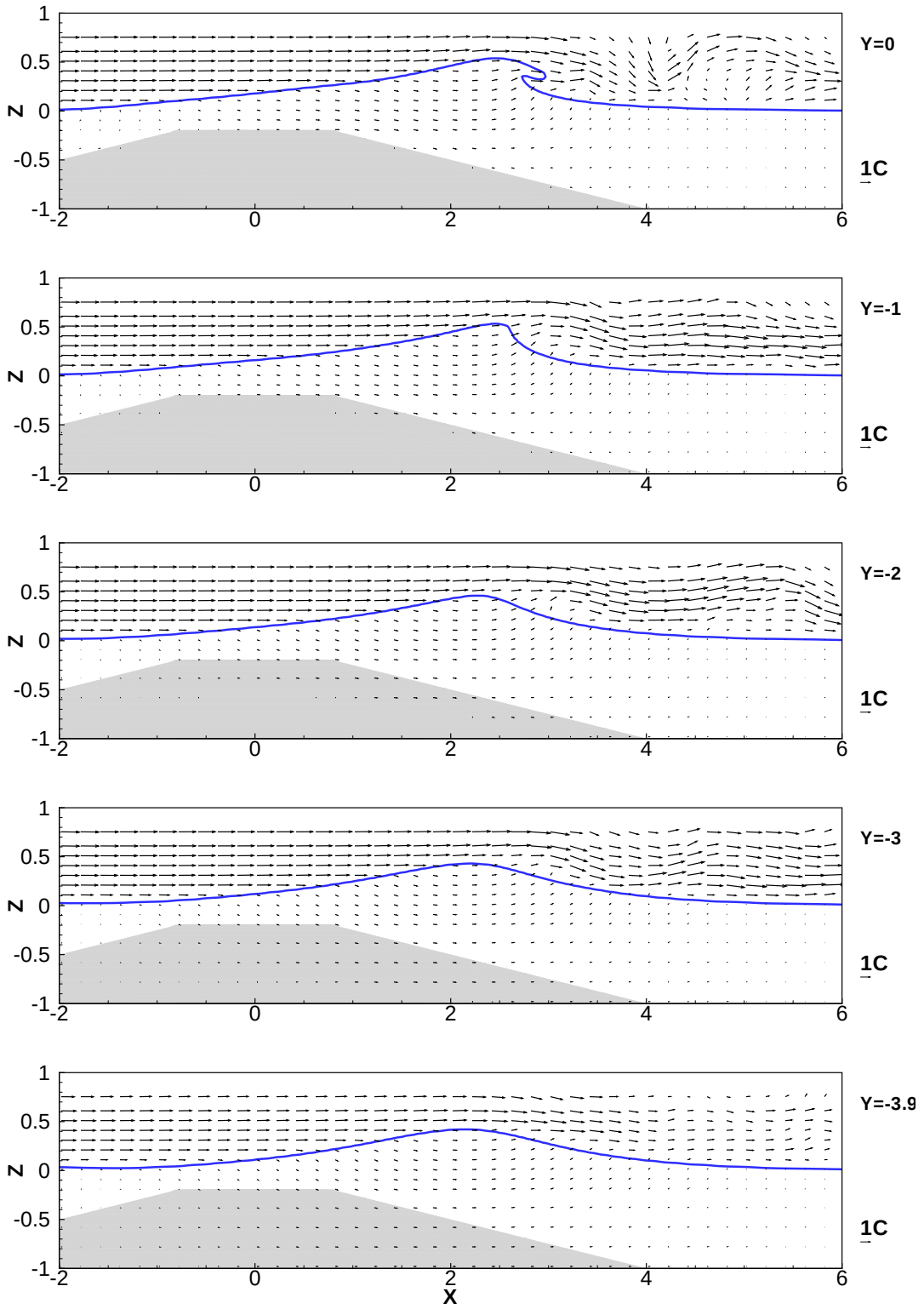

Figure 6.26: Velocity vectors of the vertical Y-planes during wave breaking under the influence of wind $U/C = 2$ at $t = 1.8$ s.

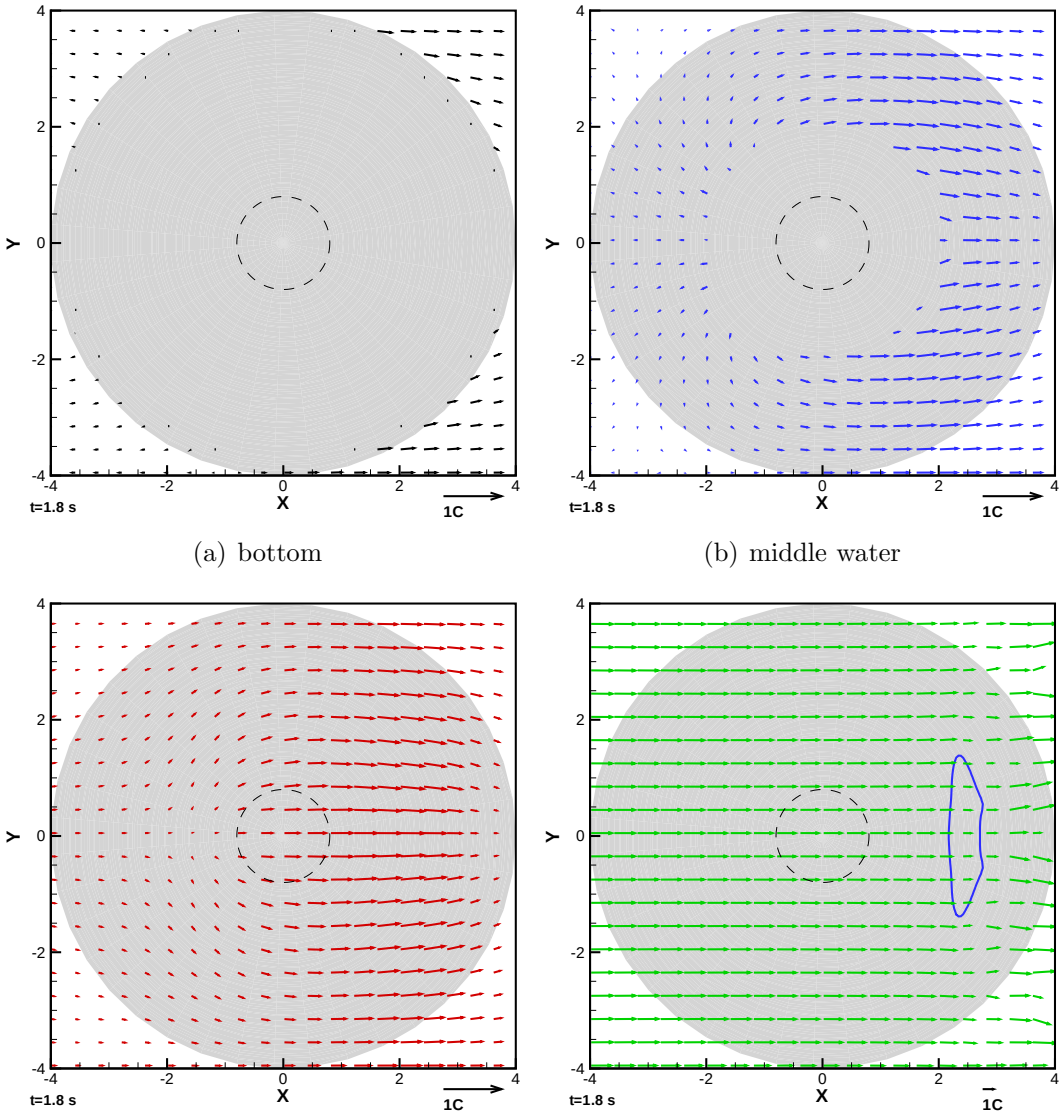

(a) bottom (b) middle water

(c) surface (d) middle air

Figure 6.27: Velocity vectors of the horizontal Z-planes during wave breaking under the influence of wind $U/C = 2$ at $t = 1.8$ s. The solid line in (d) is the water surface profile and it is noted that different length scale is used in (d).

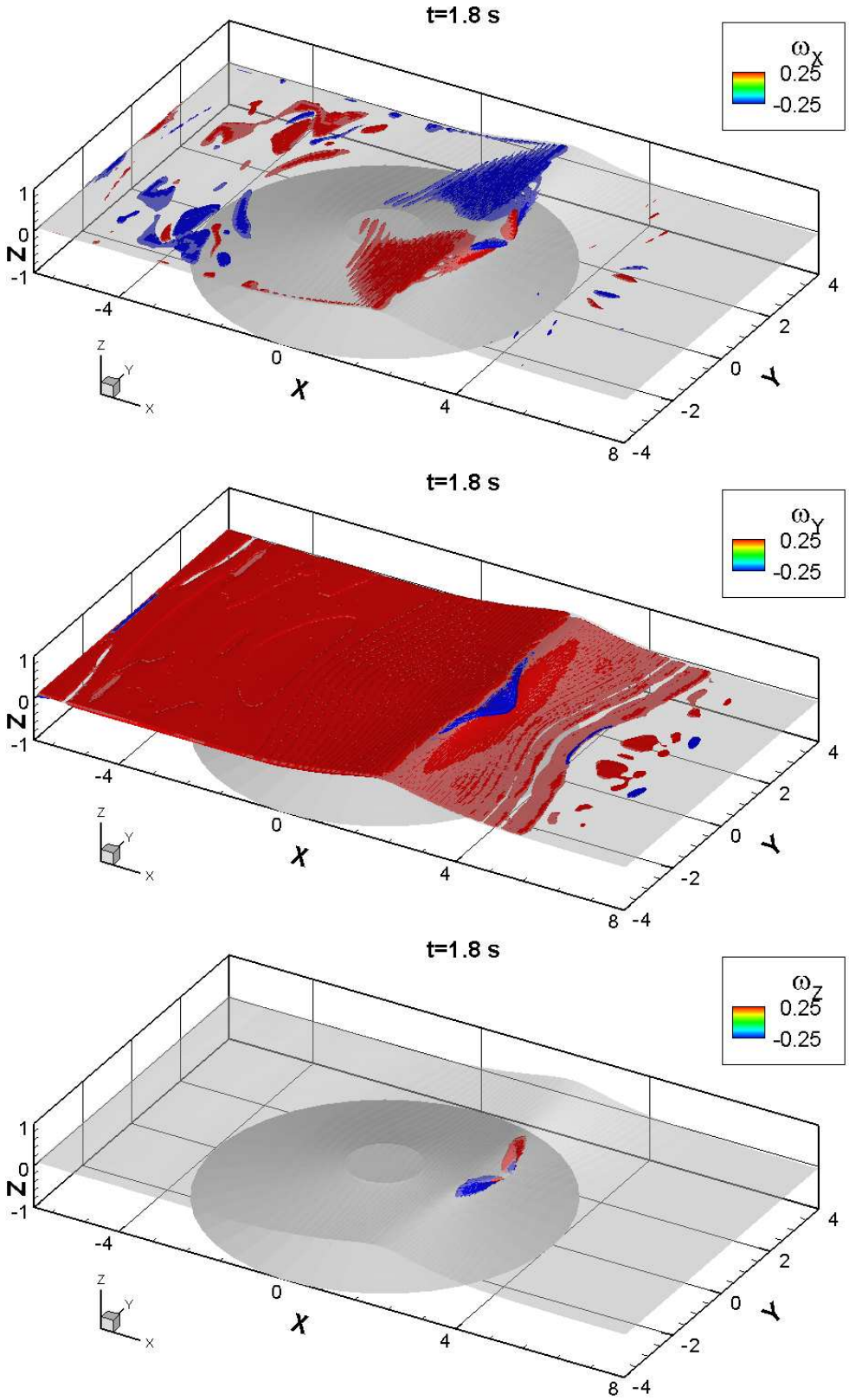

Figure 6.28: Isosurfaces of the streamwise (top), spanwise (middle) and vertical (bottom) vorticity during wave breaking under the influence of wind $U/C = 2$ at $t = 1.8$ s. Isosurfaces are only shown for the value ± 0.25.

$U/C = 2$. It is shown that the energy transformation under the influence of wind is similar to that for the case $U/C = 0$. As the wave receives the energy from the wind during wave propagation, all energies increase compared to those when there is no wind. In the whole process, the kinetic energy increases more than the potential energy which indicates that the energy input from wind forcing is mostly transformed into the momentum of the wave. Overall, the total energy increases about 3% under the influence of wind $U/C = 2$.

6.8 Concluding Remarks

In this chapter, the three-dimensional breaking waves have been investigated by the large eddy simulation with the Smagorinsky subgrid-scale model. The benchmark test, solitary wave run-up on a conical island, is used to validate the 3D model, where a good agreement between numerical and experimental results for the water surface elevation and maximum run-up heights around the island is obtained.

Later the model is further used to investigate three-dimensional overturning waves over a submerged conical island. The detailed water surface profiles and wave kinematics are analyzed, and the overturning jet and subsequent jet-splash cycles are presented.

Finally, the three-dimensional overturning waves under the influence of wind are studied, where the discussion is focused on the wind effects on breaking waves and the differences of important phenomena between $U/C = 0$ and $U/C = 2$. It is found that wind affects the wave profiles during wave overturning, increases the surface velocities of the wave and causes the wave to break earlier. In addition, the wind also leads to the increase of the generation of the vorticity and the total energy of the wave.

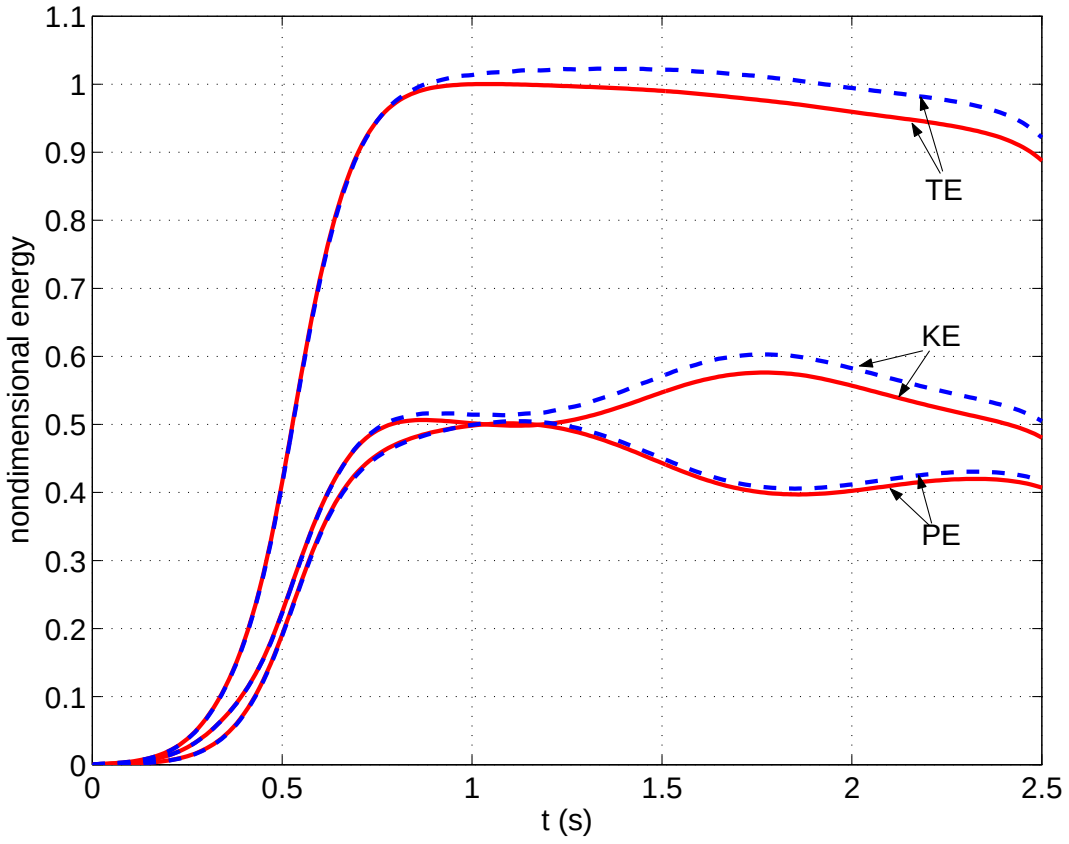

Figure 6.29: The time history of the normalized energy for the overturning wave over a submerged conical island: $U/C = 0$: red solid lines; $U/C = 2$: blue dashed lines. The energies have been normalized by the total energy $E_0 = [\text{TE}]$ for $U/C = 0$ at $t = 1.0$ s when the solitary wave nearly completely enters the computational domain.

Chapter 7

Conclusions and Future Work

The objective of the thesis is to develop a numerical model to study two- and three-dimensional breaking waves under the influence of wind, which has implications in air-sea interaction and coastal engineering. In this chapter, the main findings and conclusions are summarized first, and then possible recommendations for further work are discussed.

7.1 Conclusions

Numerical model

A two-phase flow model, which solves the flow in the air and water simultaneously, was developed in the present study. The model was based on the Reynolds averaged Navier–Stokes equations with a $k-\epsilon$ turbulence model in 2D and a large eddy simulation with the standard Smagorinsky subgrid-scale model in 3D. The governing equations were solved by the finite volume method in a Cartesian staggered grid and the partial cell treatment was implemented to deal with complex geometries, which is slightly different from other commerical CFD codes. The SIMPLE or PISO algorithms were employed for the pressure-velocity coupling and a backward finite difference discretization was used for the time derivative, which lead to an implicit scheme for the governing equations. The air-water interface was captured by the high resolution VOF scheme CICSAM, which can

predict the overturning jet and splash-up during wave breaking. In order to validate the model, 2D overturning waves on a sloping beach and over a reef, and 3D solitary wave run-up on a conical island were computed and compared with experimental measurements. Overall, good agreement was obtained which showed the capability of the numerical model in simulating breaking wave problems.

2D breaking solitary waves

In Chapter 4, the RANS model was utilized to investigate effects of wind on 2D breaking solitary waves. In the absence of wind, the computed water surface profiles were in agreement with previous experiments.

The wind effects on breaking solitary waves are summarized as follows:

- Wind affects the water surface profile during wave breaking and splash-up. Onshore wind causes water waves to break earlier, in deeper water further from shore.

- The water particle velocity in breaking waves increases with the wind speed and thus affects the wave breaking process. There is a recirculation of air above the crest of the wave in the absence of wind while there is a separation of air flow in the presence of a sufficiently strong wind.

- During wave breaking, the wind affects the pressure field in both the air and water, and increases the form drag and friction drag along the water surface. Wind increases the generation of vorticity and turbulent stress near the air-water interface.

- Wind affects the breaking characteristics of the wave, such as the evolution of maximum wave height and maximum particle velocities. The maximum run-up of solitary waves increases with the wind speed. Wind increases the potential and kinetic energy of water waves and alters the energy transformation during wave breaking.

2D periodic breaking waves

In Chapter 5, the RANS model was employed to simulate 2D periodic breaking waves in the surf zone. Both spilling and plunging breakers were investigated, and numerical results of the distribution of wave amplitudes, vertical variations of the undertow and turbulence field were compared with the experimental data and previous numerical studies in the absence of wind. The water surface profiles and velocity fields during wave breaking were discussed, and the overturning jet in both spilling and plunging breakers, which are rarely shown in previous studies, were presented in the numerical simulation.

The wind effects on periodic breaking waves are summarized as follows:

- Wind affects the distribution of wave amplitudes and mean water level for both spilling and plunging breakers. The effect of wind on the breaking point is significant and onshore winds cause the wave to break earlier in deeper water further from the shore. The slope of the mean water level has been slightly changed in the presence of wind due to the wind-induced shear formed in the vicinity of the water surface.

- Onshore wind assists the development of water particle velocity towards the critical wave phase speed, leading to earlier wave breaking. The wind affects the wave breaking process due to the wind-induced shear and the change of the breaking water depth. The recirculation of air flow, which is observed above the crest of both spilling and plunging breakers in the absence of wind, do not exist in the presence of wind due to the wind forcing.

- The shape of the overturning jet in both spilling and plunging breakers has been changed in the presence of wind and the wind also affects the subsequent jet-splash cycles.

- Wind affects the generation of vorticity during wave breaking due to the change of breaking water depth.

3D overturning waves

In Chapter 6, the LES model was used to investigate three-dimensional overturning waves over a submerged conical island. The detailed water surface profiles and wave kinematics from pre-breaking to post-breaking were analyzed, and the overturning jet and subsequent jet-splash cycles were presented.

The wind effects on 3D overturning waves are summarized as follows:

- Similar wind effects on breaking waves in 2D, which cause the wave to break earlier, are also observed in 3D overturning waves. In addition, it was found that the effect of wind is significant in the region where the wave overturns.

- Wind affects the wave kinematics during wave overturning. It was found that there is significant change of the surface velocities on the back face of the wave and there is slight change on the front side of the wave. The effect of wind on the wave is dominated by its wind direction and the effect on other perpendicular directions is weak. The structure of air flow in front of the overturning jet changes significantly in the presence of wind.

- The structure of the steamwise vorticity has been modified by the wind, the spanwise vorticity is strengthened due to the wind-induced shear, and there is little change of the vertical vorticity.

- As the wave receives the energy from the wind during wave propagation, all energies increase compared to those in the absence of wind. In the whole process, the kinetic energy increases more than the potential energy which indicates that the energy input from the wind forcing is mostly transformed into the momentum of the wave.

7.2 Future Work

The present study should be regarded as a step towards understanding the kinematics and dynamics of breaking waves. Due to the complex processes during wave breaking, much future effort should be devoted to further this study. In this section, two areas of future work are identified as: improvements of the numerical model and extension of the application.

Due to the length of study, it is unlikely that the developed numerical model can perfectly simulate all kinds of wave breaking phenomenon. The improvements of the numerical model are discussed as follows:

- Two-phase flow validation cases are needed to improve the performance of the model. Although good agreement between numerical results and experimental measurements was obtained in the water, there is little known for the flow in the air, as it is difficult to measure the flow in the water and air simultaneously in the experiment. With the development of measuring techniques, detailed two-phase PIV measurements of breaking waves are expected in the near future to validate the two-phase flow field in the present model.

- In two-phase flow models, the discretization of the mass flux plays an important role in the numerical solutions. The consistency between mass and momentum conservation has to be guaranteed otherwise non-physical velocities might be generated in the vicinity of the air-water interface. The consistency can be fulfilled in a collocated grid when using the same mass flux for all equations. However, to the author's best knowledge, it is not clear yet how to deal with this consistency in a single staggered grid if the mass flux is not calculated based on the explicit interface advection (such as surface capturing methods), and especially when the implicit scheme is employed for the momentum equation. In this study, interpolation was adopted to obtain the mass flux on the face of the momentum control volume, and further improvements should be addressed to tackle this problem in the future.

- In order to resolve the turbulent flow field in the vicinity of the air-water interface, the wall function for the air above the air-water interface is proposed and applied in the 2D RANS model. Similar ideas should be taken into account in future developments of the 3D LES model.

- Surface tension, which is weak for long waves, is neglected in the present study. In order to take full length scales of water waves into account, the method for modelling surface tension should be implemented in the numerical model in the future.

- Due to the step by step development of the numerical model, only the standard $k-\epsilon$ model and the Smagorinsky subgrid-scale model were adopted for the turbulence effect in the 2D RANS and 3D LES models, respectively. Dynamic subgrid-scale models should be implemented in the future to better represent the turbulence in the LES.

- Running 3D two-phase simulations is still expensive in terms of CPU times and computational effort. There are three ways to improve the efficiency and reduce computational efforts in 3D calculations. One is to use the adaptive mesh during the computation, in which a fine mesh is used in the vicinity of the interface during wave propagation whereas a coarse mesh is employed away from the interface. Another is to perform parallel computing, in which calculations are carried out simultaneously on several CPUs. Finally, the development of hybrid models for water waves is recommended to study large scale problems, in which the two-phase flow model is used in the breaking and post-breaking region whereas other more efficient models are used in the pre-breaking region.

Extension of the application in the present study is discussed as follows:

- The present study focused on unsteady breaking waves in shallow water, which has practical implications in coastal engineering. However, other wave breaking phenomena, such as unsteady breaking waves in deep water and steady breaking waves over submerged bodies, can also be investigated through the numerical model.

- Due to the CPU time for 3D calculations, only 3D breaking solitary waves were considered in the present study. The numerical model should be further employed to investigate 3D periodic breaking waves in the future. In addition, irregular waves should also be taken into account in the future.

- Much attention has been paid to the wave overturning process in this study. The detailed wave post-breaking process should also be considered in the future and compared with available experimental measurements of aeration in spilling breakers.

- The numerical model can be modified to investigate three-dimensional wave-structure interaction and moving body problems. In addition, the numerical model is capable of simulating a wide range of free surface flow problems, which will be our future research direction.

Appendix A

Coefficients in Cnoidal Wave Theory

The coefficients A_n and B_{nm} in equation (5.1) of the third-order cnoidal wave theory (Horikawa, 1988) are

$$
\begin{aligned}
A_0 &= \epsilon(\lambda-\mu)+\epsilon^2(-2\lambda+\mu-2\lambda^2+2\lambda\mu)/4 \\
&\quad +\epsilon^3(133\lambda-16\mu+399\lambda^2-466\lambda\mu+100\mu^2 \\
&\qquad +266\lambda^3-466\lambda^2\mu+200\lambda\mu^2)/400 \\
A_1 &= \epsilon+\epsilon^2(-3/4)+\epsilon^3(50-\lambda-60\mu)/80 \\
A_2 &= \epsilon^2(3/4)+\epsilon^3(-151+\lambda+60\mu)/80 \\
A_3 &= \epsilon^3(101/80) \\
B_{00} &= \epsilon(\lambda-\mu)+\epsilon^2(\lambda-\mu-2\lambda^2+2\mu^2)/4 \\
&\quad +\epsilon^3(-71\lambda+47\mu-23\lambda^2+97\lambda\mu-50\mu^2 \\
&\qquad +153\lambda^3-153\lambda^2\mu-25\lambda\mu^2+25\mu^3)/200 \\
B_{01} &= \epsilon^2(-3\lambda/4)+\epsilon^3(6\lambda+24\lambda^2-21\lambda\mu)/8 \\
B_{02} &= \epsilon^3(3\lambda-3\lambda^2)/16 \\
B_{10} &= \epsilon+\epsilon^2(1-6\lambda+2\mu)/4 \\
&\quad +\epsilon^3(-19-27\lambda+10\mu+101\lambda^2-100\lambda\mu+15\mu^2)/40
\end{aligned}
\tag{A.1}
$$

$$
\begin{aligned}
B_{11} &= \epsilon^2(-3+3\lambda)/2 + \epsilon^3(6+36\lambda-21\mu-24\lambda^2+21\lambda\mu)/4 \\
B_{12} &= \epsilon^3(6-39\lambda+6\lambda^2)/16 \\
B_{20} &= \epsilon^2(-1) + \epsilon^3(-2+32\lambda-15\mu)/10 \\
B_{21} &= \epsilon^2(9/4) + \epsilon^3(30-120\lambda+63\mu)/8 \\
B_{22} &= \epsilon^3(-45+45\lambda)/16 \\
B_{30} &= \epsilon^3(6/5) \\
B_{31} &= \epsilon^3(-15/2) \\
B_{32} &= \epsilon^3(45/16)
\end{aligned}
$$

with

$$\epsilon = H/d_0 \tag{A.2}$$

$$\lambda = (1-\kappa^2)/\kappa^2 \tag{A.3}$$

$$\mu = E/\kappa^2 K \tag{A.4}$$

where K and E are the complete elliptic integrals of the first and second kind, respectively, and κ is the modulus of the elliptic integrals and functions.

Once d_0, T, and H are given, the modulus κ can be determined by

$$\frac{gHT^2}{d_0^2} = \left[\frac{16\kappa^2K^2}{3}\right] \Big/ \left[1+\epsilon\frac{-1-2\lambda}{4} + \epsilon^2\frac{8+33\lambda-10\mu+33\lambda^2-20\lambda\mu}{40}\right]. \tag{A.5}$$

From κ, the wavelength L can be calculated as

$$
\begin{aligned}
L = T\sqrt{gd_0}\Big[1 &+ \epsilon(1+2\lambda-3\mu)/2 + \epsilon^2(-6-16\lambda+5\mu-16\lambda^2+10\lambda\mu+15\mu^2)/40 \\
&+ \epsilon^3(150+1079\lambda-203\mu+2337\lambda^2-2653\lambda\mu+350\mu^2 \\
&+ 1558\lambda^3-2653\lambda^2\mu+700\lambda\mu^2+175\mu^3)/2800\Big].
\end{aligned} \tag{A.6}
$$

Bibliography

Al-Zanaidi, M. A. & Hui, W. H. 1984 Turbulent airflow over water waves-a numerical study. *Journal of Fluid Mechanics* **148**, 225–246.

Amsden, A. A. & Harlow, F. H. 1970 The SMAC method: A numerical technique for calculating incompressible fluid flows. *Tech. Rep.* LA-4370. Los Alamos Scientific Laboratory.

Andrillon, Y. & Alessandrini, B. 2004 A 2D+T VOF fully coupled formulation for the calculation of breaking free-surface flow. *Journal of Marine Science and Technology* **8** (4), 159–168.

Ashgriz, N. & Poo, J. Y. 1991 FLAIR - flux line-segment model for advection and interface reconstruction. *Journal of Computational Physics* **93** (2), 449–468.

Baker, G. R., Meiron, D. I. & Orszag, S. A. 1982 Generalized vortex methods for free-surface flow problems. *Journal of Fluid Mechanics* **123**, 477–501.

Bakhtyar, R., Barry, D. A., Yeganeh-Bakhtiary, A. & Ghaheri, A. 2009 Numerical simulation of surf-swash zone motions and turbulent flow. *Advances in Water Resources* **32** (2), 250–263.

Banner, M. L. 1990 The influence of wave breaking on the surface pressure distribution in wind wave interactions. *Journal of Fluid Mechanics* **211**, 463–495.

Banner, M. L. & Melville, W. K. 1976 On the separation of air flow over water waves. *Journal of Fluid Mechanics* **77**, 825–842.

Banner, M. L. & Peirson, W. L. 1998 Tangential stress beneath wind-driven air-water interfaces. *Journal of Fluid Mechanics* **364**, 115–145.

Banner, M. L. & Peirson, W. L. 2007 Wave breaking onset and strength for two-dimensional deep-water wave groups. *Journal of Fluid Mechanics* **585**, 93–115.

Banner, M. L. & Peregrine, D. H. 1993 Wave breaking in deep-water. *Annual Review of Fluid Mechanics* **25**, 373–397.

Banner, M. L. & Phillips, O. M. 1974 Incipient breaking of small scale waves. *Journal of Fluid Mechanics* **65**, 647–656.

Basco, D. R. 1985 A qualitative description of wave breaking. *Journal of Waterway, Port, Coastal, and Ocean Engineering-ASCE* **111** (2), 171–188.

Battjes, J. A. 1974 Computation of set-up, longshore currents, run-up and overtopping due to wind-generated waves. PhD thesis, Delft University of Technology.

Battjes, J. A. 1988 Surf-zone dynamics. *Annual Review of Fluid Mechanics* **20**, 257–293.

Battjes, J. A. & Sakai, T. 1981 Velocity-field in a steady breaker. *Journal of Fluid Mechanics* **111**, 421–437.

Belcher, S. E. & Hunt, J. C. R. 1998 Turbulent flow over hills and waves. *Annual Review of Fluid Mechanics* **30**, 507–538.

Benjamin, T. B. 1959 Shearing flow over a wavy boundary. *Journal of Fluid Mechanics* **6**, 161–205.

Benjamin, T. B., Bona, J. L. & Mahony, J. J. 1972 Model equations for long waves in nonlinear dispersive systems. *Philosophical Transactions of the Royal Society of London Series A-Mathematical and Physical Sciences* **272** (1220), 47–78.

Berkhoff, J. C. W., Booy, N. & Radder, A. C. 1982 Verification of numerical wave-propagation models for simple harmonic linear water-waves. *Coastal Engineering* **6** (3), 255–279.

Biausser, B., Fraunie, P., Grilli, S. T. & Marcer, R. 2004 Numerical analysis of the internal kinematics and dynamics of 3-D breaking waves on slopes. *International Journal of Offshore and Polar Engineering* **14** (4), 247–256.

Blenkinsopp, C. E. & Chaplin, J. R. 2007 Void fraction measurements in breaking waves. *Proceedings of the Royal Society A-Mathematical Physical and Engineering Sciences* **463** (2088), 3151–3170.

Bole, J. B. & Hsu, E. Y. 1969 Response of gravity water waves to wind excitation. *Journal of Fluid Mechanics* **35**, 657–675.

Bonmarin, P. 1989 Geometric-properties of deep-water breaking waves. *Journal of Fluid Mechanics* **209**, 405–433.

Borthwick, A. G. L., Ford, M., Weston, B. P., Taylor, P. H. & Stansby, P. K. 2006 Solitary wave transformation, breaking and run-up at a beach. *Proceedings of the Institution of Civil Engineers-Maritime Engineering* **159** (3), 97–105.

Boussinesq, J. 1872 Thrie des ondes et des remous qui se propagent le long d'un canal rectangulaire horizontal, en communiquant au liquide contenu dans ce canal des vitesses sensiblement pareilles de la surface au fond. *Journal de Mathatique Pures et Appliqus, Deuxie Sie* **17**, 55–108.

Bradford, S. F. 2000 Numerical simulation of surf zone dynamics. *Journal of Waterway, Port, Coastal, and Ocean Engineering-ASCE* **126** (1), 1–13.

Bradford, S. F. & Sanders, B. F. 2002 Finite-volume model for shallow-water flooding of arbitrary topography. *Journal of Hydraulic Engineering-ASCE* **128** (3), 289–298.

Briggs, M. J., Synolakis, C. E., Harkins, G. S. & Green, D. R. 1995 Laboratory experiments of tsunami runup on a circular island. *Pure and Applied Geophysics* **144** (3-4), 569–593.

Broeze, J., Vandaalen, E. F. G. & Zandbergen, P. J. 1993 A three-dimensional panel method for nonlinear free-surface waves on vector computers. *Computational Mechanics* **13** (1-2), 12–28.

Bussmann, M., Kothe, D. B. & Sicilian, J. M. 2002 Modeling high density ratio incompressible interfacial flows. In *ASME 2002 Joint U.S.-European Fluids Engineering Division Conference*, pp. 707–713. Montreal, Quebec, Canada: ASME.

Cabot, W. & Moin, P. 2000 Approximate wall boundary conditions in the large-eddy simulation of high Reynolds number flow. *Flow Turbulence and Combustion* **63** (1-4), 269–291.

Casulli, V. & Cheng, R. T. 1992 Semi-implicit finite difference methods for three-dimensional shallow water flow. *International Journal for Numerical Methods in Fluids* **15** (6), 629–648.

Causon, D. M., Ingram, D. M., Mingham, C. G., Yang, G. & Pearson, R. V. 2000 Calculation of shallow water flows using a cartesian cut cell approach. *Advances in Water Resources* **23** (5), 545–562.

Chalikov, D. V. 1978 Numerical-simulation of wind-wave interaction. *Journal of Fluid Mechanics* **87**, 561–582.

Chan, R. K. C. & Street, R. L. 1970 A computer study of finite-amplitude water waves. *Journal of Computational Physics* **6** (1), 68–94.

Chang, K. A., Hsu, T. J. & Liu, P. L. F. 2001 Vortex generation and evolution in water waves propagating over a submerged rectangular obstacle Part I. Solitary waves. *Coastal Engineering* **44** (1), 13–36.

Chang, K. A., Hsu, T. J. & Liu, P. L. F. 2005 Vortex generation and evolution in water waves propagating over a submerged rectangular obstacle - Part II: Cnoidal waves. *Coastal Engineering* **52** (3), 257–283.

Chang, K. A. & Liu, P. L. F. 1998 Velocity, acceleration and vorticity under a breaking wave. *Physics of Fluids* **10** (1), 327–329.

Chang, K. A. & Liu, P. L. F. 1999 Experimental investigation of turbulence generated by breaking waves in water of intermediate depth. *Physics of Fluids* **11** (11), 3390–3400.

Chanson, H. & Lee, J. F. 1997 Plunging jet characteristics of plunging breakers. *Coastal Engineering* **31** (1-4), 125–141.

Chawla, A., Ozkan-Haller, H. T. & Kirby, J. T. 1998 Spectral model for wave transformation and breaking over irregular bathymetry. *Journal of Waterway, Port, Coastal, and Ocean Engineering-ASCE* **124** (4), 189–198.

Chen, C. J., Naseri-Neshat, H. & Ho, K. S. 1981 Finite-analytic numerical solution of heat transfer in two-dimensional cavity flow. *Numerical Heat Transfer, Part B: Fundamentals: An International Journal of Computation and Methodology* **4** (2), 179 – 197.

Chen, G., Kharif, C., Zaleski, S. & Li, J. 1999 Two-dimensional Navier-Stokes simulation of breaking waves. *Physics of Fluids* **11** (1), 121–133.

Chen, Q., Kaihatu, J. M. & Hwang, P. A. 2004 Incorporation of wind effects into Boussinesq wave models. *Journal of Waterway, Port, Coastal, and Ocean Engineering-ASCE* **130** (6), 312–321.

Chen, Q., Kirby, J. T., Dalrymple, R. A., Kennedy, A. B. & Chawla, A. 2000 Boussinesq modeling of wave transformation, breaking, and runup. II:2D. *Journal of Waterway, Port, Coastal, and Ocean Engineering-ASCE* **126** (1), 48–56.

Chen, S., Johnson, D. B., Raad, P. E. & Fadda, D. 1997 The surface marker and micro cell method. *International Journal for Numerical Methods in Fluids* **25** (7), 749–778.

Chen, X. J. 2004 A cartesian method for fitting the bathymetry and tracking the dynamic position of the shoreline in a three-dimensional, hydrodynamic model. *Journal of Computational Physics* **200** (2), 749–768.

Cherukat, P., Na, Y., Hanratty, T. J. & McLaughlin, J. B. 1998 Direct numerical simulation of a fully developed turbulent flow over a wavy wall. *Theoretical and Computational Fluid Dynamics* **11** (2), 109–134.

Choi, B. H., Kim, D. C., Pelinovsky, E. & Woo, S. B. 2007 Three-dimensional simulation of tsunami run-up around conical island. *Coastal Engineering* **54** (8), 618–629.

Chorin, A. J. 1968 Numerical solution of Navier-Stokes equations. *Mathematics of Computation* **22** (104), 745–762.

Christensen, E. D. 2006 Large eddy simulation of spilling and plunging breakers. *Coastal Engineering* **53** (5-6), 463–485.

Christensen, E. D. & Deigaard, R. 2001 Large eddy simulation of breaking waves. *Coastal Engineering* **42** (1), 53–86.

Christensen, E. D., Walstra, D. J. & Emerat, N. 2002 Vertical variation of the flow across the surf zone. *Coastal Engineering* **45** (3-4), 169–198.

Cokelet, E. D. 1977 Breaking waves. *Nature* **267** (5614), 769–774.

Cotton, M. A., Reedha, D. & Stansby, P. K. 2005 Low-reynolds-number two-equation turbulence modelling for open channel flow: development and evaluation of free surface boundary conditions on the dissipation rate equation. *Journal of Hydraulic Research* **43** (6), 632–643.

Cox, D. T. & Shin, S. W. 2003 Laboratory measurements of void fraction and turbulence in the bore region of surf zone waves. *Journal of Engineering Mechanics-ASCE* **129** (10), 1197–1205.

Craik, A. D. D. 2004 The origins of water wave theory. *Annual Review of Fluid Mechanics* **36**, 1–28.

Craik, A. D. D. 2005 George Gabriel Stokes on water wave theory. *Annual Review of Fluid Mechanics* **37**, 23–42.

Dalrymple, R. A. & Rogers, B. D. 2006 Numerical modeling of water waves with the SPH method. *Coastal Engineering* **53** (2-3), 141–147.

Davis, R. E. 1970 On turbulent flow over a wavy boundary. *Journal of Fluid Mechanics* **42**, 721–731.

De Angelis, V., Lombardi, P. & Banerjee, S. 1997 Direct numerical simulation of turbulent flow over a wavy wall. *Physics of Fluids* **9** (8), 2429–2442.

Dean, R. G. & Dalrymple, R. A. 1984 *Water wave mechanics for engineers and scientists*. Englewood Cliffs, N. J.: Prentice-Hall.

Deane, G. B. & Stokes, M. D. 2002 Scale dependence of bubble creation mechanisms in breaking waves. *Nature* **418** (6900), 839–844.

Dingemans, M. & Otta, A. 2001 Nonlinear modulation of water waves. In *Advances in coastal and ocean engineering* (ed. P. L. F. Liu), , vol. 7, pp. 1–75. World Scientific.

Dold, J. W. & Peregrine, D. H. 1986 An efficient boundary-integral method for steep unsteady water waves. In *Numerical methods for fluid dynamics II* (ed. K. W. Morton & M. J. Baines), pp. 671–679. Oxford: Clarendon Press.

Dommermuth, D. G., Yue, D. K. P., Lin, W. M., Rapp, R. J., Chan, E. S. & Melville, W. K. 1988 Deep-water plunging breakers - a comparison between potential-theory and experiments. *Journal of Fluid Mechanics* **189**, 423–442.

Douglass, S. L. 1990 Influence of wind on breaking waves. *Journal of Waterway, Port, Coastal, and Ocean Engineering-ASCE* **116** (6), 651–663.

Drazen, D. A. & Melville, W. K. 2009 Turbulence and mixing in unsteady breaking surface waves. *Journal of Fluid Mechanics* **628**, 85–119.

Drazen, D. A., Melville, W. K. & Lenain, L. 2008 Inertial scaling of dissipation in unsteady breaking waves. *Journal of Fluid Mechanics* **611**, 307–332.

van Driest, E. R. 1956 On turbulent flow near a wall. *Journal of the Aeronautical Science* **23** (11), 1007–1011.

Duncan, J. H. 1983 The breaking and non-breaking wave resistance of a two-dimensional hydrofoil. *Journal of Fluid Mechanics* **126**, 507–520.

Duncan, J. H. 2001 Spilling breakers. *Annual Review of Fluid Mechanics* **33**, 519–547.

Enright, D., Fedkiw, R., Ferziger, J. & Mitchell, I. 2002 A hybrid particle level set method for improved interface capturing. *Journal of Computational Physics* **183** (1), 83–116.

Eriksson, K., Estep, D., Hansbo, P. & Johnson, C. 1996 *Computational differential equations*. Cambridge; New York: Cambridge University Press.

Esmaeeli, A. & Tryggvason, G. 2005 A direct numerical simulation study of the buoyant rise of bubbles at O(100) Reynolds number. *Physics of Fluids* **17** (9), 093303.

Feddersen, F. & Veron, F. 2005 Wind effects on shoaling wave shape. *Journal of Physical Oceanography* **35** (7), 1223–1228.

Ferziger, J. H. & Peric, M. 2002 *Computational methods for fluid dynamics*, 3rd edn. Berlin: Springer.

Fuhrman, D. R. & Madsen, P. A. 2008 Simulation of nonlinear wave run-up with a high-order Boussinesq model. *Coastal Engineering* **55** (2), 139–154.

Fulgosi, M., Lakehal, D., Banerjee, S. & De Angelis, V. 2003 Direct numerical simulation of turbulence in a sheared air-water flow with a deformable interface. *Journal of Fluid Mechanics* **482**, 319–345.

Galloway, J. S., Collins, M. B. & Moran, A. D. 1989 Onshore offshore wind influence on breaking waves - an empirical-study. *Coastal Engineering* **13** (4), 305–323.

Galvin, C. J. 1968 Breaker type classification on three laboratory beaches. *Journal of Geophysical Research* **73** (12), 3651–3659.

Gent, P. R. & Taylor, P. A. 1976 A numerical model of air flow above water waves. *Journal of Fluid Mechanics* **77**, 105–128.

Gotoh, H. & Sakai, T. 1999 Lagrangian simulation of breaking waves using particle method. *Coastal Engineering Journal* **41**, 303–326.

Gotoh, H. & Sakai, T. 2006 Key issues in the particle method for computation of wave breaking. *Coastal Engineering* **53** (2-3), 171–179.

Greenhow, M. 1983 Free-surface flows related to breaking waves. *Journal of Fluid Mechanics* **134**, 259–275.

Grilli, S. T., Guyenne, P. & Dias, F. 2001 A fully non-linear model for three-dimensional overturning waves over an arbitrary bottom. *International Journal for Numerical Methods in Fluids* **35** (7), 829–867.

Grilli, S. T. & Horrillo, J. 1997 Numerical generation and absorption of fully nonlinear periodic waves. *Journal of Engineering Mechanics-ASCE* **123** (10), 1060–1069.

Grilli, S. T., Losada, M. A. & Martin, F. 1994*a* Characteristics of solitary wave breaking induced by breakwaters. *Journal of Waterway, Port, Coastal, and Ocean Engineering-ASCE* **120** (1), 74–92.

Grilli, S. T., Skourup, J. & Svendsen, I. A. 1989 An efficient boundary element method for nonlinear water-waves. *Engineering Analysis with Boundary Elements* **6** (2), 97–102.

Grilli, S. T. & Subramanya, R. 1996 Numerical modeling of wave breaking induced by fixed or moving boundaries. *Computational Mechanics* **17** (6), 374–391.

Grilli, S. T., Subramanya, R., Svendsen, I. A. & Veeramony, J. 1994*b* Shoaling of solitary waves on plane beaches. *Journal of Waterway, Port, Coastal, and Ocean Engineering-ASCE* **120** (6), 609–628.

Grilli, S. T., Svendsen, I. A. & Subramanya, R. 1997 Breaking criterion and characteristics for solitary waves on slopes. *Journal of Waterway, Port, Coastal, and Ocean Engineering-ASCE* **123** (3), 102–112.

Grue, J. & Jensen, A. 2006 Experimental velocities and accelerations in very steep wave events in deep water. *European Journal of Mechanics B-Fluids* **25** (5), 554–564.

Gueyffier, D., Li, J., Nadim, A., Scardovelli, R. & Zaleski, S. 1999 Volume-of-fluid interface tracking with smoothed surface stress methods for three-dimensional flows. *Journal of Computational Physics* **152** (2), 423–456.

Guignard, S., Grilli, S. T., Marcer, R. & Rey, V. 1999 Computation of shoaling and breaking waves in nearshore areas by the coupling of BEM and VOF methods. *Proceedings of the Ninth (1999) International Offshore and Polar Engineering Conference* pp. 304–309.

Guignard, S., Marcer, R., Rey, V., Kharif, C. & Fraunie, P. 2001 Solitary wave breaking on sloping beaches: 2-D two phase flow numerical simulation by SL-VOF method. *European Journal of Mechanics B-Fluids* **20** (1), 57–74.

Guyenne, P. & Grilli, S. T. 2006 Numerical study of three-dimensional overturning waves in shallow water. *Journal of Fluid Mechanics* **547**, 361–388.

Harlow, F. H. & Welch, J. E. 1965 Numerical calculation of time-dependent viscous incompressible flow of fluid with free surface. *Physics of Fluids* **8** (12), 2182–2189.

Harris, J. A., Belcher, S. E. & Street, R. L. 1996 Linear dynamics of wind waves in coupled turbulent air-water flow. Part 2. Numerical model. *Journal of Fluid Mechanics* **308**, 219–254.

Helluy, P., Golay, F., Caltagirone, J. P., Lubin, P., Vincent, S., Drevard, D., Marcer, R., Fraunie, P., Seguin, N., Grilli, S., Lesage, A. C., Dervieux, A. & Allain, O. 2005 Numerical simulations

of wave breaking. *ESAIM-Mathematical Modelling and Numerical Analysis-Modelisation Mathematique Et Analyse Numerique* **39** (3), 591–607.

Hendrickson, K. L. 2005 Navier-Stokes simulation of steep breaking water waves with a coupled air-water interface. PhD thesis, Massachusetts Institute of Technology.

Henn, D. S. & Sykes, R. I. 1999 Large-eddy simulation of flow over wavy surfaces. *Journal of Fluid Mechanics* **383**, 75–112.

Hieu, P. D., Katsutohi, T. & Ca, V. T. 2004 Numerical simulation of breaking waves using a two-phase flow model. *Applied Mathematical Modelling* **28** (11), 983–1005.

Hirsch, C. 2007 *Numerical computation of internal and external flows introduction to the fundamentals of CFD*, new edn. Oxford: Butterworth-Heinemann.

Hirt, C. W. & Nichols, B. D. 1981 Volume of fluid (VOF) method for the dynamics of free boundaries. *Journal of Computational Physics* **39** (1), 201–225.

Hodges, B. R. & Street, R. L. 1999 On simulation of turbulent nonlinear free-surface flows. *Journal of Computational Physics* **151** (2), 425–457.

Hoque, A. & Aoki, S. 2005 Distributions of void fraction under breaking waves in the surf zone. *Ocean Engineering* **32** (14-15), 1829–1840.

Horikawa, K. 1988 *Nearshore dynamics and coastal processes: Theory, measurement, and predictive models*. Tokyo: University of Tokyo Press.

Hsieh, C. M, Hwang, R. R., Chern, M. J. & Yang, W. C. 2008 Using RANS to simulate breaking wave on a sloping bed. *Proceedings of the Eighteenth (2008) International Offshore and Polar Engineering Conference* pp. 684–690.

Hsu, T. J., Sakakiyama, T. & Liu, P. L. F. 2002 A numerical model for wave motions and turbulence flows in front of a composite breakwater. *Coastal Engineering* **46** (1), 25–50.

Hubbard, M. E. & Dodd, N. 2002 A 2D numerical model of wave run-up and overtopping. *Coastal Engineering* **47** (1), 1–26.

Iafrati, A. 2009 Numerical study of the effects of the breaking intensity on wave breaking flows. *Journal of Fluid Mechanics* **622**, 371–411.

Iafrati, A. & Campana, E. F. 2005 Free-surface fluctuations behind microbreakers: space-time behaviour and subsurface flow field. *Journal of Fluid Mechanics* **529**, 311–347.

Idelsohn, S. R., Onate, E. & Del Pin, F. 2004 The particle finite element method: a powerful tool to solve incompressible flows with free-surfaces and breaking waves. *International Journal for Numerical Methods in Engineering* **61** (7), 964–989.

Ingram, D. M., Causon, D. M. & Mingham, C. G. 2003 Developments in cartesian cut cell methods. *Mathematics and Computers in Simulation* **61** (3-6), 561–572.

Issa, R. I. 1986 Solution of the implicitly discretised fluid flow equations by operator-splitting. *Journal of Computational Physics* **62** (1), 40–65.

Jahne, B. & Haussecker, H. 1998 Air-water gas exchange. *Annual Review of Fluid Mechanics* **30**, 443–468.

Jansen, P. C. M. 1986 Laboratory observations of the kinematics in the aerated region of breaking waves. *Coastal Engineering* **9** (5), 453–477.

Jeffreys, H. 1925 On the formation of water waves by wind. *Proceedings of the Royal Society of London Series A-Containing Papers of a Mathematical and Physical Character* **107** (742), 189–206.

Jensen, A., Mayer, S. & Pedersen, G. K. 2005 Experiments and computation of onshore breaking solitary waves. *Measurement Science and Technology* **16** (10), 1913–1920.

Jensen, A., Pedersen, G. K. & Wood, D. J. 2003 An experimental study of wave run-up at a steep beach. *Journal of Fluid Mechanics* **486**, 161–188.

KADOMTSEV, B. B. & PETVIASHVILI, V. I. 1970 On the stability of solitary waves in weakly dispersive media. *Soviet Physics - Doklady* **15**, 539–541.

KANOGLU, U. & SYNOLAKIS, C. E. 1998 Long wave runup on piecewise linear topographies. *Journal of Fluid Mechanics* **374**, 1–28.

KARAMBAS, T. V. & KOUTITAS, C. 1992 A breaking wave propagation model based on the Boussinesq equations. *Coastal Engineering* **18** (1-2), 1–19.

KAWAI, S. 1979 Generation of initial wavelets by instability of a coupled shear-flow and their evolution to wind waves. *Journal of Fluid Mechanics* **93**, 661–703.

KAWAI, S. 1982 Structure of air flow separation over wind wave crests. *Boundary-Layer Meteorology* **23** (4), 503–521.

KAWAMURA, T. 2000 Numerical investigation of turbulence near a sheared airater interface. Part 2: Interaction of turbulent shear flow with surface waves. *Journal of Marine Science and Technology* **5** (4), 161–175.

KHARIF, C., GIOVANANGELI, J. P., TOUBOUL, J., GRARE, L. & PELINOVSKY, E. 2008 Influence of wind on extreme wave events: experimental and numerical approaches. *Journal of Fluid Mechanics* **594**, 209–247.

KHAYYER, A., GOTOH, H. & SHAO, S. D. 2008 Corrected incompressible SPH method for accurate water-surface tracking in breaking waves. *Coastal Engineering* **55** (3), 236–250.

KIMMOUN, O. & BRANGER, H. 2007 A particle image velocimetry investigation on laboratory surf-zone breaking waves over a sloping beach. *Journal of Fluid Mechanics* **588**, 353–397.

KING, D. M. & BAKER, C. J. 1996 Changes to wave parameters in the surf zone due to wind effects. *Journal of Hydraulic Research* **34**, 55–76.

KINSMAN, B. 1965 *Wind waves : their generation and propagation on the ocean surface*. Englewood Cliffs, N.J.: Prentice-Hall.

Kirby, J. T. 2003 Boussinesq models and applications to nearshore wave propagation, surfzone processes and wave-induced currents. In *Advances in Coastal Modeling* (ed. V. C. Lakhan), pp. 1–41. Elsevier.

Kirby, J. T. & Dalrymple, R. A. 1983 A parabolic equation for the combined refraction diffraction of stokes waves by mildly varying topography. *Journal of Fluid Mechanics* **136**, 453–466.

Kleefsman, K. M. T., Fekken, G., Veldman, A. E. P., Iwanowski, B. & Buchner, B. 2005 A Volume-of-Fluid based simulation method for wave impact problems. *Journal of Computational Physics* **206** (1), 363–393.

Korteweg, D. J. & de Vries, G. 1895 On the change of form of long waves advancing in a rectangular canal, and on a new type of long stationary waves. *Philosophical Magazine* **39**, 422–443.

Koshizuka, S., Tamako, H. & Oka, Y. 1995 A particle method for incompressible viscous flow with fluid fragmentation. *Computational Fluid Dynamics Journal* **4** (1), 29–46.

Kothe, D. B., Mjolsness, R. C. & Torrey, M. D. 1991 RIPPLE: A computer program for incompressible flows with free surfaces. *Tech. Rep.* LA-12007-MS. Los Alamos Scientific Laboratory.

Kothe, D. B., Turner, J. A., Mosso, S. J. & Ferrell, R. C. 1997 A high resolution finite volume method for efficient parallel simulation of casting processes on unstructured meshes. *Tech. Rep.* LA-UR-97-30. Los Alamos Scientific Laboratory.

Lachaume, C., Biausser, B., Grilli, S. T., Fraunie, P. & Guignard, S. P. 2003 Modeling of breaking and post-breaking waves on slopes by coupling of BEM and VOF methods. *Proceedings of the Thirteenth (2003) International Offshore and Polar Engineering Conference, Vol 3* pp. 353–359.

Lamarre, E. & Melville, W. K. 1991 Air entrainment and dissipation in breaking waves. *Nature* **351** (6326), 469–472.

Lamb, H. 1932 *Hydrodynamics*, 6th edn. New York: Dover Publications.

Landrini, M., Colagrossi, A., Greco, M. & Tulin, M. P. 2007 Gridless simulations of splashing processes and near-shore bore propagation. *Journal of Fluid Mechanics* **591**, 183–213.

Launder, B. E. & Spalding, D. B. 1974 The numerical computation of turbulent flows. *Computer Methods in Applied Mechanics and Engineering* **3** (2), 269–289.

Lee, J. J., Skjelbreia, J. E. & Raichlen, F. 1982 Measurement of velocities in solitary waves. *Journal of Waterway, Port, Coastal, and Ocean Engineering-ASCE* **108** (2), 200–218.

Lee, Y. G. & Heo, J. K. 2005 Simulating nonlinear waves on the free surface in surf zones with two-dimensional sloping beach. *Ocean Engineering* **32** (1), 57–84.

Lemos, C. M. 1992 A simple numerical technique for turbulent flows with free surfaces. *International Journal for Numerical Methods in Fluids* **15** (2), 127–146.

Leonard, B. P. 1991 The ultimate conservative difference scheme applied to unsteady one-dimensional advection. *Computer Methods in Applied Mechanics and Engineering* **88** (1), 17–74.

Li, P. Y. 1995 A numerical study on energy transfer between turbulent air flow and finite amplitude water waves. PhD thesis, York University.

Li, Y. 2000 Tsunamis: Non-breaking and breaking solitary wave run-up. PhD thesis, California Institute of Technology.

Li, Y. & Raichlen, F. 1998 Discussion: Breaking criterion and characteristics for solitary waves on slopes. *Journal of Waterway, Port, Coastal, and Ocean Engineering-ASCE* **124** (6), 329–333.

Li, Y. & Raichlen, F. 2002 Non-breaking and breaking solitary wave run-up. *Journal of Fluid Mechanics* **456**, 295–318.

Li, Y. & Raichlen, F. 2003 Energy balance model for breaking solitary wave runup. *Journal of Waterway, Port, Coastal, and Ocean Engineering-ASCE* **129** (2), 47–59.

Lighthill, M. J. 1962 Physical interpretation of the mathematical theory of wave generation by wind. *Journal of Fluid Mechanics* **14**, 385–398.

Lin, C. & Hwung, H. H. 1992 External and internal flow-fields of plunging breakers. *Experiments in Fluids* **12** (4-5), 229–237.

Lin, C. Y. 2007 Simulation of breaking waves using particle level set method. PhD thesis, National Cheng Kung University.

Lin, J. C. & Rockwell, D. 1995 Evolution of a quasi-steady breaking wave. *Journal of Fluid Mechanics* **302**, 29–44.

Lin, M. Y., Moeng, C. H., Tsai, W. T., Sullivan, P. P. & Belcher, S. E. 2008 Direct numerical simulation of wind-wave generation processes. *Journal of Fluid Mechanics* **616**, 1–30.

Lin, P. 1998 Numerical modeling of breaking waves. PhD thesis, Cornell University.

Lin, P., Chang, K. A. & Liu, P. L. F. 1999 Runup and rundown of solitary waves on sloping beaches. *Journal of Waterway, Port, Coastal, and Ocean Engineering-ASCE* **125** (5), 247–255.

Lin, P. & Liu, P. L. F. 1998*a* A numerical study of breaking waves in the surf zone. *Journal of Fluid Mechanics* **359**, 239–264.

Lin, P. & Liu, P. L. F. 1998*b* Turbulence transport, vorticity dynamics, and solute mixing under plunging breaking waves in surf zone. *Journal of Geophysical Research-Oceans* **103** (C8), 15677–15694.

Lin, P. & Liu, P. L. F. 1999 Internal wave-maker for Navier-Stokes equations models. *Journal of Waterway, Port, Coastal, and Ocean Engineering-ASCE* **125** (4), 207–215.

Liovic, P. & Lakehal, D. 2007 Multi-physics treatment in the vicinity of arbitrarily deformable gas-liquid interfaces. *Journal of Computational Physics* **222** (2), 504–535.

Liu, P. L. F., Cho, Y. S., Briggs, M. J., Kanoglu, U. & Synolakis, C. E. 1995 Runup of solitary waves on a circular island. *Journal of Fluid Mechanics* **302**, 259–285.

Liu, P. L. F. & Tsay, T. K. 1984 Refraction diffraction model for weakly nonlinear water-waves. *Journal of Fluid Mechanics* **141**, 265–274.

Liu, P. L. F., Wu, T. R., Raichlen, F., Synolakis, C. E. & Borrero, J. C. 2005 Runup and rundown generated by three-dimensional sliding masses. *Journal of Fluid Mechanics* **536**, 107–144.

Liu, Y. M., Xue, M. & Yue, D. K. P. 2001 Computations of fully nonlinear three-dimensional wave-wave and wave-body interactions. Part 2. Nonlinear waves and forces on a body. *Journal of Fluid Mechanics* **438**, 41–66.

Lloyd, P. M. & Stansby, P. K. 1997*a* Shallow-water flow around model conical islands of small side slope .1. surface piercing. *Journal of Hydraulic Engineering-ASCE* **123** (12), 1057–1067.

Lloyd, P. M. & Stansby, P. K. 1997*b* Shallow-water flow around model conical islands of small side slope .2. submerged. *Journal of Hydraulic Engineering-ASCE* **123** (12), 1068–1077.

Lo, E. Y. M. & Shao, S. D. 2002 Simulation of near-shore solitary wave mechanics by an incompressible SPH method. *Applied Ocean Research* **24** (5), 275–286.

Lombardi, P., DeAngelis, V. & Banerjee, S. 1996 Direct numerical simulation of near-interface turbulence in coupled gas-liquid flow. *Physics of Fluids* **8** (6), 1643–1665.

Longuet-Higgins, M. S. 1982 Parametric solutions for breaking waves. *Journal of Fluid Mechanics* **121**, 403–424.

Longuet-Higgins, M. S. 1987 Mechanisms of wave breaking in deep water. In *Sea Surface Sound. Natural Mechanisms of Surface Generated Noise in the Ocean* (ed. B.R. Kerman), pp. 1–30. Kluwer Academic.

Longuet-Higgins, M. S. 1996 Progress toward understanding how waves break. In *21st Symposium on Naval Hydrodynamics*, pp. 7–28. Trondheim, Norway: National Academy Press.

Longuet-Higgins, M. S. & Cokelet, E. D. 1976 The deformation of steep surface-waves on water. Part 1. Numerical method of computation. *Proceedings of the Royal Society of London Series A-Mathematical Physical and Engineering Sciences* **350** (1660), 1–26.

Longuet-Higgins, M. S. & Stewart, R. W. 1962 Radiation stress and mass transport in gravity waves, with application to surf beats. *Journal of Fluid Mechanics* **13**, 481–504.

Lubin, P. 2004 Large eddy simulation of plunging breaking waves. PhD thesis, University of Bordeaux.

Lubin, P., Vincent, S., Abadie, S. & Caltagirone, J. P. 2006 Three-dimensional large eddy simulation of air entrainment under plunging breaking waves. *Coastal Engineering* **53** (8), 631–655.

Lynett, P. J. 2006 Wave breaking velocity effects in depth-integrated models. *Coastal Engineering* **53** (4), 325–333.

Lynett, P. J., Wu, T. R. & Liu, P. L. F. 2002 Modeling wave runup with depth-integrated equations. *Coastal Engineering* **46** (2), 89–107.

Ma, Q. W. & Zhou, J. T. 2009 MLPG_R method for numerical simulation of 2D breaking waves. *CMES-Computer Modeling in Engineering and Sciences* **43** (3), 277–303.

Mader, Charles L. 2004 *Numerical modeling of water waves*, 2nd edn. Boca Raton, FL: CRC Press.

MADSEN, P. A. & SCHAFFER, H. A. 1999 A review of Boussinesq-type equations for surface gravity waves. In *Advances in coastal and ocean engineering* (ed. P. L. F. Liu), , vol. 5, pp. 1–94. World Scientific.

MADSEN, P. A., SORENSEN, O. R. & SCHAFFER, H. A. 1997 Surf zone dynamics simulated by a Boussinesq type model. Part I. Model description and cross-shore motion of regular waves. *Coastal Engineering* **32** (4), 255–287.

MASTENBROEK, C 1996 Wind-wave interaction. PhD thesis, Delft University of Technology.

MAYER, S., GARAPON, A. & SORENSEN, L. S. 1998 A fractional step method for unsteady free-surface flow with applications to non-linear wave dynamics. *International Journal for Numerical Methods in Fluids* **28** (2), 293–315.

MAYER, S. & MADSEN, P. A. 2000 Simulation of breaking waves in the surf zone using a Navier-Stokes solver. In *Proceedings of the 27th International Conference on Coastal Engineering*, , vol. 1, pp. 928–941. Sydney, Australia: ASCE.

MEI, C. C. 1989 *The applied dynamics of ocean surface waves*. World Scientific.

MEI, C. C. & LIU, P. L. F. 1993 Surface-waves and coastal dynamics. *Annual Review of Fluid Mechanics* **25**, 215–240.

MELVILLE, W. K. 1982 The instability and breaking of deep-water waves. *Journal of Fluid Mechanics* **115**, 165–185.

MELVILLE, W. K. 1996 The role of surface-wave breaking in air-sea interaction. *Annual Review of Fluid Mechanics* **28**, 279–321.

MELVILLE, W. K., VERON, F. & WHITE, C. J. 2002 The velocity field under breaking waves: coherent structures and turbulence. *Journal of Fluid Mechanics* **454**, 203–233.

MENCINGER, J. & ZUN, I. 2007 On the finite volume discretization of discontinuous body force field on collocated grid: Application to VOF method. *Journal of Computational Physics* **221** (2), 524–538.

Miles, J. W. 1957 On the generation of surface waves by shear flows. *Journal of Fluid Mechanics* **3**, 185–204.

Mitsuyasu, H. & Honda, T. 1982 Wind-induced growth of water waves. *Journal of Fluid Mechanics* **123**, 425–442.

Mittal, R. & Iaccarino, G. 2005 Immersed boundary methods. *Annual Review of Fluid Mechanics* **37**, 239–261.

Miyata, H. 1986 Finite-difference simulation of breaking waves. *Journal of Computational Physics* **65** (1), 179–214.

Miyata, H., Kanai, A., Kawamura, T. & Park, J. C. 1996 Numerical simulation of three-dimensional breaking waves. *Journal of Marine Science and Technology* **1** (4), 183–197.

Monaghan, J. J. 1994 Simulating free-surface flows with SPH. *Journal of Computational Physics* **110** (2), 399–406.

Muscari, R. & Di Mascio, A. 2003 A model for the simulation of steady spilling breaking waves. *Journal of Ship Research* **47**, 13–23.

Mutsuda, H. & Yasuda, T. 2000 Numerical simulation of turbulent air-water mixing layer within surf-zone. In *Proceedings of the 27th International Conference on Coastal Engineering*, , vol. 1, pp. 755–768. Sydney, Australia: ASCE.

Nadaoka, K., Hino, M. & Koyano, Y. 1989 Structure of the turbulent-flow field under breaking waves in the surf zone. *Journal of Fluid Mechanics* **204**, 359–387.

Nepf, H. M., Wu, C. H. & Chan, E. S. 1998 A comparison of two- and three-dimensional wave breaking. *Journal of Physical Oceanography* **28** (7), 1496–1510.

New, A. L. 1983 A class of elliptical free-surface flows. *Journal of Fluid Mechanics* **130**, 219–239.

New, A. L., Mciver, P. & Peregrine, D. H. 1985 Computations of overturning waves. *Journal of Fluid Mechanics* **150**, 233–251.

Ng, C. O. & Kot, S. C. 1992 Computations of water impact on a 2-dimensional flat-bottomed body with a Volume-of-Fluid method. *Ocean Engineering* **19** (4), 377–393.

Nguyen, V. P., Rabczuk, T., Bordas, S. & Duflot, M. 2008 Meshless methods: A review and computer implementation aspects. *Mathematics and Computers in Simulation* **79** (3), 763–813.

Nichols, B. D. & Hirt, C. W. 1973 Calculating three-dimensional free-surface flows in vicinity of submerged and exposed structures. *Journal of Computational Physics* **12** (2), 234–246.

Nichols, B. D., Hirt, C. W. & Hotchkiss, R. S. 1980 SOLA-VOF: a solution algorithm for transient fluid flow with multiple free boundaries. *Tech. Rep.* LA-8355. Los Alamos Scientific Laboratory.

Noh, W. F. & Woodward, P. 1996 SLIC /simple line interface calculation/. In *5th International Conference on Numerical Methods in Fluid Dynamics* (ed. A. I. van de Vooren & P. J. Zandbergen), pp. 330–340. Springer-Verlag.

Osher, S. & Fedkiw, R. P. 2001 Level set methods: An overview and some recent results. *Journal of Computational Physics* **169** (2), 463–502.

Osher, S. & Sethian, J. A. 1988 Fronts propagating with curvature-dependent speed - algorithms based on Hamilton-Jacobi formulations. *Journal of Computational Physics* **79** (1), 12–49.

Park, J. C., Kim, M. H. & Miyata, H. 1999 Fully non-linear free-surface simulations by a 3D viscous numerical wave tank. *International Journal for Numerical Methods in Fluids* **29** (6), 685–703.

Patankar, S. V. 1980 *Numerical heat transfer and fluid flow*. London: Taylor & Francis,.

Peirson, W. L. & Banner, M. L. 2003 Aqueous surface layer flows induced by microscale breaking wind waves. *Journal of Fluid Mechanics* **479**, 1–38.

Peirson, W. L., Garcia, A. W. & Pells, S. E. 2003 Water wave attenuation due to opposing wind. *Journal of Fluid Mechanics* **487**, 345–365.

Peregrine, D. H. 1967 Long waves on a beach. *Journal of Fluid Mechanics* **27**, 815–827.

Peregrine, D. H. 1983 Breaking waves on beaches. *Annual Review of Fluid Mechanics* **15**, 149–178.

Peregrine, D. H. 2003 Water-wave impact on walls. *Annual Review of Fluid Mechanics* **35**, 23–43.

Perlin, M., He, J. H. & Bernal, L. P. 1996 An experimental study of deep water plunging breakers. *Physics of Fluids* **8** (9), 2365–2374.

Phillips, O. M. 1957 On the generation of waves by turbulent wind. *Journal of Fluid Mechanics* **2**, 417–445.

Phillips, O. M. 1977 *The dynamics of the upper ocean*, 2nd edn. Cambridge: Cambridge University Press.

Phillips, O. M. & Banner, M. L. 1974 Wave breaking in presence of wind drift and swell. *Journal of Fluid Mechanics* **66**, 625–640.

Pilliod, J. E. & Puckett, E. G. 2004 Second-order accurate volume-of-fluid algorithms for tracking material interfaces. *Journal of Computational Physics* **199** (2), 465–502.

Prosperetti, A. & Tryggvason, G. 2007 *Computational methods for multiphase flow*. Cambridge: Cambridge University Press.

Rapp, R. J. & Melville, W. K. 1990 Laboratory measurements of deep-water breaking waves. *Philosophical Transactions of the Royal Society of London Series A-Mathematical Physical and Engineering Sciences* **331** (1622), 735–800.

Reul, N., Branger, H. & Giovanangeli, J. P. 2008 Air flow structure over short-gravity breaking water waves. *Boundary-Layer Meteorology* **126** (3), 477–505.

Rhee, S. H. & Stern, F. 2002 RANS model for spilling breaking waves. *Journal of Fluids Engineering-Transactions of the ASME* **124** (2), 424–432.

Rider, W. J. & Kothe, D. B. 1998 Reconstructing volume tracking. *Journal of Computational Physics* **141** (2), 112–152.

Roberts, A. J. 1983 A stable and accurate numerical-method to calculate the motion of a sharp interface between fluids. *IMA Journal of Applied Mathematics* **31** (1), 13–35.

Roe, P. L. 1986 Characteristic-based schemes for the Euler equations. *Annual Review of Fluid Mechanics* **18**, 337–365.

Rudman, M. 1997 Volume-tracking methods for interfacial flow calculations. *International Journal for Numerical Methods in Fluids* **24** (7), 671–691.

Rudman, M. 1998 A volume-tracking method for incompressible multifluid flows with large density variations. *International Journal for Numerical Methods in Fluids* **28** (2), 357–378.

Russell, J. S. 1844 Report on waves. *14th Meeting of the British Association for the Advancement of Science* pp. 311–390.

Sagaut, P. 2002 *Large Eddy Simulation For Incompressible Fows: An Introduction*, 2nd edn. Berlin: Springer.

Scardovelli, R. & Zaleski, S. 1999 Direct numerical simulation of free-surface and interfacial flow. *Annual Review of Fluid Mechanics* **31**, 567–603.

Schaffer, H. A., Madsen, P. A. & Deigaard, R. 1993 A Boussinesq model for waves breaking in shallow-water. *Coastal Engineering* **20** (3-4), 185–202.

Sethian, J. A. & Smereka, P. 2003 Level set methods for fluid interfaces. *Annual Review of Fluid Mechanics* **35**, 341–372.

Shao, S. D. 2006 Simulation of breaking wave by SPH method coupled with k-ϵ model. *Journal of Hydraulic Research* **44** (3), 338–349.

Shao, S. D. & Ji, C. M. 2006 SPH computation of plunging waves using a 2-D sub-particle scale (SPS) turbulence model. *International Journal for Numerical Methods in Fluids* **51** (8), 913–936.

She, K., Greated, C. A. & Easson, W. J. 1997 Experimental study of three-dimensional breaking wave kinematics. *Applied Ocean Research* **19** (5-6), 329–343.

Shen, L., Zhang, X., Yue, D. K. P. & Triantafyllou, M. S. 2003 Turbulent flow over a flexible wall undergoing a streamwise travelling wave motion. *Journal of Fluid Mechanics* **484**, 197–221.

Sitanggang, K. I. & Lynett, P. J. 2010 Multi-scale simulation with a hybrid Boussinesq-RANS hydrodynamic model. *International Journal for Numerical Methods in Fluids* **62** (9), 1013–1046.

Skyner, D. 1996 A comparison of numerical predictions and experimental measurements of the internal kinematics of a deep-water plunging wave. *Journal of Fluid Mechanics* **315**, 51–64.

Smagorinsky, J. 1963 General circulation experiments with the primitive equations: I. the basic experiment. *Monthly Weather Review* **91** (3), 99–164.

Sobey, R. J. 1986 Wind-wave prediction. *Annual Review of Fluid Mechanics* **18**, 149–172.

Song, C. Y. & Sirviente, A. I. 2004 A numerical study of breaking waves. *Physics of Fluids* **16** (7), 2649–2667.

Sorensen, O. R., Schaffer, H. A. & Sorensen, L. S. 2004 Boussinesq-type modelling using an unstructured finite element technique. *Coastal Engineering* **50** (4), 181–198.

Sorensen, R. M. 2006 *Basic Coastal Engineering*, 3rd edn. Berlin: Springer.

Spalding, D. B. 1961 A single formula for the law of the wall. *Journal of Applied Mechanics* **28**, 455–458.

Stansby, P. K. 2003 Solitary wave run up and overtopping by a semi-implicit finite-volume shallow-water Boussinesq model. *Journal of Hydraulic Research* **41** (6), 639–647.

Stansby, P. K. & Feng, T. 2005 Kinematics and depth-integrated terms in surf zone waves from laboratory measurement. *Journal of Fluid Mechanics* **529**, 279–310.

Stansby, P. K., Hunt, A. C., Xu, R., Taylor, P. H., Borthwick, A. G. L., Feng, T. & Laurence, D. R. 2007 Wave overtopping from focussed wave groups: experiments and modelling. In *2nd IMA International Conference on Flood Risk Assessment*. Plymouth, UK.

Stive, M. J. F. & Wind, H. G. 1982 A study of radiation stress and set-up in the nearshore region. *Coastal Engineering* **6** (1), 1–25.

Su, M. Y., Bergin, M., Marler, P. & Myrick, R. 1982 Experiments on nonlinear instabilities and evolution of steep gravity-wave trains. *Journal of Fluid Mechanics* **124**, 45–72.

Sullivan, P. P., McWilliams, J. C. & Moeng, C. H. 2000 Simulation of turbulent flow over idealized water waves. *Journal of Fluid Mechanics* **404**, 47–85.

Sussman, M. & Puckett, E. G. 2000 A coupled level set and volume-of-fluid method for computing 3D and axisymmetric incompressible two-phase flows. *Journal of Computational Physics* **162** (2), 301–337.

Sussman, M., Smereka, P. & Osher, S. 1994 A level set approach for computing solutions to incompressible two-phase flow. *Journal of Computational Physics* **114** (1), 146–159.

Svendsen, I. A. 2005 *Introduction to Nearshore Hydrodynamics*. World Scientific.

Svendsen, I. A., Yu, K. & Veeramony, J. 1996 A Boussinesq breaking wave model with vorticity. In *Proceedings of the 25th International Conference on Coastal Engineering* (ed. B. L. Edge), pp. 1192–1204. ASCE.

Synolakis, C., Bernard, E., Titov, V., Koglu, U. & Gonzez, F. 2008 Validation and verification of tsunami numerical models. *Pure and Applied Geophysics* **165** (11), 2197–2228.

Synolakis, C. E. 1986 The runup of long waves. PhD thesis, California Institute of Technology.

Synolakis, C. E. 1987 The runup of solitary waves. *Journal of Fluid Mechanics* **185**, 523–545.

Synolakis, C. E. & Bernard, E. N. 2006 Tsunami science before and beyond Boxing Day 2004. *Philosophical Transactions of the Royal Society A-Mathematical Physical and Engineering Sciences* **364** (1845), 2231–2265.

Synolakis, C. E. & Skjelbreia, J. E. 1993 Evolution of maximum amplitude of solitary waves on plane beaches. *Journal of Waterway, Port, Coastal, and Ocean Engineering-ASCE* **119** (3), 323–342.

Takikawa, K., Yamada, F. & Matsumoto, K. 1997 Internal characteristics and numerical analysis of plunging breaker on a slope. *Coastal Engineering* **31** (1-4), 143–161.

Thais, L. & Magnaudet, J. 1996 Turbulent structure beneath surface gravity waves sheared by the wind. *Journal of Fluid Mechanics* **328**, 313–344.

Ting, F. C. K. & Kirby, J. T. 1994 Observation of undertow and turbulence in a laboratory surf zone. *Coastal Engineering* **24** (1-2), 51–80.

Ting, F. C. K. & Kirby, J. T. 1995 Dynamics of surf-zone turbulence in a strong plunging breaker. *Coastal Engineering* **24** (3-4), 177–204.

Ting, F. C. K. & Kirby, J. T. 1996 Dynamics of surf-zone turbulence in a spilling breaker. *Coastal Engineering* **27** (3-4), 131–160.

Titov, V. V. & Synolakis, C. E. 1995 Modeling of breaking and nonbreaking long-wave evolution and runup using VTCS-2. *Journal of Waterway, Port, Coastal, and Ocean Engineering-ASCE* **121** (6), 308–316.

Titov, V. V. & Synolakis, C. E. 1998 Numerical modeling of tidal wave runup. *Journal of Waterway, Port, Coastal, and Ocean Engineering-ASCE* **124** (4), 157–171.

Tome, M. F. & Mckee, S. 1994 GENSMAC - a computational marker and cell method for free-surface flows in general domains. *Journal of Computational Physics* **110** (1), 171–186.

Torrey, M. D., Cloutman, L. D., Mjolsness, R. C. & Hirt, C. W. 1985 NASA-VOF2D: a computer program for incompressible flows with free surfaces. *Tech. Rep.* LA-10612-MS. Los Alamos Scientific Laboratory.

Townsend, A. A. 1972 Flow in a deep turbulent boundary-layer over a surface distorted by water waves. *Journal of Fluid Mechanics* **55**, 719–735.

Tsai, W. T., Chen, S. M. & Moeng, C. H. 2005 A numerical study on the evolution and structure of a stress-driven free-surface turbulent shear flow. *Journal of Fluid Mechanics* **545**, 163–192.

Tsanis, I. K. 1989 Simulation of wind-induced water currents. *Journal of Hydraulic Engineering-ASCE* **115** (8), 1113–1134.

Ubbink, O. 1997 Numerical prediction of two fluid systems with sharp interfaces. PhD thesis, Imperial College of Science, Technology and Medicine.

Udaykumar, H. S., Kan, H. C., Shyy, W. & TranSonTay, R. 1997 Multiphase dynamics in arbitrary geometries on fixed cartesian grids. *Journal of Computational Physics* **137** (2), 366–405.

Unverdi, S. O. & Tryggvason, G. 1992 A front-tracking method for viscous, incompressible, multi-fluid flows. *Journal of Computational Physics* **100** (1), 25–37.

URSELL, F. 1956 Wave generation by wind. In *Surveys in Mechanics* (ed. G. K. Batchelor & R. M. Davies), pp. 216–249. Cambridge: Cambridge University Press.

VALIANI, A. & BEGNUDELLI, L. 2006 Divergence form for bed slope source term in shallow water equations. *Journal of Hydraulic Engineering-ASCE* **132** (7), 652–665.

VEERAMONY, J. & SVENDSEN, I. A. 2000 The flow in surf-zone waves. *Coastal Engineering* **39** (2-4), 93–122.

VERSTEEG, H. K. & MALALASEKERA, W. 2007 *An introduction to computational fluid dynamics : the finite volume method*, 2nd edn. Harlow: Pearson Prentice Hall.

VINCENT, C. L. & BRIGGS, M. J. 1989 Refraction - diffraction of irregular waves over a mound. *Journal of Waterway, Port, Coastal, and Ocean Engineering-ASCE* **115** (2), 269–284.

VINCENT, S. & CALTAGIRONE, J. P. 1999 Efficient solving method for unsteady incompressible interfacial flow problems. *International Journal for Numerical Methods in Fluids* **30** (6), 795–811.

VINJE, T. & BREVIG, P. 1981 Numerical simulation of breaking waves. *Advances in Water Resources* **4** (2), 77–82.

VAN DER VORST, H. A. 1992 Bi-CGSTAB - a fast and smoothly converging variant of Bi-CG for the solution of nonsymmetric linear-systems. *SIAM Journal on Scientific and Statistical Computing* **13** (2), 631–644.

WANG, H. W. 2007 Development of a 3D numerical viscous wave tank and its applications. PhD thesis, National Cheng Kung University.

WANG, P., YAO, Y. T. & RULIN, M. P. 1995 An efficient numerical tank for nonlinear water-waves, based on the multi-subdomain approach with BEM. *International Journal for Numerical Methods in Fluids* **20** (12), 1315–1336.

Wang, Z., Yang, J., Koo, B. & Stern, F. 2009*a* A coupled level set and volume-of-fluid method for sharp interface simulation of plunging breaking waves. *International Journal of Multiphase Flow* **35** (3), 227–246.

Wang, Z., Zou, Q. & Reeve, D. E. 2009*b* Simulation of spilling breaking waves using a two phase flow CFD model. *Computers & Fluids* **38** (10), 1995–2005.

Ward, D. L., Wibner, C. G. & Zhang, J. 1998 Runup on coastal revetments under the influence of onshore wind. *Journal of Coastal Research* **14** (4), 1325–1333.

Watanabe, Y. & Saeki, H. 1999 Three-dimensional large eddy simulation of breaking waves. *Coastal Engineering Journal* **41**, 281–301.

Watanabe, Y. & Saeki, H. 2002 Velocity field after wave breaking. *International Journal for Numerical Methods in Fluids* **39** (7), 607–637.

Watanabe, Y., Saeki, H. & Hosking, R. J. 2005 Three-dimensional vortex structures under breaking waves. *Journal of Fluid Mechanics* **545**, 291–328.

Waterson, N. P. & Deconinck, H. 2007 Design principles for bounded higher-order convection schemes - a unified approach. *Journal of Computational Physics* **224** (1), 182–207.

Wei, Y., Mao, X. Z. & Cheung, K. F. 2006 Well-balanced finite-volume model for long-wave runup. *Journal of Waterway, Port, Coastal, and Ocean Engineering-ASCE* **132** (2), 114–124.

Wemmenhove, R. 2008 Numerical simulation of two-phase flow in offshore environments. PhD thesis, University of Groningen.

Whalin, R.W. 1971 The limit of applicability of linear wave refraction theory in a convergence zone. *Tech. Rep.* H-71. U.S. Army Corps of Engineers, Waterways Experiment Stations, Vicksburg, MS.

Wu, C. H. & Nepf, H. M. 2002 Breaking criteria and energy losses for three-dimensional wave breaking. *Journal of Geophysical Research-Oceans* **107** (C10), 3177.

Wu, J. 1968 Laboratory studies of wind-wave interactions. *Journal of Fluid Mechanics* **34**, 91–111.

Wu, J. & Tsanis, I. K. 1995 Numerical study of wind-induced water currents. *Journal of Hydraulic Engineering-ASCE* **121** (5), 388–395.

Wu, T. R. 2004 A numerical study of three-dimensional breaking waves and turbulence effects. PhD thesis, Cornell University.

Xie, Z., Wen, X. & Ross, A. N. 2009 Numerical simulation of wind effects on breaking solitary waves by Navier-Stokes equations. In *Proceedings of the 28th International Conference on Offshore Mechanics and Arctic Engineering*, pp. OMAE2009–79054. Hawaii, USA.

Xü, H. B. 1992 Numerical study of fully nonlinear water waves in three dimensions. PhD thesis, Massachusetts Institute of Technology.

Xü, H. B. & Yue, D. K. P. 1992 Numerical study of three-dimensional overturning water waves. In *Proceedings of the 7th International Workshop on Water Waves and Floating Bodies*. Val de Reuil, France.

Xue, M., Xü, H. B., Liu, Y. M. & Yue, D. K. P. 2001 Computations of fully nonlinear three-dimensional wave-wave and wave-body interactions. Part 1. Dynamics of steep three-dimensional waves. *Journal of Fluid Mechanics* **438**, 11–39.

Yabe, T., Xiao, F. & Utsumi, T. 2001 The constrained interpolation profile method for multiphase analysis. *Journal of Computational Physics* **169** (2), 556–593.

Yamazaki, Y., Kowalik, Z. & Cheung, K. F. 2009 Depth-integrated, non-hydrostatic model for wave breaking and run-up. *International Journal for Numerical Methods in Fluids* **61** (5), 473–497.

Yan, S. & Ma, Q. W. 2010 QALE-FEM for modelling 3D overturning waves. *International Journal for Numerical Methods in Fluids* **63** (6), 743–768.

Yang, J. & Stern, F. 2009 Sharp interface immersed-boundary/level-set method for wave-body interactions. *Journal of Computational Physics* **228** (17), 6590–6616.

Yasuda, T., Mutsuda, H. & Mizutani, N. 1997 Kinematics of overturning solitary waves and their relations to breaker types. *Coastal Engineering* **29** (3-4), 317–346.

Yeh, H., Liu, P., Briggs, M. & Synolakis, C. 1994 Propagation and amplification of tsunamis at coastal boundaries. *Nature* **372** (6504), 353–355.

Youngs, D. L. 1982 Time-dependent multi-material flow with large fluid distortion. In *Numerical methods for fluid dynamics* (ed. K. W. Morton & M. J. Baines), pp. 273–285. New York: Academic.

Zelt, J. A. 1991 The run-up of nonbreaking and breaking solitary waves. *Coastal Engineering* **15** (3), 205–246.

Zhao, Q., Armfield, S. & Tanimoto, K. 2004 Numerical simulation of breaking waves by a multi-scale turbulence model. *Coastal Engineering* **51** (1), 53–80.

Zwart, P. J. 1999 The integrated space-time finite volume method. PhD thesis, University of Waterloo.